MULTICELLULAR MULTISCALE SPATIAL MODELING OF THE IMMUNE RESPONSE TO PATHOGENS AND CANCER

Josua Oscar Aponte-Serrano

Submitted to the faculty of the University Graduate School in partial fulfillment of the requirements for the degree of Doctor of Philosophy in the School of Informatics, Computing and Engineering, Indiana University

December 2021

Accepted by the Graduate Faculty, Indiana University, in partial fulfillment of the requirements for the degree of Doctor of Philosophy

Doctoral Committee:

James Glazier (chair) Ph.D.

Maria Bondesson Bolin, Ph.D.

Amit Hagar, Ph.D.

Vikram Jadhao, Ph.D.

Amber Smith, Ph.D.

Defense Date: November 5, 2021

Acknowledgments

I want to acknowledge first the members of the dissertation committee Dr.Maria Bondesson Bolin, Dr.Vikram Jadhao and Dr.Amber Smith for their mentorship and their willingness to review this thesis. I want to acknowledge Dr.Amit Hagar for his unconditional mentorship and for believing me possible of thing I did not know I was able to accomplish. I want to acknowledge my advisor Dr. James Glazier for his years of mentorship and his words (kind of though) whenever they were necessary. James always pushed me to be a better student and better scientist.

I want to acknowledge my colleagues at the Biocomplexity Institute and the Intelligent Systems Engineering program for their companionship, mentorship and support. Dr. TJ Sego was always an encouraging mentor, collaborator and had the patience to teach me how to properly code. I want to thank also to the graduate students in the lab: (now Dr.) Priyom Adhayapok and Juliano Gianlupi. I took care of Priyom plants and Juliano took care of mine.

I want to acknowledge the co-authors on the papers some of the chapter of this dissertation are based on: TJ Sego, Juliano Ferrari Gianlupi, Samuel R. Heaps, Kira Breithaupt, Lutz Brusch, Jessica Crawshaw, James M. Osborne, Ellen M. Quardokus, Richard K. Plemper, Jordan Weaver and Jason Shoemaker.

I want to thank my friends back in Puerto Rico: Estela, Erika, Rafael, Jesús, Victor, Suaz and Ray. Thanks for your complicity. I also want to thank my best friend from Bloomington Adam for unconditionally being there for me. And I want to thank my parents: mami and papi, Thanks for your love, your support and for always being my biggest fans.

Josua Oscar Aponte Serrano

Multicellular Multiscale Spatial Modeling Of The Immune Response To Pathogens And Cancer

Mathematical and computational models are essential for investigating the complex interactions of the immune response to diseases. Multiscale and multicellular spatial models can provide insight into the mechanisms leading to the observed differences in clinical outcomes. We present various methodologies and models to address some of this complexity. First, a multiscale framework is proposed to investigate the dynamics of primary viral infection and immune response. Variation over key model parameters show the distinct patterns of viral dynamics observed experimentally. Second, a multiscale model coupling intracellular signaling pathways and cell-cell interactions is proposed to investigate the dependency of viral growth on the strength of the innate intracellular response to infections via production of inhibitory signaling molecules. The viral growth pattern is shown to qualitatively reproduce the growth rates of viral plaques in vitro. Third, we propose a model of the regulation of the inflammatory response to tumors to investigate the relation between the metabolic profile of individual cancer cells and tumor progression. The model is compared and calibrated against clinical data from T1 invasive ductal carcinoma patients. Finally, we propose a research workflow for integrating ordinary differential equation models and spatial multiscale multicellular models that leverage the advantages of both modeling methodologies to study progression of diseases. We applied this workflow to investigate the dynamics of the interactions between RSV and HMPV viruses when co-infecting the same tissues.

Table of Contents

I. Systems Biology and Immunology: Concepts, Methods and Tools 1

Systems Biology and Immunology 1

Quantitative Modeling Approaches 6

Mathematical and Computational Modeling of the Immune Response to Viral Infections 12

Mathematical and Computational Modeling of the Immune Response to Cancer 17

Dissertation Organization 22

II. A multiscale, multicellular, spatiotemporal model of acute primary viral infection and immune response in epithelial tissues and its application to drug therapy timing and effectiveness 25

Introduction 25

Models and Methods 33

Modules 33

Epithelial Cell Modules 33

Transport Modules 41

Immune Cell Modules 44

Lymph Node Component 47

Initial and Boundary Conditions 49

Simulation Specifications 50

Results 54

Classification of Spatiotemporal Infection Dynamics 53

Stronger Immune Response and Lower Rates of Virus Internalization

Promote Containment of Infection 57

Moderate Inhibition of Genomic Replication by Antiviral Therapies

Significantly Reduces the Spread of Infection When Initiated Early

During Infection 61

Discussion 68

Future Perspectives 70

III. Multicellular Spatial Model of RNA Virus Replication and Interferon Responses Reveals Factors Controlling Plaque Growth Dynamics 76

Introduction 76

Material and Methods 79

Spatial Considerations of the MSIS model 79

Cell Types and Rationale 80

Cell Type Transition Probabilities 81

Intracellular Model Equations and Rationale 83

Diffusion of Extracellular Species and Implementation in CC3D 87

Initial and Boundary Conditions 88

Parameter Determination 88

Plaque Growth Metrics 90

Results 91

Multicellular Spatial Model of RNA Virus Infection and IFN Signaling (MSIS model) Reproduces ODE Model Dynamics for High MOI Infection 91

MSIS Model Recapitulates Experimentally Observed Plaque Formation and Growth Dynamics 94

Increased STAT Activity Leads to Arrested Plaque Growth and Reduces Final Plaque Diameter 98

Elevated RIG-I Activity Delays Cell Death and Increases IFN Production 101

Interferon Prestimulation Arrests Plaque Growth 103

Faster Interferon Diffusion Promotes Plaque Growth Arrest 105

Sensitivity Analysis Reveals that the Main Parameters Controlling Radial Plaque Growth Differ Between Regimes 106

Discussion 110

IV. Run for your life – an integrated virtual tissue platform for incorporating exercise oncology into immunotherapy 114

Introduction 114

Methods 115

Clinical Data 115

Model Conceptualization 116

Glycolysis and Hypoxia Tolerance 119

Immune suppressors and Immune Promoters Dynamics 121

CompuCell3D Implementation 123

Cell Types 126

Chemical Fields and Diffusion 127

Tumor Cell Transitions 129

Cell Growth and Mitosis 130

Chemotaxis 131

Immune Cell Recruitment 132

Immune Cell Cytotoxicity 134

Immune Cell Inhibition 134

Immunotherapy 135

Model Calibration 136

Effect of Aerobic Fitness on Tumor Progression Rate 136

Prevalence of Clinical Tumors in Athletes vs. Non-Athletes 138

Results 140

Time Series of Anti-Tumor Immune Response in the TME 140

Incorporating Aerobic Fitness into the Personalization of Immunotherapy 141

Discussion 143

V. Multicellular and Spatial Modeling of RSV-HMPV Co-Infection In Vitro Shows Viral Competition Cannot Recapitulate Experimental Data 147

Introduction 147

Methods 151

Model Development Workflow 151

Experimental Data 152

Single Infection ODE Model 153

Parameter Fitting and Identification 155

Single Infection ODE to ABM Model Translation 157

Coinfection ABM model 158

Results 159

Single Infection ODE Model Fitting and Parameter Identification................ 159

Single Infection ABM Model Translation 161

Coinfection ABM Model Dynamics 164

ABM Model Validation 166

Discussion 169

Appendix A: Modularity and Extensibility of Viral Infection Framework 172

Coupling IFN model with Lymph Node model and Immune Cell Recruitment......... 174

Coupling IFN model with Immune Cell Cytotoxicity 179

Interferon Pretreatment 182

Discussion 184

References 186

Curriculum Vita

Systems Biology and Immunology: Concepts, Methods and Tools

Systems Biology and Immunology

The role of the immune system is both to eliminate pathogens and to maintain physiological homeostasis when disrupted. The multiple components and interactions of the immune system constitute a complex network of feedback mechanisms that ensure its timely activation and inhibition leading to the elimination of physiological insults while avoiding massive physiological damage [1]. The networks are composed of different types of immune cells and biological molecules that facilitate communication between cells. These networks span multiple spatiotemporal scales: from microsecond and nanometers (at the molecular level) to days and several meters (at the whole organism level). Improper regulation of the immune response can lead to failures to contain pathogens, inadequate responses to malingant cells and autoimmune diseases [2]. Characterizing and understanding the interactions between the different components of the immune system is an urgent yet challenging task.

Epithelial cells constitute barriers between different physiological compartments and the external environment [3]. These cells are the first line of defense against invasive pathogens, such as viruses and bacteria, but can themselves become cancerous threats. A pathogen is an infectious agent that can lead to either acute or chronic infection in a host. Examples of pathogens that cause acute infections are respiratory viruses (Influenza, SARS) and certain types of hepatitis viruses. Examples of pathogens that lead to chronic infections are human immunodeficiency virus (HIV) and certain bacteria such as Mycobacterium tuberculosis, the causing of agent of Tuberculosis (TB) [4].

The immune system can be broadly divided into two arms: the innate and the adaptive immune response. The innate immune response is the body's initial response against physiological insults. The innate response is non-specific and short-lived. Resident macrophages are a type of innate immune cell that live permanently in tissues and are constantly surveilling against threats. When threats are detected, macrophages initiate the inflammatory immune response by alerting neutrophils and other types of circulating lymphocytes [3]. As part of this initial response, both epithelial cells and macrophages secrete a variety of proinflammatory cytokines and chemokines such as interleukins (IL-8), interferons (IFNa) and tumor necrosis factors (TNFa). Type I interferons are signaling molecules produced by virally infected cells. Downstream activation of the interferon autocrine and paracrine signaling pathways lead to upregulation of interferon stimulated genes and induction of an antiviral state in epithelial cells. These cytokines play an important role in recruiting immune cells to the inflammation site. Inflammation also increases the flux of antigen presenting cells (APCs) that are responsible for initiating the adaptative immune response.

The adaptive immune response is initiated in lymphatic tissue by a type of APC called dendritic cells (DCs). DCs phagocytose pathogenic cells and debris at the site of inflammation and undergo a maturation process that induce antigen presentation on major histocompatibility complexes (MHC) [5]. Mature DCs migrate to nearby lymph nodes via the vessels of the lymphatic system. Recognition of antigens by Naïve T cells leads to activation of intracellular signaling cascades resulting in rapid proliferation and differentiation. Mature T cells can either migrate to the inflammation site or serve helper function for B cells [5]. At the inflammation site, cytotoxic T cells induce apoptosis on target cells and secrete cytokines to further increase the adaptive immune response. B cell activation results in antibody production and creates memory of pathogen exposure. The immune response is resolved by the secretion of anti-inflammatory cytokines (IL-4, IL-6, IL-11) by certain immunoregulatory cells (such as macrophages and regulatory T cells) and apoptosis of infected/malignant cells [3]. Figure 1 provides a schematic representation of the components and interactions of the immune system.

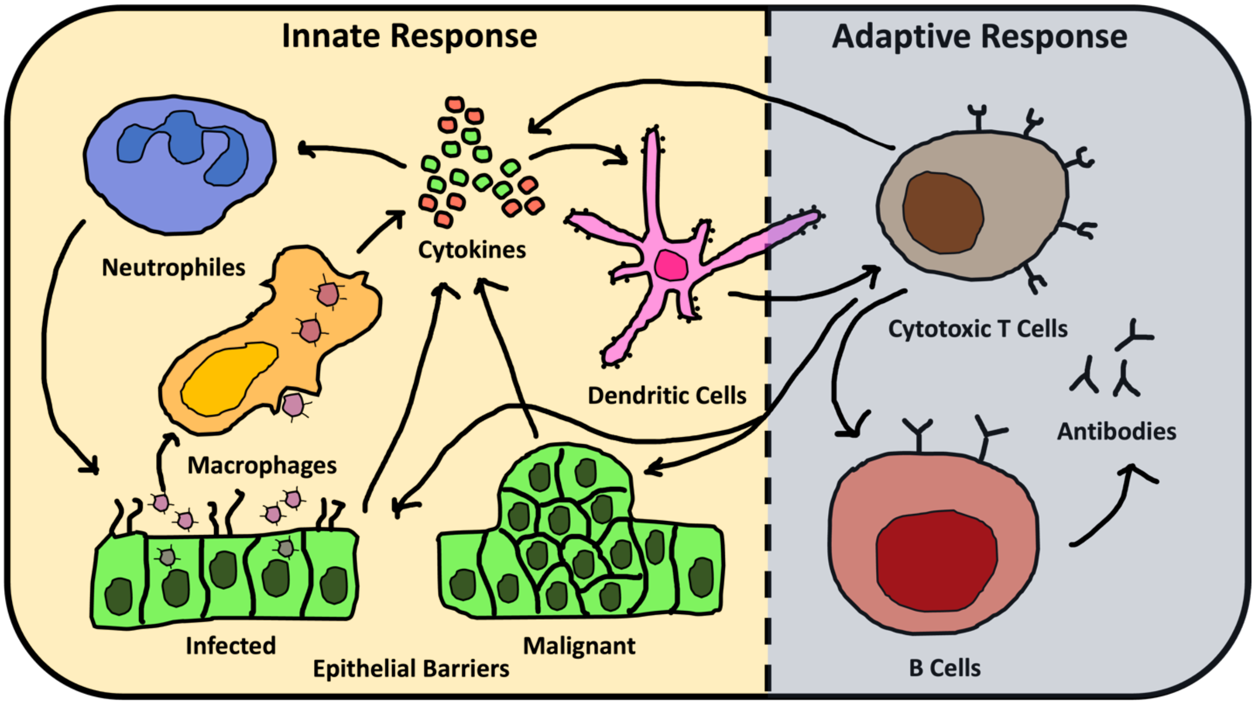
Innate Response
Adaptive Response
Neutrophiles
Cytokines
Macrophages
Dendritic Cells
Cytotoxic T Cells
Antibodies
Infected
Malignant
Epithelial Barriers
B Cells

Figure 1.1. Key Components and Interactions of the Innate and Adaptive Immune System. Schematic representation of some of the components and interactions of the immune system that are recurrent modeling targets in the following projects. Infected and malignant epithelial cells initiate the innate immune response by activating the resident macrophage population. Macrophages secrete signaling molecules known as cytokines and recruit circulating lymphocytes (such as neutrophiles) and antigen presenting cells (such as dendritic cells). Dendritic cells travel to nearby lymphatic sites where they initiate maturation of T cells. Cytotoxic T cells travel back to the inflammation site where they kill cells by

recognizing antigens. Helper T cells initiate B cell maturation leading to production of antibodies. Immunoregulatory cells and molecules resolve the immune response. Adapted from [6].

Novel experimental techniques have helped expand our understanding of the components and interactions of the immune system. Technologies such as flow cytometry, mass spectrometry and mass cytometry enable characterization of multiple immunoregulating proteins. Single cell RNA sequencing (scRNA-seq) enables discovery of immune cell types and identification of genetic markers and therapeutic targets [1]. New microscopy techniques such as fluorescence *in situ* hybridization (smFISH) allow to collect new spatiotemporal information regarding immune cell activity which was difficult to collect before. Combinations of these techniques greatly augment the type of information investigators have access to. For example, some groups have combined mass spectrometry and flow cytometry to identify antibodies per cell type. Other groups have combined smFISH and sc-RNAseq to identify cell phenotypes in mouse liver cells.

Despite the wealth of information produced by these experimental techniques, important questions remain. How can this information be used to develop a dynamic understanding of the interactions between the different components of the immune system? How can variations in the immune response between individuals be explained mechanistically? How can individual components be targeted to improve the immune response and the overall human health? [1] Addressing these pressing questions in the face of the large number of components and non-linear interactions of the immune system requires synthesizing the wealth of information into simple mechanistic explanations. Data cannot be additively added to reconstruct the dynamics of such a complex system [7]. Mathematical and computational models can aid in accomplishing such task.

Systems biology, and systems immunology in specific, provides a framework to organize and quantitatively characterize the key interactions of the immune response. The goal of such approach is to produce representative models that can be used to generate and test mechanistic hypotheses about the immune system [7]. Experimentally guided mathematical and computational models describe how the components and interactions of the immune system change in time, and in response to external perturbations, often in non-linear forms. The computational implementation of mathematical models allows for the evaluation of multiple mechanistic hypothesis while reducing complex analytical methods and expensive/time-consuming experiments [8].

Integrating data across different temporal and spatial scales is another challenge that systems immunology can help overcome. Mechanistic hypotheses that integrate multi-cellular signaling and interactions at tissue level are the most challenging to generate and experimentally validate [2]. Multiscale modeling approaches integrate hypotheses about mechanism interacting at different spatiotemporal scales. These models often include large numbers of parameters and big uncertainties about the meaning or value of such parameters. Despite of this uncertainty, multiscale models can be inquired about their predicted behaviors when exploring different ranges of their parameters [2]. These parameters explorations often show qualitatively different behaviors when parameters are altered and demarcate the regions of the parameter space that correspond to biologically realistic parameter ranges. This type of sensitivity analysis can also help distinguishing critical and noncritical parameters, suggesting key and redundant interactions as well as possible therapeutic targets [9].

Quantitative Modeling Approaches

Over the recent years, and as systems biology have become an established research paradigm, multiple quantitative approaches have been developed to address some of the issues discussed above. These approaches can be grouped in three general categories. 1) Statistical methods that identify patterns in the data by incorporating the least possible number of assumptions. Statistical methods include machine learning algorithms [10]. 2) Non-spatial mathematical methods that model the dynamics of biological systems by incorporating mechanistic hypothesis but rely on mean-field approximations [10]. 3) Spatiotemporal methods that also include mechanistic hypothesis but also incorporate spatial information. In some case, spatiotemporal models can also include information about each individual component of the complex system.

Statistical methods and machine learning algorithms produce data models as mathematical abstractions of the underlying patters in the data. These models can be predictive if the data used to train the models is sound but are rarely explanatory since they do not incorporate mechanistic hypotheses. These techniques are predominantly used in bioinformatics and biostatistics to identify gene expression patterns in cell populations. Regression models find the values of the parameters of a given mathematical function that better fits time-series data. Hidden Markov models are used to explain correlations in the data by assuming that the underlying mechanisms drive the dynamics of the system are 'unknown' but indicators can be observed [10]. Multivariate techniques can be used to build statistical models that include spatial information by correlating spatiotemporal data.

Non-spatial dynamical models use mathematical formalisms to explain the data by expressing mechanistic hypothesis about the target biological system. The key difference between statistical and dynamical models is that the explanatory and predictive capabilities of the latter depend on the soundness of the hypotheses and assumptions incorporated into them. Rule-based modeling uses semantical and notional rules to represent chemical interactions between molecular species [8]. BioNetGen is an example of a tool used for implementing rule-based modeling [11]. Boolean networks approximate the dynamics of the target systems by assuming that its key components can be in either true state or false state. The state of each of the variables of the network are updated by Boolean functions that determine the next value of the variable based on particular inputs [8]. MaBoos [12] and BoolNet [13] are some of the tools used to implement Boolean network modeling.

Ordinary differential equation (ODE) models represent the dynamics of the system by describing how each of the state variables change as continuous functions of the rest of the variable of the system. ODEs have the advantage of being tractable and easy to implement. Simple ODE systems are analytically tractable while complex ODE systems are computationally tractable [4]. Sensitivity and bifurcation techniques can be used to study the behavior of ODE models over different ranges of their parameter, often revealing multiple stable states in the system that can have clinically relevant interpretation as healthy (e.g successful viral or tumor clearance) or unhealthy states (e.g chronic viral infection or unsuccessful cancer treatment). ODE models are the state-of-the-art approach in modeling complex systems, including the immune response. These different types of dynamical models can be either stochastic or deterministic depending on whether the dynamics of the system are fully determined by transition rules and initial conditions.

Despite being analytically and computational tractable, there are limitations to these non-spatial methods. These models assume that the variables they describe are homogenously distributed in the compartments they describe. This assumption might be a good approximation when data is collected from homogenate tissue, such as blood, spleen, or the lymph, but might not be realistic in other tissues, where the resulting dynamics might be dependent on highly localized and stochastic events [10]. A continuous state alternative is using "reaction-diffusion" equations in the form of partial differential equations (PDEs). PDEs can capture changes in the dynamics of the system as a function of more than one independent variable (such as time and space). As PDEs become more complicated, computationally solving them can be challenging. Although PDEs can provide spatial information, their solutions are still mean field descriptions of the system and provide no information about the individual components of the systems [4].

Agent-based models (ABMs) are alternatives to mean-field modeling approaches. ABMs describe biological systems as composed by populations of agents, and the dynamics of the whole systems are determined by the interactions between these individual agents. ABMs can generate complex and emergent behaviors, including intricate spatial and temporal patters, from relatively simple rules [4]. The properties and behaviors of agents can be describe using a language that closely resembles the language used to describe the system itself thus facilitating collaboration between modelers and experimentalists. AMBs are intrinsically stochastic and can capture variations in the outcomes of diseases that depend on highly localized events [4]. ABMs have been used to study tumor growth, tuberculosis, and viral infections such as Influenza and SARS-CoV-2.

ABMs can be realized using different mathematical frameworks and can be simulated on-lattice or lattice-free. Cellular Automata (CA) represent agents as single pixels in a grid. CAs are computationally inexpensive but limited in terms of the spatial resolution. On the opposite end, Cellular Potts Models (CPM) represents agents as collection of pixels. CPM can provide greater spatial resolution but are more computationally expensive. Off-lattice approaches can be either centered-based or boundary-based [14]. Center-based methods can represent agents as single points or as collection of points, such as in the Subcellular Element Method. Boundary-based methods include vertex and front-tracking models [14].

We model cellular spatial dynamics using the Cellular Potts Model (CPM or Glazier-Graner-Hogeweg model) implemented in CompuCell3D [18]. CPM represents biological cells and compartments as generalized cells as occupying sets of voxels on a fixed lattice. These generalized cells can represent biological cells, cellular subcomponents, or extracellular domains. Each voxel in the lattice has a position x and an index associated with the generalized cell occupying that voxel $\sigma(x)$. To represent distinct phenotypic states, generalized cells σ are assigned a cell type $\tau(\sigma)$. In the absence of external stimuli, cytoskeletal membrane fluctuations and differential adhesion to the extracellular matrix drive migration of biological cells in a random-walk pattern. Random cell motility is stimulated by stochastic exchange of voxels occupied by each generalized cell. Other spatial properties and behaviors are modeled by associating effective energy terms with generalized cell properties such as size and shape constraints (volume, surface, elongation) and behaviors such as mechanical interactions (cell adhesion) and directed motion (chemotaxis).

The configuration of the lattice evolves to minimize the system's effective energy:

$$\mathcal{H} = \sum_{x} \sum_{y}^{N} J\big(\sigma(x)\sigma(y)\big)\left(1 - \delta_{\sigma(x),\sigma(y)}\right) + \sum_{\sigma} \lambda(v(\sigma) - V(\sigma))^2$$

The first term models cell adhesion: N is the neighborhood of site x, $\delta_{i,j}$ is the Kronecker-delta function, the term $\left(1-\delta_{\sigma(x),\sigma(y)}\right)$ enforces counting energies between voxels belonging to a different cell and $J\big(\sigma(x)\sigma(y)\big)$ is the effective contact energy per unit surface area between cells $\sigma(x)$ and $\sigma(y)$. The next terms models cell volume as a quadratic constraint: λ denote the strength of the constraint, $v(\sigma)$ denote the current volume of the cell and $V(\sigma)$ denote the target volume. Different properties of cells can be modeled by similar constraints including surface area, chemotaxis, and elongation/polarization. The values of these constraints can be assigned by individual cells or to groups of cells depending on their cell type.

The lattice configuration evolves by voxel copy attempts. A target voxel x_i and a neighboring source voxel x_j are randomly selected. If different cells occupy these voxels, the energy change ($\Delta\mathcal{H}$) associated with updating the generalized cell at x_i with the one occupying x_j is evaluated. The probability of accepting the voxel copy attempt is given by a Boltzmann acceptance function:

$$\Pr\Big(\sigma\big(x_j\big) \rightarrow \sigma(x_i)\Big) = 1\, for\ \Delta\mathcal{H}\ \leq 0, e^{\frac{\Delta\mathcal{H}}{T}} for\ \Delta\mathcal{H} > 0$$

where $\Delta\mathcal{H}$ is the change in the systems effective energy from the voxel copy attempt and T is the amplitude of the cell-membrane fluctuations leading to random motility. The intrinsic simulation unit is a Monte Carlo step corresponding to a series of voxel copy attempts. Figure 2 shows how a lattice configuration evolves to minimize the total energy of the system.

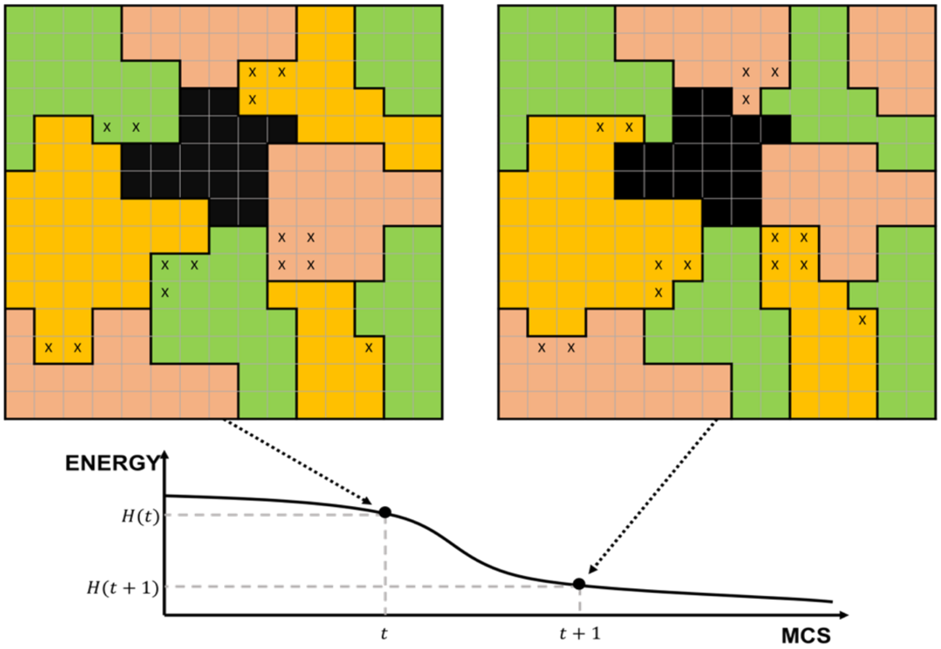

$$H = \sum_{i,j} J(\tau(i), \tau(j)) + \sum_{i} \lambda_{const}[V(i) - V_{target}(i)]^2$$

Figure 1.2. Cellular Potts Model Lattice Configuration and Effective Energy. Schematic representation of evolution of a lattice configuration of a Cellular Potts Model. Generalized cells occupy multiple lattice sites and have a corresponding type (green, yellow, red) that determines the biological characteristics. These characteristics are expressed as constraints in the Hamiltonian that encodes the effective energy of the systems. The lattice evolves by changes in the identity of each pixel that minimize the energy of the system. Adapted from [15].

ABMs are especially suited to address the modeling challenges that arise from having to integrate multiple biological scales. ODEs representing molecular, intracellular, and whole-organism processes can be coupled with ABMs representing cellular and intercellular processes [2]. These multiscale models are at the forefront of mechanistic modeling of biological complex systems. ABMs can be designed following a modular architecture that mimics the biological organization of the target system into functional units and facilitates the collaboration between research groups (Figure 3). ABMs provides a platform in which data and models from different laboratories (and different sets of experiments) can be integrated [7]. Modeling complex systems, and specifically modeling the immune system, can only be accomplished as a multidisciplinary and collaborative effort.

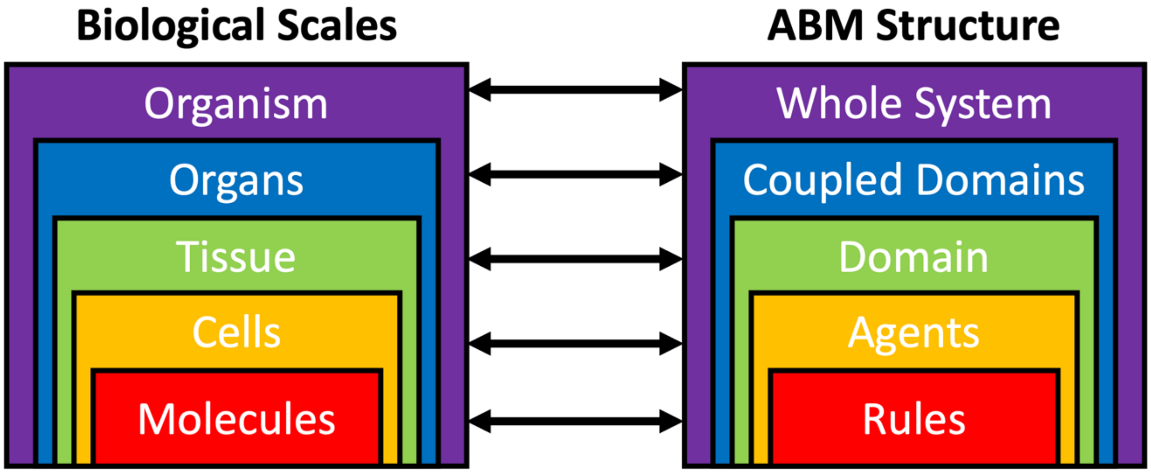

Figure 1.3. Biological and ABM Organization. Correspondence between biological scales and ABM architecture at different levels. Molecular interactions can be represented as rules that determine the states of individual cell agents. Interactions between cell agents determine the dynamics of the target tissue. Different modeling domains can be integrated to represent complex organs. Additional rules can be used to represent interactions between organs and the overall state of the organism. Adapted from [7].

Mathematical and Computational Modeling of the Immune Response to Viral Infections

Viruses are highly efficient pathogens that consist of viral genetic material and a protective protein and lipid coat. Since viruses lack the machinery to self-replicate, they must hijack the cell's own replication machinery [16]. The cellular membrane of epithelial cells is one of the first physiological barriers viruses encounter when infecting a host and they have evolved mechanisms for interacting with cellular surface receptors. Once the virus crosses the first physical barriers, it spread further by overcoming transport limitations and the immune response. Viruses spread as diffusive virions in the interstitial space above the apical surface of epithelial cells. Some viruses can also spread via cell-to-cell transmission [16].

The viral replication cycle includes multiple steps and the overall time its take for a virus to undergo a full replication cycle, from binding to the cell surface to release of new progeny, depends on the collective rates of all these processes [17]. Viruses can store their genetic information in either as DNA or RNA molecules, but all must produce mRNA and must use the cells translation machinery to produce viral proteins. Those viruses that contain a positive-sense RNA genome can directly serve as templates for viral mRNA, whereas other viruses might require additional intermediate steps. The larger viral genomes are usually composed of DNA such as Epstein-Barr virus, smallpox, and Pandoravirus [17]. Viruses like influenza virus, and hepatitis C virus (HCV) are RNA viruses and contain smaller genomes. Retroviruses such as human immunodeficiency virus type 1 (HIV-1) reverse transcribe their RNA genome to make viral DNA which is integrated into the host cell's DNA and later transcribed the cells own transcription machinery [17].

Mathematical modeling has advanced our understanding of the dynamics of viral replication, especially those mechanisms that are difficult to grasp only through experimental approaches [18]. Mathematical models have helped identify viral infection parameters such as the *in vivo* replication rate, the clearance rate of virions and the clearance rate of infected cells [16]. Modeling has also aided in identifying key druggable targets and optimal therapeutic interventions. For example, mathematical modeling was instrumental in developing successful treatments for chronic viral infections such as HIV and HCV [19]. Modeling has been used extensively to studying acute respiratory viral infections such as influenza. Modeling has shown that therapeutics must be administered before the peak of viral loads to be effective [19]. More recently, mathematical modeling has also been an important tool in gaining rapid understanding of quickly emerging viruses such as SARS-CoV-2.

ODE modeling has been extensively used to describe the intracellular processes that constitute the viral life cycle. Equations describing binding between cell surface receptors and viral particles are expressed as mass action processes that depend on the amount of free virus and unbound receptors [17]. Transcription is the amplification step in which the viral genome is replicated an is usually expresses using non-linear equations with decay. Other processes such as translation, assembly, encapsidation and release can be modeled as first other differential equations. Each of these equations contribute to the total duration of the viral replication cycle, and their parameters can be identified experimentally.

Within-host models are used to account for the dynamics of virus replication in a host organism. The standard model of viral dynamics (SMV) is a set of coupled differential equations that describe a cell population at different stages of viral infection and the production and decay of infectious virions (Figure 3). In this model cells can be in 4 stages of viral infection: uninfected, latently infected, virus producing and dead. Intracellular processes such as transcription and assembly are combined in the viral production rate [18]. The model does not include explicit immune response, and thus is referred to as “target cell limited”. The immune response is assumed to be either negligible or constant through the course of the infection and implicitly represented by parameters such as the death rate of infected cells or the clearance rate of virions [20]. When simulated, the viral load increases exponentially at first, when plenty target cells are available, peaks when most of the cells are infected and declines as infected cells die [19]. The model has been successfully calibrated with viral load data from infected patients and has proven an important tool to understand the replication dynamics of HIV and HCV [18]. The model has also been critical to improving larger scale epidemiological models [20].

$$\frac{dS}{dt} = -bVB$$

$$\frac{dE}{dt} = bVB - kE$$

$$\frac{dI}{dt} = kE - dI$$

$$\frac{dV}{dt} = pI - cV$$

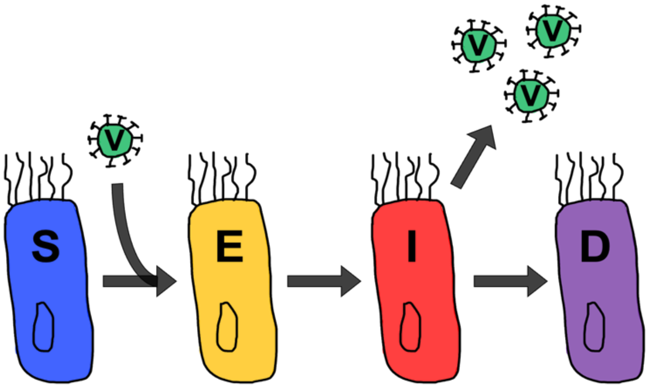

Figure 1.4. Equations and Conceptual Representation Standard Viral Load Model. The model contains four state variables representing population of cells in different stages of viral infection: susceptible/uninfected (S), latently infected (E)**,** virus producing (I) and dead (D). It contains a state variable that represents the infectious virions (V). The model contains five parameters (b, k, d, p and c) that determine the rates of transition between cell types and production/clearance of virions. Adapted from [21].

Intracellular viral cycle and within-host viral spread models can serve as the budling blocks for more complex multiscale models. Intracellular virus growth models can be coupled with reaction-diffusion equations that describe how infectious virions are transported in the extracellular environment [17]. Transitions probabilities can describe the rates at which individual cells transition from one stage of viral infection to the next. Additionally, these models can include detailed information of the immune response, including explicit representations of immune cell types such as macrophages, neutrophils, CD4+ and CD8+ T cells [19]. These multiscale models overcome the limited scope of viral cycle models and the convolution of critical kinetic parameters in the SVM. They are also able to represent non-homogenous cell populations that might differ in viral replication kinetics [18]. Multiscale approaches are well-suited to understand the dynamics of viral infection because viral spread is influenced by multiple interacting factors, including target cell availability, tissue permissibility and the immune response.

Besides HIV and HCV, the dynamics Influenza A (IAV) infection has been one of the most extensively modeled viral infections. IAV is an endemic respiratory virus that causes annual epidemic outbreaks. Most people will be infected by IAV multiple times during their lifetime [20]. IAV infects cells of the airway epithelium, specifically the non-ciliated cells. Most cases of human influenza involve infection of the upper respiratory tract, but in severe cases it can also infect the lower respiratory tract. The incubation time of influenza can vary anywhere from 24-96 hrs. The viral titers peak at day 3 post-infection (dpi). Effector immune cells CD8+ T cells peak around day 7 when the infection begins to resolve [20]. Most influenza models are epidemiological and are used as tool to inform public health policy. However, within-host models have been developed to study the dynamics of IAV infection and quantifying the processes that determine disease severity, duration, and outcome [20]. The SVM has been successfully calibrated to capture the kinetics of the course of the influenza infection, even in the absence of an explicit immune response.

SARS-CoV-2 is the etiological agent behind the ongoing COVID-19 pandemic. Mathematical modeling has been essential to develop rapid understanding of the viral infection, to develop effective treatments and vaccines, and to guide public health policy. The SVM has been used as the starting point to study within-host spread of SARS-CoV-2, calibrated with a wealth of publicly available data. More complicated models have been used to investigate mechanism driving the course of the infection. For example, adding explicit interferon-alpha to the model does not usually improves how well the model fits to the data, suggesting that interferon response is inhibited and does not play a role in reducing the spread of the infection [19]. Other approaches have been used to determine the time scales of the adaptive immune response. These models have suggested that adaptive immunity develops between one and two weeks after infection [19]. Identification of these parameters is critical when dealing with a novel viral disease spreading fast around the globe.

Mathematical and Computational Modeling of the Immune Response to Cancer

The primary characteristic of malignant cancerous cells is their ability to proliferate despite inhibitory signals, nutrient-deprived environments and immunosurveillance [9]. Cells accumulate genetic changes over time and sometimes acquire phenotypical characteristics that allow them to persist and proliferate in tissue. Carcinogenesis, the process by which cells progressively become malignant, is driven by multiple physiological factors including mutations, interactions between cells and environmental factors such as diet and radiation exposure [22]. Solid tumors grow in epithelial tissue such as epithelial ducts (carcinomas) or skin (melanomas), supportive tissue (sarcomas) or brain tissue (gliomas) [23]. Tumors induced changes in their microenvironment, such as generation of new blood vessels (angiogenesis), that allows them to sustain their elevated proliferation rate and facilitates their spreading to distant sites (metastasis). Because of the multiple interactions driving tumor initiation and progression, cancer development must be studied at multiple scales, and specially at the level of the collective interactions of cells and their environment [22].

To meet the energy demands of their high proliferation rates, cancer cells mantain elevated metabolic activity [24]. In a single tumor, different cells can rely on different metabolic pathways for energy production, including glycolysis and oxidative phosphorylation. Thanks to the work of Warburg, it is now recognized that cancer cells rely preferentially on the glycolytic metabolic pathway even at physiological oxygen tension. The Warburg effect provides multiple advantages to cancer cells. Rapid glucose metabolism helps to maintain oxygen levels above hypoxic thresholds reducing the need for new vasculature [25]. Other benefits include enhanced biosynthesis, altered cell signaling and reduced risk of reactive oxygen species damage [24].

The tumor microenvironment (TME) is composed of different cell types and matrix proteins. Endothelial cells, fibroblasts and different types of immune cells interact with the growing tumor. Some stromal cells such as myo-fibroblasts support tumor proliferation by providing growth factors and cytokine, as well as depositing matrix and modifying connective tissue. [26]. As the tumor growths, the existing (and sometimes damaged) vasculature is unable to provide nutrients and oxygen to meet the tumor metabolic demand leading to the recruitment of new vasculature. Glycolytic metabolism produces acidic waste products and contributes to the acidification of the TME. This acidic environment provides selective pressure that can give rise to more malignant phenotypes and inhibits the antitumor immune response [24].

For tumors to maintain sustained proliferation, migrate and invade secondary sites, cancer cells need to evade the constant surveillance of the immune system. Immune cells are attracted to the tumor site, either by local signaling or recruitment from the blood or the lymphatic system

[26]. Tumor cells present antigens and produce cytokines that are recognized by immune cells. Cells of the innate immune systems, such as natural killer (NK) cells and macrophages, infiltrate the tumor and kill tumor cells without the need of recognizing antigens [26]. Cells of the adaptive immune response, such as cytotoxic CD8+ T cells (CTL) are recruited to the tumor site, recognize in cancer cells by their antigen presentation and induced apoptosis. Cancer cells developed multiple mechanisms to evade the immune response. They can downregulate expression of major histocompatibility complex (MHC) class-I receptors on their cell surface, thus becoming invisible to CTLs [27]. Tumors can also increase the recruitment of regulatory T cells leading to increased inhibition of CTLs. Acidification of the TME also leads to higher thresholds for T cell activation [24].

Therapeutics that focus in targeting cancer cells directly often lead to resistance and selection of more invasive phenotypes [14]. These failures are in part due to the complex interactions between cancer cells and their environment. Immunotherapies are a relatively novel and promising set of treatments aimed at boosting the overall immune response against cancer [27]. Examples of immunotherapies include vaccines and immune checkpoint inhibitors (ICI) that target some of the mechanisms of immune evasion. For example, tumor cells secrete inhibitory molecules such as PD-L1 that suppress T cell activity via de PD-1 signaling pathway [27]. Monoclonal antibodies that target PD-L1 are used as ICI treatment [28].

Mathematical modeling in cancer research can be used to elucidate mechanisms driving tumor progression and immune suppression. Models can also be used as platforms for drug development and optimization. By redefining our understanding of the mechanisms of tumor progression, mathematical models can also challenge existing paradigms and suggest new mechanisms [22]. A wealth of mathematical models of cancer has been developed to predict patient-specific disease outcome and response to therapy. When validated with clinical data, they can be used to suggest appropriate therapeutic strategies, such as combination of chemotherapy and radiation, scheduling and dosing [22]. Scheduling and dosing are the most critical aspects of cancer treatments because improper timing can lead to relapse and evolution of resistant cells [23].

One approach to cancer modeling is the use of continuum ODE models. These types of models are appropriate to describe tumor growth in the spatiotemporal scales where the behavior of individual cancer calls can be averaged over the population [29]. These models often describe how the tumor volume growths as cancer cells interacts with their environment, including nutrients, immune cell types and therapies. Single equation ODE models usually describe tumor volume explicitly and any anti-tumoral host response as implicit saturation terms on the rate of tumor growth [30]. Systems of coupled ODEs can be used to model interactions between tumor and immune cells, cytokines, and nutrients. Two equations ODE models are usually employed to explicitly model immunological barriers that tumor must overcome to proliferate. Three equations models can be used to separate the immune response into innate and adaptive or to represent cytokine-mediated feedback mechanisms.

While ODE models provide useful frameworks to explore mechanism of interaction between tumor cells and their environment, they assume a uniform environment and do not consider spatial heterogeneity [30]. Molecular, cellular and tissue heterogeneity are hallmarks of cancer and important determinants of disease severity and treatment outcome [27]. Spatial heterogeneity has been documented in pathological screenings. For example, spatial localization of immune cells is a prognosis indicator in different types of cancer [26]. Drug resistant can be in part attributed to spatial heterogeneity in the tumor microenvironment. PDE modeling can take into consideration some of the temporal and spatial characteristics of tumor growth. For example, PDEs can be used to describe tumor growth as a function of both time and concentration of oxygen at a certain position. Oxygen will be represented as a diffusive molecule with a given diffusion constant and decay/consumption rates [22]. However, PDEs do not account for the individual variation of the different components of the tumor microenvironment [9].

The complexity of modeling tumor growth increases when taking into consideration that TME interactions span over multiple spatial and temporal scales. Because heterogeneity cuts across all these scales, mathematical models that average behavior across populations (either it be PDEs or ODEs) are insufficient to capture the complex dynamics governing tumor growth. Hybrid multiscale models that combine discrete and continuum mathematical approaches are better suited for modeling tumor growth [23]. In these models, discrete scholastic processes describe cell growth and division, migration, and phenotypical variation. Continuum models describe diffusion of nutrients and molecules and deposition of extracellular matrix. Continuum models can also describe intracellular signaling and processes.

When effectively coupled, hybrid multiscale models can bridge the several spatiotemporal scales involved in determining tumor growth dynamics [22]. They can also capture the cell-to-cell heterogeneity and individual dynamics of cell proliferation [9]. Several hybrid models have been developed and proposed to studying tumor growth. Cellular Automota have been used to study hypoxia-driven tumor invasiveness in ductal carcinoma [31]. Such model was latter extended to cell adhesion and morphology [32]. Center-based models have been used to study oxygen drive proliferation and cell death at the tumor necrotic core [33]. Cellular Potts Model have been used to study evolution in tumor cell populations [34] and angiogenesis [35].

Agent -based models have also been developed to study the interaction between tumor cells and the immune response. A model of the interaction between tumor cells and CTLs in a mouse model of melanoma showed that CTLs efficacy correlates with their ability to infiltrate the tumor [16]. Agent-based models have been developed to studying the effects of immune-enhancing and combination therapies [27]. One of the limitations of these hybrid models is that some of the modules governing the dynamics of tumor growth are qualitative [22]. In the case of models of anti-cancer therapy, these limitations could be overcome by combining ABMs with traditional pharmacokinetic and pharmacodynamic models that have been thoroughly validated. In other cases, such models can be used to identify qualitatively distinct disease and treatment outcomes, and the key mechanism and parameters controlling them.

Dissertation Organization

The next four chapters of the dissertation present frameworks, workflows and models developed to address some of the complexity of the immune system and its response to pathogens and cancer. First, we present a modeling framework that supports modeling of the immune response to viral infections. We showed how different modules can be used to represent different components of the immune system, and how variation on parameters can produce qualitatively different simulation outcomes. These regions of the parameter space can be associated with different disease and clinical outcomes: successful viral clearance versus severe viral infection. We further showed how the framework can be used to test and optimize therapeutic interventions, by modeling a treatment that inhibits viral replication.

Second, we present a spatiotemporal model of the type-1 interferon (IFN) response to viral infection. The model was generated by combining two previously calibrated models. An intracellular model describes the activation of the IFN pathway and its inhibition on viral replication. A cellular model describes transitions between different stages of viral infection and diffusion of extracellular virions and IFN molecules. We showed that the model recapitulates the dynamics of viral growth *in vivo*. We also showed that varying key parameters drives the systems to two distinct simulation outcomes: uncontrolled viral growth and plaque containment. Finally, by performing sensitivity analysis we identified key parameters driving simulation outcomes. These results suggest that the parameters of the IFN pathway are better identified in experimental conditions leading to plaque arrest.

Third, we present a spatiotemporal model of the immune response to cancer. The model incorporates the hypothesis that aerobic fitness modules the tumor microenvironment TME by shifting a glycolytic threshold in cancer cells. The acidification of the TME inhibits the immune response to tumors by increasing the recruitment of regulatory T cells. The model was calibrated and validated using clinical prevalence data. We showed that the model can be used to optimize immunotherapies using the patient’s fitness as a marker of the immunogenicity of the tumor.

Lastly, we present a spatiotemporal model of RSV-HMPV viral coinfection. Viral growth parameters for each virus are calibrated using single infection viral load data. The ODEs are then spatialized to produce ABMs equivalents. Co-infection simulations are performed under the assumption that the only interaction between viruses is competition for target cells. Simulations results are contrasted with experimental data to show that this hypothesis is insufficient to explain the fold changes in viral load observed during viral co-infections. The model is then used to suggest how additional mechanistic hypotheses can be tested and validated.

A multiscale, multicellular, spatiotemporal model of acute primary viral infection and immune response in epithelial tissues and its application to drug therapy timing and effectiveness

Introduction

Mathematical modeling methods integrate the available host- and pathogen-level data on disease dynamics that are required to understand the complex biology of viral infection and immune response to optimize therapeutic interventions [38]. Mathematical models and computer simulations built on spatial and ODE frameworks have been extensively used to study in-host progression of viral infection [39], with a recent acceleration in the development of spatial COVID-19 viral infection models in response to the ongoing global pandemic [40].

Building multiscale models of acute primary viral infection requires integrating submodels of multiple biological components across scales (*e.g.*, viral replication and internalization, immune system responses). Non-spatial, coupled ordinary differential equation (ODE) models can represent many aspects of pathogen-host interactionSpecialized ODE models can describe both the entire virus-host response at the tissue and organ levels and different stages of the viral replication cycle within cells, such as binding and internalization [41], viral genome replication and translation [42], assembly, packaging and release [43]. By fitting ODE models to clinical or experimental data, researchers have been able to estimate important parameters, such as the turnover rate of target cells, average lifetimes of viral particles and infected cells and the rate of production of new viral particles by infected cells [44].

Non-spatial models assume that the distribution of the modelled quantities (*e.g.*, cells, viruses, chemical species) are uniformly distributed in space and time [4]. This assumption might not be realistic in solid tissues, where viruses and host immune cells are not usually distributed homogeneously and infection propagates locally [44]. By averaging over spatiotemporal and individual cell variations, non-spatial models may not accurately reflect the effects of tissue heterogeneity and its effect on viral infection dynamics [45]. Compartmental ODE models, like physiologically based pharmacokinetic models (PBPK) models or multi-compartment tissue infection models, maintain some of the simplicity of single-compartment ODE models, while recognizing the critical role transport can play in viral infection, immune response and treatment [46].

The spread of and immune response to some viruses is highly spatially localized. For example, COVID-19 often begins with infection localized to the nose and throat and then spreads to the lungs [47], with the specific location, size and distribution of lesions affecting clinical outcomes. Spatial models have been increasingly used to address such issues, including partial differential equations [48] and agent-based models (ABM) [49]. ABMs represent host cells as spatially located, individual agents, and propagation of the infection emerges from individual interactions between agents. ABMs are also well suited for extending existing models by modular integration of biological subcomponents. ABMs have been developed to account for infection dynamics in different biological compartments and to model disease progression of HIV [50] and dissemination of influenza virus to the lower respiratory tract [51].

Spatial models often predict significantly different viral and immune dynamics, parameter estimates and therapy efficacies from their non-spatial counterparts. Stochastic effects arising from spatial conditions, such as local availability of target and immune cells, greatly influence early infection dynamics and lead to different infection outcomes [44]. Non-spatial models generally produce viral load titers higher than spatial models, and the peaks of infection happen significantly earlier [4]. Homogenous recruitment of immune cells in spatial models matches ODE models when the number of infected is large, but not at the beginning of the infection when the number of infected cells is small [45]. These differences can lead to inaccurate estimates of important parameters such as viral infectivity, viral diffusion and the basic reproductive ratio.

In this chapter, we present a framework for the multiscale multicellular spatiotemporal modeling and simulation of the dynamics of infection and immune response in epithelial tissue.

We consider a *primary* infection by a virus which the immune system has not previously encountered (e.g. there is no initial adaptive immune response). We focus on *acute* cases (cases with relatively rapid onset and short duration) in which a properly functioning immune system eventually eliminates the virus. Relevant components of the immune system were included. Those that are not explicitly modeled can be included within the modular, extensible modeling framework.

Viral infection generally begins when a virus breaches the barrier of one or more tissues causing a limited number of target cells to be exposed and then internalize the virus. The virus begins to replicate within the initially infected target cells, but cells do not release any newly synthesized virus for a period of hours to days (the *eclipse* or *lag* phase of infection). Within hours, infected cells release proinflammatory cytokines and complement proteins as warning signals to neighboring cells [52]. Some of these cytokines, like Type 1 interferons, can induce autocrine and paracrine anti-viral responses (*e.g.*, inhibiting viral replication, viral entry or inducing cell death) [53]. Cytokines recruit circulating innate immune cells from the blood to the infected tissue and attract immune cells within the tissue by chemotaxis [54]. The early innate immune response activates a number of cell types including dendritic cells, macrophages, neutrophils, mast cells, basophils, eosinophils, leukocytes, and natural killer (*NK*) cells [55]. As the viral load increases, immune signaling increases rapidly (this increase is associated with the onset of fever and other symptoms) recruiting more circulating cells of the innate immune system to the infection site [56].

Immune signals from infected cells and innate immune cells help trigger the adaptive immune response. Dendritic cells that have engulfed and degraded viral pathogens migrate to nearby lymph nodes and serve as viral antigen presenting cells (APCs) to naive T cells. Antigen presentation induces naive T-cell proliferation and differentiation into pathogen-specific memory and effector T-cells [57]. Cytotoxic effector T-cells migrate to the site of infection and induce apoptosis of infected cells by antigen recognition. In acute infections, adaptive immune response leads to pathogen neutralization and clearance [58]. Viral loads usually decrease rapidly as adaptive immune cells like CD8+ T-cells enter the tissue and eliminate infected cells.

Antigen presentation also induces activation of naive B-cell lymphocytes into antibody-producing memory B-cells and plasma cells, which leads to the production of antibodies. The adaptive immune response remembers its exposure to previous pathogens and provides the body with pathogen-specific effector cells and antibodies which neutralize and clear them, providing long term immunity [59]. Tissue damage results from virus and cytokine-induced cell death (which is first noticeable after 2 or 3 days) and from killing of infected and uninfected cells by immune cells, which increases steadily until the end of viral clearance. Tissue recovery and healing start around the time of viral clearance and may last for several weeks. Figure 2.1 presents a schematic of the dynamics of viral replication and the corresponding immune response.

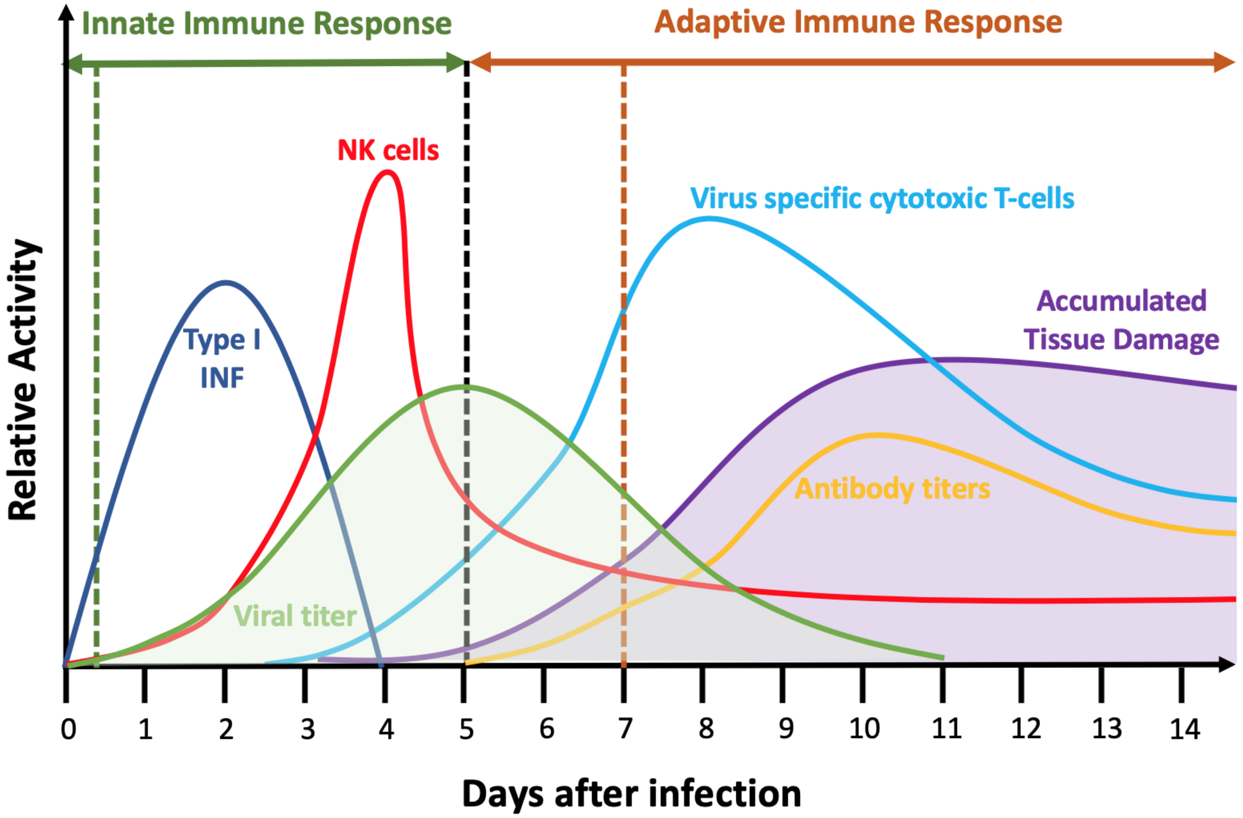

Figure 2.1. Schematic Of the Innate and Adaptive Immune Response During Primary Acute Viral Infection. After initial exposure to the virus, extracellular viral load begins to rise (shaded green curve). Initial innate immune responses include phagocytosis of virus by neutrophils and macrophages, Type I interferon-induced antiviral resistance (*IFN*) (dark blue) and killing of infected cells by Natural Killer (NK) cells and other innate cell types (red). The black vertical dashed line denotes the transition between innate and adaptive immune responses. The adaptive immune response is triggered both by cytokine signaling and the migration of antigen-presenting cells from the tissue to the lymph nodes (not shown). In the later phases of infection additional adaptive immune components come into play, including virus-specific cytotoxic T-cells (light blue). The orange vertical dashed line denotes the onset of the humoral adaptive immune response. B-cells produce virus-specific antibodies (orange line) which bind and inactivate virus directly and facilitates clearance of infected cells by other cell types. Tissue damage (shaded purple curve)

accumulates due to cell death from direct responses to virus and from immune-cell killing by contact-mediated, diffusible factor-mediated and bystander-mediated mechanisms and eventually dissipates as cells proliferate to repair the damage (Adapted from [59]). The specific time course of all components varies among viruses, host tissues and host species, but the general sequence of events and immune response components are generally preserved.

Our base model consists of three interconnected components (Figure 2.2A): an epithelium component, an extracellular environment component and a lymph node component. The model represents the epithelium as a compact monolayer of initially identical immobile epithelial cells that can adopt three types depending on the state of viral infection (*i.e.*, uninfected, infected, virus releasing, dead, Figure 2.2C). Cells can internalize extracellular virus, modulate their number of surface receptors, replicate virus and release virus (Figure 2.2B). They also release an extracellular cytokine signal when infected and die in response to virus production. The model represents the extracellular environment as a space above the epithelium which provides the space in which immune cells are recruited and move, and into which cells release viruses and chemicals. We include a single type of immune cell that exhibits many key immune-cell behaviors associated with macrophage, neutrophil, NK cell and T-cells, including activation, chemotaxis, relaying and amplification of cytokine signals and contact and bystander cytotoxicity. We simulate extracellular-virus particle density as a continuum field and particle transport and clearance as continuous diffusion and decay. We model recruitment of immune cells to the simulation domain using an ordinary differential equation for the immune signal (S) which represents the balance between pro- and anti-inflammatory signaling and the delay due to antigen-presenting cell transport from the tissue through the lymphatic system to the lymph node and due to the time required for T-cell amplification. In the absence of infection, the lymph node maintains a small resident immune cell population in the tissue.

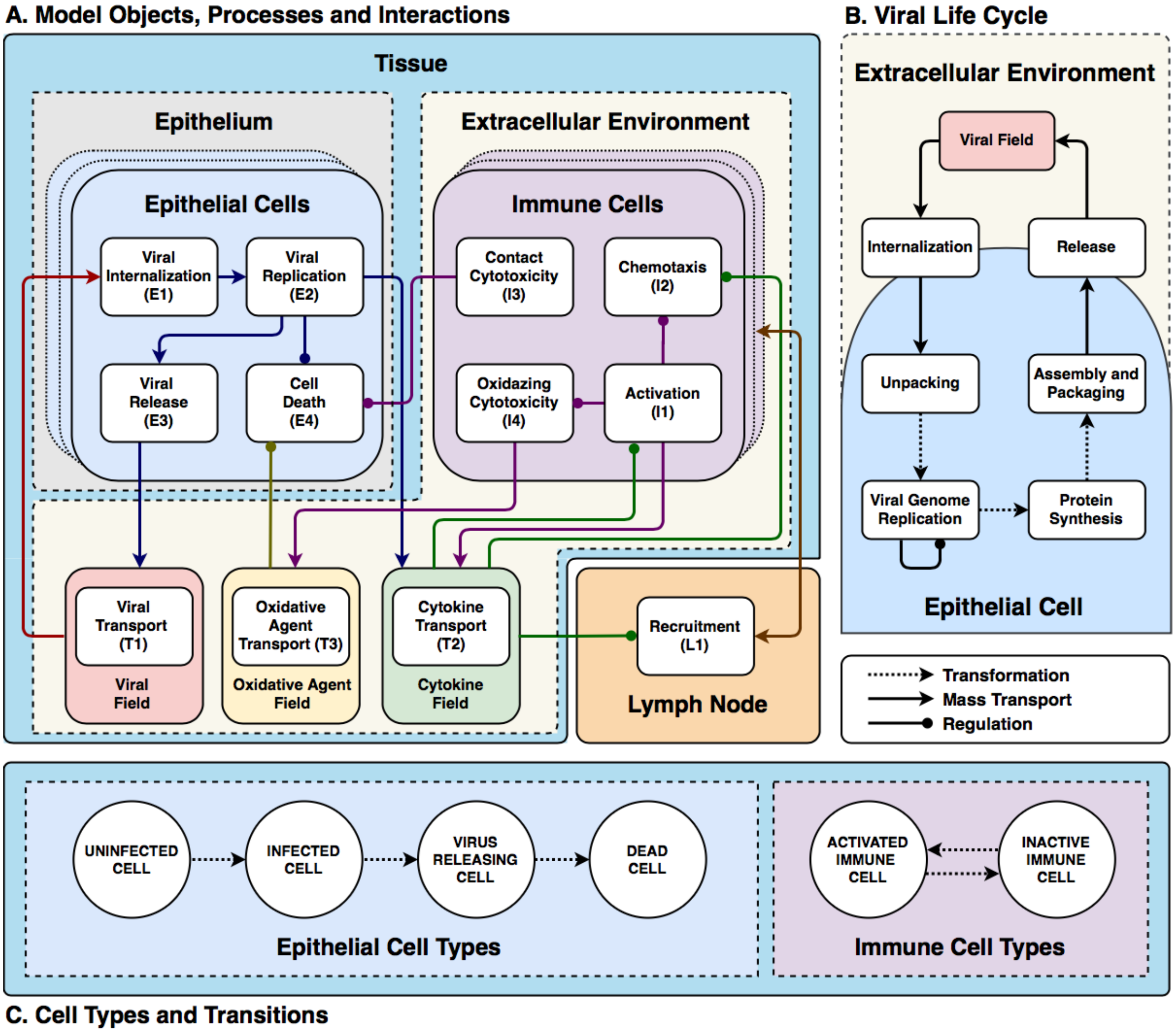
A. Model Objects, Processes and Interactions
Tissue
Epithelium
Epithelial Cells
Viral Internalization (E1)
Viral Replication (E2)
Viral Release (E3)
Cell Death (E4)
Extracellular Environment
Immune Cells
Contact Cytotoxicity (I3)
Chemotaxis (I2)
Oxidazing Cytotoxicity (I4)
Activation (I1)
Viral Transport (T1)
Viral Field
Oxidative Agent Transport (T3)
Oxidative Agent Field
Cytokine Transport (T2)
Cytokine Field
Recruitment (L1)
Lymph Node
B. Viral Life Cycle
Extracellular Environment
Viral Field
Internalization
Release
Unpacking
Assembly and Packaging
Viral Genome Replication
Protein Synthesis
Epithelial Cell
Transformation
Mass Transport
Regulation
UNINFECTED CELL
INFECTED CELL
VIRUS RELEASING CELL
DEAD CELL
Epithelial Cell Types
ACTIVATED IMMUNE CELL
INACTIVE IMMUNE CELL
Immune Cell Types
C. Cell Types and Transitions

Figure 2.2. Full Model Schematic. A. Model objects, processes and interactions. Conceptual model of an epithelial tissue and lymph node. Schematic representation of the model objects, processes and interactions. Epithelial and immune cells refer to the two main classes of cells. Interactions occur within an extracellular environment, and a compartmental model of a lymph node controls immune-cell recruitment to the tissue. Together the epithelial-cell, extracellular-environment and immune-cell components represent the epithelial tissue. Each model object has associated processes that dictate its

states and behaviors. Epithelial-cell processes include viral internalization (E1), viral replication (E2), viral release (E3) and cell death (E4). Immune cell processes include activation (I1), chemotaxis (I2), contact cytotoxicity (I3) and oxidative cytotoxicity (I4). *Activated* immune cells participate in oxidative cytotoxicity (I4) and secrete oxidative agents into the oxidizing-agent field (T3). The virus field (T1), cytokine field (T2) and oxidizing-agent field (T3) describe spatially-varying densities of extracellular components. Field processes describe diffusive transport and clearance of material in the extracellular environment and activated transport to the lymph nodes. The lymph node is a single-compartment model whose pro- or anti-inflammatory state specifies the recruitment or removal rate (L1) of immune cells in the epithelial tissue. The transport of cytokines to the lymph node promotes its proinflammatory state**. B. Viral Life Cycle**: Interactions in the viral internalization, replication and release models. Schematic representation of inputs, outputs and interactions between stages of the viral replication model. Extracellular viral particles are internalized by the viral internalization model and initiate the viral replication model. The main stages of the viral replication model are unpacking, viral genome replication, protein synthesis and viral assembly and packaging. The output of the viral replication model passes to the viral release model, which transfers newly assembled viral particles from the cells into the extracellular environment. **C. Cell Types and Transitions**. Epithelial cells are of type *uninfected* if they have not yet internalized any virus (E1). They are of type *infected* if they have internalized virus but are not yet releasing virus into the virus field (inactive E3). They are of type *virus releasing* if they are releasing virus into the extracellular virus field (activated E3). Immune cells are initially *inactive* and do not participate in the oxidative cytotoxicity (I4) or chemotax towards higher concentrations of the cytokine field (I2). Inactive immune cells become activated (I1). In all panels, dashed arrows with barbed heads represent transformations, solid arrows with barbed heads represent transport and solid arrows with lollipop heads represent regulation.

We create representations of the main types of components and biological mechanisms associated with acute, primary viral infection and immune response, with a special emphasis on modularity that supports the development of more detailed models in future work (e.g., the creation of additional cell types, signals and detailed cell responses of various aspects of the immune response).

Models and Methods

All quantitative models are implemented in a modular, extensible simulation architecture built using the CompuCell3D simulation environment, which is publicly available for download and further development by interested members of the scientific community.

Conceptual Model: Biological Hypotheses and Assumptions

We consider viral propagation in an epithelial tissue and a lymph node. The tissue contains two interacting spatial components: an epithelium component (consisting of a monolayer of epithelial cells), and an extracellular environment component (containing immune cells, extracellular virus, and diffusive chemicals). The state of the lymph node component is determined by signaling from the tissue. In proinflammatory state, the lymph node model adds immune cells to the extracellular space. It removes immune cells when in an anti-inflammatory state.

Epithelial Cell Modules

The epithelium component of the model represents the layer of epithelium in the tissue and is composed of epithelial cells of four types: uninfected, infected, virus-releasing and dead (Figure 2.2C). We assume that epithelial cells are immobile. Epithelial cells contain modules that model the viral life cycle and approximate the number of internal virus as a continuous quantity (Figure 2.2B): binding and internalization of viral particles from the extracellular environment (E1), intracellular replication (E2) and release (E3) of synthesized virus into the extracellular environment, as well as cell death caused by viral-replication-associated damage, immune-cell killing and oxidative agent killing (E4). Processes E1-E4 describe epithelial cell functions. E1, E2 and E4 govern the cell-type transitions of epithelial cells (Figure 2.3). E1 transforms an uninfected epithelial cell into an infected epithelial cell. E2 transforms an infected epithelial cell into a virus-releasing epithelial cell. E4 transforms a virus-releasing epithelial cell into a dead cell.

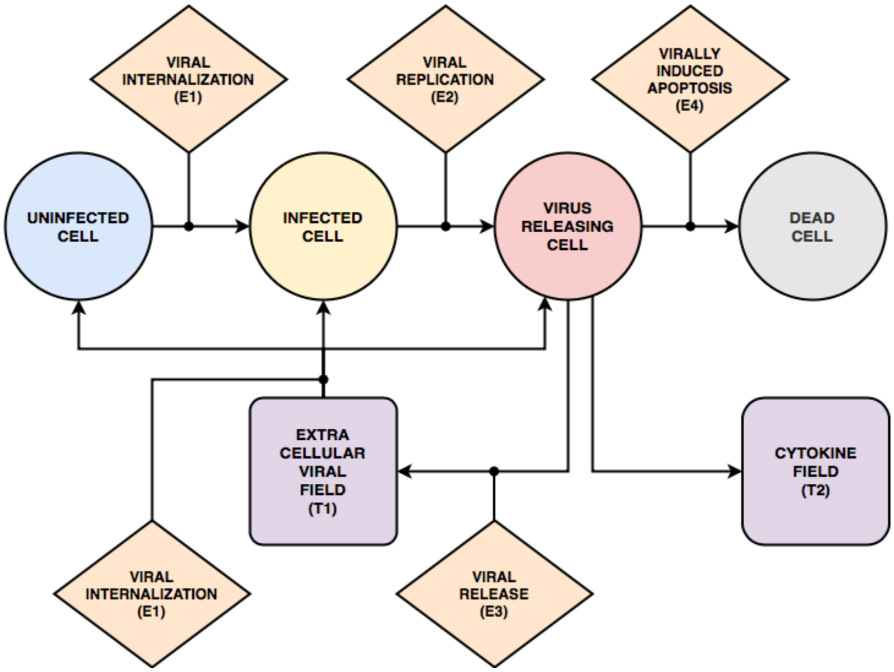
VIRAL INTERNALIZATION (E1)
VIRAL REPLICATION (E2)
VIRALLY INDUCED APOPTOSIS (E4)
UNINFECTED CELL
INFECTED CELL
VIRUS RELEASING CELL
DEAD CELL
EXTRA CELLULAR VIRAL FIELD (T1)
CYTOKINE FIELD (T2)
VIRAL INTERNALIZATION (E1)
VIRAL RELEASE (E3)

Figure 2.3. State diagram and interactions of epithelial cells. Epithelial cells can have one of four "cell types": uninfected, infected, virus-releasing and dead. Uninfected cells become infected cells when the viral uptake model (E1) internalizes viruses from the extracellular virus field (T1). Infected cells continue internalizing viruses from the extracellular virus field and become virus-releasing cells when the viral replication model (E2) produces sufficient newly assembled virions. Virus-releasing cells secrete viruses into the extracellular virus field (T1) according to the viral release module (E3) and secrete cytokines directly into the extracellular cytokine field (T2). Virus-releasing cells can die if the conditions of the virally induced cell-death model (E4) are met.

E1 - Viral internalization

Internalization of viral particles involves binding of the viral spike protein to target cell-surface receptors, truncation by surface proteins and receptor-mediated endocytosis or fusion with the host plasma membrane. These module models extracellular virus binding to epithelial cell receptors and internalization (including endocytosis-dependent and -independent routes). We assume the dynamics of internalization can be modeled by considering the amount of extracellular virus and target surface receptors and the binding affinity between them (T1→E1).

We also consider the depletion of bound target surface receptors on a cell when it internalizes a virus and superinfection of infected cells. Internalized viral particles initiate the viral replication process (E1→E2 and Figure 2.2B).

To capture the stochasticity associated with internalization of discrete virus particles in terms of discrete binding events, we assign each uninfected, infected and virus-releasing epithelial cell a probability of absorbing diffusive viral particles from the extracellular virus field. The uptake probability $\Pr(Uptake(\sigma) > 0)$ for each cell σ is given by a Hill equation of the total amount of diffusive viral particles in the domain of the cell $c_{vir}(\sigma)$, the number of unbound cell surface receptors $SR(\sigma)$ and the binding affinity between them.

$$\Pr(Uptake(\sigma) > 0) = \frac{\Delta t}{\alpha_{upt}} \frac{\left(c_{vir}(\sigma)\right)^{h_{upt}}}{\left(c_{vir}(\sigma)\right)^{h_{upt}} + V_{upt}^{h_{upt}}}, \text{ where } V_{upt} = \frac{R_o k_{off}}{2 k_{on} v(\sigma) SR(\sigma)}. \quad (2.1)$$

Here h_{upt} is a Hill coefficient, R_o is the cell's initial number of unbound receptors, k_{on} is the virus-receptor association affinity, k_{off} is the virus-receptor dissociation affinity, α_{upt} is a characteristic time constant of uptake and Δt is the time represented by one MCS. At each simulation time step, the uptake probability is evaluated against a uniformly-distributed random variable. When uptake occurs, the uptake rate is proportional to the local amount in the virus field and the probability of uptake is used to define the amount ($Uptake$) of virus taken up during the MCS,

$$Uptake(\sigma) = \frac{1}{\Delta t} \Pr(Uptake(\sigma) > 0)\, c_{vir}(\sigma), \tag{2.2}$$

$$\frac{dSR(\sigma)}{dt} = -Uptake(\sigma). \tag{2.3}$$

The amount absorbed by each cell is uniformly subtracted from the virus field over the cell's domain and the cell's number of cell surface receptors is reduced by the same amount. The amount of virus taken up is also passed to the cell's viral replication model. Infected epithelial cells continue taking up viral particles from the environment until their cell surface receptors are depleted.

E2 - Viral Replication

Individual cells infected with many non-lytic viruses show a characteristic three-phasic pattern in their rate of viral release. After infection and during an *eclipse phase*, a cell accumulates but does not yet release newly assembled viruses. In a second phase, the rate of viral release increases exponentially until the virus-releasing cell dies. In a third phase, the cell saturates its rate of virus synthesis and release. Viral replication hijacks host synthesis pathways and may be limited by the availability of resources (amino acids, ATP, *etc.*), synthesis capability (ribosomes, endoplasmic reticulum, *etc.*) or intracellular viral suppression.

We model viral replication based on processes associated with positive sense single-stranded RNA (+ssRNA) viruses. +ssRNA viruses initiate replication after unpacking of the viral genetic material and proteins into the cytosol (E1→E2). The viral RNA-dependent RNA polymerase transcribes a negative RNA strand from the positive RNA strand, which is used as a template to produce more RNA strands (denoted by "Viral Genome Replication" in Figure 2.2B). Replication of the viral genome is the only exponential amplification step in the growth of most viruses within cells. Subgenomic sequences are then translated to produce viral proteins ("Protein Synthesis" Figure 2.2B). Positive RNA strands and viral proteins are transported to the endoplasmic reticulum (ER) where they are packaged for release. After replication, newly synthesized viral genetic material is translated into new capsid protein and assembled into new viral particles ("Assembly and Packaging" in Figure 2.2B). These newly assembled viral particles initiate the viral release process (E2→E3).

Our viral replication model combines equations and parameters from several sources to represent the replication of a generic virus [41]. The model contains four variables representing viral quantities in different states of the viral replication process: internalized virus U (Equation (2.4), viral genome taking part in genomic replication R (Equation (2.5), synthesized protein P (Equation (2.6), and assembled and packaged virions A (Equation (2.7). Biologically, the only process which can exponentially increase the rate of virus production by a single cell is viral genome replication, so the equations include the positive feedback by R in Equation (2.5). Biologically, factors like the cell's metabolism, limited number of ribosomes, maximum rate of endoplasmic reticulum function and activation of intracellular viral suppression pathways all limit production of viral components, so we include a Michaelis-type saturation term for the rate of replication in Equation (2.5). Each uninfected, infected and virus-releasing cell in the simulation contains an independent instance of the system of ordinary differential equations modeling the viral replication process,

$$\frac{dU}{dt} = Uptake\ - r_u U, \tag{2.4}$$

$$\frac{dR}{dt} = r_u U\ + r_{max} R \frac{r_{half}}{R\ + r_{half}}\ - r_t\, R, \tag{2.5}$$

$$\frac{dP}{dt} = r_t R - r_p P, \tag{2.6}$$

$$\frac{dA}{dt} = r_p P - Release. \tag{2.7}$$

Here r_u is the unpacking rate, r_{max} is the viral replication rate, r_t is the translating rate (rate at which viral genomes turn into RNA templates for protein production) and r_p is the packaging rate. $Uptake$ is defined in E1 and $Release$ is defined in E3. The saturation of the rate of viral genome replication is represented by a Michaelis-Menten function, $\frac{r_{half}}{R\ + r_{half}}$, where r_{half} is the amount of R at which the viral genome replication rate is reduced to $\frac{r_{max}}{2}$ (and the flux is reduced to $\frac{1}{2} r_{max}\, r_{half}$). The duration of the eclipse phase of single-cell infection (the time between the first entry of the virus into the cell and the first release of newly synthesized virus) is approximately $t_{eclipse} \approx \frac{1}{r_u} + \frac{1}{r_{max}} + \frac{1}{r_t} + \frac{1}{r_p}$ (11.7 hours for the reference parameter set in Table 2.1), with the additional complication that in our model, an epithelial cell does not release virus until A reaches a threshold value. The timescale for tenfold increase of virus release when viral replication is maximal is $t_{10}\ \approx \frac{log(10)}{r_{max}}$ (7.7 hours for the reference parameter set in Table 2.1). The number of newly assembled virions is passed to the viral release module (E3). Figure 2.4 shows a representative time series from the viral internalization, replication and release modules inside a single cell.

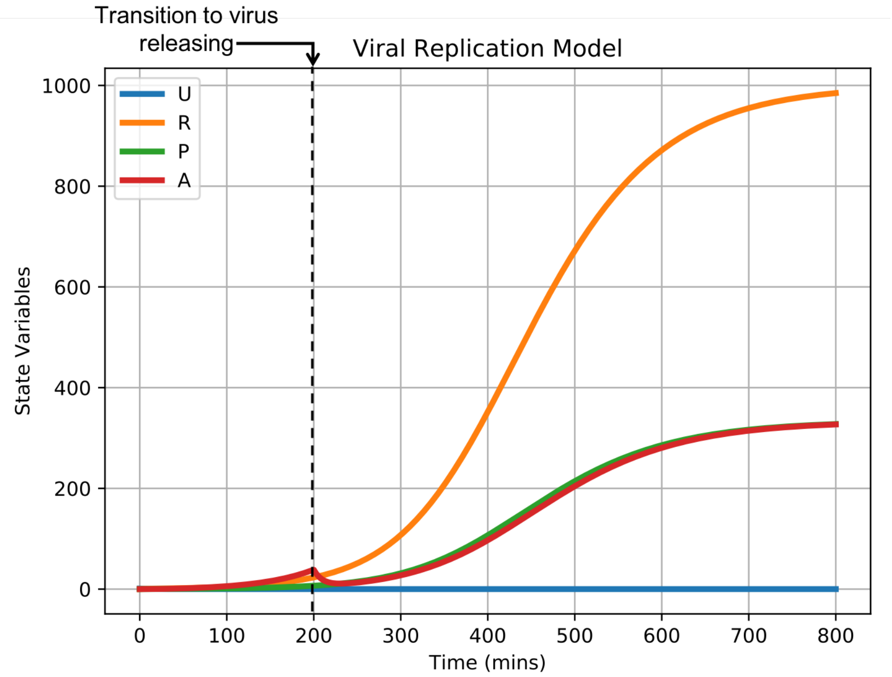

Figure 2.4. Representative Time Series Of Viral Internalization, Replication And Release Models. A sample simulation of the viral replication model in a single epithelial cell. The model is initialized with one unit of internalized virus (U = 1), and the rest of the state variables set to zero (R = 0, P = 0, A = 0). No additional virus internalization occurs during this sample simulation. Dashed line indicates the time of the cell's transition from the infected to virus-releasing cell type.

E3 - Viral Release

Newly assembled virions are packed into vesicles and transported to the cell membrane for release into the extracellular environment. This module models intracellular transport of newly assembled virions and release into the extracellular environment (E3→T1 and Fig 2B "Release"). We assume virus is released into the extracellular fluid above the apical surfaces of epithelial cells. (E2→E3). No regulation occurs after assembly of new virus particles.

The amount of virus released by a cell per unit time is proportional to the state variable for assembled virions in the viral replication module (E2),

$$Release = r_s A. \tag{2.8}$$

Here r_s is the release rate of viral particles and A is the level of assembled virus in the cell (defined in E2). The total amount released by each cell $r_s A \Delta t$ is subtracted from the cell's state variable for assembled virions A and passed to the source term of the extracellular virus field (T1) to maintain mass balance.

E4 - Virally-Induced Cell Death

Models the combined effect of the many types of virus-induced cell death. The production of viral proteins interferes with the host cell's metabolic, regulatory and delivery pathway (E2→E4). Internally assembled virions are not released to the environment. The rate of death is defined as a stochastic function of the state variable for assembled new virions from the viral replication module (E2). If a virus releasing cell dies then it changes its cell type to dead and the cell's instances of the viral internalization, replication and release modules are disabled. The probability of virally-induced apoptosis per simulation step is a Hill equation of the current load of assembled virus,

$$\mathrm{Pr}(\tau(\sigma) \rightarrow \mathrm{Dead} | \tau(\sigma) = \mathrm{Virus\ releasing}) = \frac{\Delta t}{\alpha_{apo}} \frac{\left(A(\sigma)\right)^{h_{apo}}}{\left(A(\sigma)\right)^{h_{apo}} + V_{apo}^{h_{apo}}}. \tag{2.9}$$

where $A(\sigma)$ is the number of assembled virions in cell σ, h_{apo} is a Hill coefficient,V_{apo} is the number of assembled virions at which the apoptosis probability is 0.5 per unit time and α_{apo} is a characteristic time constant of virally induced apoptosis.

Extracellular Environment Component

The extracellular environment contains the immune cells, extracellular virus, cytokines and oxidative agent, and is the space where viral particles (T1), cytokine molecules (T2) and the oxidizing agent (T3) are transported. Immune cells are motile and can be either activated or inactive (I1). Inactive immune cells move through random cell motility and activated immune cells move along the cytokine field (I2). The immune cell modules also account for cytotoxic effects of immune cells on contact due to antigen recognition (I3) and through the secretion of oxidizing agents (I4).

Transport Modules

T1 - Viral transport

Viral particles are transported and eliminated by different mechanisms (*e.g.*, ciliated active transport, diffusion) and media (*e.g.*, air, mucus) at different physiological locations and through different types of tissue (*e.g.*, nasopharyngeal track, lung bronchi and alveoli). This module models extracellular viral particles as a diffusive virus field in a thin layer above the apical surfaces of epithelial cells. Viral internalization results in the absorption of a small amount of virus from the extracellular environment into a cell (T1-E1).

The change in concentration of the virus field c_{vir} is calculated at each location in the simulation domain by solving the following reaction-diffusion equation,

$$\frac{\partial c_{vir}(x)}{\partial t} = D_{vir}\nabla^2 c_{vir}(x) - \gamma_{vir} c_{vir}(x) + \frac{1}{v(\sigma(x))}\Big(Release\big(\sigma(x)\big) - Uptake\big(\sigma(x)\big)\Big) \quad (2.10)$$

Here D_{vir} is the diffusion constant of the extracellular virus and γ_{vir} is the decay rate is the decay rate. Uptake and release by a cell at each location are determined using the viral internalization (E1) and the viral release (E3) modules and are uniformly applied over all sites of the domain of the cell.

T2 - Cytokine Transport

Models diffusion and clearance of immune signaling molecules in the extracellular environment

The immune response involves multiple signaling molecules acting upon different signaling pathways. We assume that the complexity of immune signaling can be functionally represented using a single chemical field that diffuses and decays in the extracellular environment. Once infected, epithelial cells secrete signaling molecules to alert the immune system (E2-T2). Local exposure to cytokine signaling results in activation of immune cells (T2-I1). Upon activation, immune cells migrate towards infection sites guided by the cytokine (T2-I2). Lastly, activated immune cells amplify the immune signal by secreting additional cytokines into the extracellular environment (I1-T2). We model cytokine systemic, long-range effects by assuming that cytokine exfiltrates tissues and is transported to immune recruitment sites (T2-L1).

The change in concentration of the cytokine field c_{cyt} is obtained by solving a reaction-diffusion equation of the following general form,

$$\frac{\partial c_{cyt}}{\partial t} = D_{cyt}\nabla^2 c_{cyt} - \gamma_{cyt} c_{cyt} + s_{cyt}. \tag{2.11}$$

The decay term $\gamma_{cyt} c_{cyt}$ represents cytokine leaving the simulation domain (*e.g.*, in immune recruitment). To model immune signaling, the rate of cytokine secretion is described by an increasing Hill function of $c_{sig}\big(\sigma(x)\big)$ with Hill exponent $h_{cyt} = 2$. The meaning of $c_{sig}\big(\sigma(x)\big)$ depends on the cell type and the Hill exponent can differ for other cell types and states. The rate of cytokine secretion s_{cyt} is written as,

$$s_{cyt}(x,t) = \sigma_{cyt}\big(\tau(\sigma(x),t)\big)\frac{\big(c_{sig}(\sigma(x),t)\big)^{h_{cyt}}}{\big(c_{sig}(\sigma(x),t)\big)^{h_{cyt}} + \Big(V_{cyt}\big(\tau(\sigma(x),t)\big)\Big)^{h_{cyt}}} - \omega_{cyt}\big(\tau(\sigma(x),t)\big) \tag{2.12}$$

Here $\sigma_{cyt}\big(\tau(\sigma(x),t)\big)$ is the maximum cytokine secretion rate for the cell type at x, $c_{sig}\big(\sigma(x)\big)$ is a quantity that affects the cells cytokine secretion, $\omega_{cyt}\big(\tau(\sigma(x),t)\big)$ is the cytokine uptake rate of the cell type at x and $V_{cyt}\big(\tau(\sigma(x),t)\big)$ is a dissociation coefficient of cytokine secretion for the cell type at x. σ_{cyt} is nonzero for infected epithelial cells, virus-releasing epithelial cells and activated immune cells. For infected and virus-releasing epithelial cells c_{sig} is the amount of assembled virus A in the viral replication module, and for activated immune cells c_{sig} is the total amount of cytokine in the domain of the cell. Similarly, for epithelial cells V_{cyt} is the amount of assembled virus, and for immune cells V_{cyt} is the amount of cytokine in the domain of the cell. $\omega_{cyt}\big(\tau(\sigma(x),t)\big)$ is constant and nonzero for activated and inactive immune cells.

T3 - Oxidizing Agent Burst and Transport

Models diffusion and clearance of a general oxidizing agent in the extracellular environment. One of the cytotoxic mechanisms of immune cells is the release of different oxidizing agents, reactive oxygen species like H_2O_2 and nitric oxide. The mechanism of action of such agents varies but we assume that we can generalize such effects by modeling a single diffusive and decaying oxidizing agent field in the extracellular environment. The oxidizing agent is secreted by activated immune cells after persistent exposure to cytokine signals (I4→T3). We assume that the range of action of the oxidizing agent is short. Cell death is induced in uninfected, infected and virus-releasing epithelial cells when exposed to sufficient oxidizing agent (T3→E4).

The oxidizing agent field diffuses according to the reaction-diffusion equation,

$$\frac{\partial c_{oxi}}{\partial t} = D_{oxi}\nabla^2 c_{oxi} - \gamma_{oxi} c_{oxi} + s_{oxi}. \tag{2.10}$$

Bursts of oxidizing agent are implemented as a source term at a rate σ_{oxi}. An oxidizing burst occurs in immune cells with an activated state when the total cytokine in the immune cell's domain exceeds a threshold τ_{oxi}^{sec}.

Immune Cell Modules

The four processes I1-I4 capture immune cell functions which are defined below. These processes control how immune cells are activated, translocate, and kill other cells. Their interactions with epithelial cells and other model components are illustrated in Figure 2.5.

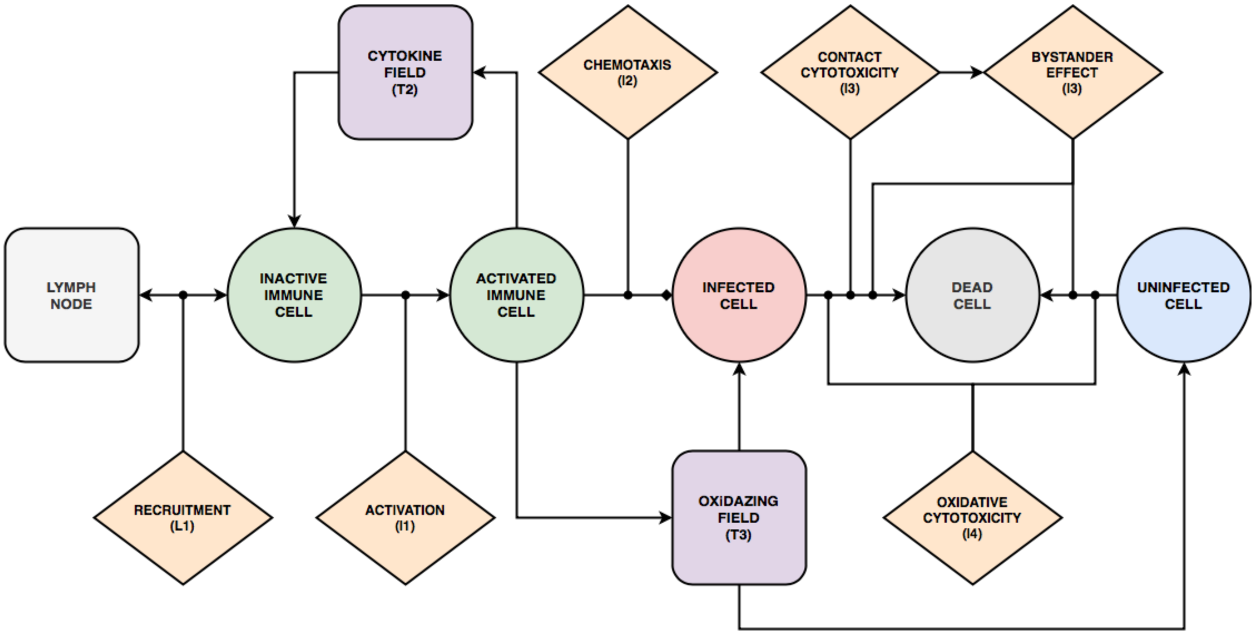
CYTOKINE FIELD (T2)
CHEMOTAXIS (I2)
CONTACT CYTOTOXICITY (I3)
BYSTANDER EFFECT (I3)
LYMPH NODE
INACTIVE IMMUNE CELL
ACTIVATED IMMUNE CELL
INFECTED CELL
DEAD CELL
UNINFECTED CELL
RECRUITMENT (L1)
ACTIVATION (I1)
OXIDAZING FIELD (T3)
OXIDATIVE CYTOTOXICITY (I4)

Figure 2.5. State diagram and interactions of Immune cells. Immune cells can adopt two different generalized types: inactive and activated. Inactive immune cells are recruited by the cytokine levels according to the immune recruitment module (L1). Transition from inactive to activated immune cells is determined by the immune activation module (I1) when cells are exposed to cytokines in the tissue. Activated immune cells amplify the cytokine signal by secreting cytokines to the extracellular environment. Activated immune cells chemotax towards virus-releasing cells (I2). Immune cells induce death of epithelial cells by direct cytotoxicity when coming into contact with infected cells (I3), bystander

effect by killing neighbors of infected cells (I3) and through oxidative cytotoxicity (I4) by releasing cytotoxic oxidizing agents (T3) into the extracellular environment.

I1 - Immune Cell Activation

Models immune cell maturation due to cytokine signaling. Immune cells mature at the recruitment site before being transported to the infection site as inactive immune cells (**L1→Immune Cells**). After infiltration, immune cells need to be exposed to local cytokine signals before activating (**T2→I1**). Once activated, immune cells move along a gradient of the cytokine field (**I2**) and amplify immune signaling by releasing cytokine molecules into the extracellular environment (**I1→T2**). Immune cells can become deactivated after a period of activation (**I1** and Fig 2C). Inactive immune cells become activated with a probability according to a Hill equation of the total cytokine bound to the cell $B_{cyt}(\sigma, t)$,

$$\begin{aligned} &\Pr(\tau(\sigma,t) \rightarrow \text{activated immune} | \tau(\sigma,t) = \text{inactive immune}) \\ &= \frac{\left(B_{cyt}(\sigma,t)\right)^{h_{act}}}{\left(B_{cyt}(\sigma,t)\right)^{h_{act}} + \left(EC50_{cytact}\right)^{h_{act}}}. \end{aligned} \quad (2.11)$$

After ten hours, an activated immune cell becomes inactive, in which case evaluations of activation (Equation (15)) recommence. The immune cells "forget" a percentage $(1 - \rho_{cyt})$ of the bound cytokine each time step while taking up an amount of cytokine from the environment ($\omega_{cyt}(\tau(\sigma), t)$ defined in **T2**),

$$B_{cyt}(\sigma, t) = \rho_{cyt} B_{cyt}(\sigma, t - \Delta t) + \omega_{cyt}\left(\tau\left(\sigma(x)\right), t\right). \quad (2.12)$$

I2 - Immune Cell Chemotaxis

Module I2 models activated immune cell chemotactic migration towards infection. Activated immune cells experience a motile force as a response to a signaling field. We assume that upon activation (I1→I2), immune cells move preferentially towards higher concentrations of local cytokine (T2→I2). The chemotactic effective energy $\mathcal{H}_{chemotaxis}$ associated with the gradient is calculated according to a chemotactic sensitivity parameter $\lambda_{chemotaxis}$ and calculated chemotactic force $F_{chemotaxis}$. The chemotactic force at a location x is saturated by normalizing the chemotactic sensitivity parameter by the concentration of cytokine at the center of mass of the cell at x, $c_{cyt,CM}\left(\sigma(x)\right)$,

$$F_{chemotaxis}(x) = \frac{\lambda_{chemotaxis}}{1 + c_{cyt,CM}\left(\sigma(x)\right)} \nabla c_{cyt}(x). \tag{2.13}$$

I3 - Immune Dell Direct Cytotoxicity and Bystander Effect

Models immune cell cytotoxicity when immune cells (both activated and inactive) identify and induce death in epithelial cells. Immune cells identify epithelial cells with internal virus on contact by antigen recognition and induce cell death by activating the caspase cascade (I3→E4). Other epithelial cells in contact with an epithelial cell that is killed by direct cytotoxicity can die through a bystander effect. At each simulation step, immune cells trigger cell death in the infected and virus-releasing epithelial cells with which they come in contact. When an infected cell is killed by direct cytotoxicity, each of its first-order neighbors is evaluated for cell death by a bystander effect model. Each of those neighbors $\sigma' \in N(\sigma)$ has a probability $k_{bystander}$ of dying from the bystander effect given by,

$$\Pr(\tau(\sigma', t) \to \text{Dead} | Direct\ Cytotoxicity(\sigma) = \text{True}) = k_{bystander}\ \forall \sigma' \in N(\sigma). \tag{2.14}$$

I4 - Immune Cell Oxidizing Agent Cytotoxicity

Models activated immune cell killing of target cells through the release of a diffusive and decaying oxidizing agent into the environment. Immune cells release a short-range, diffusive oxidizing agent when exposed to high cytokine concentration (**T3**). Cell death is induced in uninfected, infected, and virus-releasing epithelial cells when sufficiently exposed to the oxidizing agent (**T3→E4**). The oxidizing agent kills an epithelial cell of any type when the total amount of oxidizing agent in the domain of the cell $c_{oxi}(\sigma)$ exceeds a threshold for death τ_{oxi}^{death},

$$\Pr\left(\tau(\sigma,t) \rightarrow \text{Dead} | c_{oxi}(\sigma) > \tau_{oxi}^{death}\right) = 1. \qquad (2.15)$$

Lymph Node Component

The lymph node component models the net pro- or anti-inflammatory state of the immune system. It responds to cytokines received from the tissue and adds or removes immune cells from the tissue (**L1**).

L1 - Immune Cell Recruitment

Infected cells secrete signaling molecules into the extracellular environment (**E2→T3**), which alerts resident immune cells and recruits new immune cells from the blood, distant lymph nodes and bone marrow. Module L1 models immune cell recruitment and infiltration into the tissue in response to cytokine signaling by infected cells and activated immune cells. We model long-distance signaling by assuming that cytokine molecules in the extracellular environment exfiltrate the infection site and are transported through the lymphatic system to the lymphatic system to lymph nodes and through the bloodstream to initiate immune-cell recruitment (**T2→L1**). A delay on the order of minutes to hours would represent semi-local recruitment (*e.g.*, at the blood vessels). A delay on the order of days would represent long-range, systemic recruitment (*e.g.*, the time required for a dendritic cell to reach a lymph node and an induced T cell to return). Recruited immune cells are then transported and infiltrate the infection site (L1→Immune Cell).

The total immune cell population is governed by an ordinary differential equation of a dimensionless state variable S that represents immune response due to local conditions and long-distance signaling. When $S > 0$, immune cells are recruited to the simulation domain; likewise, immune cells are removed from the simulation domain when $S < 0$. Probability functions of S describe the likelihood of immune cell seeding and removal,

$$\Pr(\text{add immune cell}) = \operatorname{erf}(\alpha_{immune}S)\,, \qquad S > 0, \tag{2.16}$$

$$\Pr(\text{remove immune cell}) = \operatorname{erf}(-\alpha_{immune}S)\,, \qquad S < 0. \tag{2.17}$$

Here the coefficient α_{immune} is the sensitivity of immune cell addition and removal to the state variable S. The dynamics of S are cast such that, in a homeostatic condition, a typical number of immune cells can be found in the simulation domain, and production of cytokine (T2) results in additional recruitment via long-distance signaling (*i.e.*, with some delay). We model this homeostatic feature using the feedback mechanism of the total number of immune cells N_{immune} in the simulation domain. Cytokine signaling is modeled as perturbing the homeostatic state using the term $\alpha_{sig}\delta$. Here δ is the total amount of decayed cytokine in the simulation domain and $\alpha_{sig} > 0$ models signaling by transmission of cytokine to some far-away source of immune cells. We write the rate of change of S as

$$\frac{dS}{dt} = \beta_{add} - \beta_{sub}N_{immune} + \frac{\alpha_{sig}}{\beta_{delay}}\delta - \beta_{decay}S. \tag{1}$$

Here β_{add} and β_{sub} control the number of immune cells in the simulation domain under homeostatic conditions. β_{delay} controls the delay between transmission of the cytokine to the lymph node and corresponding immune response by adjusting the rate of recruitment due to total cytokine (*i.e.*, increasing β_{delay} increases the resulting delay). β_{decay} regulates the return of S to an unperturbed state (*i.e.*, $S = 0$, increasing β_{decay} increases the rate of return to $S = 0$). To determine the seeding location, the simulation space is randomly sampled $n_{seeding}$ times, and an immune cell is seeded at the unoccupied location with the highest amount of the virus field. If no location is unoccupied, then the immune cell is not seeded. The removal probability is evaluated for each immune cell at each simulation step. Immune cells are removed by setting their volume constraint to zero.

Initial and Boundary Conditions

The domain of all simulations had dimensions of 90 x 90 x 2 lattice sites. The initial cell configuration consisted of a 30 x 30 sheet of uninfected epithelial cells, each of size 3 x 3, on the lower layer of lattice sites. Epithelial cells were “frozen”, in that they were immobile, leaving the remaining 90 x 90 subdomain for occupancy by recruited immune cells. For cellular dynamics and mass transport, periodic boundary conditions were applied in the plane of the epithelial sheet, and Neumann conditions were applied along the direction orthogonal to the epithelial sheet. All field values for the diffusive viral, cytokine and oxidizing agent fields were initialized as zero everywhere.

At each first simulation step, the epithelial cell in the center of the sheet was set to infected, and the amount of internalized virus U of the viral replication model was set to a value of one. All epithelial cells were initialized with a number of unbound surface receptors $SR = R_o$. All immune cells, when introduced to the simulation by recruitment, were initialized in an inactive state, and with a bound cytokine value equal to zero ($B_{cyt} = 0$). During transition of an uninfected epithelial cell to the infected type, all state variables of the viral replication model were initialized with a value of zero.

Simulation Specifications

A baseline parameter set was constructed for all CPM parameters and modules developed in this work (Table 2.1). Non-dimensionalization was performed on model parameters for a lattice dimension of 4 µm per pixel along each dimension, at 20 minutes (1/3 hours) per MCS. All replicas were simulated for ten trials, each 1,000 MCS (14 days) long. Simulation data was collected at a frequency of 10 MCSs (3 hours) for all simulations.

Results

To illustrate the full range of dynamics of viral infection in the presence of an immune response, we established a baseline set of parameters (Table 2.1) for which the immune response is strong enough to slow the spread of the infection, but insufficient to prevent widespread infection and death of all epithelial cells (Fig 6). While we adjusted the parameters for the viral replication model to agree with reported time scales for SARS-CoV-2 replication *in vitro* [70], and we have selected parameter values in physiologically reasonable ranges, we have not attempted to match other model parameters to a specific tissue, virus or host species.

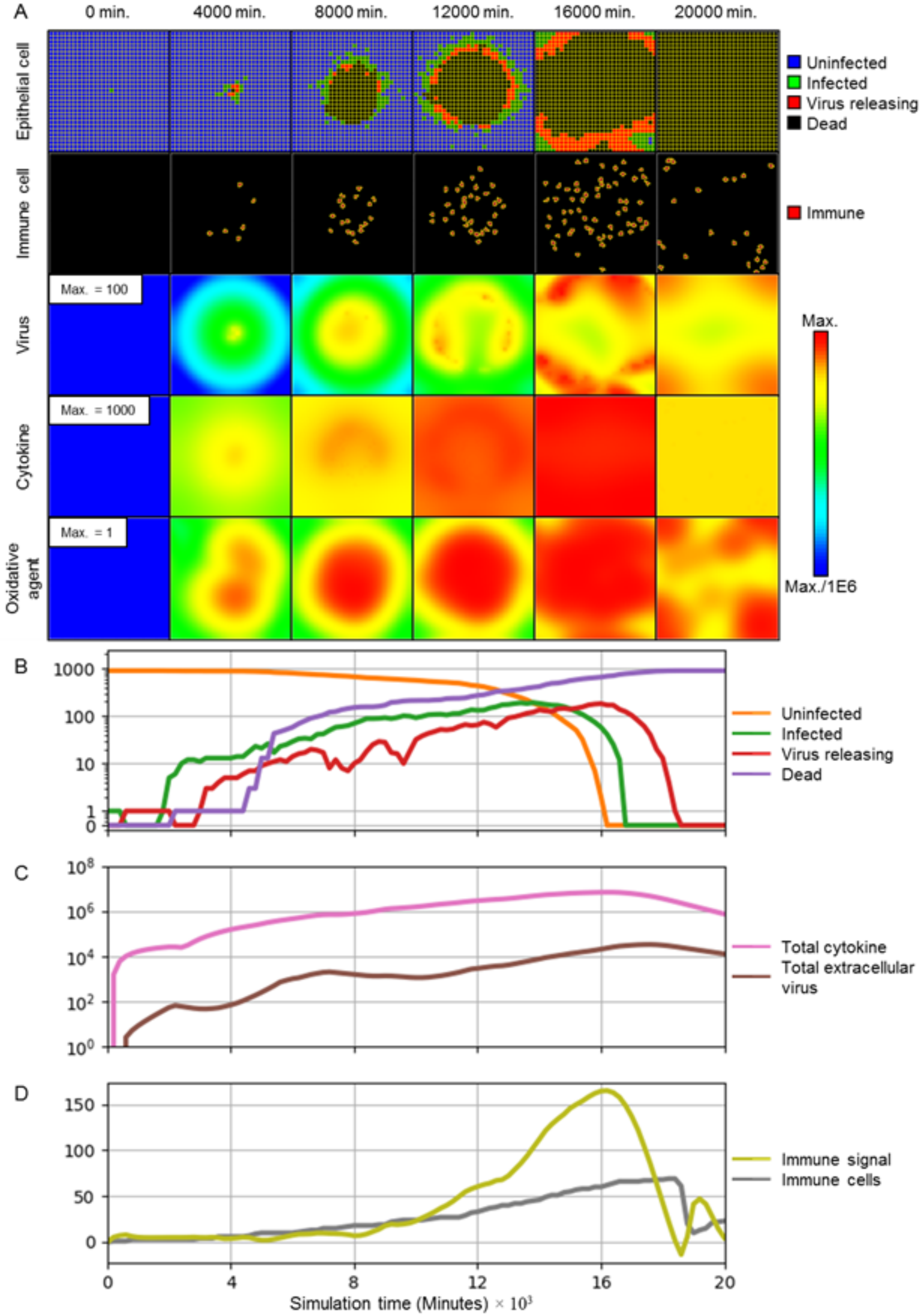
A
0 min.
4000 min.
8000 min.
12000 min.
16000 min.
20000 min.
Epithelial cell
Immune cell
Virus
Cytokine
Oxidative agent
Max. = 100
Max. = 1000
Max. = 1
🟦 Uninfected
🟩 Infected
🟥 Virus releasing
⬛ Dead
🟥 Immune
Max.
Max./1E6
B
1000
100
10
1
0
Uninfected
Infected
Virus releasing
Dead
C
10^8
10^6
10^4
10^2
10^0
Total cytokine
Total extracellular virus
D
150
100
50
0
Immune signal
Immune cells
0
4
8
12
16
20
Simulation time (Minutes) × 10^3

Figure 2.6. Simulation of the progression of infection in a patch of epithelial tissue of size 360 µm x 360 µm starting from a single infected cell for a representative simulation using the baseline parameters given in Table 2.1. A. Snapshots of spatial configuration *vs* time, showing progression of a simulated infection. Columns, left to right: 0 minutes (time of initial infection), 4000 minutes (67 hours, 2 ¾ days) after infection, 8000 minutes (133 hours, 5 ½ days), 12000 minutes (200 hours, 8 ⅓ days), 16000 minutes (267 hours, 11 days), and 20000 (333 hours, 14 days) minutes. **First row:** epithelial-cell layer composed of uninfected (blue), infected (green), virus-releasing (red) and dead epithelial cells (black). **Second row:** position of immune cells in the extracellular environment layer. **Third row:** concentration of extracellular virus field. **Fourth row:** concentration of extracellular cytokine field. **Fifth row:** concentration of extracellular oxidative agent field. Fields are shaded on a logarithmic scale: red corresponds to the chosen maximum value specified in the first panel and blue corresponds to six orders of magnitude lower than the maximum value; colors saturate for values outside this range. **B-D.** Simulation time series. **B.** Number of uninfected (orange), infected (green), virus-releasing (red) and dead (purple) epithelial cells *vs* time on a logarithmic scale. **C.** Total extracellular cytokine (magenta) and total extracellular virus (brown) *vs* time on a logarithmic scale. **D.** Value of the immune recruitment signal S (yellow) and number of immune cells (grey) *vs* time on a linear scale. Simulations use periodic boundary conditions in the plane of the epithelial sheet, and Neumann conditions [61] normal to the epithelial sheet.

Initially infected cell immediately starts releasing cytokines into the extracellular environment. After an incubation period (2 ½ hours), the first infected epithelial cell (green) transitions from infected to virus releasing and starts releasing viruses into the extracellular environment. Initial release of extracellular virus causes additional epithelial cells to become infected. Release of cytokines leads to delayed addition of immune cells to the simulation domain (Fig 2.6D). By 2 ¾ days, the number of infected cells increases 10-fold and the epithelial cells start undergoing virally-induced death as the infection spreads radially outward from the initial site. This results in the formation of an annular region of infected cells spreading radially outwards from the initial infection site (Fig 2.6A), analogous to the Fisher equation for deterministic front propagation [62]. The increase in the number of infected cells and the local cytokine concentration is accompanied by a similar increase in the local immune cell population. By 5 ½ days, the number of dead epithelial cells around the initial infection site increases sharply. Following this phase of rapid cell death, the number of infected, virus-releasing and dead epithelial cells continues to increase exponentially but at a slower rate. Total extracellular virus and cytokine continue to increase exponentially. The increase in cytokine results in continued recruitment of immune cells. By 11 days, the number of uninfected epithelial cells reaches zero and the number of infected and virus-releasing cells peaks. Despite the declining number of infected and virus-releasing epithelial cells, the delayed immune response continues to add immune cells to the tissue. After 11 days, the extracellular virus and the amount of cytokine decrease exponentially as the remaining virus-releasing epithelial cells die. By 14 days, all epithelial cells die, and many immune cells leave the tissue.

Classification Of Spatiotemporal Infection Dynamics

The rate at which infection propagates and the strength (speed and amplitude) of the immune response depend on multiple model parameters. Interplay between these rates leads to a wide spectrum of qualitatively distinct spatiotemporal dynamics. The virus-receptor binding affinity k_{on} and the immune response delay coefficient β_{delay} are critical parameters affecting the rate of infection of epithelial cells and the strength of the immune response, respectively. Increasing k_{on} increases the rate of internalization of extracellular viral particles into epithelial cells. Decreasing β_{delay} increases the strength of immune-cell recruitment.

Varying these two parameters around the baseline simulation values yields six patterns of spatiotemporal infection dynamics, ranging from unopposed infection to clearance (Fig 2.7). We defined these classes based on the transient dynamics and the final state of the simulation at 14 days. We define the six patterns (*classes*) of infection dynamics as follows:

No immune response: a limiting case (corresponding to *in vitro* and organoid culture experiments on viral infection, which lack immune cells) that serves as a reference simulation showing the spread of unopposed infection. When the cellular immune response is absent, an infection front travels across the epithelium until all epithelial cells have died due to intracellular virus (Fig 2.7A).

Widespread infection: when the immune response is weak (large β_{delay}) or the rate of infection propagation is large (large k_{on}), the immune cannot prevent the propagation of the infection front. No uninfected epithelial cells survive at the end of the simulation (Figs 2.7B).

Slowed infection: for moderate immune response (moderate β_{delay}) and a moderate rate of infection propagation (moderate k_{on}), both uninfected and infected epithelial cells and some extracellular virus remain at the end of the simulation (Fig 2.7C). These cases are functionally distinct from widespread infection, since even a single remaining uninfected epithelial cell could initiate tissue regeneration. In most cases of slowed infection, the numbers of infected cells and the extracellular virus continue to increase. A special case of slowed infection occurs when oscillations in the amount of virus.

Containment: for strong immune response (small β_{delay}) and low to moderate rate of infection propagation (moderate k_{on}), a few infected and virus-releasing cells are present for most of the simulation. However, the immune cells eventually kill all infected and virus-releasing epithelial cells. At the end of the simulation, no infected or virus releasing cells remain, while uninfected cells survive, and some extracellular virus remains in the extracellular environment (Fig 2.7D).

Recurrence: for strong immune response (small β_{delay}) and a fast infection propagation (large k_{on}), relatively few epithelial cells become infected early in the simulation. All infected and virus-releasing epithelial cells die. However, the remaining extracellular virus infects additional epithelial cells later, restarting the spread of infection (Fig 2.7E).

Clearance: for strong immune response (small β_{delay}) and a slow infection propagation (small k_{on}), the number of infected and virus-releasing epithelial cells goes to zero without recurrence and the extracellular virus drops rendering the frequency of recurrence negligible (Fig 2.7F). A special case of clearance occurs when the initially infected epithelial cells fail to infect any other epithelial cells.

To quantitatively characterize simulation results, we measured the number of uninfected, infected, virus-releasing and dead epithelial cells, the total number of immune cells, the number of activated immune cells, the total amount of extracellular virus (integral over the virus field), the total diffusive cytokine (integral over cytokine field), the maximum total extracellular virus (over all simulation time) and the maximum total diffusive cytokine (over all simulation time). Fig 2.7 shows these quantitative metrics, together with a series of spatial configurations for all model components, corresponding to each pattern of infection dynamics.

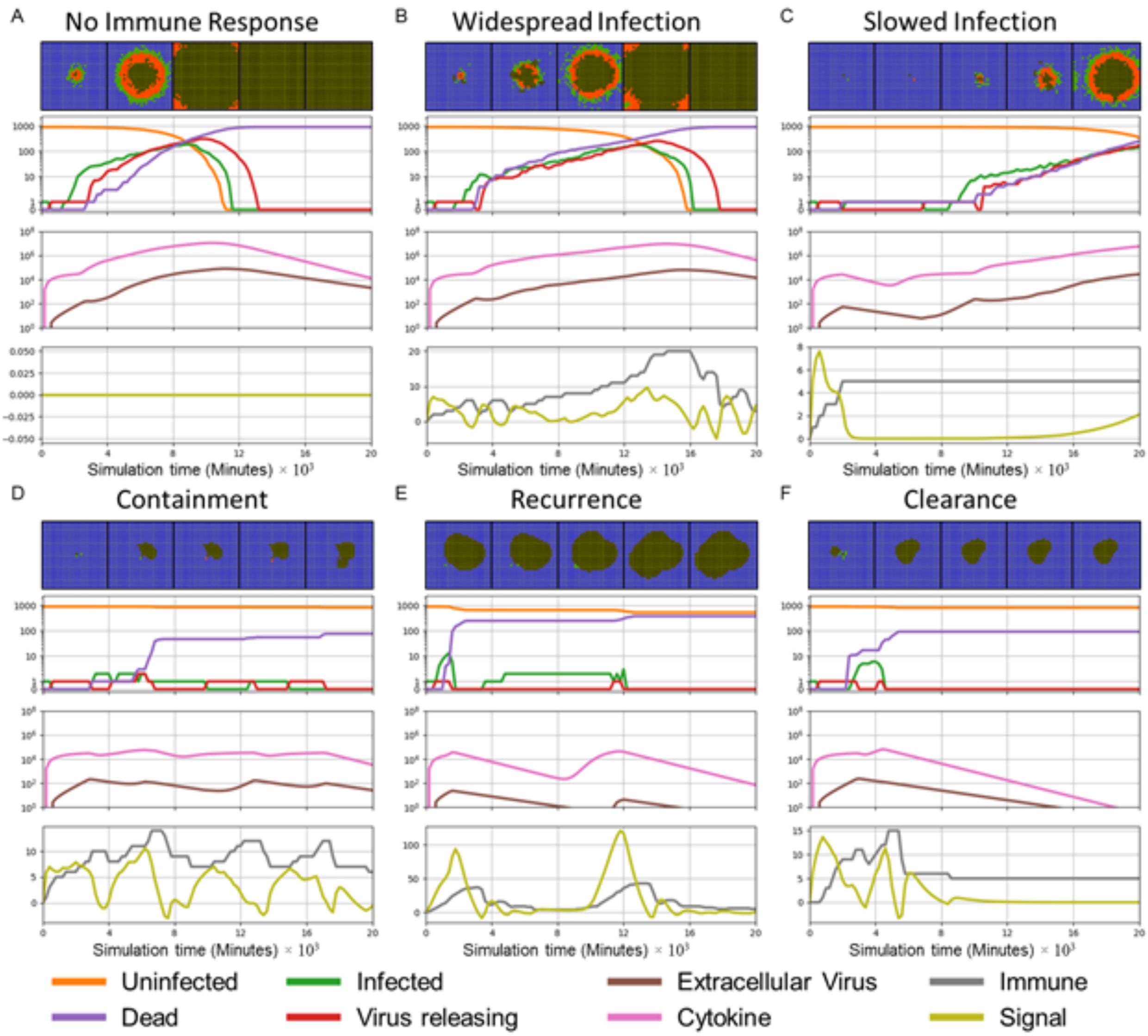

Figure 2.7. Patterns (Classes) Of Spatiotemporal Infection Dynamics. First row: snapshots of spatial configurations of the epithelial cells. Color coded: uninfected (blue), infected (green), virus releasing (red), dead (black). TImes from left to right 2 ¾, 5 ½, 8 ⅓, 11 and 14 days. **Second row:** number of uninfected (orange), infected (green), virus-releasing (red) and dead (purple) epithelial cells *vs* time on a logarithmic scale (with 0 included for clarity). **Third row:** total extracellular cytokine (magenta) and total extracellular virus (brown) *vs* time on a logarithmic scale. **Fourth row:** value of the immune recruitment signal S (yellow) and number of immune cells (grey) *vs* time on a linear scale. **A. No immune response:** infection propagates unopposed until all epithelial cells have died from intracellular virus. **B. Widespread infection:**

weak immune response slows propagation of the infection, but no uninfected cells survive at the end of the simulation. **C. Slowed infection:** uninfected and infected epithelial cells coexist at the end of the simulation. **E. Containment of infection:** no infected or virus-releasing epithelial cells remain, uninfected cells survive and virus remains in the extracellular environment at the end of the simulation. **F. Recurrence:** the number of infected and virus releasing epithelial cells goes to zero, but persistent extracellular virus infects new epithelial cells later on. **G. Clearance:** the number of infected and virus-releasing epithelial cells goes to zero and the level of extracellular virus is negligible at the end of the simulation.

Stronger Immune Response And Lower Rates Of Virus Internalization Promote Containment Of Infection

To explore tradeoffs between the rate of virus internalization and the strength of the immune response, we performed a multidimensional parameter sweep of the virus-receptor association affinity k_{on} and immune response delay coefficient β_{delay}. Variations in virus receptor association affinity represent factors that affect the binding affinity of cellular viral receptors (*e.g.*, ACE2 and TMPRSS-2 in the case of SARS-CoV-2) with a virus (*e.g.*, mutations in viral coat protein or drugs to block viral entry). Variations in immune response delay coefficient represent factors that affect the strength of the systemic immune response (*e.g.*, anti-inflammatory corticosteroids, IL-7 treatment or age, since older individuals tend to have slower adaptive immune responses).

We ran ten simulation replicas for each parameter set, increasing and decreasing the baseline parameter values 10-fold and 100-fold (Figs 2.8-2.10). For each simulation replica, we examined the number of uninfected epithelial cells (Fig 2.8), the number of infected epithelial cells (Fig 2.9), the total extracellular virus (Fig 2.10). We identified regions of the parameter space where all ten simulation replicas resulted in either containment/clearance (green-shaded subplots) or widespread infection (orange-shaded subplots). In the intermediate regions (unshaded subplots) different replicas for the same set of parameters showed combinations of the different classes of infection dynamics.

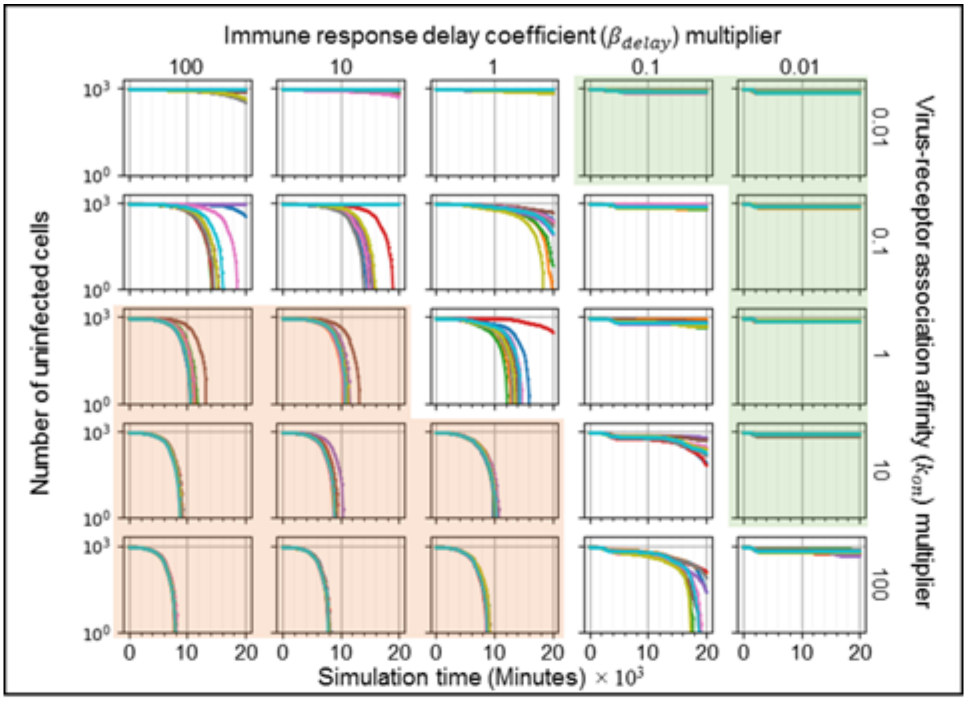

Figure 2.8. **Global Logarithmic Sensitivity analysis of the number of uninfected epithelial cells vs time for variations in virus-receptor association affinity k_{on} and immune response delay coefficient β_{delay}, showing regions with distinct infection dynamics**. Logarithmic pairwise parameter sweep of the virus-receptor association affinity k_{on} and the immune response delay β_{delay} around their baseline values, with ten simulation replicas per parameter set. The number of uninfected epithelial cells for each simulation replica for each parameter set, plotted on a logarithmic scale, *vs* time.

For large k_{on} and large β_{delay} (Figs 2.8-2.10, orange-shaded regions), simulation replicas result in widespread infection and variability between simulation replicas is small. In this region, the initial release of virus into the extracellular environment results in a rapid increase in the number of infected and virus releasing epithelial cells early during the simulation (Figs 2.9). After 3 ½ days, the number of uninfected epithelial cells rapidly decays to zero. Because of the large β_{delay}, the immune recruitment signal is less responsive to the cytokine signal produced by infected and virus-releasing epithelial cells and no significant recruitment of immune cells occurs throughout the simulations. The number of virus-releasing epithelial cells peaks around 5 days, the level of extracellular virus peaks 6 ¼ days and the number of dead epithelial cells peaks around 7 days. With no remaining uninfected epithelial cells to infect, all remaining infected die, causing the total amount of extracellular virus to decrease.

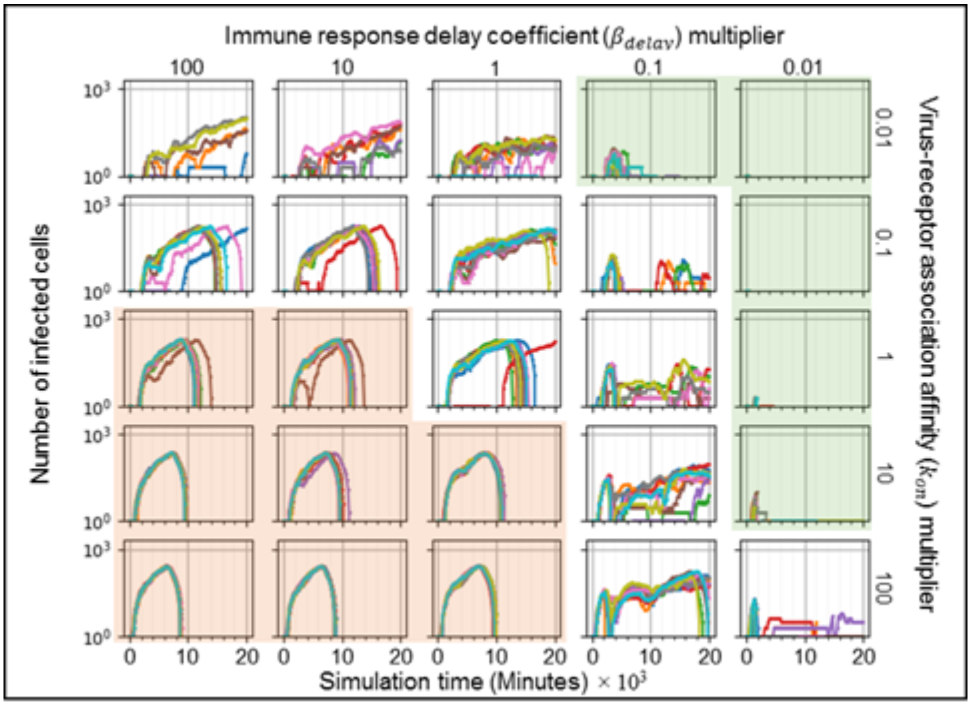

Figure 2.9. **Global Logarithmic Sensitivity analysis of the number of infected epithelial cells vs time for variations in virus-receptor association affinity k_{on} and immune response delay coefficient β_{delay}, showing regions with distinct infection dynamics**. The number of infected epithelial cells for each simulation replica for each parameter set, plotted on a logarithmic scale, *vs* time displayed in minutes.

For small k_{on} and small β_{delay} (Figs 2.8-2.10, green-shaded subplots), simulation replicas result in either clearance or containment and variability between simulation replicas is also small. Initial release of virus to the extracellular environment results in a small decrease in the number of uninfected cells and increase in the number of infected epithelial cells. Because of the small β_{delay}, the immune recruitment signal is very sensitive to the cytokine produced by infected cells, resulting in rapid recruitment of immune cells and an early first peak in the population of immune cells around 1 ⅓ days. The increase in the number of immune cells is followed by a rapid increase in the number of dead epithelial cells. The number of immune cells and the number of dead epithelial cells peak around 1 ⅓ days, after which the number of immune cells decreases. With no remaining infected cells, the total extracellular virus decays until the infection is cleared.

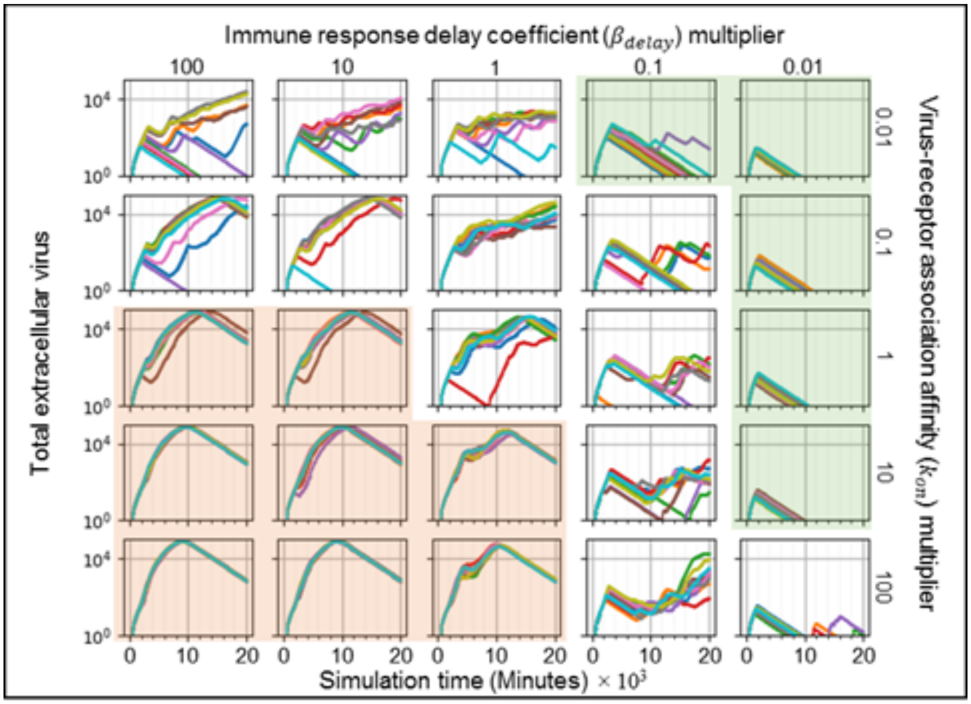

Figure 2.10. **Global Logarithmic Sensitivity analysis of the total amount of extracellular virus vs time for variations in virus-receptor association affinity k_{on} and immune response delay coefficient β_{delay},**

showing regions with distinct infection dynamics. The total amount of extracellular virus for each simulation replica for each parameter set, plotted on a logarithmic scale, *vs* time displayed in minutes.

For moderate to high k_{on} and moderate to low β_{delay} (right unshaded subplots in Figs 2.8-2.10), the rate of new infection nearly balances the rate of elimination of cells, resulting in replicas showing clearance, contaminant, recurrence and slowed infection for the same parameter values, with very few cases of widespread infection. The initial release of virus into the extracellular environment by the first virus-releasing cells infects a moderate number of uninfected cells. The resulting cytokine secretion elicits a moderate to high response of the immune recruitment signal and high number of immune cells. Early recruitment of immune cells leads to many epithelial cells dying by 2 ⅔ days. For high rate of virus internalization (high k_{on}), low amounts of extracellular virus are sufficient to cause recurrence.

For moderate to low k_{on} and moderate to high β_{delay} (upper left unshaded subplots in Figs 2.8-2.10), the rate of new infection is slightly faster than the immune system's response, resulting in a combination of widespread infection, slowed infection and containment, and a few cases of clearance. The immune system is only moderately responsive to the cytokine signal, resulting in a slow to moderate increase in the immune recruitment signal and in the number of immune cells.

Moderate Inhibition Of Genomic Replication By Antiviral Therapies Significantly Reduces The Spread Of Infection When Initiated Early During Infection

Optimal therapeutic use of antiviral drugs requires considering the relationship between molecular *efficacy* (how effectively the drug blocks a particular aspect of the viral life cycle at saturation concentration), *potency of therapy* (the effect of the drug at a molecular level at a given dose) and clinical *effectiveness* (how well the drug reduces the severity or duration of the infection), as well as the tradeoff between side effects and bioavailability. One drug might have moderate efficacy but have few side effects. Another drug might have high efficacy but have severe side effects. A drug might also have a combination of beneficial and adverse effects (*e.g.*, it might reduce viral replication early in infection, but also be immunosuppressive). Antiviral drugs like Tamiflu retain their ability to block aspects of the viral life cycle (efficacy) but become much less clinically effective as the time for treatment increases (in adults Tamiflu is most effective when given within 48 hours after exposure and thus is often used prophylactically) [52]. To simulate the effects of treatment that targets RNA synthesis using different drug efficacies and times of administration, we generated a series of simulations in which we reduced r_{max}, the replication rate of genomic material in the viral replication model by different amounts and at different times in the simulation. We focus on RNA-synthesis blockers because viral genome synthesis exponentially increases the production rate of viruses per cell. The “viral replication multiplier” represents the potency of the treatment, the factor by which r_{max} is reduced (either a low dose with high efficacy, or a high dose with a less efficacy). The “time delay of application” is the simulation time at which r_{max} is reduced, which corresponds to the time after infection at which the treatment is administered. To characterize therapeutic effectiveness, we distinguished three classes of simulation outcomes:

Positive outcomes: effective treatment, where at least 50% of the epithelial cells remain uninfected at the end of the simulation (green-shaded subplots).

Negative outcomes: ineffective treatment, where less than 10% of the epithelial cells remain uninfected at the end of the simulation (orange-shaded subplots).

Intermediate outcomes: partially effective treatment, where between 10-50% of the epithelial cells remain uninfected at the end of the simulation (unshaded or intermediate-shaded subplots). To characterize how the potency and time of treatment affect the dynamics of the simulation, we examined the time courses of the number of uninfected epithelial cells (Fig 2.11), virus-releasing epithelial cells (Fig 2.12), the total amount of extracellular virus (Fig 2.13), the number of dead epithelial cells and the number of immune cells. Intensity of green indicates the percent of simulation replicas that produced positive outcomes for a given set of parameters. Intensity of orange indicates the percent of simulation replicas that produced negative outcomes.

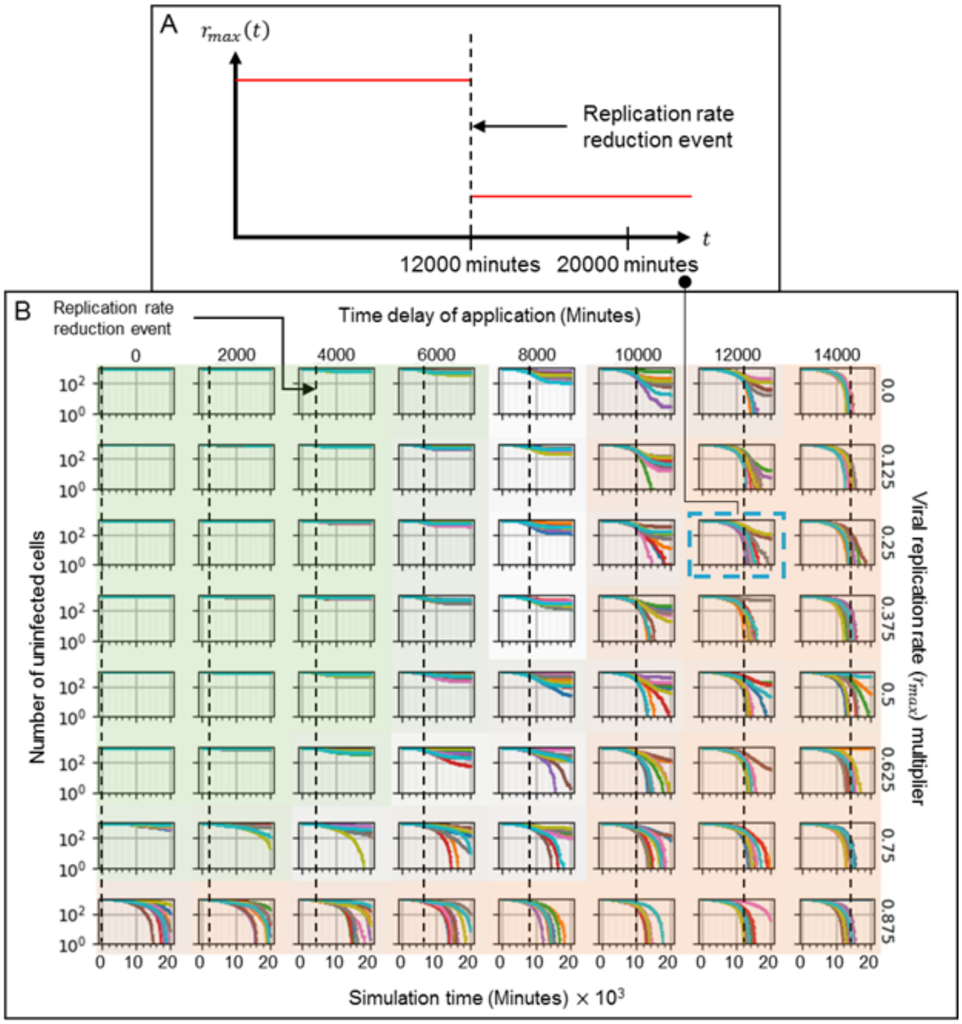

Figure 2.11. Number of uninfected cells vs time in simulations of a hypothetical drug treatment reducing the viral genome (*e.g.* RNA for SARS-CoV-2) replication rate (r_{max}) as a function of treatment potency and time of initiation of treatment. Drug therapy is administered at a fixed time after infection and remains activated for the duration of the simulation. **A**. Sample treatment, showing the time course of r_{max}. r_{max} is reduced by a multiplier which is one minus the potency of the drug at the given dose, 75% in **A**, at a particular time of initiation of treatment (time delay of application) 8 ⅓ days in **A**. **B**. Parameter sweep of the potency of treatment (reduction in baseline viral replication rate r_{max}, vertical) and the time of treatment (dashed lines, horizontal) shows parameter regions where the majority of simulation replicas produce positive outcomes (green-shaded subplots), negative outcomes (orange-shaded subplots) and intermediate cases (intermediate shading or unshaded). Intensity of green and orange indicates the number of positive and negative outcome replicas for each parameter combination (treatment effectiveness). Green regions show that early intervention leads to positive outcomes (is effective) for most ranges of treatment potency, with high numbers of uninfected epithelial cells at the end of the simulation for almost all simulation replicas. Orange regions show that late interventions result in mostly negative outcomes (ineffective treatment) regardless of the potency, and that outcomes are more variable between replicas, with both positive and negative outcomes for most parameter sets. The number of uninfected epithelial cells for each simulation replica for each parameter set, plotted on a logarithmic scale, *vs* time displayed in minutes.

When treatment is given early, most of the simulation replica outcomes are positive. If the drug is administered prophylactically or very soon after infection the treatment potency needs to be only 25% to achieve mostly positive outcomes. Increasing the time to treatment increases the potency required to achieve similar numbers of positive outcomes: the treatment is effective for a potency of at least 37.5% if administered by 2 ¾ days, and at least 87.5% if administered 4 days. For all potencies greater than 12.5%, early intervention prevents significant increase in the number of infected cells (Fig 2.12, green-shaded subplots), and a small number of immune cells is sufficient to stop the spread of infection. In this region, delaying treatment results both in a higher level of extracellular virus (Fig 2.13, green-shaded subplots) and more dead epithelial cells at the end of simulation. With inhibited viral replication, the extracellular virus decays until it is mostly cleared by the end of simulation (Fig 2.13). Variability between simulation replicas for a given parameter set increases with both decreasing potency and increasing time of initiation of treatment.

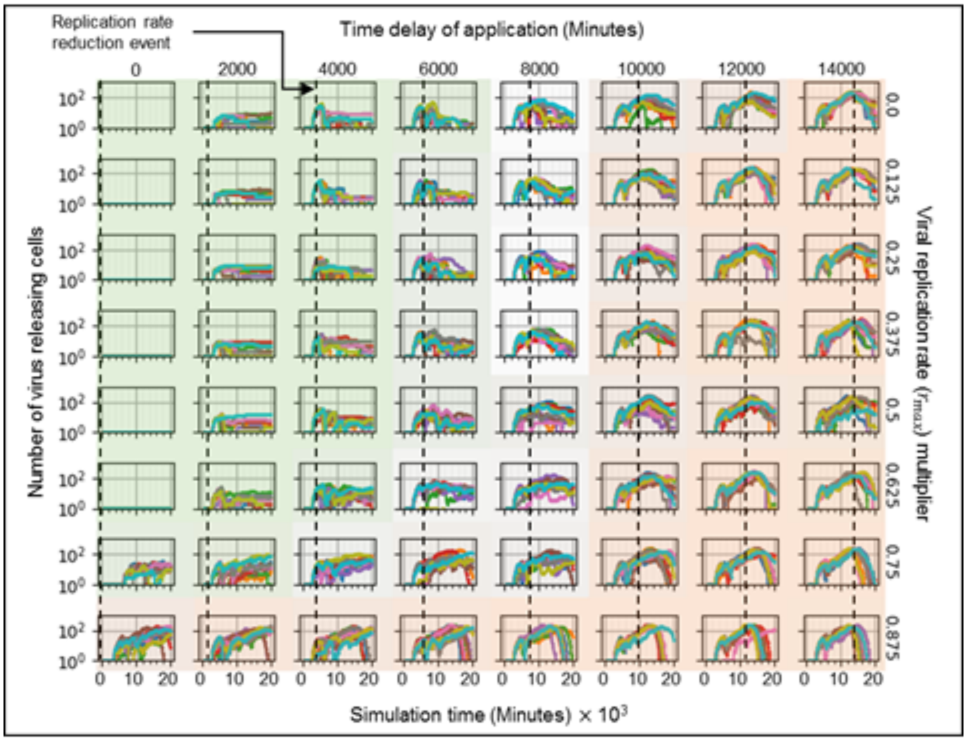

Figure 2.12. Number of virus releasing cells vs time in simulations of a hypothetical drug treatment reducing the viral genome (*e.g.* RNA for SARS-CoV-2) replication rate (r_{max}) as a function of treatment potency (one minus the viral replication rate multiplier) and time of initiation of treatment. The number of virus-releasing epithelial cells stays low when the intervention occurs early during infection (when the

amount of extracellular virus is increasing rapidly), but continues to increase when the intervention occurs later (when the level of extracellular virus is at or near its maximum in the untreated case).

If the potency of the treatment is less than 12.5%, most of the simulation replicas have negative outcomes even if the drug is administered early (Figs 2.11-2.13, bottom row). In these cases, the time after infection at which the drug is given makes no significant difference. When the treatment is given late (after 7 days), regardless of the potency of the drug, most simulation replicas have negative outcomes (Figs 2.11-2.13, orange-shaded regions). By the time of treatment, a significant number of cells have been infected (Fig 2.11, orange-shaded regions) and a significant amount of virus has been released into the extracellular environment (Fig 2.12, orange-shaded regions). In addition, a significant number of epithelial cells have died and significant recruitment of immune cells has occurred. For higher treatment potency, the level of extracellular virus starts decreasing immediately after treatment, even when a significant number of virus-releasing epithelial cells remain, indicating that viral replication inside cells has been significantly reduced. Later intervention also increases variability between simulation replicas and, although most simulation replicas have negative outcomes, the same set of parameter values produced two distinct qualitative outcomes (some more and some less favorable) for higher potency. Thus in a few cases, even late treatment can be effective.

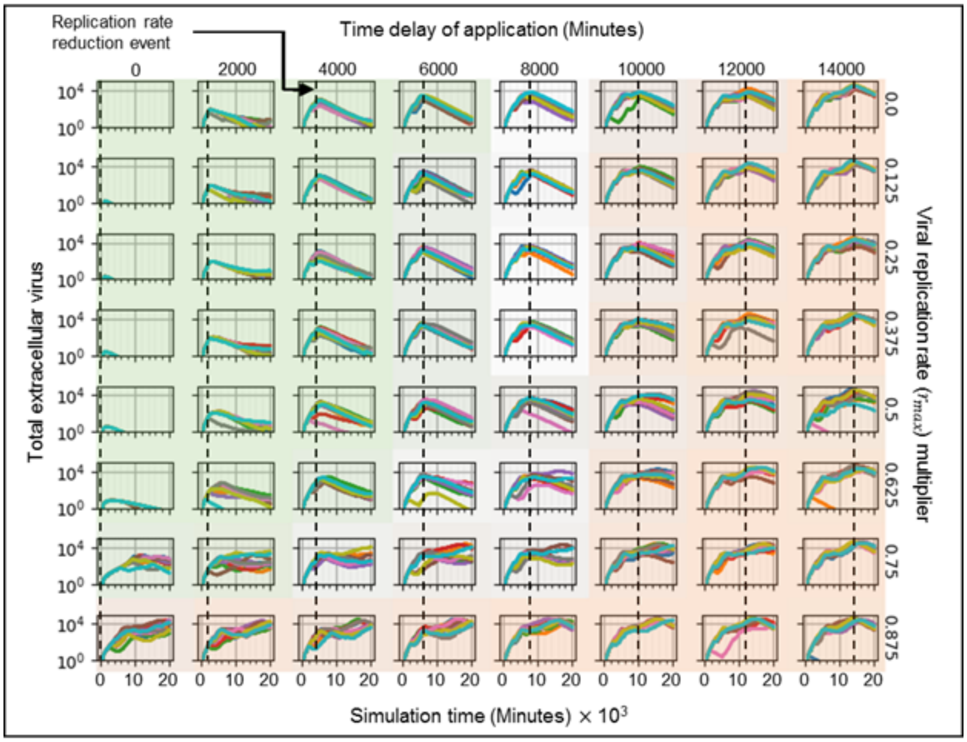

Figure 2.13. Levels of extracellular virus vs time in simulations of a hypothetical drug treatment reducing the viral genome (*e.g.* RNA for SARS-CoV-2) replication rate (r_{max}) as a function of drug potency (one minus the viral replication rate multiplier) and time of initiation of treatment. Extracellular virus is cleared or near-cleared when intervention occurs soon after infection. Parameter values, axis types and time-scale and shading as in Fig 8.

When treatment is given at intermediate times (4 to 7 days), most simulation replicas have intermediate outcomes. For potencies above 50%, the fraction of uninfected epithelial cells at the end of simulation is relatively and the treatment is usually moderately effective (Fig 2.11). For potencies below 50%, the infected cells remain approximately constant or continues to increase after treatment (Fig 2.12) and significant levels of extracellular virus remain at the end of the simulation (Fig 2.13). In most cases the treatment is ineffective. Variability between outcomes for the same parameter values is higher than for potencies above 50%.

Discussion

Our spatial, multicellular model of primary acute viral infection of an epithelial tissue includes key aspects of viral infection, viral replication, and immune response. By investigating sensitivity to model parameters and simulating drug therapies, we identified six distinct spatiotemporal classes of infection dynamics based on the model's transient behaviors and final simulation outcomes. Each of classes corresponds to biologically or clinically observable outcomes. No immune response represents *in vitro* experiments (*e.g.*, organoids). Widespread infection corresponds to an infection that is likely to spread to surrounding tissue and cause major tissue damage. Slowed infection corresponds to an initial infection whose spread is more likely to be eliminated by the adaptive immune response. Containment corresponds to immune-cell elimination of all infected cells but where remaining extracellular virus could result in new sites of infection elsewhere. Recurrence corresponds to the situation when new lesions form within the observed tissue patch. Clearance corresponds to immune-cell-based elimination of all infected cells and extracellular virus (classical viral clearance).

We showed that key parameters of the model, such as those affecting viral internalization (*i.e.*, virus-receptor association affinity k_{on}), can lead to both containment/clearance (*e.g.*, small k_{on}, Figs 2.5-2.7) or widespread infection (*e.g.*, large k_{on}, Figs 2.5-2.7). Multidimensional parameter sweeps showed how the interplay between immune response (*e.g.* immune response delay coefficient β_{delay}) and viral spread could lead to widespread infection (*e.g.*, large β_{delay}, large k_{on}, Figs 2.5-2.7), rapidly cleared infection (*e.g.*, small β_{delay}, small k_{on}, Figs 2.5-2.7) or containment/clearance after substantial damage (*e.g.*, small β_{delay}, moderate k_{on}, Figs 2.5-2.7). Some of these outcomes would be expected biologically (*e.g.*, very fast internalization with a slow immune response is likely to lead to widespread infection; faster and stronger immune responses should control the spread of viral infection within the tissue. Others, like the coexistence of replicas with containment/clearance or failure to control for the same parameter set, are less expected, and could not occur in a deterministic non-spatial model (though they might occur in some stochastic non-spatial models).

We studied the influence of timing and potency of an RNA-polymerization inhibitor on the spread of viral infection within tissue (Figs 2.9-2.11). In the model, drugs with this mode of action can improve viral control in tissue if administered prophylactically at high potency, and their effectiveness decreases the later they are administered. Less obviously, the lower-left region of Figs 2.9-2.11 shows how therapies with even reduced potency could control the infection when administered sufficiently early. While we expect prophylactic or early treatment at the same potency to be more effective than later treatment, our model suggests that time of treatment is a more significant factor than potency in determining the effectiveness of the therapy. Our model thus suggests that drugs that interfere with virus replication are significantly more effective if used even at very low doses prophylactically than they would be if used even at a high dose as a treatment given later after exposure. Specifically, a prophylactic treatment in simulation which reduces the rate of viral RNA synthesis by only 35% is more effective than a treatment with 100% potency given two and a half days after infection and has about the same efficacy as a treatment with 50% potency given one day after infection.

Differences in spatiotemporal dynamics and variability of outcomes critically depend on the ability of the model to resolve the spread of virus and immune response spatially. Since the viral replication module is deterministic, the primary cause of this difference in simulation outcomes for the same set of parameter values is the spatial distribution of cells. Spatial structure (*e.g.*, infection of neighboring cells), stochastic events (*e.g.*, early cell death of infected cells before significant virus release) and cell-to-cell variation (*e.g.*, difference in viral release between cells) all affect the variation between replicas. The spectrum of outcomes in our parameter sweeps (Figs 8-10 and 11-13) depends on the emergent spatial patterns of cytokine and virus fields (*e.g.*, variations within the infection front expose different numbers of uninfected epithelial cells to the immune response).

Future perspectives

Our modeling framework can improve with the inclusion of additional cellular and immune mechanisms. Modules accounting for viral clearance, tissue recovery and persistent adaptive immune response can also be added to the framework. The current immune model does not include important signaling factors (*e.g.*, interferon-induced viral resistance in epithelial cells) and the different roles of tissue-local and systemic signals (*e.g.*, various cytokines). It also omits many cell types associated with both innate and adaptive immune response and their roles (*e.g.*, viral scavenging by macrophages, relaying and amplification of immune signals by dendritic cells). The specific roles of different immune cell phenotypes must be incorporated because the timing of their activities can be quite different (*e.g.*, early neutrophil release of oxidative agent contrasted with later effector T-cell contact-mediated killing). The model does not currently consider the production and role of antibodies in the humoral immune response or tissue recovery after damage. The model also greatly simplifies the structure of the epithelium and its environment, but could be easily generalized to a detailed, three-dimensional geometry, albeit at the cost of computational performance.

The immune response to viral infection depends on locus of infection, degree of infection and patient immune state. Understanding the reasons for immune failure to contain infection, or pathological responses like cytokine storms or sepsis, requires models of immune response at multiple locations and scales. The same is true for understanding and predicting the possible protective or adverse effects of coinfection. We can also study the systemic effects of possible therapies with known molecular modes of action. Evaluating therapies in a simulated context prior to performing animal or human trials could lead to more effective and rapid drug discovery and to optimized dosage and timing of treatments. Understanding the origins of population variability in disease progression is crucial to providing optimal personalized treatment. While the simulations presented here begin with a single infected cell, a simulation which begins with multiple infected cells might better represent the infection dynamics of patients that have been subject to high level exposure, such as healthcare workers. Factors such as hypertension, immunosuppression and diabetes affect tissue state and immune response and could also be incorporated into our model. More detailed studies of these factors using our model could reveal more about the effects of population variability (due to age, genetic variation, prior drug treatment or immune status) on disease progression. Such computational studies could be accomplished using concomitant, calibrated ODE-based simulations of COVID-19 treatment.

The COVID-19 crisis has shown that drug discovery and therapy development both require new predictive capabilities that improve their effectiveness and efficiency. We have developed our framework to explore the relationship between molecular, cellular-level and systemic mechanisms and outcomes of acute viral infections like SARS-CoV-2, and to support development of optimal, patient-specific treatments to combat existing and new viruses.

Conversion Factors	Value	References / Justification
Simulation step Δt	1200.0 s	Selected for approximately 14 days of simulation time in 1k simulation steps
Lattice width	4.0 μm	Selected according to cell diameter
Scale factor for concentration	1×10^{-14} mol	Selected for conversion from mol L^{-1} to mol μm^{-1} (10^{-15}) with 10x adjustment for fewer concentrations less than 1
Simulation parameters	Value	References / Justification
Cell diameter	12.0 μm	Selected according to typical epithelial cell size
Replication rate r_{max}	$(1/12)\times10^{-3}$ s^{-1}	Calibrated to timescale of SARS-CoV-2 [60]
Translating rate r_t	$(1/18)\times10^{-3}$ s^{-1}	Calibrated to timescale of SARS-CoV-2 [60]
Unpacking rate r_u	$(1/6)\times10^{-3}$ s^{-1}	Calibrated to timescale of SARS-CoV-2 [60]
Packaging rate r_p	$(1/6)\times10^{-3}$ s^{-1}	Calibrated to timescale of SARS-CoV-2 [60]
Release rate r_s	$(1/6)\times10^{-3}$ s^{-1}	Calibrated to timescale of SARS-CoV-2 60]
Scale factor for number of mRNA per infected cell $mRNA_{avg}$	1000 $cell^{-1}$	Selected for average production of 2000 virions per cell before death per influenza [70]
Viral dissociation coefficient r_{half}	2000	Derived from $mRNA_{avg}$, r_{max} and r_t
Viral diffusion coefficient D_{vir}	0.01 μm^2 s^{-1}	Selected according to sensitivity analysis and estimated from physiological ranges for lung mucus[1]
Viral diffusion length λ_{vir}	36 μm	Selected according to sensitivity analysis
Viral decay rate γ_{vir}	7.71×10^{-6} s^{-1}	Derived from λ_{vir} and D_{vir}

Cytokine diffusion coefficient D_{cyt}	0.16 µm^{2} s^{-1}	[67] (IL-2 cytokine)
Cytokine diffusion length λ_{cyt}	100 µm	[65] (IL-2 cytokine)
Cytokine decay rate γ_{cyt}	1.32×10^{-5} s^{-1}	Derived from λ_{cyt} and D_{cyt}
Maximum cytokine immune secretion rate $\sigma_{cyt}(immune\ activated)$	3.5×10^{-4} pM s^{-1}	Estimated as 1/10 of $\sigma_{cyt}(infected)$
Immune secretion midpoint $V_{cyt}(immune\ activated)$	1 pM	[66]
Cytokine immune uptake rate $\omega_{cyt}(immune\ activated)$	3.5×10^{-4} pM s^{-1}	[65]
Maximum cytokine infected cell secretion rate $\sigma_{cyt}(infected)$	3.5×10^{-3} pM s^{-1}	[65]
Infected cell cytokine secretion mid-point $V_{cyt}(infected)$, $V_{cyt}(virus\ releasing)$	0.1	Chosen from typical simulation values of assembled virus. Values stay around 0.1 and increase as infection progresses
Cytokine secretion Hill coefficient h_{cyt}	2	Selected for simplest form with inflection of model response
Immune cell cytokine activation $EC50_{cyt,act}$	10 pM	[65]
Immune cell equilibrium bound cytokine EQ_{ck}	210 pM	Chosen to be 2.1 x $EC50_{cyt,act}$
Immune cell bound cytokine memory ρ_{cyt}	0.99998 s^{-1}	Derived from $\omega_{cyt}(immune\ activated)$ and EQ_{ck}
Immune cell activated time	10 h	[34]
Oxidation Agent diffusion coefficient D_{oxi}	0.64 µm^{2} s^{-1}	Selected to be 4 x D_{cyt} to model high diffusivity relative to IL-2
Oxidation Agent diffusion length λ_{oxi}	36 µm	Selected to be 3 cell diameters to model high reactivity
Oxidation Agent decay rate γ_{oxi}	1.32×10^{-5} s^{-1}	Derived from λ_{oxi} and D_{oxi}
Immune cell oxidation agent secretion rate σ_{oxi}	3.5×10^{-3} pM s^{-1}	Selected to be the same as $\sigma_{cyt}(infected)$

Immune cell C_{cyt} threshold for Oxidation Agent release τ_{oxi}^{sec}	10 A.U. = 1.5625 pM	Selected according to sensitivity analysis
Tissue cell C_{oxi}threshold for death τ_{oxi}^{death}	1.5 A.U. = 0.234375 pM	Selected according to sensitivity analysis
Initial density of unbound cell surface receptors R_o	200 cell^{-1}	Selected for potential limiting factor (availability of receptors) from typical simulation extracellular virus field values
Virus-receptor association affinity k_{on}	1.4×10^{4} M^{-1}s^{-1}	[68]
Virus-receptor dissociation affinity k_{off}	1.4×10^{-4} s^{-1}	[68]
Infection threshold	1	Calibrated to timescale of SARS-CoV-2 [60]
Uptake Hill coefficient h_{upt}	2	Selected for simplest form with inflection of model response
Uptake characteristic time constant α_{upt}	20 min	Selected to be the same as Δt
Virally-induced apoptosis Hill coefficient h_{apo}	2	Selected for simplest form with inflection of model response
Virally-induced apoptosis dissociation coefficient V_{apo}	100	Selected according to sensitivity analysis
Virally-induced apoptosis characteristic time constant α_{apo}	20 min	Selected to be the same as Δt
Immune cell activation Hill coefficient h_{act}	2	Selected for simplest form with inflection of model response
Immune response add immune cell coefficient β_{add}	1/1200 s^{-1}	Selected for sensitivity analysis of β_{delay}
Immune response subtract immune cell coefficient β_{sub}	1/6000 cell^{-1} s^{-1}	Selected according to β_{add} for 5 resident immune cells (mean of all immune cell counts per epithelial cell from Control in [47] applied to 900 epithelial cells)
Immune response delay coefficient β_{delay}	1.2×10^{6} s	Selected according to sensitivity analysis
Immune response decay coefficient β_{decay}	1/12000 s^{-1}	Selected for sensitivity analysis of β_{delay}

Immune response cytokine transmission coefficient α_{sig}	0.5	Selected for sensitivity analysis of β_{delay}
Immune response probability scaling coefficient α_{immune}	0.01	Selected for sensitivity analysis of β_{delay}
Number of immune cell seeding samples $n_{seeding}$	10	Selected for sensitivity analysis of β_{delay}
Initial target volume	$64\ \mu\text{m}^3$	Derived from cell diameter and lattice width
Lambda volume λ_{volume}	9	Selected for acceptable deformation of immune cells
Initial number of immune cells	0	Selected to demonstrate model feature of resident immune cells
Lambda chemotaxis $\lambda_{chemotaxis}$	1	Selected for appreciable chemotaxis without excessive cell deformation
Intrinsic Random Motility $\mathcal{H}^*$	10	[64]
Contact coefficients J (all interfaces)	10	Selected comparably to [31] for low adhesion immune cell-immune cell and immune cell-medium interfaces

Table 2.1. Parameter values in baseline parameter set. [1] The diffusivity in water for a virus of radius 0.1 microns like SARS-CoV-2 according to Stokes-Einstein is about 3 microns^2/s. The average steady-shear viscosity for lung mucus varies significantly and is shear thinning, but in the more viscous regions is found to vary for frequencies between 10^{-4} and 102 Hz, spanning viscosity values as high as 103 Pa-s and as low as 10^{-2} Pa-s. In general, at low shear rates, the viscosity of human mucus is as high as 104−106 times that of water [69]. Thus the minimal diffusion constant possible would be 3×10^{-6} microns^2/s and the maximal rate in water would be 3 microns^2/s. 0.01 microns^2/s is a reasonable geometric interpolation.

Multicellular Spatial Model of RNA Virus Replication and Interferon Responses Reveals Factors Controlling Plaque Growth Dynamics

Introduction

Respiratory viruses present major public health challenges, as evidenced by the 1918 Spanish Flu, the 1957 H2N2, 1968 H3N2, and 2009 H1N1 influenza pandemics, and the severe acute respiratory syndrome coronavirus 2 (SARS-CoV-2) pandemic. Typical seasonal influenza virus strains are responsible for 290,000 – 650,000 annual deaths globally [71], and occasional, highly pathogenic pandemic strains, such as the 1918 Spanish Flu [72], and the 1957 H2N2 [73], 1968 H3N2 [74], and 2009 H1N1 [76] influenzas result in significantly higher mortality rates.

Severe RNA virus respiratory infections often correlate with high viral load and excessive inflammation. Both influenza and SARS-CoV-2 are RNA viruses, and studies of severe SARS-CoV-2 and influenza infections find that impaired interferon responses correlate with more severe outcomes [76]. In some severe cases, respiratory diseases trigger a severe inflammatory condition known as a cytokine storm. In highly pathogenic infections, an aberrant inflammatory response – specifically a prolonged, elevated inflammatory state and a high level of type-I interferons in the bloodstream, clinically called hypercytokinemia (colloquially known as a cytokine storm) [77] – is believed to be a significant driver of mortality [78]. Excessive inflammation exacerbates tissue damage and hinders clinical recovery [79]. Understanding the dynamics of the innate immune response at the cell and tissue levels is vital to understanding the mechanisms of immunopathology and to developing strain-independent treatments.

Influenza studies show that immunomodulation can improve infection outcomes. Prestimulation of toll-like receptors to induce earlier interferon production protects against highly pathogenic influenza strains in mice [80], while cell culture prestimulation with type-I interferons prevents viral plaque growth by SARS-CoV (the original 2003 SARS virus) [81], SARS-CoV-2 [81], and influenza [82]. Nebulized interferon α2b and interferon β are being investigated as an early treatment for COVID-19 [83]. Collectively, these studies demonstrate that immune response regulation must balance tissue damage from inflammatory responses and efficient viral clearance. Computational modeling may reveal how complex responses emerge during infection and aid in identifying immune-targeted treatments. Recent computational models have considered many aspects of inflammatory responses to viral infection [84]. Recent models [86] of interferon response to viral infection commonly invoke a generic virally resistant cell type. A cell of this type is either immune to viral infection or stops ongoing viral replication completely. This all-or-nothing response does not capture the dynamics of interferon stimulated genes' (ISGs') effects on viral growth [94].

Plaque growth assays seed the virus at low multiplicity of infection (MOI) and allow it to replicate and form plaques across a monolayer of host cells in cell culture. Plaques are visible areas of infected and dead cells that occur in cell cultures infected with a virus. A previous spatial model of influenza viral spread and plaque growth [95] replicated the linear growth of viral plaques *in vitro* and explored the impact of diffusion coefficients on viral plaque formation but did not incorporate the cells' interferon signaling response to the infection. Recent studies of DNA virus infection (Herpes simplex virus 2; HSV-2) used agent-based models to examine the role of adaptive immune cells in restricting plaque growth [87] while another study found that the degree of stochastic signaling minimized the amount of interferon needed to restrict cell death

[88]. However, HSV-2 is a DNA virus that activates different signaling pathways from RNA viruses, such as influenza.

We created a computational model of the early stages of infection that simulates lung cells infected with RNA viruses, the type of virus responsible for both COVID-19 and flu to help explore how the disease forms viral plaques. We developed a multicellular spatial interferon signaling model (which we will call the MSIS model) of the early inflammatory response to RNA viral respiratory infections *in vitro* using CompuCell3D [37] (CC3D). The model is parameterized using data from influenza virus-infected cell cultures. Consistent with experimental observations, simulations exhibit either linear radial growth of viral plaques or arrested plaque growth depending on the local concentration of type I interferons. The MSIS model allows us to determine conditions that lead to either arrested or persistent plaque growth during a simulated infection of a monolayer of lung epithelial cells with an RNA virus. Plaque growth assays are commonly used to compare virus growth rates across cell lines [89], to quantify the concentration of infective agent [90], and to observe the effects of drugs and compounds on virus spread [91]. Simulation of *in vitro* experiments *in silico* allows for cheaper, faster, higher-throughput hypothesis generation than experiments. The MSIS model replicates familiar biological plaque growth assays and cell staining experiments, making its simulation methodology and results readily accessible to wet-lab biologists. Our model suggests that the treatment of cells with type-I interferons, which are currently being evaluated for the treatment of COVID-19, may have a protective effect. We also found that enhancing certain aspects of the inflammatory response, such as the JAK/STAT pathway, may be able to arrest viral plaque growth, suggesting molecules involved in this pathway as possible drug target candidates

Our model focuses on two interacting processes: viral replication and the host cells' early interferon response. The modeled virus is produced in infected cells, released into the extracellular environment, and diffuses in this environment. The modeled inflammatory response includes interferon production, export, diffusion and decay, and the induction of virally resistant cell states via ISGs. The model represents a monolayer of immobile human bronchial epithelial cells (HBECs). Each cell contains a separate model of epithelial cell interferon signaling, viral replication and release, and cell death, which is an ODE model [92] calibrated to data from influenza-infected HBECs, that has been modified to include species release or export to the extracellular environment. We adapted a standard model of cell type transition during viral infection [93], with cells transitioning from uninfected, to eclipse phase, virus releasing, and dead cell types. The extracellular environment allows for diffusion of both virus, which leads to the formation of viral plaques, and type-I interferons, which are responsible for paracrine interferon signaling. The MSIS model gives insight into the mechanisms of IFN regulation and the arrest of viral plaques.

Materials and Methods

The MSIS model simulates the replication and spread of an RNA virus infection in a monolayer of epithelial cells and the interferon response induced by the infection.

Spatial Considerations of the MSIS model

During virus infection, lung epithelial cells produce and export virus and anti-viral type-1 interferon (IFN) proteins. In cell culture, these extracellular species diffuse freely in the medium above the apical surface of cells. The apical surface of the epithelium interacts with the bottom surface of the medium in which extracellular IFN (IFN_e) and virus (V_e) diffuse and decay. Cells export IFN and release virus from their apical surface into the adjacent domain in the chemical field. We simulate the model on a lattice that represents the interface between the extracellular space and the cell's apical surface, each voxel length representing 3.0 microns. Unless otherwise specified, the simulation domain is a 300 by 300 lattice, representing a tissue patch of 900 by 900 µm. The layer of epithelial cells is a 100 by 100 array of square cells, each occupying 3 by 3 voxel sites. Cells are infected by V_e and respond to IFN_e in the same adjacent domain.

Due to the spatial aspect of the model, the concentrations of extracellular species (IFN_e and V_e) can be reported at specific lattice sites, averaged over the area of a cell, or averaged over the entire lattice. V_e and IFN_e indicate the concentration at a specific lattice site while $[V_e]_{per\ cell}$ and $[IFN_e]_{per\ cell}$ indicate the average concentration over a specific cell for extracellular virus and extracellular IFN, respectively. The model assumes no spatial variability over the domain of the cell.

Cell Types and Rationale

Lung epithelial cells are interferon-competent and produce interferon in response to infection by a virus. During an infection, both infected and healthy cells are capable of responding to changes in extracellular IFN [94] via the JAK/STAT pathway. After infection, cells enter an eclipse phase for about 6 hours, during which they produce, but do not release, virus [95]. After the eclipse phase, cells begin to release virus and continue to do so until the cell's resources are depleted, resulting in cell death.

The MSIS model cells (agents) with 4 distinct types: uninfected (U), eclipse phase (I1), virus releasing (I2), and dead cells (D). Figure 3.1 provides a conceptual overview of the MSIS model. Uninfected cells, U, contain no virus but can produce and export IFN in response to extracellular

IFN via the STAT pathway. Paracrine signaling occurs when interferon external to the cell induces the phosphorylation of STAT (STATP in Fig 1). U cells transition to the eclipse phase (I1) immediately after a successful infection event. Eclipse-phase (I1) cells can produce and export IFN, and replicate, but not release virus [96]. Extracellular IFN (via paracrine signaling activation of the JAK/STAT pathway) and viral sensor protein (RIGI and TLR7) activation both stimulate cells to produce and export IFN. When an I1 cell transitions to the virus-releasing type (I2), all properties of the cell remain the same except that cells can now release the intracellular virus into the extracellular virus field. When an I2 cell transitions to dead (D), it ceases to produce and export IFN or release virus but continues to occupy space in the simulation.

Cell Type Transition Probabilities

Transitions between cell types are stochastic, and the probability of a transition occurring during depends on the cell's local extracellular and intracellular concentration of virus (V_e and V respectively), the cell's health (H; described under *Intracellular Model Equations and Rationale*), and the transition rate coefficient (β, k or $\gamma_{H,V}$). $[V_e]_{per\ cell}$ is measured as the local extracellular virus concentration each cell is exposed to over its entire cell area. We derived the rates in Eq. 3.1 – 3.3 from the rate laws in [93], following the transformation rules given in [85]. When a cell is infected (transitions from U to I1), the internal viral concentration changes from 0 to 6.9E-8 (unitless), equivalent to a single virus particle entering the cell [92]. This amount of virus was considered negligible compared to V_e and is thus not removed from the extracellular virus. Within CC3D, cell-type transitions are implemented by sampling a random number for each cell between 0 and 1, inclusive, at each time step. The cell's transition occurs when the probability, *P*, is greater than the random number. Each transition must occur in order.

Cell-Type Transition Probabilities

$$P(U \to I1) = 1 - \exp\left(-\beta\ [V_e]_{per\ cell}\ \Delta t\right), \tag{3.1}$$

$$P(I1 \to I2) = 1 - \exp\left(-\tau_{I1} \Delta t\right) \tag{3.2}$$

$$P(I2 \to D) = 1 - \exp\left(-\gamma_{H,V}\ [V]\ \{1 - H\}\ \Delta t\right) \tag{3.3}$$

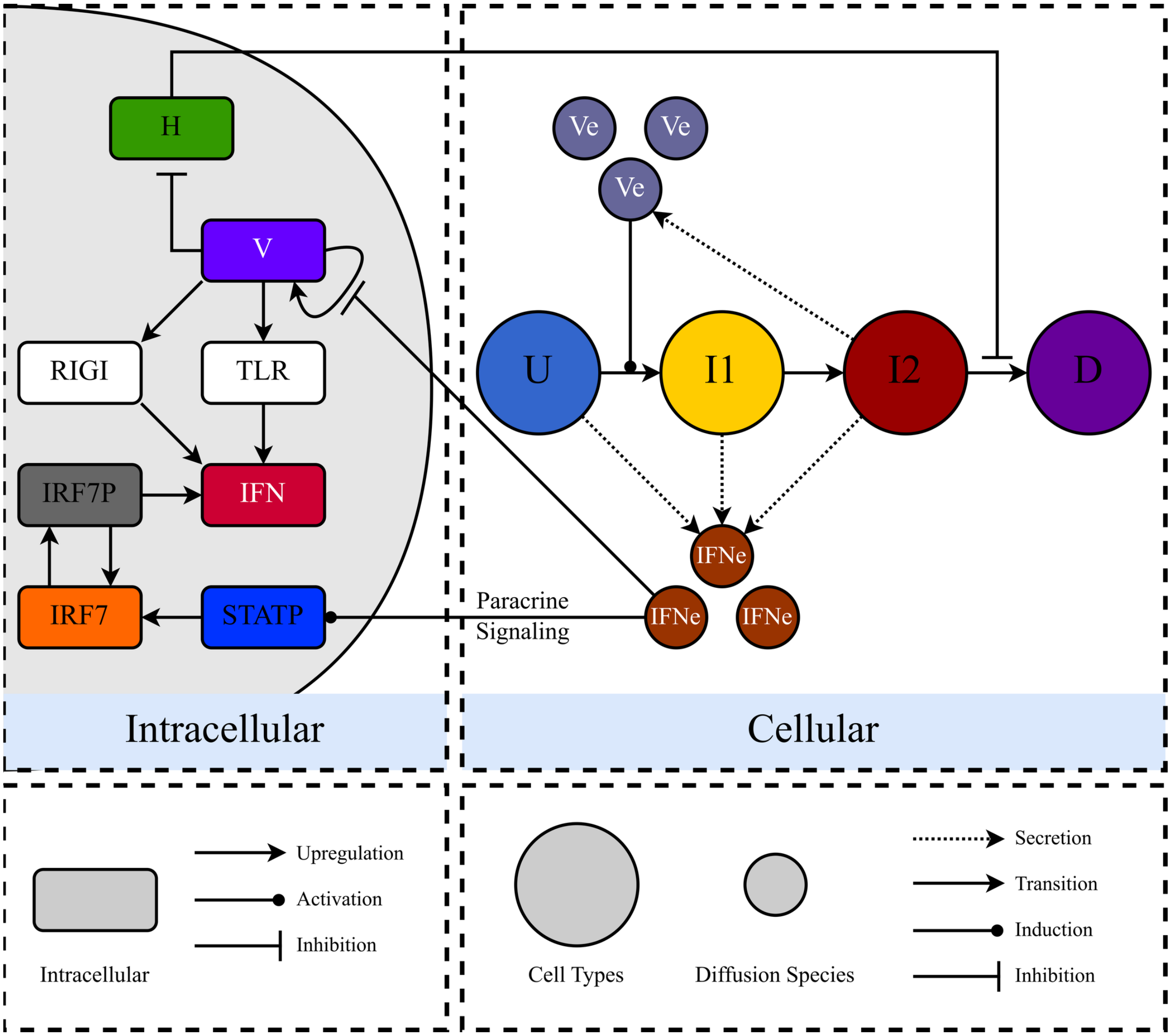
H
V
RIGI
TLR
IRF7P
IFN
IRF7
STATP
Ve
Ve
Ve
U
I1
I2
D
IFNe
IFNe
IFNe
Paracrine Signaling
Intracellular
Cellular
Upregulation
Activation
Inhibition
Intracellular
Cell Types
Diffusion Species
Secretion
Transition
Induction
Inhibition

Figure 3.1. Conceptual diagram of the MSIS model. The MSIS model consists of an intracellular sub-model, which describes interferon signaling during infection, and a cellular sub-model, which defines changes in cell types and extracellular molecular diffusion. Uninfected cells (U, blue) produce IFN via paracrine signaling alone since no virus is present in these cells. Eclipse-phase cells (I1, yellow) produce

IFN via viral sensor proteins (RIG-I and TLR7) and paracrine signaling (through the JAK/STAT pathway). I1 cells also export IFN into the extracellular environment. I1 cells allow virus replication but do not release virus into the extracellular environment. Virus-releasing cells (I2, red) produce IFN identical to I1 cells and export IFN and release virus into the extracellular environment. Dead (D, purple) cells do not interact with their surroundings and have no intracellular sub-model. Each cell contains an instance of the intracellular sub-model representing interferon signaling (variables RIG-I, TLR, IFN, IRF7, IRF7P, and STATP), viral infection, replication, and release (V), and cell health (H). Type-I interferons (IFN_e) exported by U, I1, and I2 cells, and virus (V_e) released by I2 cells diffuse and decay in the extracellular environment. Paracrine interferon signaling occurs through the JAK/STAT pathway, indicated by the arrow from IFN_e to STATP across the intracellular/cellular border.

Intracellular Model Equations and Rationale

During RNA virus infection of lung epithelial cells, the first immune system action is type I interferon production (IFNα and IFNβ), which suppresses virus replication and activates many downstream components of the innate and adaptive immune systems [97]. Interferons establish an antiviral state through the activity of interferon stimulated genes (ISGs), which include antiviral Mx proteins, RNA-activated protein kinases, and the 2 – 5A system [98]. The presence of an RNA virus is primarily sensed in the cytoplasm by retinoic acid-inducible gene 1 (RIG-I) and in endosomes by Toll-like receptors 7 and 9 (TLR7/9) [99]. Both RIG-I and TLR7/9 bind viral RNA that has been exposed by the uncoating of the virus. The activation of either sensor leads to the phosphorylation of interferon regulatory factor 7 (IRF7) and the production of interferons (see [94] for a detailed map of the relevant molecular interactions).. IFN excreted from the cell can bind interferon receptors (IFNR), which in turn activate the JAK/STAT pathway, leading to the production of more interferon. This positive feedback allows infected cells to produce a more robust interferon response (autocrine effect) while also priming an antiviral state in neighboring uninfected cells (paracrine effect). In summary, epithelial cells rely on interferon signaling to rapidly establish an antiviral state, and interferons are regulated through several pathways to ensure robust virus detection and response.

Another process that impacts virus reproduction is cell health. Studies have shown that the amount of virus produced by an infected cell decreases dramatically as the cell's health decreases (quantified by its concentration of ATP [100]). Thus, even minimal models that seek to predict virus and interferon production dynamics should represent virus replication, interferon signaling dynamics, and the cell's health.

The MSIS model adapts and extends to single cells the Weaver model of the dynamics of virus replication, interferon signaling, and cell health. The adapted Weaver model includes six ODEs (Eq. 3.4 – 3.9) that define the rate equations for intracellular virus replication, interferon signaling, and cell health. Specifically, the equations define changes in the intracellular concentrations of virus (V [unitless]), interferon (IFN [µM]), phosphorylated STAT (STATP [µM]), IRF7 protein (IRF7 [µM]), and phosphorylated IRF7 (IRF7P [µM]). Eq. 3.9 defines the dynamics of the health of the cell (H [unitless]). $[\mathrm{IFN_e}]_{per\ cell}$ is the average extracellular interferon concentration each cell is exposed to over its entire cell area.

Rate equations for intracellular species and health adapted from Weaver

$$\frac{d[V]}{dt} = \frac{k_{V,V}[H][V]}{1+\frac{[IFNe]_{per\ cell}}{K_{V,IFNe}}} - Q_V[V] \tag{3.4}$$

$$\frac{d[IFN]}{dt} = [H]\left(k_{IFN,V(RIGI)}V + \frac{k_{IFN,V(TLR)}V^n}{K_{IFN,V(TLR)}+V^n} + k_{IFN,IRF7P}[IRF7P]\right) - Q_{IFN}[IFN] \tag{3.5}$$

$$\frac{d[STATP]}{dt} = \frac{k_{STATP,IFNe}[H][IFNe]_{per\ cell}}{K_{STATP,IFNe}+[IFNe]_{per\ cell}} - \tau_{STATP}[STATP] \tag{3.6}$$

$$\frac{d[IRF7]}{dt} = [H](k_{IRF7,STATP}[STATP] + k_{IRF7,IRF7P}[IRF7P]) - \tau_{IRF7}[IRF7] \tag{3.7}$$

$$\frac{d[IRF7P]}{dt} = k_{IRF7P,IRF7}[H][IRF7] - \tau_{IRF7P}[IRF7P] \tag{3.8}$$

$$\frac{d[H]}{dt} = -\gamma_{H,V}[H][V] \tag{3.9}$$

Below, we provide a brief description of the Weaver model and then discuss how we modified the model to support its implementation in the MSIS model (Fig 3.1).

The Weaver model groups interferon α and β into a single representative species, interferon (IFN). We modeled the inhibition of virus production in response to the cell's spatially averaged level of extracellular interferon ($[IFN_e]_{per\ cell}$) using non-competitive inhibition-like kinetics (Eq. 3.4). We used mass-action kinetics to describe the induction of IFN (Eq. 3.5) by virus (via the RIG-I pathway) and IRF7P, and Hill kinetics to define the effect of the concentration of virus on IFN production via the TLR pathway. The rate of export of intracellular IFN into the extracellular environment obeys the concentration of IFN times a rate constant, Q_{IFN}. We model extracellular IFN's ($[IFN_e]_{per\ cell}$) activation of STAP with Michaelis–Menten kinetics (Eq. 3.6), and mass-action kinetics are used to model the effect of STATP and IRF7P on the rate of production of IRF7 (Eq. 3.7). We also use mass-action kinetics to describe the rate of IRF7P production as a function of IRF7 (Eq. 3.8). In all equations, production terms are multiplied by the cell's health (H) to represent the loss of production capacity in an infected cell. Heath is a relative metric bounded between 0 and 1, and the rate of the decay of health (Eq. 3.9) is proportional to the concentration of virus in the cell and the health of the cell.

We made three changes to the Weaver model to employ it in the MSIS model. We reinterpreted the first-order virus degradation term in the original Weaver model to represent the release of virus into the extracellular environment in the MSIS model. This term appears in Eq. 3.4, where the rate of release of virus to the extracellular environment is proportional to the concentration of virus times a rate constant, Q_v. The Weaver model was a population level model, while Eq. 3.4 – 3.9 represent single cell intracellular regulation. The Weaver model has a state, P, which represents the fraction of live cells in the population. The mathematical equation for health is unchanged from the original Weaver model, but we reinterpreted P to represent the health (H) of each individual cell. All production terms in Eq. 3.4 – 3.8 are multiplied by the cell's health (bound between 0 and 1) to represent the diminished production capacity of unhealthy, virus-infected cells. And, lastly, due to the spatial aspect of the MSIS model, we redefined the concentration of extracellular IFN in Eq. 3.4 and 3.6 to be the average IFN_e over the area of a given cell; namely $[\text{IFN}_e]_{per\ cell}$.

In the multicellular spatial MSIS model, each live cell (U, I1, I2 types) has a replica of the rate equations describing intracellular singaling and r viral eplication (Eq. 3.4 – 3.9). Table 3.1 gives the initial conditions for each cell type. Table 3.2 lists the parameters for the rate equations. For U and I2 cell types, the equations and their parameter values are unaltered. In I1 cells, the equations are the same and all parameter values are unchanged except for the parameter value that defines the rate of virus release into the extracellular environment, Q_v, which is set to zero because eclipse phase cells (I1) do not release virus. All parameter values are listed in Table 3.2.

		Cell Type			Units
		U	I1	I2	
Intracellular Species Initial Value	IFN	0	0	0	µM
	STATP	0	0	0	
	IRF7	0	0	0	
	IRF7P	0	0	0	
	H	1	1	1	unitless

	V	0	6.90E-8	6.90E-8	

Table 3.1. Initial conditions for each cell type when present at the start of a simulated infection.

Diffusion of Extracellular Species and Implementation in CC3D

Virus releasing cells (I2) release intracellular virus into the extracellular environment. Uninfected, eclipse phase and virus releasing cells (U, I1, and I2) produce and export type-1 interferons in response to either virus sensing proteins or autocrine/paracrine signaling. In cell culture, these extracellular species diffuse freely in the medium above the apical surface of cells. The MSIS model contains a cell lattice next to two chemical field lattices (and the diffusion of extracellular species across either chemical field lattice is unaffected by the presence of cells in the adjacent cell lattice. Eq. 3.10 models diffusion of extracellular interferons, where D_{IFNe} is the diffusion coefficient of interferon, Q_{IFN} is the rate constant for export of interferon by cells into the extracellular environment, and IFN is the internal amount of interferon inside each cell. Cell types U, I1, and I2 can produce and export interferon.

Eq. 3.11 models diffusion of the extracellular virus, where D_{Ve} is the diffusion coefficient of virus and Q_v is the secretion rate constant for release of virus by late infected (I2) cells. Intracellular virus (V) is a normalized, unitless quantity representing the per cell viral load, while extracellular virus (V_e) has units of PFU mL^{-1} and represents the concentration of infectious virus in the extracellular environment. The unit conversion is achieved via Q_v's units of PFU mL^{-1} hr^{-1}.

Extracellular Species

$$\frac{\partial[IFN_e]}{\partial t} = D_{IFNe}\nabla^2[IFN_e] + Q_{IFN}[IFN] - \tau_{IFNe}[IFN_e] \qquad (3.10)$$

$$\frac{\partial[V_e]}{\partial t} = D_V\nabla^2[V_e] + Q_V[V] - \tau_{Ve}[V_e] \qquad (3.11)$$

CompuCell3D calculates the integrated amount of V_e and IFN_e directly above each cell to calculate $[V_e]_{per\ cell}$ and $[IFN_e]_{per\ cell}$ and passes these values to Eq. 3.1, 3.4, and 3.6. It then integrates the diffusion and the intracellular species' rate equations and calculates the amount of virus released and the amount of IFN exported from each cell. It then evaluates the probabilities for cell type transitions for each cell following Eq. 1 – 3 to determine whether each cell experiences such a transition.

Initial and Boundary Conditions

All simulations use periodic boundary conditions along the *x* and *y* axes. When simulating low MOI conditions, at time zero all cells are U type, except for one I1 cell at the center of the simulation. To simulate high MOI conditions, all cells are initially I2 type. Table 3.1 gives the initial conditions for the intracellular variables of each cell type at time zero. In all simulations, the extracellular environment initially contains no V_e or IFN_e.

To simulate interferon pretreatment, the simulation starts at 12 hrs pre-infection, with all cells U type (initial conditions listed in Table 3.1) and exposed to IFN_e at 0.04 µM. At time = 0 hrs (12 hours after IFN_e exposure), we simulate washing of the cells by setting IFN_e = 0 µM and initiate the infection by setting a cell at the center of the simulation's lattice to the I1 type. Due to the IFN pretreatment, all cells have the same intracellular state at time zero except for the single I1 cell, for which V is set to 6.9E-8 (unitless) [92].

Parameter Determination

Many MSIS model parameters come directly from the Weaver model [92]. The Weaver model was parameterized using the lowest sum-of-squares error resulting from a parallel tempering Markov chain Monte Carlo fit to data collected from HBECs infected with wild-type A/Puerto

Rico/8/1934 Influenza A [101]. Each cell's ODE model in the MSIS model is the Weaver model, modified as described previously. Table 3.2 gives a comprehensive list of model parameters and their origin. Virus diffusion coefficients can vary by several orders of magnitude depending on media type, based primarily on the medium's viscosity [85]. We set the diffusion coefficient for both V_e and IFN_e to 54.0 $\mu m^2\ s^{-1}$, within the range of experimental measurements [102] for both species. For these diffusion coefficients, the baseline parameter set led to continuous plaque growth. We rescaled the cell type transition parameter *β* [93] from units of median tissue culture infectious dose ($TCID_{50}^{-1}\ hr^{-1}$) to plaque-forming units ($mL\ PFU^{-1}\ hr^{-1}$) for consistency with the Weaver model's units for viral loa**d.**

Parameter	Value	Units	Process
$k_{IFN,V(RIGI)}$	0.0	$\mu M\ hr^{-1}$	Rate of IFN production via RIG-I virus sensing
$k_{IFN,V(TLR)}$	9.746	h^{-1}	Maximal rate of IFN production via TLR virus sensing
$K_{IFN,V(TLR)}$	12.511	[unitless]	Apparent dissociation constant of TLR virus sensing
$k_{IFN,IRF7P}$	13.562	h^{-1}	Rate of IFN production via IRF7P
Q_{IFN}	10.385	h^{-1}	Coefficient of export of IFN to the extracellular environment
$k_{STATP,IFNe}$	675.323	$\mu M\ h^{-1}$	Maximal rate of STAT phosphorylation via IFN_e
$K_{STATP,IFNe}$	80.353	μM	Michaelis-Menten constant for STAT phosphorylation via IFN_e
τ_{STATP}	0.3	h^{-1}	Dephosphorylation rate of STATP
$k_{IRF7,STATP}$	0.115	h^{-1}	Rate of IRF7 induction via STATP
$k_{IRF7,IRF7P}$	1.053	h^{-1}	Rate of IRF7 induction via IRF7P
τ_{IRF7}	0.75	h^{-1}	Decay rate of IRF7
$k_{IRF7P,IRF7}$	0.202	h^{-1}	Rate of IRF7 phosphorylation via IRF7

τ_{IRF7P}	0.3	h^{-1}	Dephosphorylation rate of IRF7P
$\gamma_{H,V}$	0.635	h^{-1}	Rate of cell health loss due to viral load and rate of transition from virus releasing (I2) to dead (D) cells
$k_{V,V}$	1.537	h^{-1}	Rate of viral replication
$K_{V,IFNe}$	0.020884	µM	Michaelis-Menten constant for IFN$_e$ inhibition of viral replication
Q_V	0.197	PFU mL^{-1} h^{-1}	Coefficient of the rate of viral release into the extracellular environment
n	3	[unitless]	Hill coefficient of TLR virus sensing
β	1E3	mL PFU^{-1} hr^{-1}	Rate of transition from uninfected (U) to eclipse phase (I1) cells
τ_{I1}	0.167	h^{-1}	Rate of transition from eclipse phase (I1) to virus releasing (I2) cells.
τ_{Ve}	0.542	h^{-1}	Decay rate of virus in the extracellular environment
τ_{IFNe}	3.481	h^{-1}	Decay rate of IFN$_e$ in the extracellular environment
D_{Ve}	54.0	μm^2 s^{-1}	Diffusion coefficient of V_e
D_{IFNe}	54.0	μm^2 s^{-1}	Diffusion coefficient of IFN$_e$
L_{Ve}	0.09	µm	Calculated diffusion length of extracellular virus
L_{IFNe}	0.23	µm	Calculated diffusion length of IFN$_e$
Voxel Width	3	µm	Width of lattice voxels
Cell Size	9	µm	Width of cells

Table 3.2. Baseline parameter values and sources

Plaque Growth Metrics

Viral plaques are visible areas of dead or damaged cells that occur where a virus has spread across a continuous patch of cells in cell culture. At early times, a growing plaque consists of a central domain of I2 cells surrounded by a ring of I1 cells. At later times, the plaque consists of a domain of dead cells surrounded by a ring of I2 cells, in turn, surrounded by a ring of I1 cells. We measure the radial growth speed of the outer border of the domain of eclipse (I1), virus releasing (I2), and dead (D) cell types. In the simulations, we determine these speeds by seeding a single I1 cell in the center of a simulated sheet of cells and measuring the total area of each cell type over time. We assume the plaques are circular to estimate their radius. We averaged plaque growth metrics over 20 simulations for each parameter set. In experiments, plaque-plaque interference occurs when two or more plaques grow into the same spatial region, slowing the radial growth of the colliding plaques. This paper simulates only the growth of isolated plaques.

Results

Multicellular Spatial Model of RNA Virus Infection and IFN Signaling (MSIS model) Reproduces ODE Model Dynamics for High MOI infection

We first checked whether the MSIS model reproduced the dynamics of the Weaver model for the same simulated experimental conditions [92]. The Weaver model was fitted to data from HBECs [101] that were uniformly infected with an influenza virus at MOI = 5. For such high MOI initial conditions, the spatial inhomogeneity of the multiscale model should have a negligible effect on the population-level dynamics, because all cells are infected simultaneously. To replicate the Weaver model simulations for an MOI = 5 infection, we initialized the MSIS model with only virus releasing (I2) cells and no eclipse phase (I1) cells. A non-uniform cell type distribution (Fig 3.2A) and local IFN_e concentration field (Fig 3.2B) emerge in the MSIS model simulations due to the stochastic cell transitions, which lead to spatially varying IFN_e and V_e, and to non-uniform rates of death of I2 cells.

Figure 3.2C compares the average fraction of live cells and average levels of chemical species in the MSIS and Weaver models. The fraction of live cells has the same shape in the two models, but dead cells start accumulating slightly later in the MSIS model than in the Weaver model. A major distinction between the MSIS model and the Weaver model is that the number of MSIS cells is discrete. For homogeneous, high MOI starting conditions, all concentrations grow rapidly after the onset of viral release, reach a maximum, and then decay nearly exponentially on a slower time scale. For each variable, the MSIS model value is always greater than or equal to the Weaver model value. Relative errors are largest at times when the values are near their maxima and are always less than 15%. Cell death begins slightly later in the MSIS model than in the Weaver model and the cell death rate increases slightly faster, so that all cells die at nearly the same time. Since the MSIS model produces dynamic responses like those of the Weaver model under high MOI, we will assume that differences between the dynamics of the two models at low MOI result from stochastic spatial effects, not from differences in parameters or errors in spatializing the Weaver model.

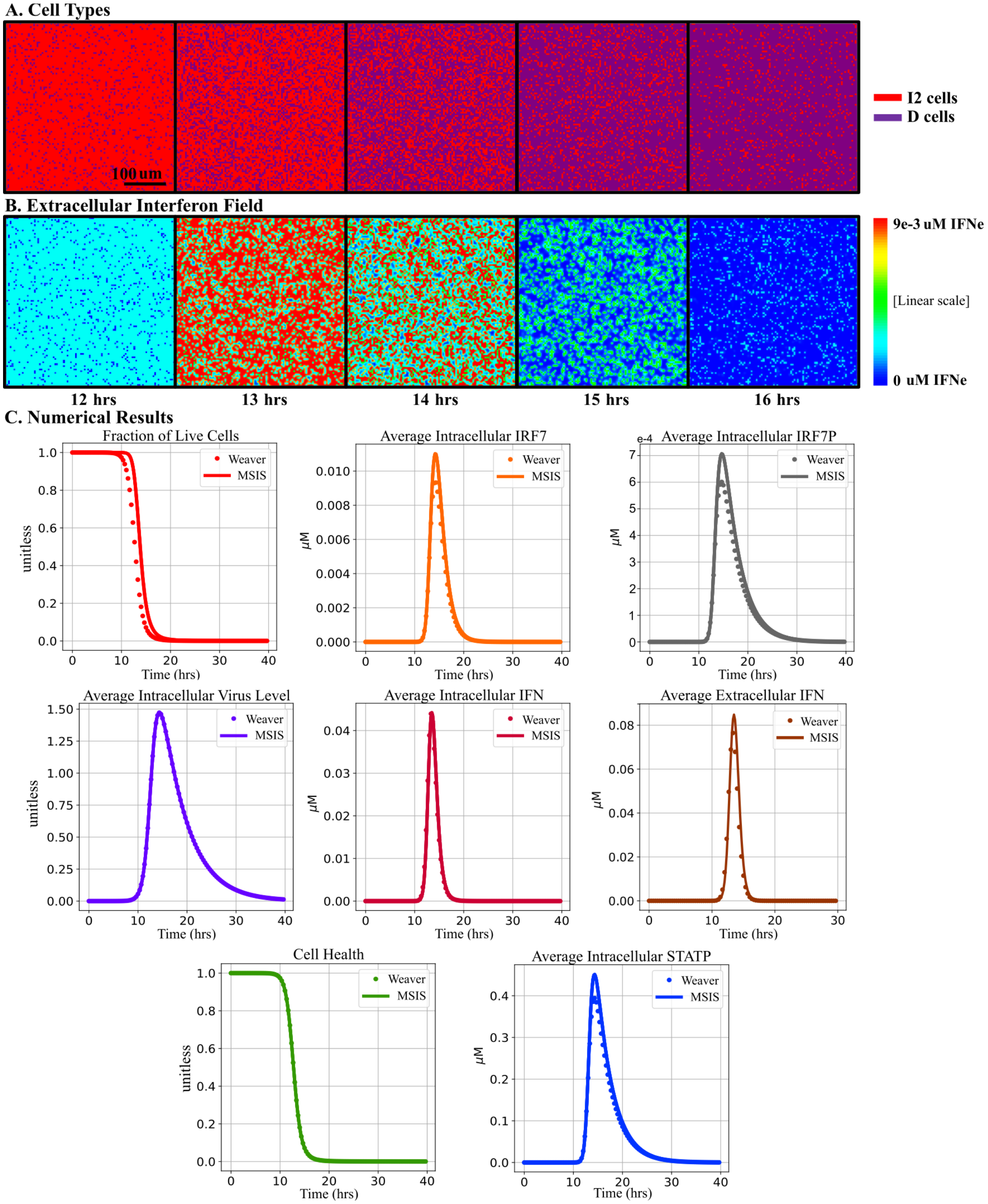

Figure 3.2. Comparison of time series for key variables between the multicellular spatial interferon signaling (MSIS) model and Weaver model for high MOI. All cells are initially infected with 6.9E-8 (unitless) virus, matching the original data to which the Weaver model was fit [101]. (A) Snapshots of the cell field showing cell type (virus releasing [I2] in red and dead [D] in purple) at different times in a

representative MSIS simulation. (B) Snapshots of the concentrations of extracellular interferon (high concentrations in red, low concentrations in blue) at different times in a representative MSIS simulation. (C) Time series for key variables for the Weaver and MSIS models. MSIS simulations are averaged over 20 replicas at matching times. Error bars are included but are too small to be visible. For the MSIS model, average concentrations for intracellular species and Health are calculated over all live (I2) cells at each time point while the Average Extracellular IFN for the MSIS model is the average of IFN_e across the entire simulation domain.

MSIS Model Recapitulates Experimentally Observed Plaque Formation and Growth Dynamics

High MOI experiments are useful for determining the time course of viral titer and how long cells survive a viral infection, but, unlike plaque assays, they do not provide information about viral spread and the spatial aspects of cytokine responses. We explored low MOI plaque assay experiments *in silico*. Fig 3 (left) shows multiple plaques that formed in a culture of cells infected with an H5N1 influenza virus. We first evaluated if the MSIS model produced plaque-like structures beginning with a single point of infection, similar to those in experiments for low MOI. We created a simulation with two I1 cells seeded in similar locations to a subset of the plaques shown in Fig 3's left image. Figure 3,3 shows simulation results at 80 hours. The MSIS model reproduces the circular geometry of experimental plaques. The length scales differ between the experimental and simulated plaques because the MSIS model is parameterized for an H1N1 virus, while the experiment shown used a faster replicating H5N1 virus.

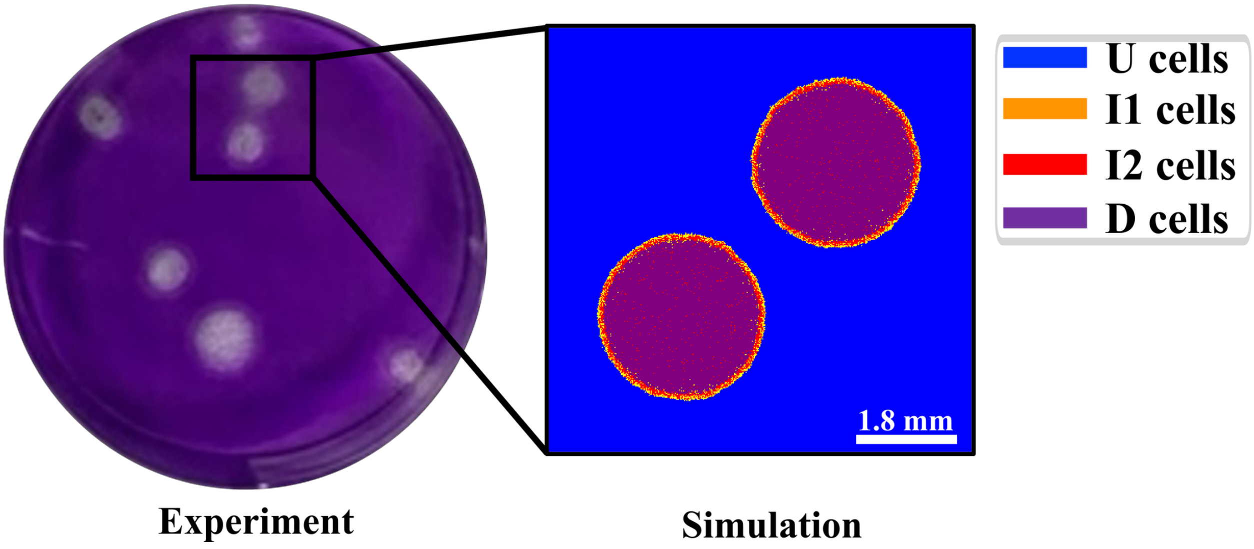

Figure 3.3. Comparison of an experimental plaque assay for influenza (H5N1; left) with an MSIS model plaque simulation (for H1N1; right). The simulation seeded two plaques in a simulation domain to replicate a subset of the experimental area. The simulated plaques have a similar structure to the experiment. Outlined area in the experimental image corresponds roughly to the area of the simulation domain.

Next, we explored plaque growth dynamics in the MSIS model. Figure 3.4A and 3.4B show experimental plaque radii vs time (data reproduced from [85]). While the increase in viral load during infection is typically exponential, plaque radius grows linearly in time. The experiment measured the radius of the outer edge of the domain of dead cells (equivalent to D in the model) and the outer edge of the domain of infected cells (equivalent to I1 in the model). The MSIS model distinguishes the eclipse phase (I1) from virus releasing (I2) cells, which normally cannot be distinguished in experimental plaque growth assays. For simulations beginning with a single I1 cell, Fig 4C shows that the MSIS model replicates several experimental observations. Both experiments (Fig 4A and 4B) and the MSIS model (Fig 4C) show a lag phase with no plaque growth. During the lag phase, cells are not releasing virus and no new cells are being infected. The simulation follows Tables 3.1 and 3.2 for initial conditions and model parameters, respectively. Figure 3.4E shows snapshots of the cell types at 17 hours, 33 hours, 50 hours, and 67 hours in a single replica simulation. Figure 3.4D shows snapshots of the V_e field at corresponding times in the same simulation replica. Figure 3.4F shows the IFN_e concentration field at corresponding times for the same simulation replica. Figure 3.4G shows the cell type composition of the culture over time. Dead cells first appear after 20 hours, after which the radius of plaque's central, circular domain of dead cells increases linearly in time. The radial growth rate of the plaque remains constant until the plaque reaches the edge of the simulation domain. Around 18 hours post-infection, V_e (Figure 3.4H) and IFN_e in the culture (Figure 3.4I) decrease briefly because the initially infected cell has died and stopped releasing virus and exporting IFN. During this time, the second generation of infected cells (those infected by the virus released by the initially infected cell) are primarily I1 phase and not yet releasing virus.

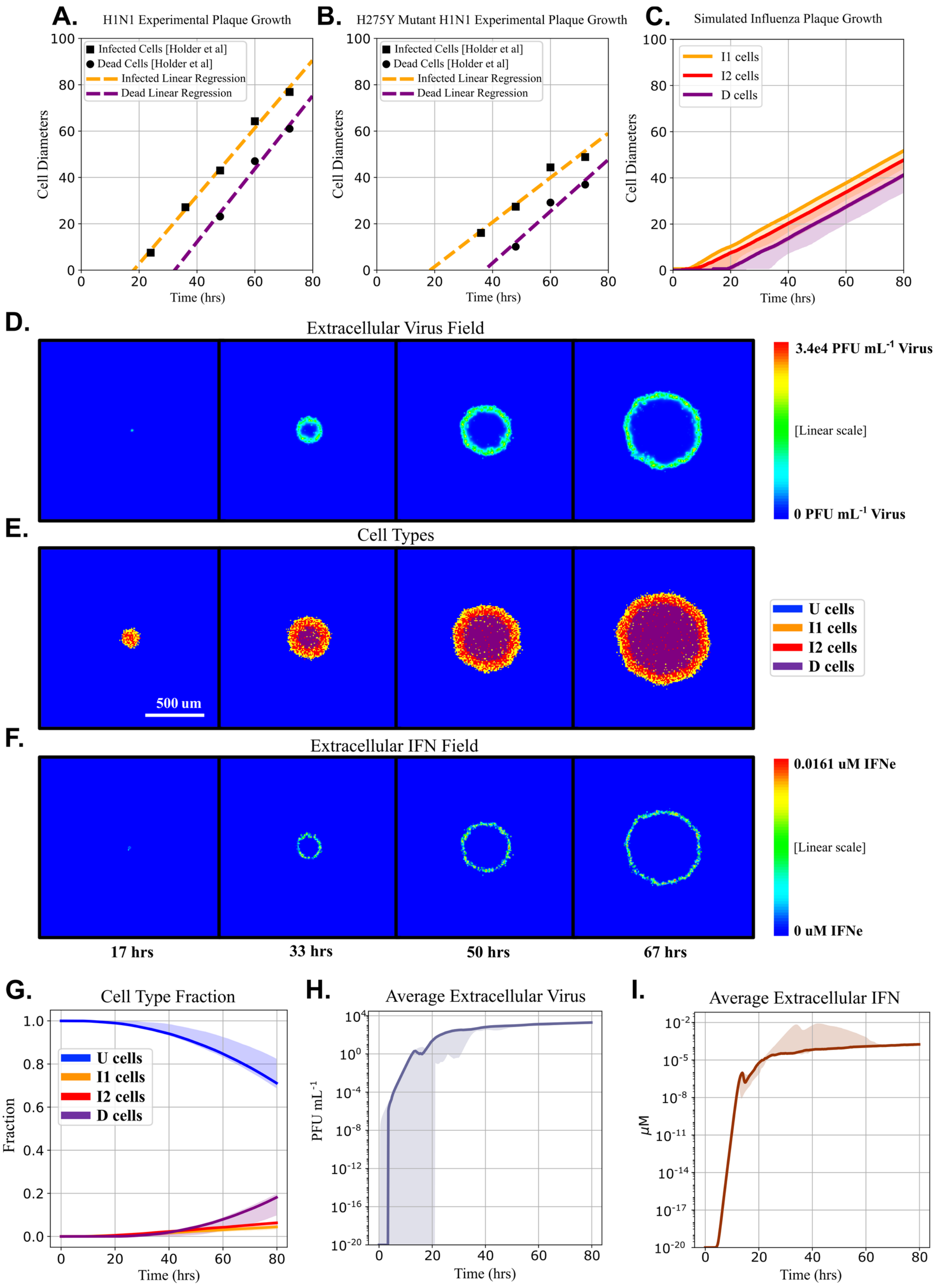
A.
H1N1 Experimental Plaque Growth
Infected Cells [Holder et al]
Dead Cells [Holder et al]
Infected Linear Regression
Dead Linear Regression
Cell Diameters
Time (hrs)
B.
H275Y Mutant H1N1 Experimental Plaque Growth
Infected Cells [Holder et al]
Dead Cells [Holder et al]
Infected Linear Regression
Dead Linear Regression
Cell Diameters
Time (hrs)
C.
Simulated Influenza Plaque Growth
I1 cells
I2 cells
D cells
Cell Diameters
Time (hrs)
D.
Extracellular Virus Field
3.4e4 PFU mL^{-1} Virus
[Linear scale]
0 PFU mL^{-1} Virus
E.
Cell Types
500 um
U cells
I1 cells
I2 cells
D cells
F.
Extracellular IFN Field
0.0161 uM IFNe
[Linear scale]
0 uM IFNe
17 hrs
33 hrs
50 hrs
67 hrs
G.
Cell Type Fraction
U cells
I1 cells
I2 cells
D cells
Fraction
Time (hrs)
H.
Average Extracellular Virus
PFU mL^{-1}
Time (hrs)
I.
Average Extracellular IFN
μM
Time (hrs)

Figure 3.3. Plaque growth simulations replicate experimentally observed linear radial plaque growth. (A, B) Radius vs time of outer boundaries of the domains of infected and dead cells for wild-type and H275Y mutant A/Miss/3/2001 (HIN1) infection-induced plaques, respectively. Data reconstructed from [85]**.** Squares indicate the radius of the outer edge of the plaque (the boundary between infected cells and uninfected cells) and circles indicate the radius of the boundary between dead cells and infected cells in the plaque. Dotted lines show a linear regression for visualization of plaque radius vs time. (C) Simulated plaque growth shows the lag phase and linear growth of the experimental plaques. The solid line indicates the median for 20 simulation replicas and the shaded areas indicate the 5th and 95th percentiles of observed values. Figs 3.4D, 3.4E, and 3.4F show sequential snapshots (at 17, 33, 50 and 67 hours) of the V_e field (D), cell type (E), and IFN_e field for a single simulation replica of a growing plaque. Time progresses from left to right. Figs 3.4G, 3.4H, and 3.4I show the median (solid line) and 5th to 95th percentile (shaded areas) of the simulated cell types, average V_e, and IFN_e, respectively, calculated for an ensemble of 20 simulation replicas.

The MSIS model recapitulates the experiments' linear radial growth of viral plaques. The MSIS model's ability to simulate both high and low MOI experiments and reproduce experimental observations, without additional parameter fitting to these conditions, gives confidence in its predictive capabilities in the novel circumstance of low MOI simulations.

Increased STAT Activity Leads to Arrested Plaque Growth and Reduces Final Plaque Diameter

The JAK/STAT pathway triggers an inflammatory reaction via auto/paracrine signaling and inhibition of this pathway has been implicated in improved H1N1 influenza survival in mice [103]. We wished to assess the impact of STATP activity on plaque growth dynamics in the MSIS model. We simulated plaque growth while altering the ability of extracellular interferons to activate the JAK/STAT pathway in the MSIS model by increasing the value of $k_{STATP,IFNe}$ (Eq. 3.6 and Table 3.2) from its baseline value (45.9 µM hr^{-1}, Table 3.2) up to 125.89x this value. For three values of $k_{STATP,IFNe}$, we show the plaque size and shape at 80 hours post-infection (Fig 3.5A) and the cell type dynamics over time (Fig 3.5B). The baseline value leads to unconstrained plaque growth. Values of $k_{STATP,IFNe} \geq 459.22$ µM hr^{-1} (10x baseline value) led to the arrest of plaque growth. Increasing $k_{STATP,IFNe} \geq 4592.2$ µM hr^{-1} (100x baseline value) reduces the time to plaque growth arrest, resulting in smaller plaques. These simulations use Table 3.1 initial conditions and Table 3.2 parameters except for the modified values of $k_{STATP,IFNe}$. Increasing the degree to which IFN_e promotes STATP production arrests plaque growth and reduces the final plaque size.

Figure 3.5C shows the rate of change of plaque radius at the end of the simulation as a function of $k_{STATP,IFNe}$, which controls the degree to which a given level of IFN_e leads to active STATP, Eq. 3.6. For $k_{STATP,IFNe}$ multipliers of 15.85 and above, the plaque growth rate is always zero at the end of the simulation, indicating plaque arrest. Arrest occurs earlier for higher $k_{STATP,IFNe}$ (Fig 3.5B, 2nd and 3rd panels). $k_{STATP,IFNe}$ multipliers above 6.31 reduce the area under the curve (AUC) for average V_e (Fig 5D), while multipliers between 1.0 and 6.31 have little to no effect on viral AUC. The AUC of average IFN_e (Fig 3.5E) increases with increasing $k_{STATP,IFNe}$, with a dramatic increase in the range of multipliers of 6.31 to 10.0. Note logarithmic ordinate scale for both average V_e and IFN_e AUC. Larger $k_{STATP,IFNe}$ would correspond to a stronger interferon response and reduced viral titer. $k_{STATP,IFNe} \geq 4592.2$ µM hr^{-1} leads to non-physiological unbounded production of IFN, due to the lack of an IFN-mediated cell death mechanism in both the Weaver and MSIS models.

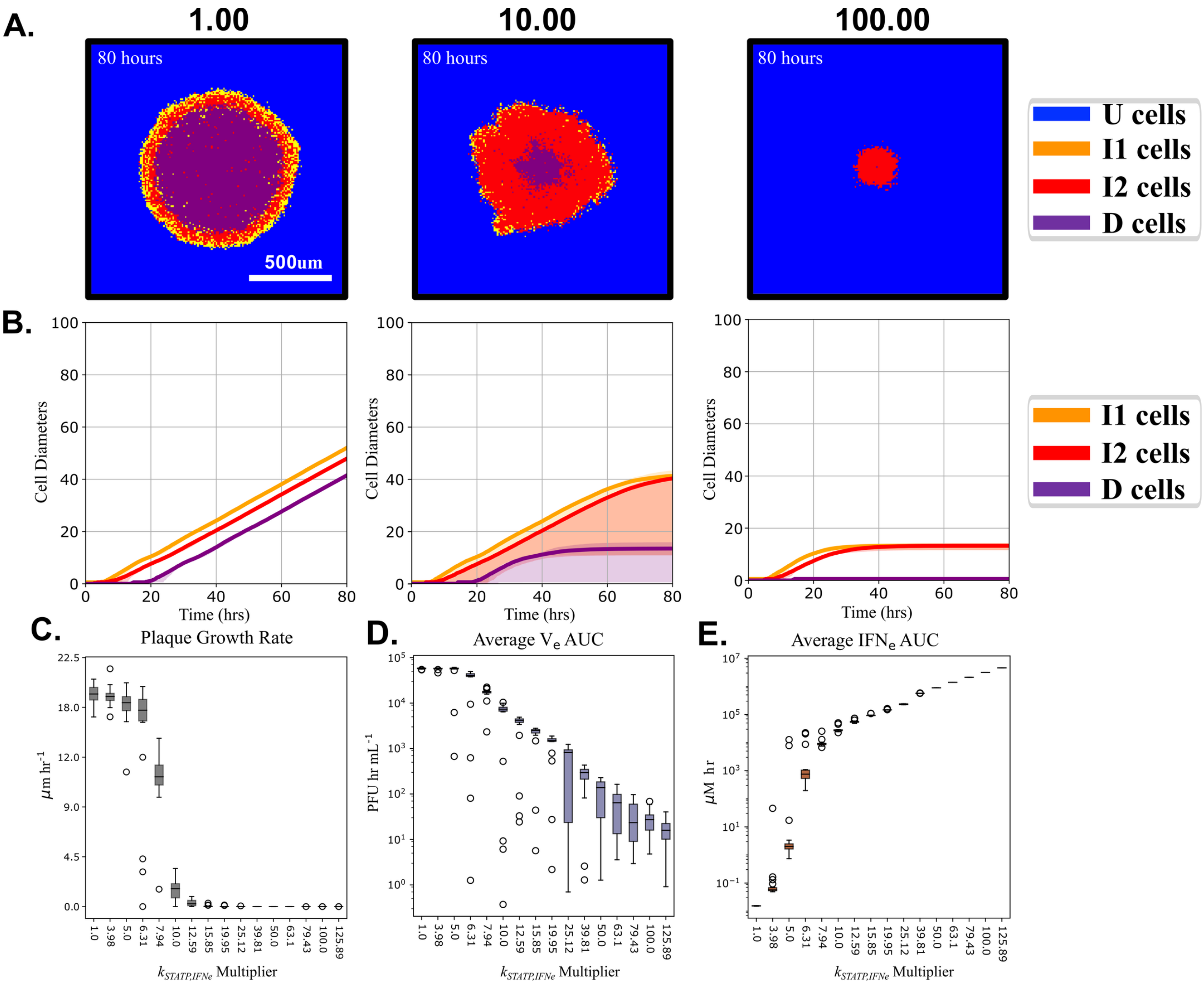

Figure 3.4. Elevated STATP activity (larger $k_{STATP,IFNe}$) leads to arrested plaque growth. (A) Images of the simulated plaques at 80 hours post-infection for a single simulation replica when $k_{STATP,IFNe}$ was 1x, 10x, or 100x larger than its baseline value. Arrested plaque growth occurs when $k_{STATP,IFNe}$ is 10x or 100x larger than baseline. (B) The median (solid line) and 5th and 95th percentiles (shaded regions) for 20 simulation replicas of the cell types over time for $k_{STATP,IFNe}$ at 1x, 10x, or 100x larger than its baseline value of 45.9 μM hr^{-1}. (C) The plaque radius' linear growth rate at 80 hours, (D) the area under the curve (AUC) of the average V_e, and (C) the AUC of the average IFN_e when $k_{STATP,IFNe}$ is changed between its nominal value to 125.98x nominal, over 20 simulation replicas.

Elevated RIG-I Activity Delays Cell Death and Increases IFN Production

In influenza infection, greater viral inhibition of RIG-I signaling via NS1 protein often increases viral infection severity [104]. We wished to investigate the effects of decreasing this antagonistic strength on plaque growth dynamics *in silico.* In our simulations $k_{IFN,V(RIGI)}$ controls the strength of the RIG-I response, with larger values corresponding to a stronger response (more IFN produced per unit of virus, Eq. 3.5). Our simulations so far assumed that the invading virus completely inhibited the RIG-I pathway ($k_{IFN,V(RIGI)} = 0$, Eq. 5). Previous work used data from cells infected with an NS1-knockout influenza virus (A/Puerto Rico/8/1934 [dNS1PR8]) to estimate the rate of IFN production via RIG-I virus sensing ($k_{IFN,V(RIGI)}$ = 10E5 µM hr^{-1} [92]). We ran single-plaque growth simulations for 14 values of $k_{IFN,V(RIGI)}$ between 0% and 100% of this estimate. These simulations use Table 3.1 initial conditions and Table 3.2 parameters except for the value of $k_{IFN,V(RIGI)}$. At 80 hours post-infection (Fig 3.6A) the plaque radius is nearly the same for all cases, shown for 0%, 50%, and 100% activity. However, the cell type composition of the plaque (Fig 3.6B) differs significantly, with significantly less cell death and thus a higher fraction of I2 cells, for $k_{IFN,V(RIGI)}$ multipliers greater than 50%. Higher levels of RIG-I signaling (larger values of $k_{IFN,V(RIGI)}$) only slightly reduce the radial plaque growth at the end of the simulations (Fig 3.6C). The AUC of the average V_e decreases steadily with increasing RIG-I activity (Fig 3.6D), decreasing more rapidly for $k_{IFN,V(RIGI)}$ multipliers greater than 25%. The AUC of average IFN_e increases dramatically for parameter multipliers less than 0.03x nominal and more gradually thereafter (Fig 3.6E).

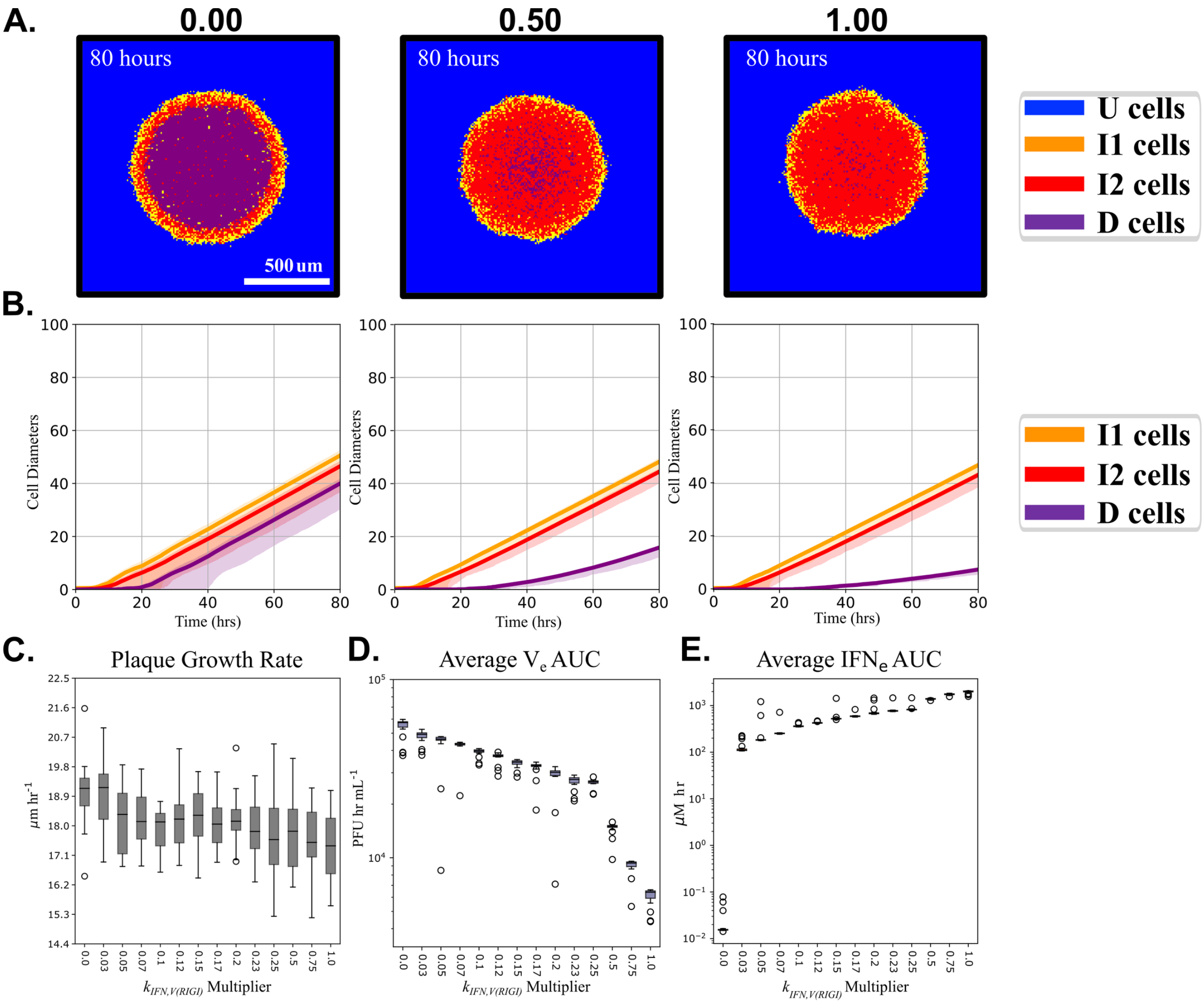

Figure 3.5. Increased RIG-I activity ($k_{IFN,V(RIGI)}$) lowers plaque growth rates and viral titers, slows cell death, and increases interferon production. (A) Images of plaques at 80 hours post-infection for a representative simulation replica for three values of $k_{IFN,V(RIGI)}$ (0, 5E5 µM hr^{-1}and 10E5 µM hr^{-1}) and (B) the median (solid line) and 5th and 95th percentiles (shaded regions) of the plaque radius over time for 20 simulation replicas for $k_{IFN,V(RIGI)}$ equal to 0x, 0.5x, or 1x its nominal value of 10E5 µM hr^{-1}. (C) The plaque growth rate at 80 hours, (D) the area under the curve (AUC) of the average V_e, and (E) the AUC of the average IFN_e for different values of $k_{IFN,V(RIGI)}$, over 20 simulation replicas.

Increasing levels of RIG-I activity for a given level of virus (larger $k_{IFN,V(RIGI)}$) increases the intracellular production of IFN (eq. 3.5). This higher intracellular IFN leads to higher IFN_e due to cell export (Eq. 11). Higher IFN_e leads to a reduction of intracellular viral levels (Eq. 3.4). Since the rate of decrease of cell health (H) is linear with respect to intracellular virus level (Eq. 3.9), and the death rate of cells is proportional to both the virus level and H (Eq. 3), higher values of $k_{IFN,V(RIGI)}$ increase the survival time of infected cells both by decreasing the intracellular virus level and by slowing the decrease of H. Overall, the model predictions are consistent with the expectations that greater RIG-I activity leads to reduced virus production (i.e. reduced virus titers).

Interferon Prestimulation Arrests Plaque Growth

Prestimulation of cell cultures with type-I interferons reduces the amount of virus produced in cells infected with SARS-CoV, SARS-CoV-2 [81], or influenza [82]. We simulated prestimulation experimental conditions in the MSIS model to explore these protective effects by exposing uninfected (U) cells to IFN_e at 0.04 µM at 12 hours pre-infection (-12 hours, since infection is referenced as time = 0), using the values of the parameters in Table 3.2. All cells were exposed to the same concentration of IFN_e. Since cell type transitions do not occur in the absence of virus, after 12 hours, all cells had identical intracellular chemical concentrations shown in Table 3.3. At 0 hours, IFN_e is set to zero to simulate washing IFN_e out of the cell culture, and a single cell is infected *in silico* by setting it to the I1 type. We then assessed the impact of IFN prestimulation on plaque growth.

Species	Initial Conditions
IFN	0.035 µM
IRF7	0.097 µM
IRF7P	0.028 µM
STATP	0.714 µM

Table 3.3. Intracellular chemical concentrations in cells 12 hours after *in silico* exposure to IFN_e. These values provide the initial conditions for IFN prestimulation simulations.

Simulated prestimulation entirely arrests plaque growth after 35 hours (Fig 3.7A), while the same initial infection in a field of naïve, unstimulated cells resulted in the infection and eventual death of all simulated cells (Fig 4C and 4G). Only the initially infected cell dies. The proportion of eclipse phase (I1) cells steadily decreases after 20 hours, indicating a cessation of new infections (Fig 3.7B). The average V_e concentration (Fig 3.7C) also decreases after 20 hours. The average IFN_e concentration (Fig 3.7D) is higher than in the baseline simulation.

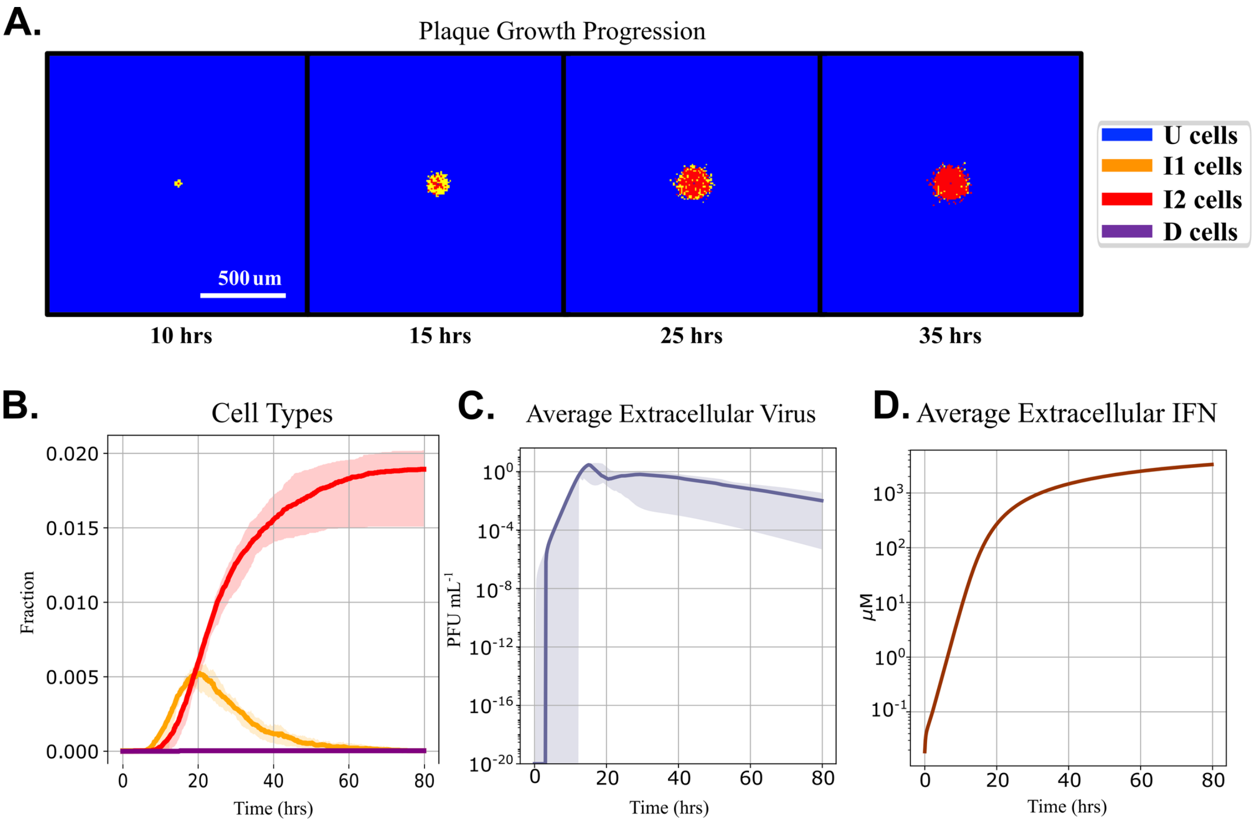

Figure 3.6. Prestimulating cells with type-I interferon led to plaque growth arrest in simulations. We simulate an experiment with 0.04 μM IFN_e prestimulation for 12 hours, which is removed immediately before infection. (A) Sequential snapshots (at 10, 15, 25 and 35 hours post-infection) of plaques for a representative simulation replica. (B) Cell type fractions vs time. (C) Average V_e vs time and (D) the average IFN_e vs time. The solid lines indicate medians and shaded areas represent the 5th and 95th percentiles over 20 replicas.

Faster Interferon Diffusion Promotes Plaque Growth Arrest

Diffusion coefficients for the virus and interferon will depend on virion diameter and the viscosity and chemistry of the medium *in vitro* [85]. We varied virus and interferon diffusion coefficients simultaneously. Because the actual diffusion coefficient of the extracellular IFN is likely to be 11x to 17x greater than that of the virus, we varied the interferon diffusion coefficient from 54 μm^2 s^{-1} to 2160 μm^2 s^{-1} (1x to 40x the baseline interferon diffusion coefficient) and the virus diffusion coefficient from 54 μm^2 s^{-1} to 216 μm^2 s^{-1} (1x to 4x the baseline virus diffusion coefficient). Simulations used initial conditions from Table 3.1 and parameters from Table 3.2 except for the revised diffusion coefficients. We calculated the median growth rate of the plaque radius at the end of the simulation over 20 replicas. If the median linear growth rate was 0 at the end of the simulation, we classified the parameters as leading to plaque arrest (orange); otherwise, we classified the parameters as leading to continued growth (blue). In our simulations, an interferon diffusion coefficient of 8x to 10x the viral diffusion coefficient led to plaque growth arrest (Fig 3.8). The boundary between the domains suggests that for high viral diffusion coefficients, virus diffusion ceases to be the rate-limiting factor in plaque growth. In summary, there is a broad range of values for both diffusion coefficients in which plaque arrest and continuous growth may occur. Better estimates of these diffusion coefficients can help clarify the relative importance of intracellular versus extracellular processes in viral infection.

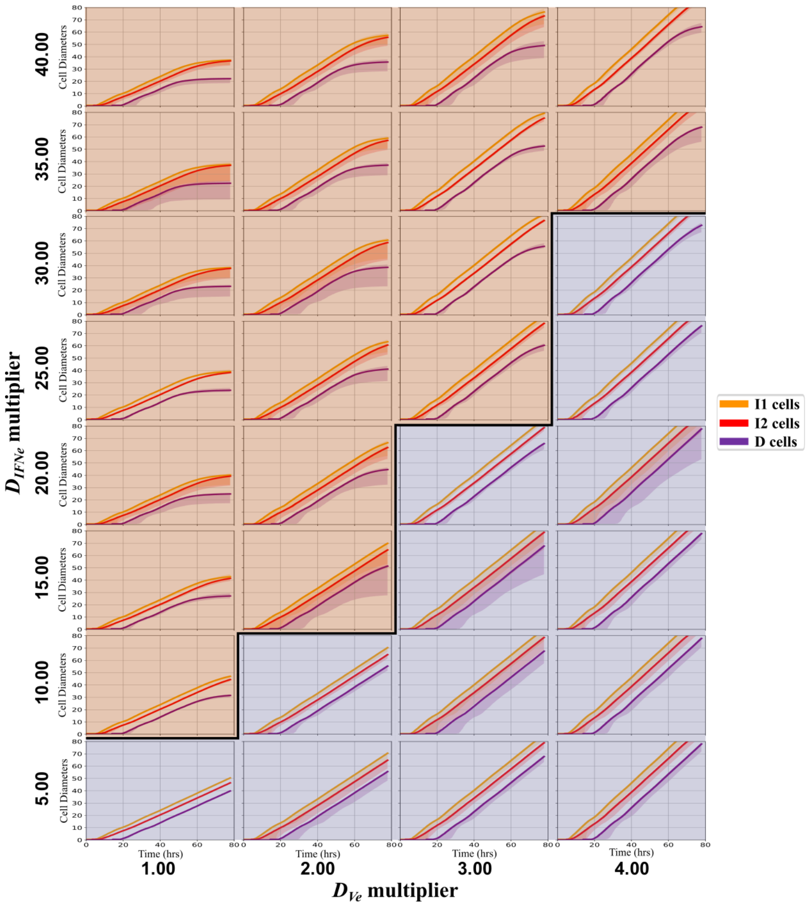

Figure 3.7. Dependence of plaque growth rate and arrest on viral and IFN diffusion coefficients. Each box shows 20 replica simulations' cell type progression over time for the indicated diffusion coefficient multiplier combination. The solid-colored lines indicate the medians of the radii, and the shaded regions indicate the 5th and 95th percentile radii over 20 replicas. In the orange shaded region (above the bold line) plaques arrest by 80 hours. In the blue shaded region (below the bold line), plaques continue to grow until the end of the simulation.

Sensitivity Analysis Reveals that the Main Parameters Controlling Radial Plaque Growth Differ Between Regimes

To determine how individual parameters affect the growth of plaques, we performed local sensitivity analyses around parameter sets in three regimes in parameter space; the baseline parameter set (Table 3.2), the High JAK/STAT regime ($k_{STATP,IFNe}$ = 688.5 µM hr^{-1}, 15x baseline value, all other parameter values as in Table 3.2), and the High IFN Diffusion regime (D_{IFNe} = 540.0 $\mu m^2 s^{-1}$, 10x baseline value, all other parameter values as in Table 3.2). For each regime, we ran 20 simulation replicas using the regime's nominal parameter values. Then, we perturbed each parameter individually ±25%, ran 20 simulation replicas for each perturbed parameter set, and performed statistical analyses on several sensitivity metrics derived from the simulated trajectories. Sensitivity metrics include the percent change from the average of the baseline simulations of the plaque radius growth rate, the maximum value of V_e and IFN_e that occurred over time, and the AUC of average V_e and IFN_e. We determined the statistical significance of the change in each metric from its unperturbed value using a Student's t-test. The top row of Figure 3.9 shows the cell type progression for plaque growth assays for each regime.

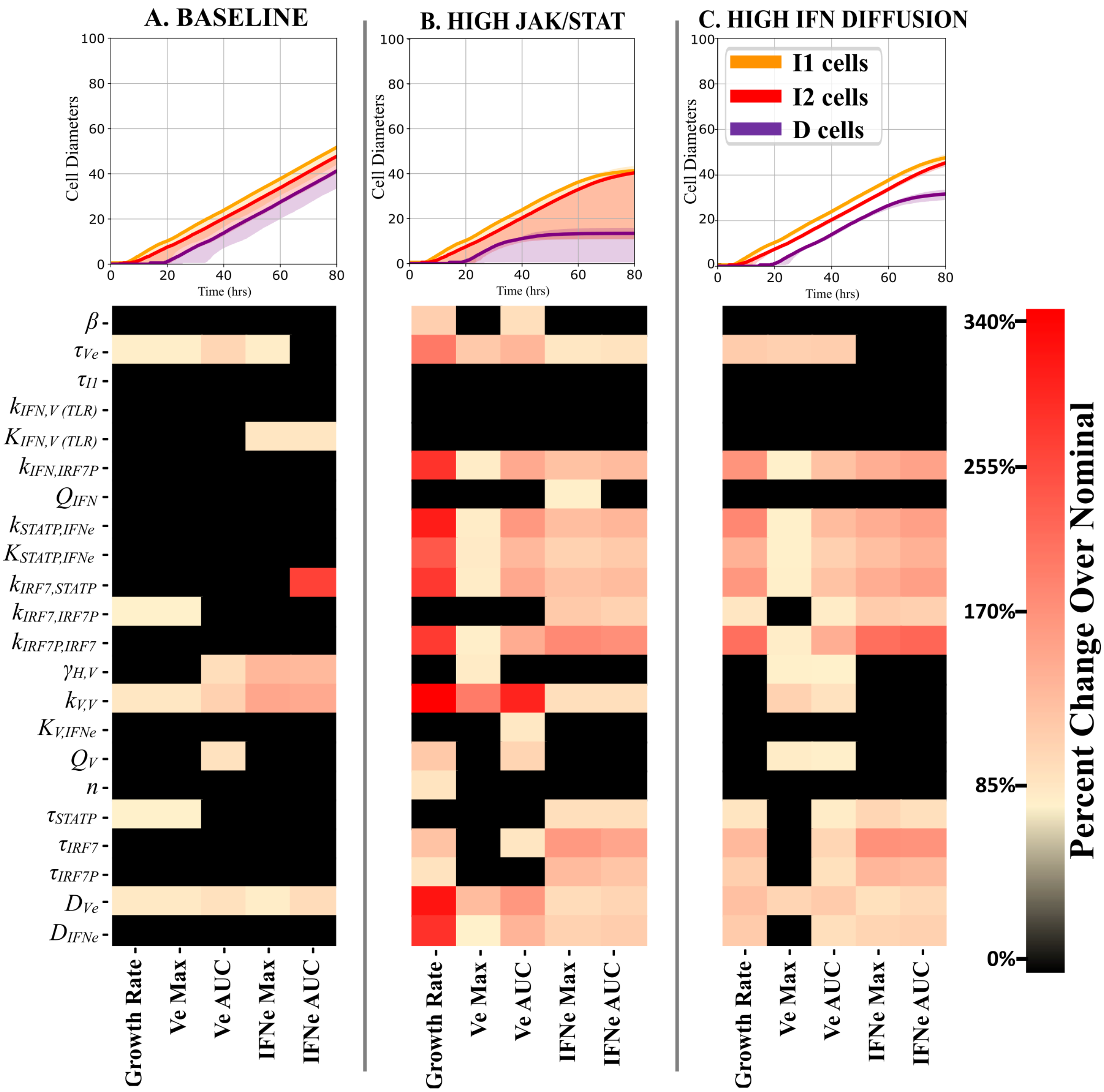

Figure 3.8. Local single-factor sensitivity analysis for three simulation regimes. (A) "Baseline" corresponds to the baseline parameters in Table 3.2. (B) "High JAK/STAT" corresponds to a 15x increase in the phosphorylation rate of STATP via the JAK/STAT pathway (parameter $k_{STATP,IFNe}$), with all other parameters as in Table 3.2. (C) "High IFN Diffusion" corresponds to a 10x increase in the diffusion coefficient of IFN_e, with all other parameters as in Table 3.2. Sensitivity analyses varied each parameter one-at-a-time ± 25% around its unperturbed value and quantified the average plaque radius growth rate

at the end of the simulation, the maximum extracellular virus (V_e) and interferon (IFN_e) levels that occurred, and the area under the curve (AUC) for both average V_e and IFN_e. The sensitivity metrics average the absolute values of the metric for increased and decreased parameters over 20 replicas for each parameter set.

Previous sections demonstrated that variation in multiple parameters could lead to either continuous or arrested plaque growth. The baseline parameter set leads to the continuous growth of the plaque. In this regime, the rate of STATP dephosphorylation (determined by τ_{STATP}, Eq. 3.6), the strength of induction of IRF7 by STATP and IRF7P (determined by the $k_{IRF7,STATP,}$ and $k_{IRF7,IRF7P}$ rate parameters in Eq. 3.7), the maximal rate of viral replication (represented by the rate parameter $k_{V,V}$ in Eq. 3.4), the extracellular virus diffusion coefficient (D_{Ve} in Eq. 3.10), and the rate of nonspecific extracellular viral clearance (τ_{Ve} in Eq. 3.10) have the largest effects on the metrics. For example, increasing the maximal viral replication rate, the probability of transition from U to I1 cell types or the extracellular virus diffusion coefficient (D_{Ve}, effect shown in Fig 3.8) leads to faster plaque growth, whereas increasing the virus release rate to the extracellular environment (Q_V, results not shown) or the extracellular IFN diffusion coefficient slows plaque growth. The High JAK/STAT and High IFN Diffusion regimes both have arrested plaque growth. In these regimes, the parameters associated with the activation of paracrine signaling have statistically significant sensitivity to perturbations tested. The magnitude of the effects is higher in the High JAK/STAT regime than in the High IFN Diffusion regime. This suggests that paracrine signaling is a more feasible target for immunomodulation. The increase in parameter sensitivity in arrested plaque growth regimes also suggests that experimental conditions leading to arrested growth could improve the parameterization of future models and investigations into the interferon signaling response to viral infection.

Discussion

We developed a mechanistic, multicellular spatial model of interferon signaling (the MSIS model) that we used to evaluate how changes in key parameters impacted plaque growth in RNA virus-infected cell cultures. The MSIS model produced plaque-like structures (Fig 3.3). The MSIS model includes parameters that were fit to data from H1N1-infected cell culture experiments (see Table 3.2). Without additional parameter training, we showed that the model produced plaque growth dynamics (Fig 3.4C) similar to those observed in cells infected with two different H1N1 influenza viruses (Fig 3.4A and 3.4B). We then focused on using the MSIS model to evaluate how altering intracellular signaling rates and/or diffusion rates might impact plaque growth and performed sensitivity analyses to determine the experimental conditions under which the model's parameter values can best be estimated.

One of the most significant outcomes of this study is that the sensitivity analysis of the MSIS model suggests that experiments should be performed in conditions that lead to plaque growth arrest rather than unlimited growth to improve the identifiability of interferon signaling parameters (Fig 3.8). Often, cell culture experiments of virus growth dynamics employ cell lines or conditions that promote virus plaque growth. For example, Vero cells are frequently used in studies because they do not produce interferon and therefore support robust virus replication. However, our sensitivity analysis shows that performing experiments in cells with more robust IFN responses will provide more informative data to estimate 19 of the interferon signaling parameters, compared to only 9 parameters being significantly sensitive in regimes leading to unconstrained plaque growth. And 8 of these 9 parameters significantly affect the model outputs under both constrained and unconstrained plaque growth. In all, the model suggests that experiments performed in IFN-competent cells under conditions that lead to plaque arrest are best for accurately inferring interferon signaling-associated parameter values.

We also used the MSIS model to evaluate the effects of increased paracrine activity (via STATP), increased intracellular virus detection (via RIG-I), and prestimulating cells with IFNe. All three changes lead to increased concentrations of extracellular IFN but only elevated paracrine signaling resulting from enhancing STATP activation (Fig 3.5) and interferon prestimulation (Fig 3.7) led to plaque growth arrest. Both IFN prestimulation and enhanced STATP production via extracellular IFN resulted in a reduced concentration of extracellular virus and an increased concentration of extracellular IFN. The final plaque size at the end of the simulations is similar when comparing the IFN prestimulation simulations (Fig 3.7A) to the simulation when STATP activation via extracellular IFN is enhanced by 100x (Fig 3.5A; furthest panel on the right). Enhanced STATP activation and IFN prestimulation leading to suppressed virus production and plaque growth are consistent with known biology and experimental observations.

However, the model's predictions on the effects of enhancing intracellular detection of virus via the RIG-I pathway differs significantly from experimental observations. Experiments show that enhanced RIG-I binding of viral RNA leads to increased IFN production, reduced virus production, and smaller plaques [105]. Increasing RIG-I activity *in silico* increased IFN production and decreased virus production but did not significantly change the plaque size at the end of the simulation (Fig 3.6A). It did affect the cell type demographics, leading to significantly fewer dead cells and many persistent I2 cells (Fig 3.6B). Future work could investigate the effect of intracellular IFN and viral load on the rate of cell death, which is independent of these factors in the MSIS model (Eq. 3.3).

We then considered how diffusion coefficients impact plaque growth (Fig 3.8). A Stokes-Einstein estimate of diffusion coefficients for virus particles (with an effective radius of 80 – 120 nm) [106] and interferon proteins (with an effective radius of 7 nm) [107] predict 11x – 17x larger diffusion coefficients for interferon in most media. While diffusion coefficients can vary over several orders of magnitude during the course of a single cell culture experiment (due to cell secretion of molecular species like collagen which increase medium viscosity or proteases which can decrease it) [85], we used a constant, equal, diffusion coefficient for both species ($54.0\ \mu m^2\ s^{-1}$) in our baseline simulations, resulting in continuous radial plaque growth. The decay rates (τ_{Ve} and τ_{IFNe}) yield effective diffusion lengths for V_e and IFN_e of 0.09 µm and 0.23 µm, respectively. In Fig 3.8, we explored how changing the diffusion coefficients impacts plaque growth, identifying a clear boundary between regimes of arrested and continuous plaque growth. Fig 8 shows that even when D_{IFNe} is significantly larger than D_{Ve} both arrested and unconstrained plaque growth can occur for different values of D_{IFNe}. In summary, we show that the model can produce unconstrained and constrained plaque growth over a wide range of diffusion coefficient combinations. Future work will focus on refining these values and may consider time-dependent diffusion coefficients.

One major shortcoming of the MSIS model is the lack of additional mechanisms to model cell death. During infection, cell death occurs via several mechanisms, including via programmed cell death (apoptosis) and pyroptosis, cell death induced via inflammasomes [108]. Lacking these mechanisms, cell death only occurs in the MSIS models as the intracellular concentration of virus increases and the cell health declines (Eq. 3.3). But as seen in Fig 3.5A, 3.6A, and 3.7A, cells can become stuck in the I2 cell type as the reduced concentration of intracellular virus and the slow rate of health decline significantly reduces the likelihood of a cell transitioning to the dead type. The equation that defines how cell health declines (Eq. 3.9) was directly translated from a population-level model where health translated to the fraction of uninfected cells. In that context, Eq.3. 9 is reasonable, but as a model of the health of a single cell, having the rate of health decline be linearly dependent on the current health of the cell (i.e., health declines more rapidly for healthier cells) might not be reasonable. To improve the model's relatability to experimentation, future work will focus on including additional mechanisms of cell death as well as improving the kinetic description of how cell health impacts a cell’s transition to death.

The SARS-CoV-2 and influenza viruses for which this model was constructed have many similarities. Like influenza’s NS1 protein, SARS-CoV’s NSp1 antagonizes RIG-I signaling [104], and genome analysis shows an 87% conservation of NSp1’s genome between SARS-CoV and SARS-CoV-2 [81]. This similarity suggests that the MSIS model could readily be adapted to model SARS-CoV-2-induced interferon signaling from measurements of SARS-CoV-2-specific virus kinetics. The MSIS model can also be extended to consider additional spatial aspects of infection. The modular architecture supports independent and collaborative development of extensions to account for additional immune response mechanisms in vitro such as IFN-mediated cell death. It also supports extending the model to include aspects of the immune response in vivo such as propagation of IFN signaling by local innate immune cells and recruitment of adaptive immune cells to the site of infection.

Run for your life – an integrated virtual tissue platform for incorporating exercise oncology into immunotherapy

Introduction

Computational modeling is playing increasingly important roles in advancing system-level mechanistic understanding of complex biological processes. *In silico* simulations guide experimental and clinical efforts and can accelerate therapeutic. Here we present a computational platform that can interrogate the potential mechanisms underlying the enhancing effect of aerobic fitness on anti-tumor immune response. These effects, documented in pre-clinical [109] and clinical studies [110], furnish us with a natural backdrop for probing patient variability and support the inclusion of aerobic fitness as a biological variable in clinical contexts. Doing so may contribute to the personalization of immunotherapy by optimizing dosage and frequency of treatment, reducing the risk of cardiotoxicity [111] and other adverse side effects.

We developed an *in silico* platform for simulating early-stage solid tumor growth and anti-tumor immune response. We calibrated the model with clinical data from exercise oncology experiments. We performed two virtual experiments that demonstrate the potential of the model in guiding pre-clinical and clinical studies of immunotherapy. The first virtual experiment simulates the dynamics between the tumor and the infiltrating immune cells. Such fine-grained spatiotemporal dynamics is difficult to probe in pre-clinical studies as it requires significant redundancy in lab animals and is prohibitively time-consuming and labor-intensive. The result is a series of spatiotemporal snapshots of the tumor and its microenvironment that can serve as a platform to test mechanistic hypotheses on the role and dynamics of different immune cells in anti-tumor immune response. The second virtual experiment shows how dosage and/or frequency of immunotherapy drugs can be optimized based on the aerobic fitness of the patient, so that possible adverse side effects of the treatment can be minimized.

The model is based on the open-source platform CompuCell (CC3D) and based on previous work modeling tumor growth and evolution as a function of available resources [34]. The original model focused solely on differential cell-adhesion and somatic evolution. We used the same framework to build a model that includes immune cell types, cytokines, chemokines, and metabolic signals, and employed it to interrogate immune response to tumor progression as a function of aerobic fitness. Our model is a 2D spatiotemporal representation of a cross section in the tumor microenvironment (TME). Our basics assumption is that aerobic fitness acts as a tumor suppressor through a systemic enhancement of anti-tumor immune response. This systemic effect is a result of metabolic and endocrinal modifications, which can be modulated with chronic exercise training. While the exact mechanisms behind this effect are currently under investigation, documented pre-clinical experiments point at two potential candidates: (1) increased trafficking of NK cells into the TME, triggered by up-regulation of epinephrine and (2) hypoxia-tolerant suppression of the recruitment of immune inhibitory cells (CD4+FOXP3+ Tregs) into the TME which increases cytotoxic T lymphocytes (CD8+ Lymphocytes CTLs) efficiency [113]. In the model presented here we chose to focus on candidate (2) but the platform can be easily adjusted to incorporate candidate (1) or any other potential mechanism in the future.

Methods

Clinical Data

The clinical data supporting the hypotheses incorporated into the model was obtained from a pilot study where 14 recently diagnosed early stage Invasive Ductal Carcinoma post-menopausal patients were subjected to a short submaximal aerobic exercise (for a complete description of the study cohort see [114]) and were assigned an aerobic score [115]. Tumor size estimated in two time points (the diagnostic mammogram and an earlier mammogram where the radiologist could identify the tumor with hindsight), along with the time between the two mammograms, yielded an estimation of tumor doubling time for each patient. A statistically significant correlation was then detected between the aerobic score and the tumor doubling time: the more aerobically fit were the patients, the longer were their doubling times. Further pre-clinical studies detailed below allowed us to replicate this phenomenon and to interrogate the potential mechanisms underlying it.

Model Conceptualization

The model is a spatiotemporal representation of a TME of a solid tumor in its early stages (T0 to T1) that includes key aspects of the interactions between tumor cells, the TME, and the host immune response. Tumor cells adopt four different phenotypes: “oxphos” (relying mostly on oxidative phosphorylation), “glycolytic” (elevated glycolysis when the surrounding tissue becomes hypoxic), “necrotic” and “apoptotic”. Tumor cells grow, divide, and invade their environment. The growth rate of tumor cells is limited by the availability of oxygen which cells consume from the environment. The level of tumor immunogenicity is mediated by aerobic tumor cell transition from one metabolic phenotype to another (due to oxygenation levels). As oxygen gets depleted, tumor cells change their metabolic phenotype from “oxphos” to “glycolytic”. Glycolytic tumor cells can change phenotype back to “oxphos” if the oxygenation of the tissue is restored. When oxygen is severely depleted, glycolytic cells become necrotic and die (this phenomenon is typically observed at the tumor core). Glycolytic cells and necrotic cells secrete lactate to the TME that serves as a recruiting signal for the tumor promoter cells.

Our model includes two types of immune cells: CD8+ Lymphocytes Tumor suppressors (“CTLs” in our model) and CD4+FOXP3+ tumor promoters (“Tregs” in our model). CTLs are constantly recruited to the tumor site, infiltrate the TME and induce apoptosis in the tumor cells they come into contact with. Upon contact with tumor cells, CTLs also release a cytokine signal to the TME (“IFNγ” field), thus attracting other CTLs to their vicinity. The acidification of the TME by the glycolytic cells results in recruitment of Tregs to the tumor site. These recruited Tregs move through the tissue to areas of higher concentration of Lactate. Tregs inhibit the CTLs they come near to. This inhibition prevents CTLs from inducing apoptosis in cancer cells they come into contact with.

We implemented the model in CompuCell3D (CC3D), an open-source modeling environment that allows specification and simulation of multicellular models, diffusing fields and biochemical networks [37]. CC3D simulates spatial dynamics using the Cellular Potts Model, a modeling framework where cells are represented on a lattice and their spatial properties are governed by an effective energy function. Spatial dynamics are decided using a Monte Carlo approach, making each independent run stochastic, in which time is measured in Monte Carlo steps (MCS). Our model is simulated over10^6 lattice sites representing up to 5×10^4 individual cells. Diffusion solvers integrate partial differential equations describing the diffusion of oxygen, Lactate, and cytokines across the whole simulation domain. The different outcomes of the simulation are dependent on the parameter values associated with aerobic fitness and with the emergent patterns of TME invasion associated with availability of resources and immune response. Figure 4.1 shows the model conceptualization.

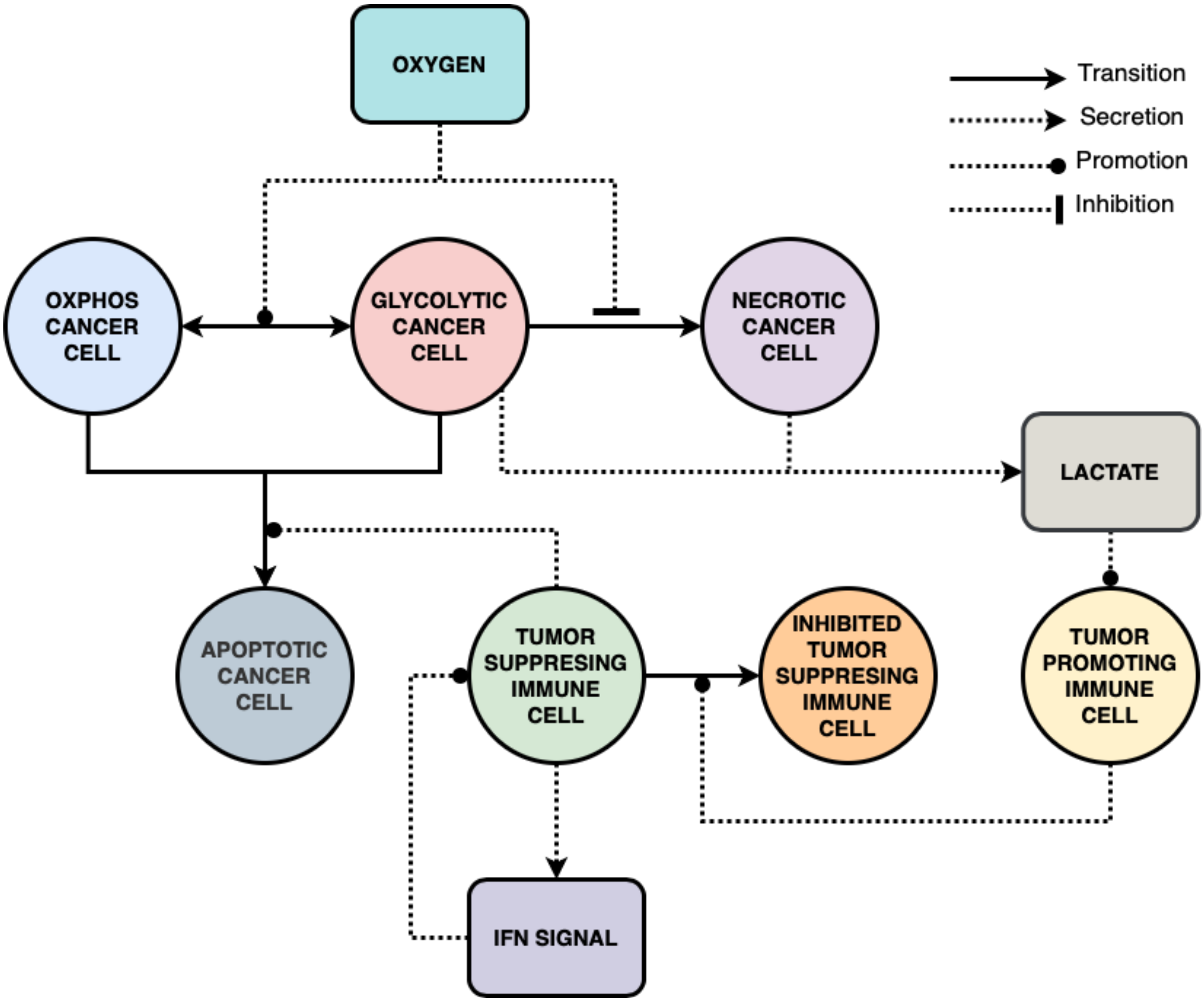
OXYGEN
Transition
Secretion
Promotion
Inhibition
OXPHOS CANCER CELL
GLYCOLYTIC CANCER CELL
NECROTIC CANCER CELL
LACTATE
APOPTOTIC CANCER CELL
TUMOR SUPPRESING IMMUNE CELL
INHIBITED TUMOR SUPPRESING IMMUNE CELL
TUMOR PROMOTING IMMUNE CELL
IFN SIGNAL

Figure 4.1. Model Conceptualization. The model simulates the early stage of 2D solid tumor progression from which a growth rate (in terms of tumor area) can be calculated. Once initialized, tumor cells grow in the TME, and with time become more glycolytic, at a rate that depends on the host's aerobic fitness and tolerance to hypoxia. Tumor cells die through necrosis or apoptosis (lack of oxygen or death by immune response, respectively). Tumor suppressors ("CTLs") and tumor promoters ("Tregs") react to cytokine and chemoattractant fields secreted by tumor cells.

Glycolysis and hypoxia tolerance

The underlying hypothesis of exercise oncology is that aerobic exercise leads to systemic modifications of non-skeletal-muscle tissue. Consistent with several studies that point at hypoxia and elevated glycolysis as a hallmark of solid tumor progression [116] we hypothesize further that aerobic exercise can modify the tissue's ability to tolerate hypoxia and to degrade HIF1α, a known upstream factor in recruitment of Tregs in the TME. To represent this biological feature in our model we introduced the Lactate field (L), secreted by the tumor cells (Fig. 4.2). According to our hypothesis, a solid tumor in aerobically fit (sedentary) hosts will generate weak (strong) L field depending on that host's tolerance to hypoxia. This hypothetical differential drives the variation in immune response to the solid tumor. The model presented here thus embodies our working hypothesis (supported by clinical and pre-clinical studies [117]) that early stage solid tumors of aerobically fit individuals – who have higher tolerance to hypoxia – will go through the shift from the "oxphos" phenotype to the "glycolytic" phenotype in lower levels of oxygen in the TME than sedentary individuals, and, as a result, will exhibit less glycolysis-initiated immunosuppressive response than similar tumors of sedentary subjects for the same levels of oxygen in the TME.

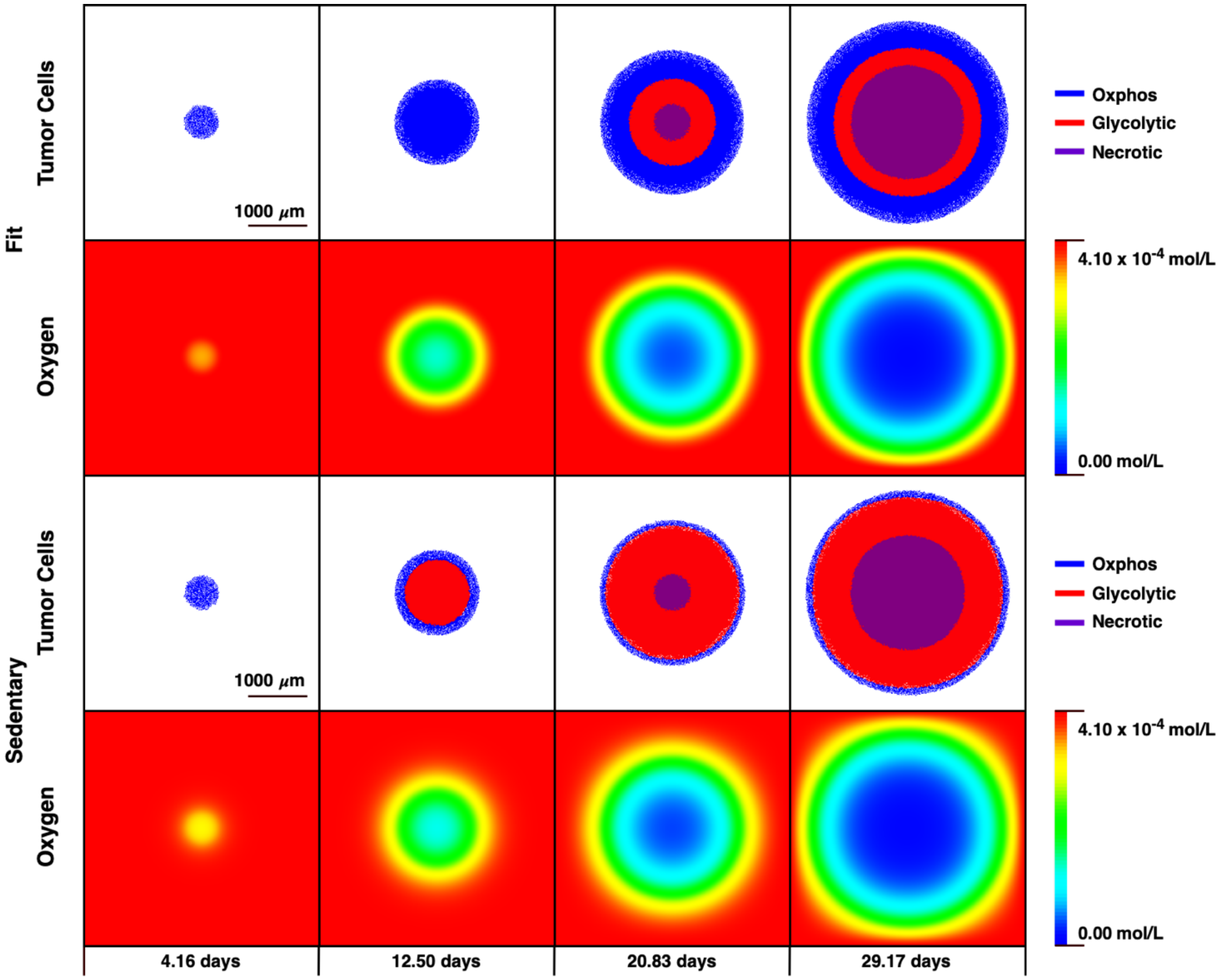

Figure 4.2. Aerobic Fitness Modulates Hypoxia-Tolerance in the TME. While oxygen levels are identical in the two examples above, the two representative TME react to them differently: the more aerobically fit is the host (FIT), the more tolerant to hypoxia its TME is, and as a result, tumor cells are less glycolytic relative to sedentary hosts (SED).

Immune suppressors and immune promoters dynamics.

Clinical studies have shown that intratumoral CTLs/Treg ratio is a significant prognostic marker for cancer patients [118] and several pre-clinical studies have tied this marker to hypoxic conditions in the TME [113]. To represent these biological features in our model we introduced two types of immune cells (immune suppressors, or “CTLs” and immune promoters, or “Tregs”) and implemented two scales of trafficking (Fig. 4.3). The first is the appearance of these cells in the TME, implemented with different densities; the second is movement within the TME, implemented with chemotaxis mechanisms. The seeding rates and densities were calibrated using data on respective densities from hot vs. cold tumors in humans [119]. The chemotaxis mechanisms are sensitive to two fields. CTLs react to a cytokine secreted by tumor cells killed by other CTLs (the “IFNγ” field); Tregs react to the L field secreted into the TME (the more glycolytic is the tumor, the stronger is the Treg recruiting signal).

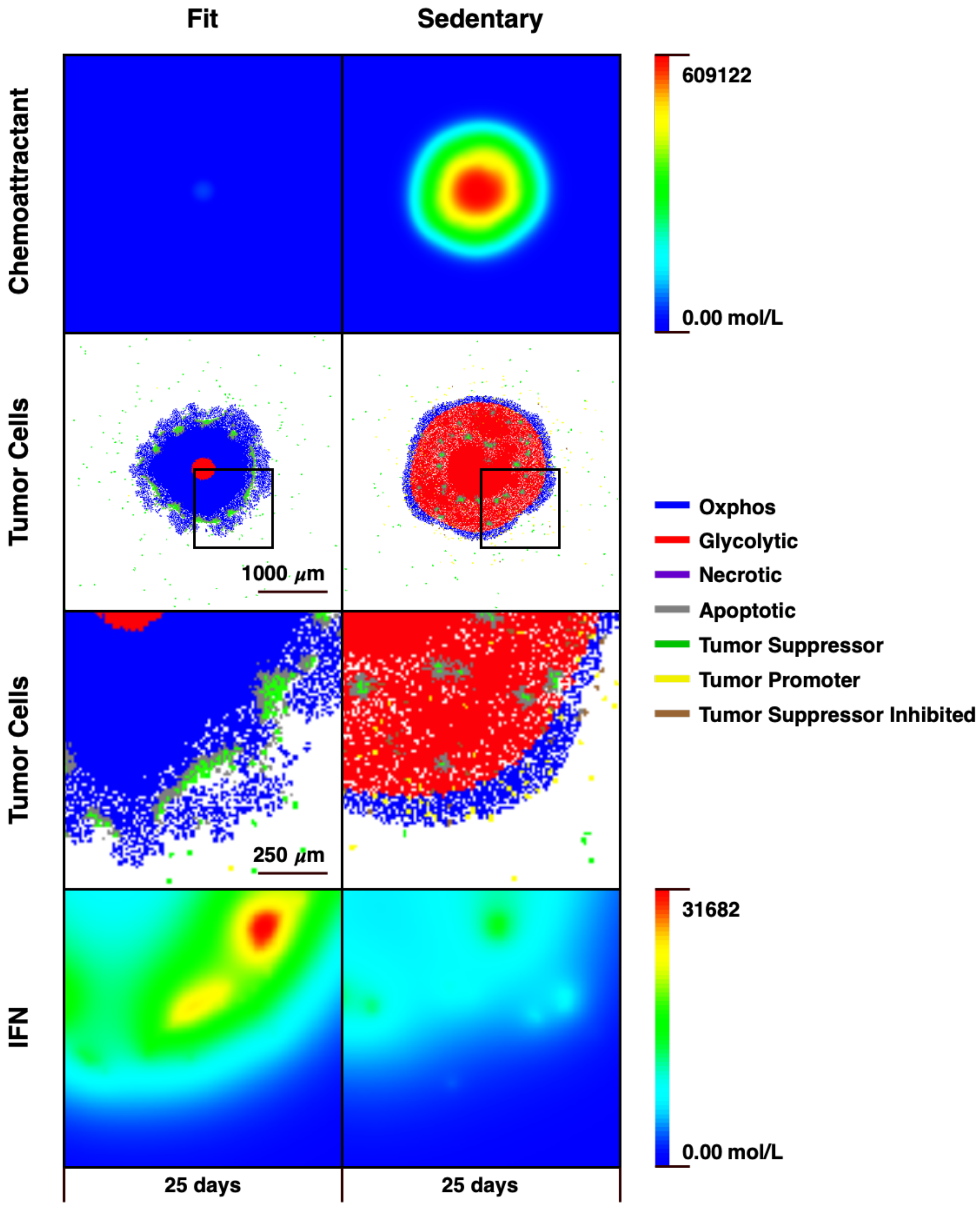

Figure 4.3. Aerobic Fitness Modulates Anti-Tumor Immune Response. The more aerobically fit is the host, the less glycolytic its tumor cells are relative to a sedentary host. Consequently, recruitment of tumor

promoters that can block tumor suppressors is down regulated relative to a sedentary host, and tumor growth will be relatively suppressed. Tumor promoters move towards the tumor along the chemo-attractant gradient that glycolytic tumor cells secrete. Tumor suppressors move towards the tumor along a cytokine gradient (“IFNγ”) that necrotic tumor cells secrete. Once infiltrated into the TME, tumor promoters can inhibit the ability of nearby tumor promoters to kill tumor cells.

CompuCell3D Implementation

We adopted a voxel length of 4μm, such that the each voxel represents an area of $16\ \mu m^2$. The total simulation domain consists of 1000×1000 voxels, corresponding to a tissue cross-section of $16\ mm^2$. The initial tumor cell target volume is $256\ \mu m^2$ which is between twice and 3 times the average size of epithelial cells [119]. The immune cell target volume is $384\ \mu m^2$. The initial tumor cell surface is $64\ \mu m$ and the immune cell target surface is $78.4\ \mu m$.The cell surface is calculated from the cell volume assuming that the area occupied by cells is a square. Note that ‘cell volume’ and ‘cell surface’ are CC3D-specific cell properties denoting the number of voxels occupied by each cell and the number of outer voxels of each cell respectively. As such, they correspond to the cross-sectional area and the perimeter of cells. The MCS to time conversation is $6\ mins$. This estimate is based on experimental tumor cell migration speed [34]. For the contact energies, we assigned values that result in a highly negative surface tension between tumor cells and the surrounding general medium such that tumor cells invade the surrounding tissue.

Simulation parameters corresponding to the spatial properties of human solid tumor cells, transport of chemicals and rates of immune response were estimated from the literature. We assumed that when sufficient resources are available, tumor cells grow and divide every $24\ hrs$. Conversely, when resources are depleted cells die within $12\ hrs$, and when CTLs induce apoptosis, cells die within $8\,hrs$. We estimated the infiltration rates of CTLs (1 cell every 1.5 hours) and Tregs (1 cell every 1 hour) using intramural density data, showing that the “CTL”/“Treg” ratio is 5:1 [120]. We assumed that the homeostatic concentration of oxygen in tissue is $4.3 \times 10^{-4} Mol/L$ [121]. Aerobic fitness was defined as the oxygen concentration threshold at which tumor cells changed from “oxphos” to “glycolytic”. Different virtual populations were defined with respect to different thresholds. The more aerobically fit a virtual subject is, the more tolerant its tissue will be to hypoxia, and as a result, the threshold for the shift from “oxphos” to “glycolytic” is lower. These parameters are CC3D-specific and the values are shown in Table 4.1.

Conversion Factors		
MCS	360.0 s	
Lattice length	4.0 um	
Concentration conversion factor	1.0 X 10 16 mol	
Parameter	Symbol	Value
Initial target volume tumor cell (Eq 4.1)	V_T	256 um^2
Lambda volume (Eq 4.1)	λ_{vol}	16
Initial target surface tumor cell	S_T	64 um
Lambda surface	λ_{sur}	16
Target volume immune cell (Eq 4.1)	V_T	384 um^2
Lambda volume (Eq 4.1)	λ_{vol}	24
Target surface immune cell	S_T	78.4 um
Lambda surface	λ_{sur}	19.6
Membrane fluctuation (Eq 4.2)	T	50.0

Oxygen diffusion coefficient (Eq 4.3)	D_O	1460.0 um^2/s
Oxygen uptake by OXPHOS tumor cells (Eq 4.3)	d_{OXPHOS}	6.00 x 10-17 mol/(cell*s)
Global oxygen decay rate (Eq 4.3)	d_{global}	0.01 1/s
Oxygen production by Medium (Eq. 4.3)	P_{Medium}	8..00 x 10-16 mol/s
Chemoattractant diffusion coefficient (Eq 4.4)	D_L	0.1 um^2/s
Chemoattractant decay rate (Eq 4.4)	d_L	1.0 x 10-7 1/s
Chemoattractant production by glycolytic c cells (Eq 4.4)	P_{L-Gly}	7.52 x 10-17 mol/(cell*s)
IFN-γ diffusion coefficient (Eq 4.5)	D_{IFN}	0.1 um^2/s
IFN-γ decay rate (Eq 4.5)	d_{IFN}	1.0 x 10-7 1/s
IFN-γ production by tumor suppressor cells (Eq 4.5)	$P_{IFN-Immu}$	7.52 x 10-17 mol/(cell*s)
Fitness Threshold (eq 4.6a,b)	F_t	[2.34x10^-4 to 9.38x10^-5] mol/L
Necrotic Threshold (eq 4.7)	N_t	6.25 x 10-5 mol/L
Cell Transition Probability (eqs 4.6-4.7)	TP	0.000111 1/s
Maximum tumor growth rate (Eq 4.8)	G	2.96 x 10-3 um^2/s
Oxygen concentration at which tumor growth rate is half maximum (Eq 4.9)	K_O	2.15 x 10 -4 mol/L
Chemotaxis sensitivity of tumor suppressors to oxygen field (Eq 4.10)	λ_{O-Supp}	-500
Chemotaxis sensitivity of tumor suppressors to IFN field (Eq 4.10)	$\lambda_{IFN-Supp}$	500
Chemotaxis sensitivity of tumor promoters to chemoattractant field (Eq 4.10)	λ_{L-Prom}	500
Recruitment rate of tumor suppressor immune cells (Eq 4.11)	R_{Supp}	0.0111 cell/s
Recruitment rate of tumor suppressor immune cells (Eq 4.11)	R_{Prom}	0.0167 cell/s

Apoptosis rate (Eq 4.12)	A	3.70 x 10-4 um^2/s
Tumor promoter inhibition radius (Eq 4.13)	I_d	96 um

Table 4.1 CompuCell 3D Simulation Parameters

Cell Types

‘Cell types’ are CC3D-specific attributes that allow to classify individual cells based on different phenotypes and behaviors. We represented the different population of cells in the TME by including four types of tumor (OXPHOS, Glycolytic, Necrotic and Apoptotic) cells and two types of immune cells (Tumor Suppressors and Tumor Promoters). OXPHOS represents tumor cells that mostly rely on oxidative phosphorylation as their main metabolic pathway. Glycolytic represents tumor cells that mostly rely on glycolysis as their main metabolic pathway. OXPHOS and glycolytic tumor cells grow and divide at the same rate based on the availability of metabolic resources. OXPHOS cells rapidly consume oxygen from the TME while glycolytic cells produce pro and anti-inflammatory signals that recruit immune cells. Necrotic represents tumor cells at the necrotic core of the tumor dying due to lack of metabolic resources. Necrotic cells also produce proinflammatory and anti-inflammatory signals. Apoptotic represents tumor cells undergoing apoptosis due to immune cell-mediated cytotoxicity. Apoptotic tumor cells shrink and die. Tumor Suppressors represent cytotoxic immune cells that can induce apoptosis in the tumor cells they encounter. The cytotoxic mechanism is described in *Immune Cell Cytotoxicity*. Tumor suppressors have two states: active or inhibited. ‘Active tumor suppressors’ are capable of inducing apoptosis whereas ‘Inhibited tumor suppressors’ are not. Tumor Promoters immune cells represent the anti-inflammatory response of the immune system by inducing the transition of tumor suppressors from active to inhibited. Figure 4.1 shows the different cell types, their interactions and transitions.

Chemical Fields and Diffusion

Oxygen Transport.

Although tumor growth in vivo depends on multiple chemical substances (including glucose, growth factors, fatty acids) we introduce the chemical field oxygen (O) to represent both tissue oxygenation and availability of other metabolic resources. The change in concentration of O is calculated by solving the reaction-diffusion equation at each location in the simulation domain:

$$\frac{\partial O(x)}{\partial t} = D_O \nabla^2 O(x) - d_{O-OXPHOS} O(x) \; - d_O \; O(x) \; + P_{O-Medium}(x)(3) \quad (4.1)$$

whereD_O is the diffusion coefficient of oxygen, $d_{O-OXPHOS}$ is the decay rate of oxygen inside OXPHOS cells (accounting for the oxygen consumption by cells relaying in oxidative phosphorylation), $d_O \; O$ is the global decay rate of oxygen inside all other cells (accounting for consumption and decay of oxygen in general tissue) and $P_{O-Medium}$ is the production rate of oxygen by medium (representing oxygenation from blood vessels).

Parameter estimation. Based on in vitro assays, we assumed that the homeostatic oxygen tension of tissue (in the absence of tumor cells) is $4.3 \times 10^{-4} Mol/L$ [121]. We followed the same method as Maciek et al [34], to determine the rate of oxygen production by Medium by assuming that in real tissue stromal cells consume oxygen at a rate $4.3 \times 10^{-17} Mol/(cell \times s)$ and that stromal cells occupy 20% of the TME [122]. To maintain a steady state concentration of oxygen, the production rate of oxygen by Medium is $4.3 \times 10^{-16} Mol/s$ and the global decay rate of Oxygen is $0.01 \; s^{-1}$. We assumed that at the steady state levels, tumor cells consume oxygen at a rate

$6.0 \times 10^{-17} mol/(cell \times s)$, 3 times faster than stromal cells because of higher metabolic demands. The diffusion coefficient of oxygen in water is $1460\ \mu m^2/s$ [123].

Chemoattractant Transport. We introduced the chemical field chemoattractant (L) to represent the signaling cascade that starts with HIF1a stabilization, higher ratio of glycolysis to OXPHOS, lactate secretion and production of chemokines such as CCL-28 that recruit Tregs into the TME [124]. The change in concentration of L is calculated by solving the reaction-diffusion equation at each location in the simulation domain:

$$\frac{\partial L(x)}{\partial t} = D_L \nabla^2 L(x) - d_L L(x) + P_{L-Gly}(x) \quad (4.2)$$

where D_L is the diffusion coefficient of the chemoattractant, d_Ls the decay rate of the chemoattractant in the TME andP_{L-Gly} is the production rate of chemoattractant by glycolytic cells. Although *in vivo*, every cell produces lactate as a byproduct of their metabolism, our chemical field L represents the excess of lactate produced by cells with a higher ratio of glycolysis to OXPHOS.

Parameter Estimation. The diffusion coefficient of the chemoattractant is in same order of magnitude of the diffusion coefficient of glucose: $0.1\ \mu m^2/s$ [125]. We assumed that the chemoattractant signal is short ranged, such that the diffusion length of the signal is 3 cell diameters ($48\ \mu m$). Based on this assumption, we estimated the decay rate of the chemoattractant to be: $1.0 \times 10^{-7}\ s^{-1}$. Glycolytic cells produce chemoattractant at the same rate cells produce lactate in vitro: $7.52 \times 10^{-17} mol/(cell \times s)$ [126].

IFN-γ. Active immune cells relay information and recruit more immune cells by secreting a variety of chemokines. We simplified the complexity of immune cell signaling by introducing a single chemical field IFN-γ (IFN). The change in concentration of IFN is calculated by solving the reaction-diffusion equation at each location in the simulation domain:

$$\frac{\partial IFN(x)}{\partial t} = D_{IFN}\nabla^2 IFN(x) - d_{IFN}IFN(x) \ + P_{IFN-Immune}(x) \text{ (4.3)}$$

where D_{IFN} is the diffusion coefficient of IFN, d_{IFN} is the decay rate of IFN in the TME and $P_{IFN-Immune}$ is the production rate of IFN by tumor suppressor cells.

Parameter Estimation. Given we are modeling the TME, in this short scale we can assume the same transport coefficients for the IFN field and the chemoattractant field. The real-life difference between the two (the diffusivity of IFN is two orders of magnitude faster [127]) is small given the role the field play in the model, namely, the gradient that provides recruitment and chemotaxis signals.

Tumor Cell Transitions

The transition between OXPHOS and glycolytic types is determined by the amount of oxygen available to the cell and the fitness threshold (a parameter that represents the overall aerobic fitness of the patient).

$$P\big(\sigma(OXPHOS) \rightarrow \sigma(Glycolytic)\big) = TP \quad if\ O(\sigma_{com}) < F_t \text{ (4.4a)}$$

$$P(\sigma(Glycolytic) \rightarrow \sigma(OXPHOS)) \ = TP\ if\ O(\sigma_{com}) > F_t \text{ (4.4b)}$$

Where $\sigma(OXPHOS)$ represents the cell type OXPHOS, $\sigma(Glycolytic)$ represents the cell type Glycolytic, σ_{com} represents the concentration of oxygen at the center of mass of the cell. The fitness parameter F_t represents the oxygen concentration at which tumor cells switch metabolic profile. Equation 4.4a describes the transition probability TP from OXPHOS to Glycolytic when the oxygen concentration drops below the fitness threshold F_t. Equation 4.4b describes the transition probability TP from Glycolytic to OXPHOS when the oxygen concentration increases above the fitness threshold F_t. Both OXPHOS and Glycolytic cells can transition to the Necrotic cell type if the oxygen available to the cell drops below the necrotic threshold.

$$P(\sigma(OXPOS\ or\ Glycolytic) \rightarrow \sigma(Necrotic)) \ = TP \quad if\ O(\sigma_{com}) \ < N_t (4.5)$$

Where $\sigma(Necrotic)$ represents the cell type Necrotic and N_t is the oxygen concentration below which tumor cells transition to Necrotic. Tumor cells can also transition to the Apoptotic cell type if they encounter an active tumor suppressor immune cell.

Parameter Estimation. The transition probability was determined assuming that tumor cells persist in their current state for $2.5\ hrs$ after the metabolic resources in their environment dropped below a certain threshold. The ranges of the fitness threshold were determined by the sensibility analysis. The fitness parameter is related to the experimental fitness score by the following linear relation: $1.85 \times F_t + 0.08$. The necrotic threshold was determined by assuming that cells become necrotic when the oxygen tension drops below 10% of the steady state concentration of oxygen in the tissue [128].

Cell Growth and Mitosis

Although we do not model the cell cycle explicitly, we represent it implicitly by having tumor cells grow and divide once they have doubled their volume. We assumed that tumor cells divide at a rate that is independent of their glycolysis/OXPHOS ratio. “Sedentary” and “trained” tumors show similar KI-67 levels [129]. The cell volume growth rate is a function of the local availability of oxygen, which in this case represents metabolic resources:

$$\frac{\partial V(\sigma)}{\partial t} = G\,\frac{O(\sigma)^2}{O(\sigma)^2 + K_O^2} \ (4.6)$$

where V is the target volume of the cell σ, G is the maximum growth rate of individual tumor cells, O is the concentration of oxygen at the center of mass of cell σ and K_O is the concentration of oxygen at which the growth rate decreases to half maximum. We assumed this Michaelis-Menten form for the growth rate to model a smooth transition between actively dividing and quiescent tumor cells. Although the target volume of the cell increases at a rate that is dependent only on the availability of oxygen, the actual volume of the cell depends on other factors, such as availability of space. The target surface of the cell was also adjusted such that $S(\sigma) = 4\sqrt{V(\sigma)}$, where S is the new target surface of the growing tumor cell σ.The plane of division was assumed to be random.

Parameter estimation. We assumed that the average time for tumor cell division is 24 hours. Since cells must double their initial target volume to divide, we estimated the maximum growth rate of the cell to be $2.96 \times 10^{-3}\ \mu m^2/s$. The parameter K_O is the oxygen concentration at which the growth rate is half maximum ($G/2$) and we assume this threshold is reached when the oxygen concentration inside the tumor drops to half the steady state oxygen tension in tissue $2.15 \times 10^{-4}\ mol/L$. The growth rate is the same for OXPHOS and glycolytic cells.

Chemotaxis

Immune cells respond to chemokine signals in the TME and can actively migrate to areas of higher concentrations of such signals. In particular, IFNγ enhances the cytolytic ability and the kinematics of Cytotoxic CD8+ T lymphocytes (CTL) both by paracrine and autocrine signaling mechanisms. CTLs' search patterns in peripheral tissues are mainly dictated by informed motion in which haptotaxis and haptokinesis cues restrict their movements, and chemoattractants guide them through signaling gradients. To model CTL migration inside the tumor, we assumed that tumor suppressors migrate against the gradient of the oxygen field, which is an indicator of highly proliferative tumor cells. We assume that both immune tumor promoters are attracted by the chemoattractant field, which drives immune cell migration to highly glycolytic areas of the TME. We also assume that immune tumor suppressors are attracted by the IFNγ field, which drives them to areas of high density of active immune suppressors. In CPM, chemotaxis is represented as an additional energy term in the effective energy function H. The change in energy due to chemotaxis is calculated by considering the chemotactic force that favors voxel attempts in which cells move up or down the gradient of the field. The chemotactic force exerted over each voxel of the cells is given by:

$$F_{chem}(x) = \frac{\lambda_{f_i}}{1+f_i(\sigma)} \nabla f_i(x) \text{ (4.7)}$$

where $\lambda_{f_i}$is the chemotactic sensitivity parameter of the cell at position x to the chemical field F_i, $f_i(\sigma)$ is the concentration of the field at the center of mass of cell σ, and $\nabla f_i(x)$ is the gradient of the field at position x with respect to the source voxel. Parameters $\lambda_{(O-Supp)}$ and $\lambda_{(IFN-Supp)}$ are the sensitivity of tumor suppressors to the oxygen and the IFNγ fields, respectively. Parameter $\lambda_{(L-Prom)}$ is the sensitivity of tumor promoters to the chemoattractant field.

Parameter estimation. The chemotactic sensitivity λ_{f_i} parameter is a CPM-specific parameter, and as such does not correspond to a measurable experimental quantity. However, since λ_{f_i} modulates the chemotactic strength and the speed of cell migration, we chose values of -500 and 500 for $\lambda_{(IFN-Supp)}$ and $\lambda_{(L-Prom)}$ such that immune cells migrate faster than tumor cells and penetrate the highly packed tumor while still preserving their shape.

Immune Cell Recruitment

Our model currently covers the TME only and thus ignores the complex signaling networks behind immune cells migration, search strategies and recruiting mechanisms from the lymphoid organs to target organs. We model the recruitment of Immune cells into the TME by assigning probabilities to different immune cells appearing in the TME. In the case of a tumor suppressor immune cell, the probability is constant:

$$Pr\ (adding\ tumor\ suppressor) = R_{Supp} \quad (4.8)$$

Where R_{Supp} is the probability per simulation unit time. To determine the seeding location of the tumor suppressor, the simulation space is randomly sampled 6 times, and a tumor suppressor immune cell is seeded at the unoccupied location with the highest amount of the IFN field. The immune cell is not seeded if none of the 6 locations is unoccupied. The probability of adding a tumor promoter immune cell depends on the fraction of glycolytic cells to all proliferative tumor cells, which we use as a proxy of the glycolytic state of the tumor.

$$Pr\ (adding\ tumor\ promoter) = R_{Prom} \frac{N_{Gly}}{N_{OXP}+N_{Gly}} \quad (4.9)$$

Where R_{Prom} is the maximum probability per simulation unit time, N_{Gly} is the number of glycolytic tumor cells and N_{OXP} is the number of OXPHOS tumor cells. To determine the seeding location of the tumor promoter, the simulation space is randomly sampled 6 times, and a tumor promoter immune cell is seeded at the unoccupied location with the highest amount of the chemoattractant field. The immune cell is not seeded if none of the 6 locations is unoccupied. Once the cells are in the TME, they react to their respective recruiting signals: Tumor suppressors move along the oxygen and the IFNγ gradient and immune suppressors move along the chemoattractant.

Parameter estimation. The constant recruitment rate of tumor suppressors was determined such that at the end of the simulation, the density of tumor cells was $50\ cells/mm^2$. This density is 10 times smaller than the average density observed in vivo [120]. This scaling factor was adopted because of limitations to the spatial dimensions of the immune cells imposed by their interactions with the tumor. The recruitment rate of tumor promoters was calibrated such that by the end of the simulation, the average density of tumor suppressors was half of the density of tumor promoters and ranged from 1:8 to 1:1 [130].

Immune Cell Cytotoxicity

CTLs are found in many solid tumors and provide an attractive target for immunotherapeutic manipulation. We modeled CTL-mediated cytotoxicity by having tumor suppressors kill all the tumor cells they come in contact with. When a tumor suppressor cell encounters a tumor cell, the tumor cell transitions to an apoptotic tumor cell. To model cell death, the target volume of the apoptotic cell decreases at a constant rate:

$$\frac{\partial V(\sigma)}{\partial t} = -A \; (4.10)$$

where V is the target volume of the cell σ, Ais the death rate of the apoptotic tumor cell. Since we assume that our cells occupy the space of a square, the target volume of the cell was also adjusted such that $S(\sigma) = 4\sqrt{V(\sigma)}$, where S is the target surface of the apoptotic tumor cell σ. We assumed that tumor suppressors can kill more than one target tumor cell at a time.

Parameter Estimation. We assumed that a tumor cell dies after 12 hrs of encountering a CTL cell. This number is relatively low death rate compared to the experimental observation that apoptotic cells die within an hour of encountering cytotoxic immune cells. We justify this choice of parameter value by noting that our tumor suppressor cells kill multiple cells at a time (from 1 to 6), such that the effective per CTL killing rate varies from 12 to 2 hrs [131].

Immune Cell Inhibition

Foxp3+ T regulatory (Treg) cells are an important population of leukocytes that control immunity, mainly by dampening effector T cell responses. We assumed that CTL inhibition occurs either by contact with Trges or via inhibitory molecules secreted by Tregs (e.g., transforming growth factor (TGF)-β, IL-10, and IL-35 that bind to immune cells and result in immunosuppressive effects). We modeled the inhibitory effect of Tregs by having tumor suppressor become inhibited if they were within a given distance of a tumor promoter immune cell. We measure the distance between the center of mass of every tumor promoter cell and every tumor suppressor. If the tumor suppressor is within the inhibition radius of a tumor promoter, then it changes type to inhibited. Inhibited tumor suppressors can become active if they move away from the inhibition radius of the tumor promoter.

$$I_d \geq \sqrt{(X(\sigma_i(supp) - X(\sigma_j(prom))^2 + (Y(\sigma_i(supp) - Y(\sigma_j(prom))^2} \quad (4.11)$$

where $X(\sigma_i(supp))$ is the position of the center of mass of tumor suppressor cell σ_i in the x dimension, $X(\sigma_j(prom))$ is the position of the center of mass of tumor promoter cell σ_j in the x dimension, $Y(\sigma_i(supp))$ is the position of the center of mass of tumor suppressor cell σ_i in the y dimension, $Y(\sigma_j(prom))$ is the position of the center of mass of tumor promoter cell σ_j in the y dimension and I_d is the inhibition radius.

Parameter Estimation. We assumed that the effect of inhibitory molecules secreted by regulatory immune cells into the TME span over six cell diameters ($96\ \mu m$). This assumption is justified because inhibition by T-regs occurs not only by contact, but also by secretion of inhibitory chemokines.

Immunotherapy

In this paper we focused on ICI (Immune Checkpoint Inhibitors) which mirror the effect of immune suppressors. For this reason, and as recently shown in vivo we assumed a tradeoff between immune suppressors density in the TME (which is a function of aerobic fitness, according to our hypothesis) and ICI dosage. When the dosage is personalized to the subject's aerobic fitness the more aerobically fit the subject, the lower dosage of ICI they can be given, with similar tumor reduction outcomes relative to a sedentary subject, but with lower cytotoxicity. We model the mechanism of action of ICI dosage by reducing the inhibition radius of tumor promoters. ICI dosages are represented as different magnitudes of the reduction in the inhibition radius. ICI-associated cytotoxicity is measured as the additional exposure (area under the curve) to IFNγ produced by tumor suppressors with respect to the baseline (no treatment).

Calibration

Effect of aerobic fitness on tumor progression rate.

We simulated our model for a virtual cohort of 200 virtual subjects divided into 10 aerobic fitness levels. Sensitivity analysis on the aerobic fitness parameter detected the upper and lower bounds below and above which changing the fitness parameter has no significant effects on tumor growth. Table 4.2 shows the p-values between the different groups. The model connects variations in fitness levels to variations in anti-tumor immune response and consequently to variations in tumor growth rates. To calibrate the fitness parameter it we matched it to clinical results from breast cancer patients (where the aforementioned aerobic score metric was used, and the study relied on hindsight from pre-diagnostic screening mammograms to estimate tumor growth rates in 14 recently diagnosed patients) [114]. The model yielded a classification of distinct aerobic fitness levels, each of which results in a distinct tumor growth curve (Fig. 4.4A). A similar effect of suppression of tumor growth when inoculation followed endurance exercise was qualitatively demonstrated in pre-clinical studies [132]. These values were then matched to the fitness score reported in [114] (where athletes were scored below 0.5 and sedentary above 2 based on their cardiorespiratory fitness (Fig. 4.4B,C)).

Fitness Parameter Pair	p-value
0.05 - 0.06	0.7376007368052694
0.06 - 0.07	0.17069549494379443
0.07 - 0.08	0.13780438758905694
0.08 - 0.09	0.09456554045876897
0.09-0.10	0.23643686583200896
0.10-0.11	0.11812682730957082
0.11-0.12	0.34610341421792135
0.12-0.13	0.21273526017530378
0.13-0.14	0.10195752002748157
0.-14-0.15	0.03583599939175715
0.15-0.16	0.41735667350462025

Table 4.2. Sensitivity between fitness groups.

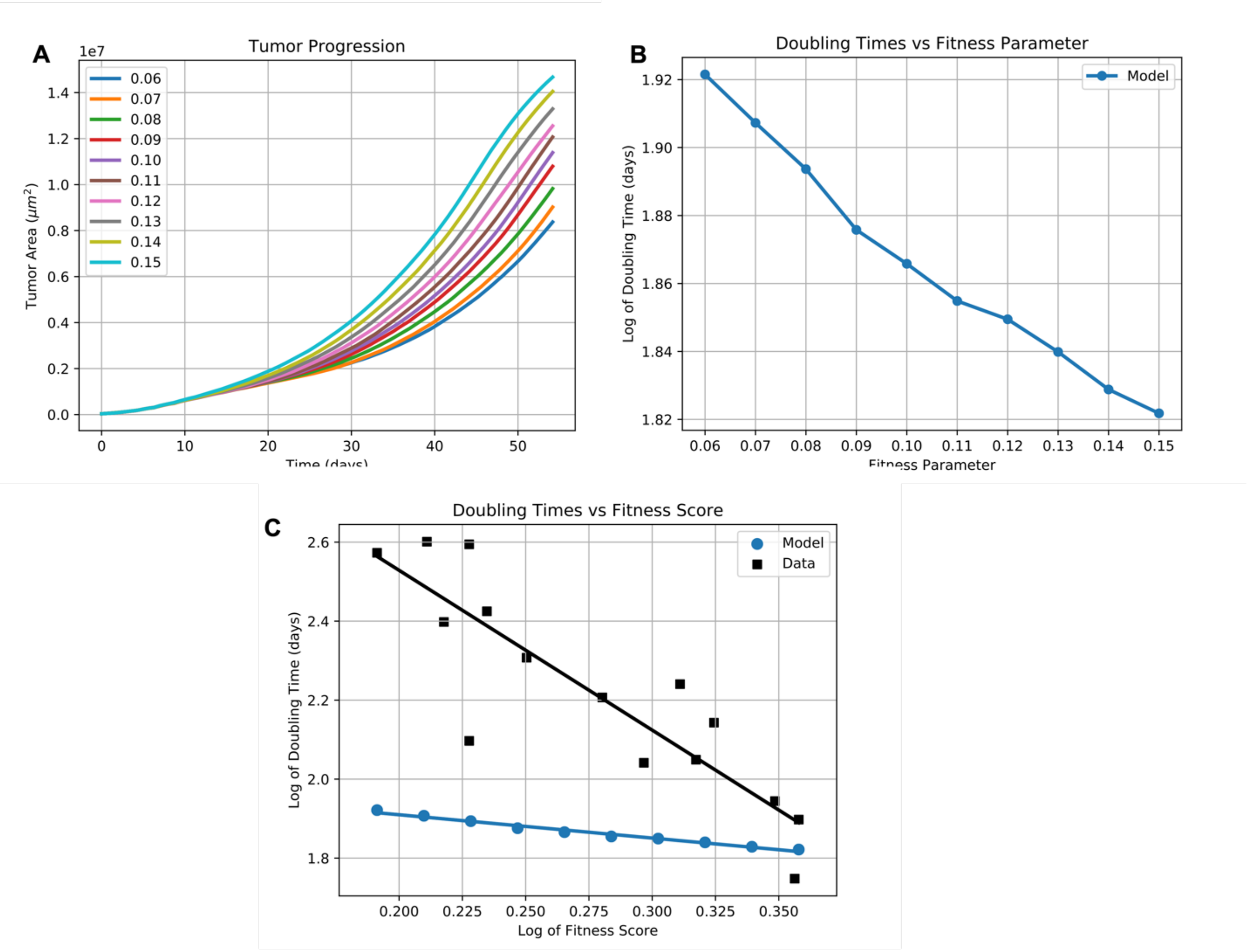

Figure 4.4. Effect of aerobic fitness on tumor progression rate. The model was simulated for 200 virtual subjects, divided into 10 distinct aerobic fitness levels, each with 20 subjects. Each fitness level generated an average growth rate (4A). These average growth rates were plotted against the fitness levels on a logarithmic scale (4B). The model behaves qualitatively in accordance with a similar plot of tumor doubling times vs. fitness levels from a pilot study in 14 recently diagnosed T1 invasive ductal carcinoma post-menopausal patients (4C, “Data”) [114]. The comparison between the two correlations (the observed and the mechanistically generated by the model) can be used to further constrain further calibrations of model parameters.

Prevalence of clinical tumors in athletes vs. non-athletes.

To identify a fitness threshold that can match real-life aerobically fit from sedentary subjects with the fitness parameter in our model we used epidemiological studies on tumor incidence among athletes and non-athletes [111] (Fig. 4.6A). The comparison allowed us to designate as “athletes” populations whose fitness parameter value in our model is below 0.060, and sedentary whose fitness parameter value in our model is above 0.150 (Fig. 4.6B). Lacking additional granularity of staging variations upon detection in both parameter values groups, we limited this calibration to the identification of a biologically significant spatiotemporal scale for the model: the incidence ratio observed in athletes and non-athletes humans is achieved in our model for tumor size of 2.9mm and after 13,000 MCS (equivalent to 54 days in real life, and 7 hrs in our simulation) (Fig. 4.6B). Assuming a clinical (detectable) tumor threshold is 2mm, we can use the incidence ratio to compare the scale of our virtual platform to clinical data: our simulated tumors are at least at a scale of ~ 3:2 (thus within the same spatial order of magnitude of a real tumor).

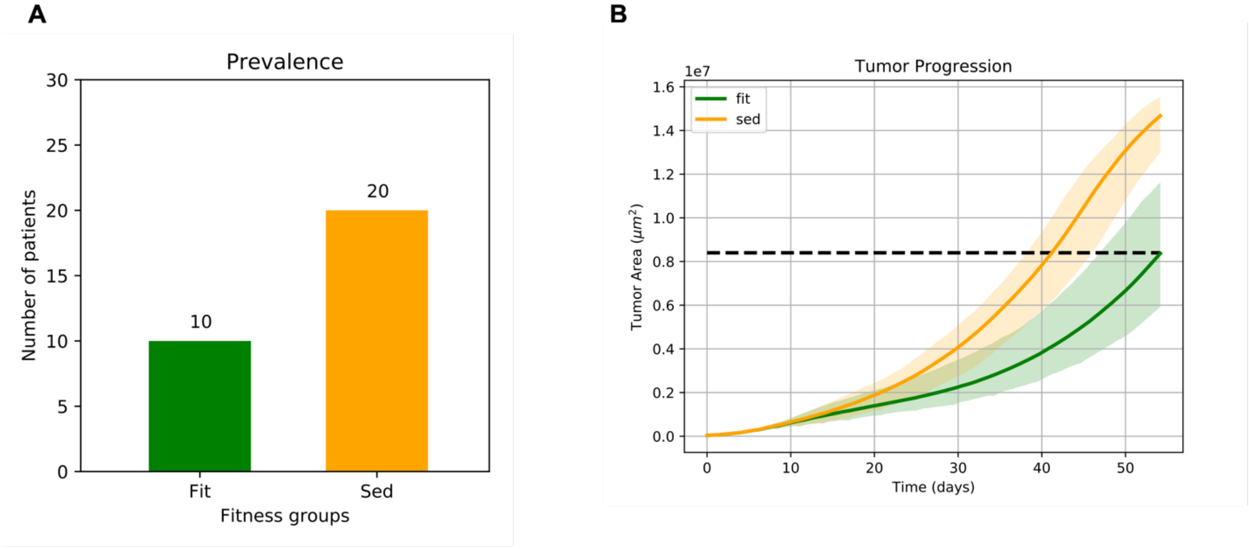

Figure 6. Prevalence of clinical tumors in athletes vs. non-athletes. Epidemiological data shows prevalence of solid tumors in non-athletes to be around twice the prevalence in athletes (6A) [3]. We used this data point to extract a spatiotemporal calibration of the model by running 40 subjects, aerobically fit and

sedentary, and identifying the tumor size (in terms of tumor area) and the time after initiation of 200 cells (in model time steps MCS) in which such a prevalence ratio is achieved (6B). The prevalence ratio allows us to impose a spatiotemporal scale on our model (in this case, a scale of 3:2 between model to reality).

Results

Time series of anti-tumor immune response in the TME.

Our first virtual experiment probes the intricate dynamics in the TME between the tumor and the infiltrating immune cells. Such dynamics is impossible to probe in humans and is hard to observe during a pre-clinical study as it requires significant of redundancy in lab animals (so to achieve high resolution with statistical significance for successive endpoints during the experiment), prohibiting such time and labor-intensive studies. Our simulation generates, with no physical cost, a time series of spatiotemporal snapshots of the TME (Fig. 4.7) that can serve as a platform to test several mechanistic hypotheses on the role and dynamics of different immune cells in ant-tumor immune response, by comparing it to immunohistochemistry slides from different stages of tumor development. While here we focused only on two types of immune cells (“CTLs” and “Tregs”), and two types of signaling fields (“IFNγ” and “chemoattractant”, or L), the platform is modular and can incorporate many more cells and fields (hence more pre-clinical end points) with relatively small modifications.

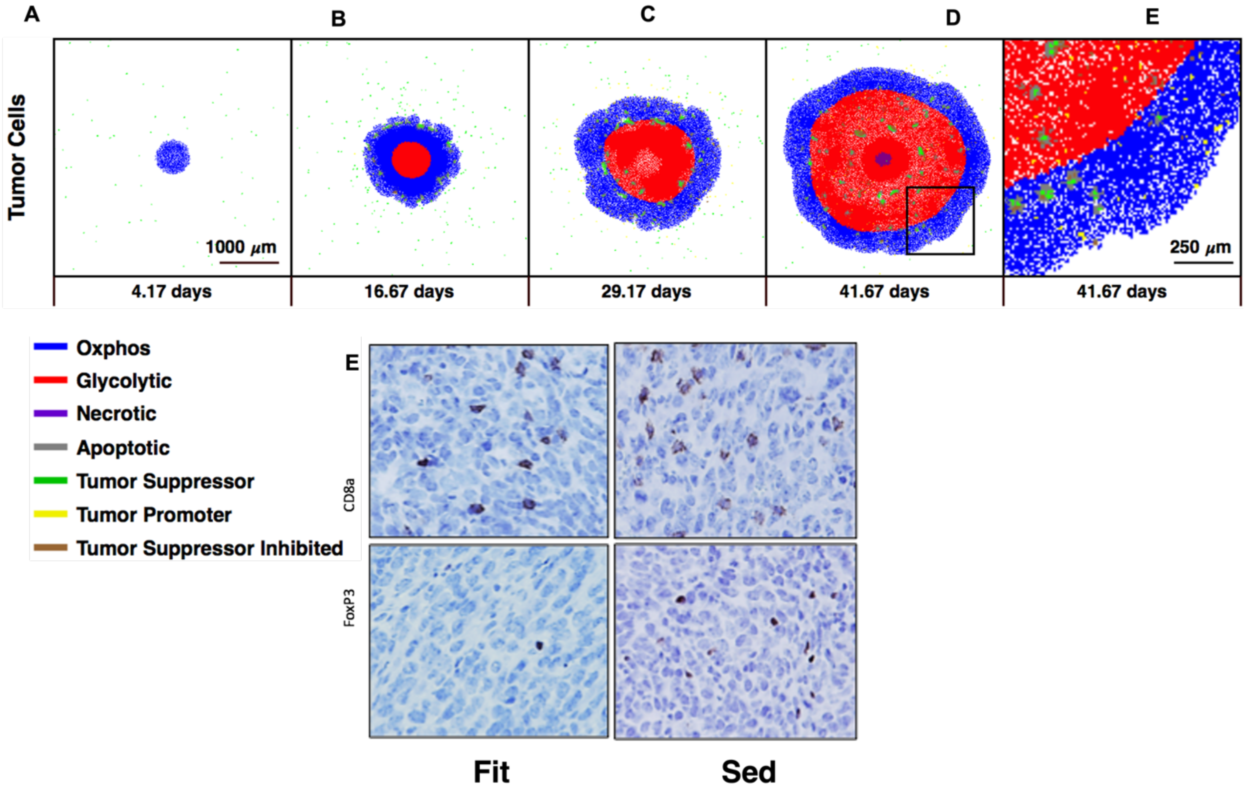
A
B
C
D
E
Tumor Cells
1000 μm
250 μm
4.17 days
16.67 days
29.17 days
41.67 days
41.67 days
Oxphos
Glycolytic
Necrotic
Apoptotic
Tumor Suppressor
Tumor Promoter
Tumor Suppressor Inhibited
E
CD8a
FoxP3
Fit
Sed

Figure 4.7. Time series of TME sections in early stage progression of a solid tumor. To probe the intricate dynamics of anti-tumor immune response in the early stages of a solid tumor progression, the model can yield an observation window into the TME in different stages of growth (7A-D), and can be used to test competing hypotheses on tumor immune cells population dynamics by comparing these snapshots to real life immunohistochemistry end points (7E, [25]), where cross sections from exercised ("FIT") and sedentary ("SED") mice show different intratumoral CD8+/ CD4+FOXP3+ ratios.

Incorporating aerobic fitness into the personalization of immunotherapy.

While showing remarkable success in some patients, immunotherapy treatments can lead to severe autoimmune adverse effects such as myocarditis, pericardial diseases, and vasculitis, including temporal-arteritis and vision loss [111]. To mitigate these adverse effects, careful dosing is essential. There is independent support for our hypothesis on aerobic fitness as a biological variable from pre-clinical studies on the combination of Immune Checkpoint Inhibitors

(ICI) with aerobic exercise [133] and from small pre-treatment exercise intervention in humans [129], and our own clinical pilot study [114] (Fig. 4.8F) . Aerobically fit patients may require lower dosage of ICI than sedentary patients, which may lead to personalization of treatment and reduction of adverse effects. We implemented ICI in our model as an increased efficacy of CTLs killing, by limiting the inhibitory radius of the “Trges”. Cytotoxicity was then quantified with the “IFNγ” field, where the probability of an adverse effect [134] increased exposure to the cytokine. Performing a virtual experiment on both aerobically fit and sedentary virtual subject populations treated with ICI shows how aerobically fit subjects are more prone to adverse effects than their sedentary counterparts without mitigating dosing (Fig. 4.8A,B). Conversely, lowering the dosage of ICI for aerobically fit patients can achieve the same reduction of tumor growth relative to their sedentary counterparts but with a lower probability for adverse effects (Fig. 4.8C,D). In order to translate this result to a clinical setting future studies should identify potential markers of aerobic fitness with which such personalization can be accomplished and clinical studies could test the appropriate dosage of ICI in sedentary vs aerobically fit patients (Fig 4.8E,F,).

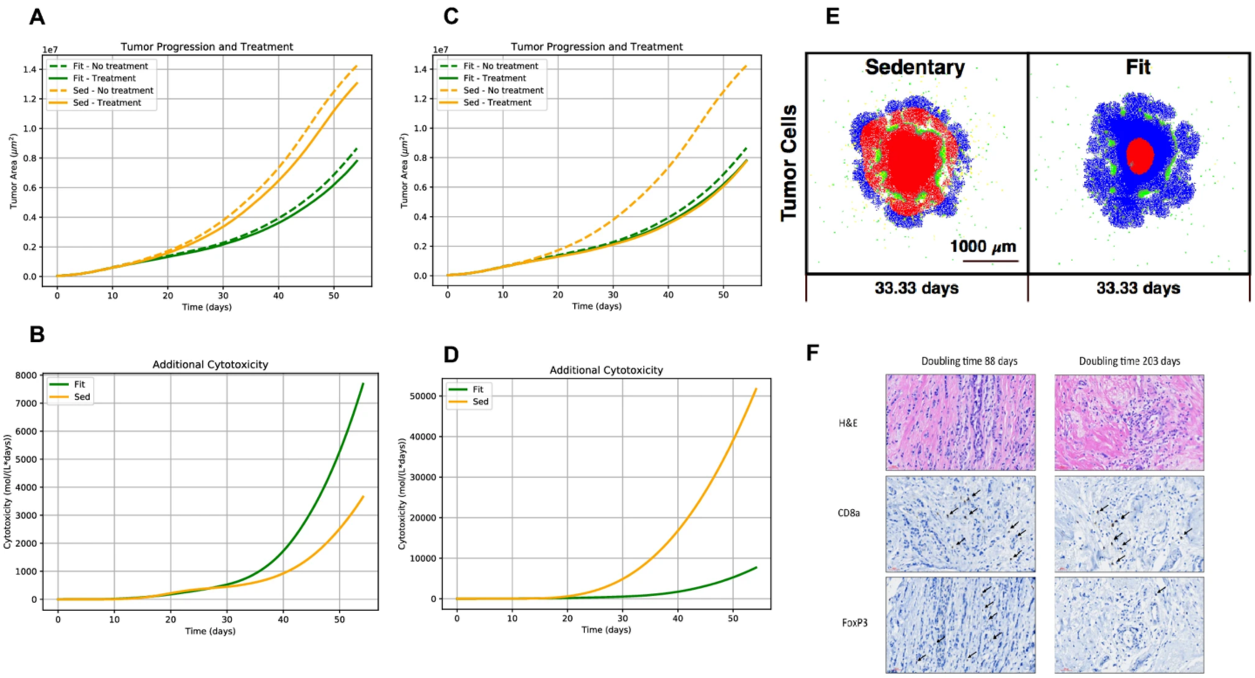

Figure 4.8. Precision immunotherapy. Aerobically fit patients may require smaller dosage of ICI than sedentary patients, which may lead to personalization of treatment and reduction of adverse effects. Without a mitigated dosage, aerobically fit subjects are more prone to ICI adverse effects than their sedentary counterparts (4.8A,B). Lowering the dosage of ICI for aerobically fit patients relative to their sedentary counterparts can achieve the same reduction in tumor growth (4.8C) but with a lower added toxicity hence lower probability for adverse effects (4.8D). As a result of the ICI, the two tumors in 8E (sedentary and fit hosts), treated with high and low dosage, respectively, are of the same size, regardless of their initial immunogenicity. IHC of fast and slow growing Invasive Ductal Carcinomas in human females from the study reported in [114] show respectively lower and higher ratios of CD4+FOXP3+ to CD8+ T cells (4.8F).

Discussion

After calibrating our model with clinical and epidemiological data, we performed two virtual experiments that showcase the potential usefulness of the model as a tool to guide and improve pre-clinical and clinical studies. We have shown how to generate a time series of TME snapshots during anti-tumor immune response, and how to personalize dosing of ICI for aerobically fit patients in order to lower the risk of adverse effects. Further collaboration with cancer biologists and would allow to use the model for improving *in vivo* experimental design and personalization of clinical outcomes

Endurance exercise has been shown to be a systemic modulator of metabolic and endocrinal activities, and, through these, a modulator of immune competence and a natural element in cancer prevention. Here we propose to treat aerobic fitness as a biological variable that can be incorporated into cancer immunotherapy and improve personalization of treatment. The exact underlying mechanisms behind the suppressive effects of aerobic exercise on early tumor progression are currently unknown. Several pre-clinical studies have narrowed the possibility space down to two main hypotheses [135]. The first involves exercise-induced up-regulation of epinephrine that mobilizes NK cells into the TME [112] together with increased trans-signaling of IL-6 [136] as a re-distributing factor (increased adhesion, infiltration and activation). However, these effects were induced on mice by exposing them to voluntary running and their human relevance is suspect [137]. Voluntary running in mice mimics high intensity interval training (HIIT) in humans, and no human, even an elite athlete, can endure the level of HIIT exhibited in those studies [138]. Since there are currently no experiments testing this hypothesis with more human-relevant, lower HIIT levels and since our goal is to use the model for personalization of patient outcomes, our model focuses on the second candidate the human-relevance of which is more significant.

This second hypothesis connects exercise-induced increased hypoxia-tolerance to more efficient anti-tumor immune response and requires chronic endurance training (CET) which can be achieved in pre-clinical exercise oncology with forced running wheels [137]. The idea here is that CET induces hypoxia tolerance in the skeletal muscles and in other tissues, and as a result, TMEs are more susceptible to the degradation of HIF1α [124]. This degradation is an upstream factor in a signaling cascade leading to increased anti-tumor immune efficiency, as HIF1α is known to recruit Trges into the tumor micro-environment via myokine signaling [139]. Our pre-clinical study detected a twofold decrease in intratumoral Tregs/CTLs ratio in exercised mice relative to their sedentary counterparts [132]. Attempts to utilize aerobic fitness as a predictor for patient outcomes are not new. For example, frailty indices (which include aerobic fitness, or lack thereof, as one of their components) have been recently used to predict adverse health outcomes in cancer patients post surgery or chemotherapy [140].

To obtain simulation results in a reasonable time we must limit the computational cost. Consequently, our grid size is currently bounded by 5.0×10^4 cells. The model was simulated as a two-dimensional domain. Specific circumstances may require scaling up to 3D (e.g., angiogenesis). For most clinical endpoints a cross section of the TME may be a good approximation. The model presented here includes only two types of immune cells: tumor suppressors and immune inhibitors (or tumor promoters). We deliberately chose to start from the simplest model under the assumption that any introduction of additional immune cells could increase the ability of the model to replicate observed phenomena, rather than decrease it. Increasing the number of immune cell types and chemical fields would add complexity (and computational cost) to the model. A direct dialogue between model developers and clinicians may help optimize the model for each specific usage. We deliberately calibrated the model solely with quantitative clinical and epidemiological data and limited the usage of pre-clinical studies to qualitatively probing mechanistic hypotheses. The model faces a challenge prevalent in biomedical research in general: spatiotemporal scaling between mice models and human models. If the different components of the model are calibrated separately, series from pre-clinical simulations could be compared to observed clinical endpoints to help to characterize the scaling between murine and human immunological clocks.

Perhaps more than any other therapy, cancer immunotherapy is particularly sensitive to timing [141]. Efforts invested in examination of combination dose scheduling can yield qualitatively significant returns in terms of improved efficacy and decreased toxicity; all without necessitating regulatory approval. The *in silico* platform is a safe playground for such experimentation in dosage scheduling and frequency, as it can easily allow modulation of duration and timing to achieve the most effective treatment, thus ruling out extreme scenarios and refocusing the researcher on an optimal treatment window. Our platform can easily incorporate and test combination of different types of immunotherapies with other standard-of-care therapies [142] and probe potential synergistic effects. For example, since aerobic exercise promotes oxygenation, it can mimic the effects of Anti Angiogenic Therapy, where different aerobic fitness levels can be calibrated to represent different dosage of such a therapy.

Multicellular Spatial Model of RSV-HMPV Co-Infection In Vitro Suggests Viral Competition Cannot Recapitulate Experimental Data

Introduction

Respiratory viral infections are a leading cause of hospitalization and death worldwide [21]. These diseases are caused by viruses, such as influenza A virus (IAV), parainfluenza virus (PIV), respiratory syncytial virus (RSV), rhinoviruses (RV), human metapneumovirus (HMPV), and coronaviruses (CoVs). These viruses often cause seasonal outbreaks and can simultaneously circulate [21]. RSV and HMPV are amongst the most prevalent respiratory viruses and, together, account for 50% of viral infections requiring hospitalization [143]. Both viruses share clinical manifestations and epidemiological characteristics and co-circulate [144]. They can cause acute respiratory tract infections, such as bronchiolitis and pneumonia, and can be life-threatening among high-risk populations, including children and the elderly [145]. There are currently no effective antiviral treatments or vaccines against these two viruses. Although ribavirin is often prescribed against RSV, it is not very effective [145].

RSV is the most common cause of pediatric hospitalizations due to respiratory illness, and the second biggest cause of mortality worldwide after Influenza disease [145]. There are an estimated 33 million cases of RSV annual respiratory infection, 3 million which require hospitalization and 60,000 RSV-related deaths globally [143]. Seasonal outbreaks of RSV occur in the winter [146]. RSV is a single-stranded RNA virus. The viral genome includes 10 genes that encode 11 proteins. Common RSV symptoms include wheezing and difficulty breathing in part due to the inflammatory response, increased mucous production, and infection of cells [2]. Risk factors include age and chronic lung/heart diseases [146].

HMPV was discovered in 2001 and was immediately recognized as one of the viral respiratory pathogens [143]. Epidemiological studies have shown that most children will have already been infected with HMPV by age 5 [6]. HMPV accounts for 15% of pediatric hospitalizations [143]. Adults present mild flu-like clinical symptoms, but it can be more severe in patients with comorbidities. HMPV is closely related to RSV, although RSV tends to cause more severe diseases [146]. HMPV is a negative-sense single-stranded RNA virus. Its genome has 8 genes that encode 9 proteins. Its genomic structure and surface glycoproteins are similar to RSV [143]. The incubation period is between 4 and 6 days, and the course of the infection can last between 5 days and 3 weeks [148].

Both RSV and HMPV can be transmitted via airborne respiratory droplets. Both RSV and HMPV belong to the family of pneumoviruses and both primarily targets ciliated alveolar epithelial cells. Nucleic-acid molecular testing in pediatric patients with lower respiratory tract infections has shown more than one coinfecting virus [149]. Several respiratory viruses are known to participate in simultaneous infections including PIV, RSV, RV, IAV, HMPV, and CoV [150]. Epidemiological studies have shown frequent cases of RSV-HMPV coinfections [145]. These studies have suggested an association between coinfections and increased disease severity. RSV-HMPV coinfections have been associated with an increased risk of ICU admission in children [151]. These results are however inconclusive, and more studies are necessary to establish causal relations. There is still a lack of understanding of how co-infecting respiratory viruses interact among each other and with the host immune response.

The interactions between coinfecting pathogens and the host might be nonlinear and involve multiple spatiotemporal scales, complicating the task of understanding their interaction mechanisms [21]. Respiratory virus-virus interactions can be either synergistic or inhibitory. They often target the same type of epithelial cells and activate the same inflammatory and immune response pathways [21]. PIV can increase IAV pathogenicity by facilitating cell-to-cell spread due to cellular fusion [152]. IAV can inhibit RSV and both RSV and RV can reduce IAV disease severity [153]. Because viral coinfections of the respiratory tract are prevalent, studying viral-viral interactions is necessary to understand their pathogenicity and clinical significance.

Mathematical models have been essential to studying interactions between host and pathogens and between co-infecting pathogens. These models aid in determining the mechanisms driving the infection and identifying regulatory feedback [21]. Single infection models have been used to quantify viral load kinetics and the dynamics of the immune response and to test different therapeutic interventions. Along with the model structure, multi-dimensional parameter variations and perturbation analysis can reveal mechanisms that cannot be inferred directly from the data or are hard to test experimentally [21]. Simple mathematical models describing epithelial cell transitions and free virions have successfully recapitulated viral load kinetics of Influenza infection. Such models can be extended to include explicit representations of the immune system or to study pathogen-pathogen interactions.

The enhancing effect of simultaneous infection with influenza virus and the gram-positive Streptococcus pneumonia bacteria has been one of the most studied respiratory pathogen-pathogen interactions. Serious influenza infection facilitates invasion of opportunistic bacterial pathogens as the tissue in the lower respiratory tract is damaged and the immune response weakens. The maximum synergistic effect is attained if the bacteria invade at the resolution phase of the viral infection (7-days post influenza exposure) [154]. Viral load rebounds and bacterial titers peak 24 hours after exposure [21]. Mathematical models have been instrumental in identifying the mechanisms of interactions between both pathogens. For example, the standard viral kinetic model was paired with a model of pneumococcal replication and the macrophage immune response [155]. The model suggested that bacteria increase the rate of production of the virus and this hypothesis was later tested experimentally [21].

Viral-viral interactions have been subjected to less experimental and quantitative scrutiny. The most notable exception is co-infections involving the human immunodeficiency virus (HIV). HIV interactions with other pathogens can be characterized by general immunosuppression which in turn results in increase pathology of other infectious diseases [156]. In this project, we focus more narrowly on the interactions between respiratory viruses. Viral-viral interactions can be quantified as measurable differences in the course of infection (e.g. viral load, tissue damage) of a virus due to the concurrent infection of another virus [156]. Viruses can interact directly via their gene products or indirectly by changing the host's environment or the immune response [156]. Coinfection exclusion, where infection with a virus prevents cells from getting infected by a secondary virus, is an example of direct virus interactions. Superinfection is known to occur between bacteriophages and retroviruses [156]. Viruses can interact indirectly by breaking down physiological barriers, altering receptor expression modifying the interferon response. They can also interact through adaptive immune mechanisms, like the activation of cytotoxic T cells and antibody-mediated interactions [156].

Mathematical modeling of respiratory virus coinfection has been more limited even though co-infection can be easily modeled by adding no more than 3 additions equations to the standard viral kinetic model [21]. Recently, a model was developed to study the interactions between different respiratory viruses [150]. The model was calibrated used with single infection data of influenza, respiratory syncytial virus, rhinovirus, parainfluenza virus, and human metapneumovirus and was used to test whether competition for target cells was a plausible mechanism of interaction between viruses. The model was able to replicate in vitro data from coinfection data of IAV-RSV and IAV-PIV [145].

Given how prevalent HMPV and RSV single and dual infections are, there is a need for more experimental and qualitative studies that elucidate the mechanism of interactions between both viruses. Here we develop a multicellular mathematical model of RSV-HMPV co-infection in vitro. The model is based on a previous experimental study of RSV-HMPV co-infection in a three-dimensional cell culture ex vivo model. The study showed that HMPV is less pathogenic than RSV and elicits a smaller IFN response. HMPV replication is further inhibited in the presence of RSV, but not the other way around. By neutralizing IFN the inhibition of HMPV was partially prevented. From this data, the authors concluded that the interactions between RSV-HMPV was partially mediated by the IFN response. We used the model to test whether competition of resources was sufficient to explain the observed data and suggest how other possible interactions could be tested both quantitatively and experimentally.

Methods

Model Development Workflow

We implemented a model development workflow to study viral-viral coinfection using a multicellular spatial model (Figure 5.1). We first started with a differential equation model of a single viral infection. The model was calibrated and fit to experimental data to estimate the values of the parameters. Once the parameters of the ODE model were identified, the model was translated into a spatial model following a previously published method [157]. The spatial models were combined to simulate dual infection experiments. Results from the spatial model were compared to additional experimental data for model validation. This project served the dual purpose of showcasing this proposed workflow and investigating potential interactions between HMPV and RSV.

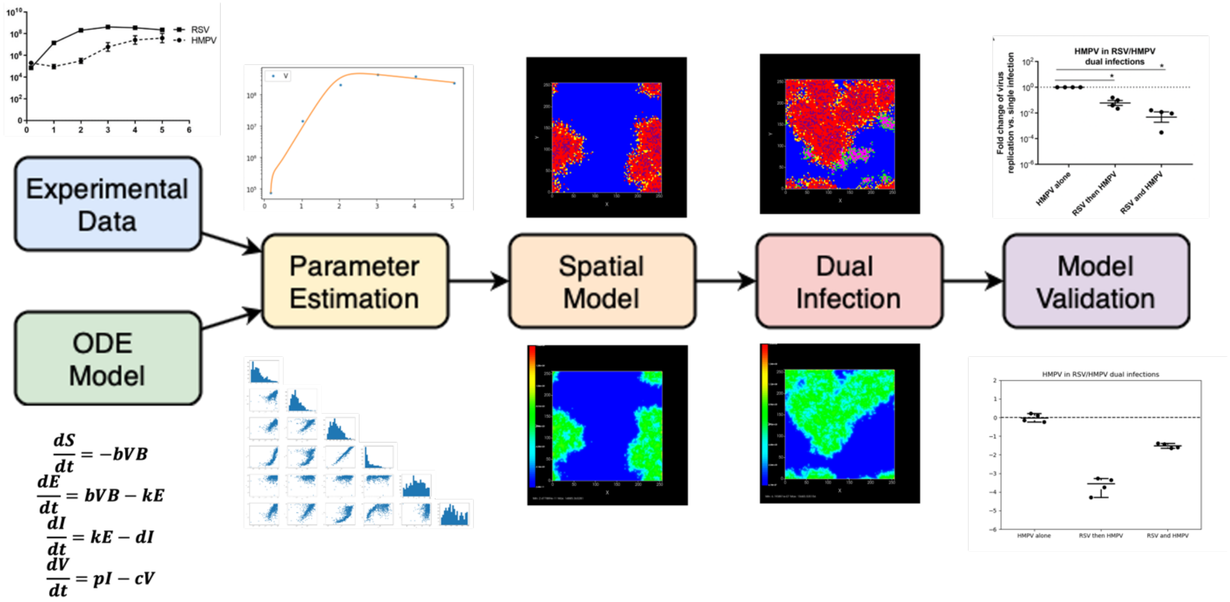
RSV
HMPV
V
HMPV in RSV/HMPV dual infections
Fold change of virus replication vs. single infection
HMPV alone
RSV then HMPV
RSV and HMPV
Experimental Data
ODE Model
Parameter Estimation
Spatial Model
Dual Infection
Model Validation
HMPV in RSV/HMPV dual infections
HMPV alone
RSV then HMPV
RSV and HMPV

$$\frac{dS}{dt} = -bVB$$
$$\frac{dE}{dt} = bVB - kE$$
$$\frac{dI}{dt} = kE - dI$$
$$\frac{dV}{dt} = pI - cV$$

Figure 5.1. Methodological Workflow**.** Workflow to translate experimentally guided ODE models to spatial models. An ODE model is formulated to quantitatively represent mechanistic hypotheses about the target biological system and the experimental data. Model parameters can be estimated and identified using standard optimization techniques. Calibrated ODE models can then be translated to ABMs, minimizing uncertainties about ABM model parameters. ABM models can be used to represent additional hypothesis about the target system. Model outputs can be validated against additional experimental data.

Experimental Data

We used single viral load data collected in an ex vivo model and published in a previous study [145]. Recombinant HMPV group A C-85473 and RSV-Mcherry strains were used, and ex vivo infections were performed in reconstituted 3D airways MucilAir™. Single and dual infections were performed at a MOI of 0.02. Apical washes were collected daily. Viral RNA was quantified from those apical washes by real-time RT-PCR using primers specific to RSV-A and HMPV. RSV peaked between 2-3 d post-infection (pi) at around 108 viral RNA copies. HMPV peaked between 3-5 d pi. Transepithelial electrical resistance, an indicator of tissue integrity, was measured for each infected tissue. None of the viral infections compromised tissue integrity. Cilia beating, an indicator of cytopathogenicity, was measured using confocal microscopy.

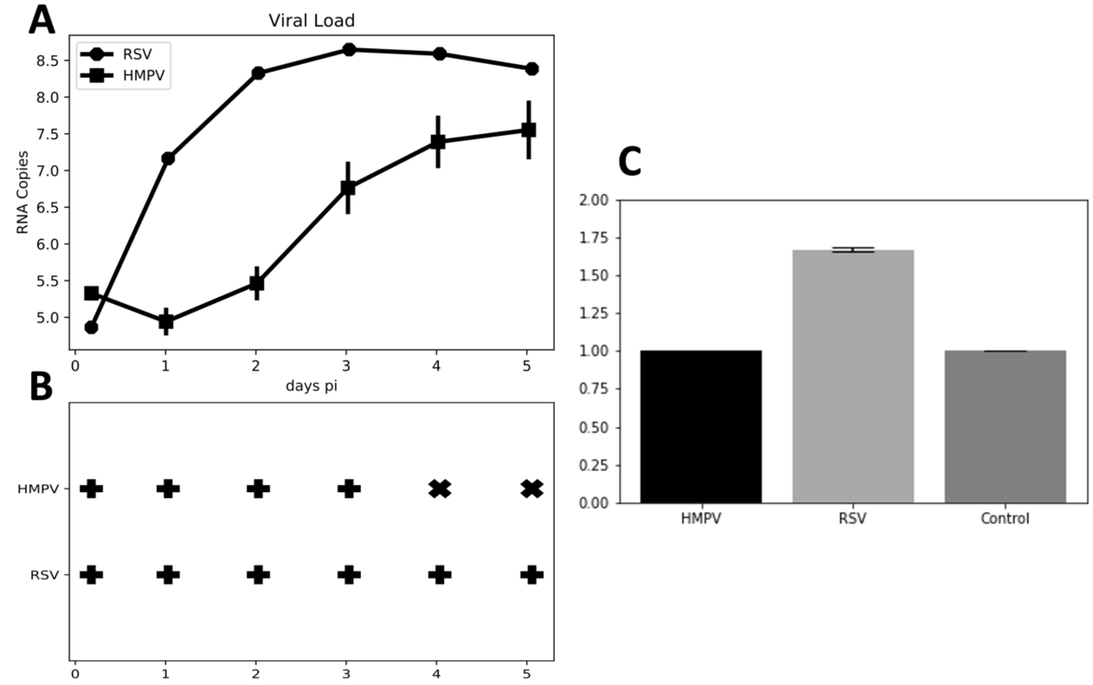

Figure 5.2. Experimental Data for Model Parametrization. A) Viral load data of RSV and HMPV single infection *ex vivo*. Viral loads were collected over 5 days in a multi-cycle experiment. Viral loads were measured in RNA viral copies. B) Cytopathogenicity of each virus was measured using confocal microscopy and determined by cilia beating. C) Tissue resistance was measured to quantify cytopathogenicity Adapted from [145].

Single Infection ODE Model

To quantify the dynamics of single infections, we used the standard viral kinetics model (SVM). The model is composed of five ordinary differential equations. Four of the state variables describe cells in different stages of viral infection: uninfected (S), latent phase (E), virus-producing (I), and dead (D). The fifth state variable describes free infectious virions. The model contains 5 parameters: viral infectivity (b), eclipse phase duration (1/k), mean lifetime of a virus producing cell (1/d), virus production rate (p), and non-specific viral clearance rate (c). Initial conditions such as the initial number of susceptible cells (T0), the inoculum (V0), and the initial number of infected cells (E0) need to be specified as well. The model has been used to study influenza dynamics in humans [21]. Because of the simplicity of the model, multiple biological processes are convoluted into single model parameters. For example, the infected cell death rate (d) encompasses apoptosis of cells, viral cytopathogenicity, and immune cell cytotoxicity. The viral clearance rate (c) encompasses phagocytosis and antibody-mediated neutralization among other processes involved in the loss of viral infectivity [1].

$$\frac{dS}{dt} = -bVB \quad (5.1)$$

$$\frac{dE}{dt} = bVB - kE \; (5.2)$$

$$\frac{dI}{dt} = kE - dI \; (5.3)$$

$$\frac{dD}{dt} = dI \; (5.4)$$

$$\frac{dV}{dt} = pI - cV \quad (5.5)$$

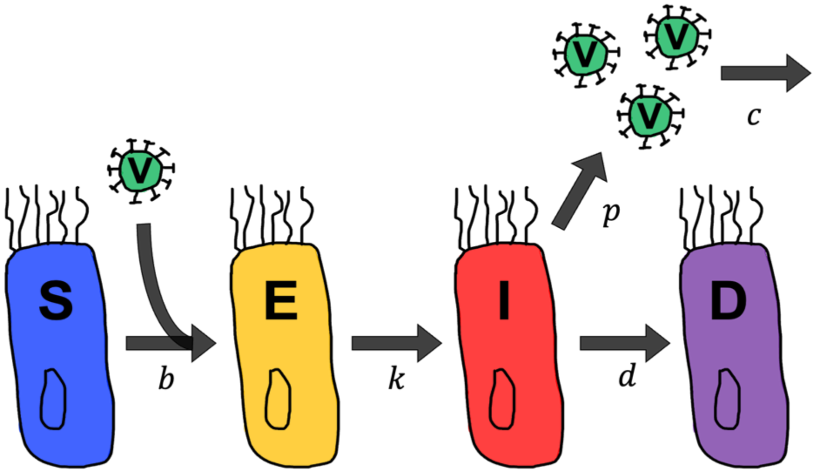

Figure 5.3. Schematic Representation of Standard Viral Kinetics Model. Cells can be in four stages of viral infection: uninfected (S), latently infected (E), virus producing infected (I) and dead (D). The virus (V) released by the virus producing cells (I) infects susceptible cells (S). The model has five rate parameters: viral infectivity (b), eclipse phase (1/k), infected cell death rate (d), virus production rate (p) and viral clearance (c).

Parameter Fitting and Identification

We used the *lmfit* python package to estimate model parameters. We used Dual Annealing for global search and Nelder-Mead for local search. We used the chi-squared distance to perform optimization and minimize the distance between experimental data and model prediction:

$$\chi^2 = \sum_t^T \sum_r^R (D_{i,j} - M_{i,j})^2 \text{ (5.6)}$$

We measured the distance from the model prediction Mi,j to the model prediction Mi,j for every technical replicate $r \in R$ at every time $t \in T$. Because the individual data points in the study were not published, we generated 5 synthetic data sets by assuming that the error was normally distributed and sampling the technical replicates from the reported distributions (Figure 5.2A). We used the *random.normal* from the *numpy* package.

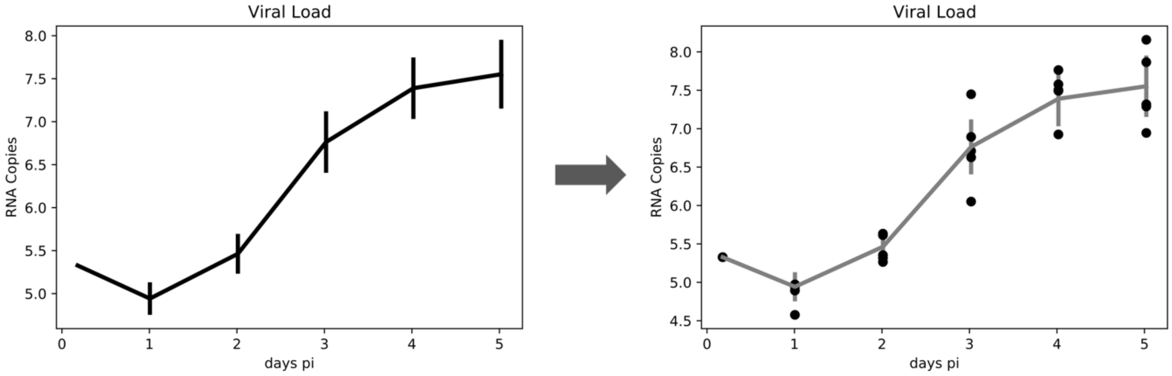

Figure 5.4. Generating Technical Replicates. Five synthetic technical replicates data sets were generated from the reported viral load data. Replicates were generated by sampling from a normal distribution with mean and standard deviation determined by the data reported at each time point.

We nondimensionalized the cell population by setting the initial number of susceptible cells (S) to 1. We adopted two different strategies to fit model parameters: 1) Using the full viral load data and including the least number we estimated the inoculum (V0) and the remaining parameters (b, k, p, c and d). Since HMPV was reported to have no cytopathic effect, we set the infected cell death rate to zero. 2) Using viral load data from the first day onwards, we fixed the inoculum to zero (V0 = 0) and the ratio of the initial number of infected cells based on the reported MOI (E0 = 0.0196). Because the experiment was a multicycle in vitro experiment, we assumed that the viral clearance rate was negligible (c = 0). Using TEER and cilia beating data (Figure 5.2B,C), we fixed the cell death rate to be d= 0 in the case of HMPV and d = 0.4 in the case of RSV, such that 75% of the cells were dead by the end of the simulation.

1st Strategy				2nd Strategy			
HMPV		RSV		HMPV		RSV	
V0	Fitted	V0	Fitted	V0	0	V0	0
E0	0	E0	0	E0	0.0196	E0	0.0196
b	Fitted	b	Fitted	b	Fitted	b	Fitted
k	Fitted	k	Fitted	k	Fitted	k	Fitted
d	Fitted	d	Fitted	d	0	d	0.4

p	Fitted	p	Fitted	p	Fitted	p	Fitted
c	Fitted	c	Fitted	c	0	c	0

Table 5.1. Fitting strategies

Single Infection ODE to ABM model translation

To translate the single infection ODE model into a multicellular spatial agent-based model (ABM), we followed a previously published method [157]. Rate equations in the ODE model were translated into an individual cell transition probability. Some of the parameters of the model also need rescaling based on the size of the cell population in both the ODE and the ABM models. The transition probabilities were assumed to follow a Poisson distribution. For an individual cell located in position x the transition probabilities were as follow:

$$\Pr(S(x) \rightarrow E(x)) = 1 - e^{-\frac{bV(x)}{S0}} \quad (5.7)$$

$$\Pr(E(x) \rightarrow I(x)) = 1 - e^{-k} \quad (5.8)$$

$$\Pr(I(x) \rightarrow D(x)) = 1 - e^{-d} \quad (5.9)$$

The parameters of the transition probabilities were adopted from the ODE model. S_0 corresponds to the initial number of susceptible cells in the ABM model. The ABM translation also required spatializing the free virions V→V(x). The reaction-diffusion equation specified the change in the amount (or concentration) of free virions as a function of time and location.

$$\frac{\partial V(x)}{\partial t} = D\frac{\partial^2 V}{\partial x} + \frac{p}{A(x)} - cV(x) \quad (5.10)$$

The production of free virions at a particular location x was determined by the production rate in the ODE model divided by the surface area of the cell that occupies that position. This was equivalent to assuming that the production of free virions was uniform over the cell surface. We assumed a one-to-one correspondence between viral RNA and free infectious virions. The viral clearance rate was adopted from the ODE model. Spatialization required introducing an additional parameter: the diffusion coefficient of free virions, D. This parameter can often be estimated from the literature or calculated from the molecular weight of the virus using the Einstein-Stokes equation. The ABM was implemented in CompuCell3D [37].

Coinfection ABM model

To model viral-viral coinfection, we combined the two independently calibrated single infection models under the assumption that the only interaction between viruses is competition for target cells. We excluded the possibility of two viruses infecting the same cell (superinfection). The probability of target cells becoming infected depended on the free virions of RSV or HMPV in their vicinity. The transition probabilities were the same as in Equations (5.6)-(5.8). Both viruses diffused in the extracellular environment according to Equation (5.9). We assumed no interaction between viruses in the extracellular environment. We further assumed that both viruses had the same diffusion coefficients.

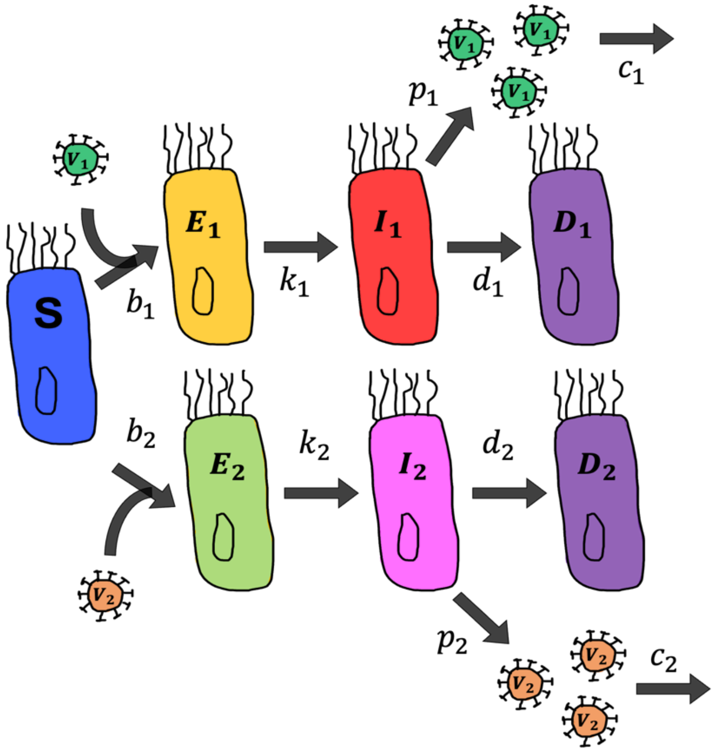

Figure 5.5. Coinfection Model.

Results

Single Infection ODE Model Fitting and Parameter Identification

We fit SVM (Equations 5.1-5.5) to RSV viral load data using fitting strategy 2 (Table 5.1). Parameter estimates are reported in Table 5.2. The fitted model recapitulated the experimental data (Figure 5). The viral load increased rapidly at 1 d pi from 10^5 to 10^7 viral RNA copies. Viral load peaked at 3 d pi at 10^8 dpi. Because viral clearance was fixed to reflect the multi-cycle experimental setting, the viral load saturated and was unable to capture the slow decay observed between 4-5 d pi. No quantitative data of the dynamics of infection in the cell culture was collected. Under the target cell limited assumption, the model suggests that all susceptible cells (S) become infected by 1.5 d pi. The number of latently infected cells I peaks at 1 d pi, and the number of virus-producing cells peaks (I) peaks at 1.5 d pi. The death rate was fixed to achieve around 80% of cell death (D) at the end of the simulation.

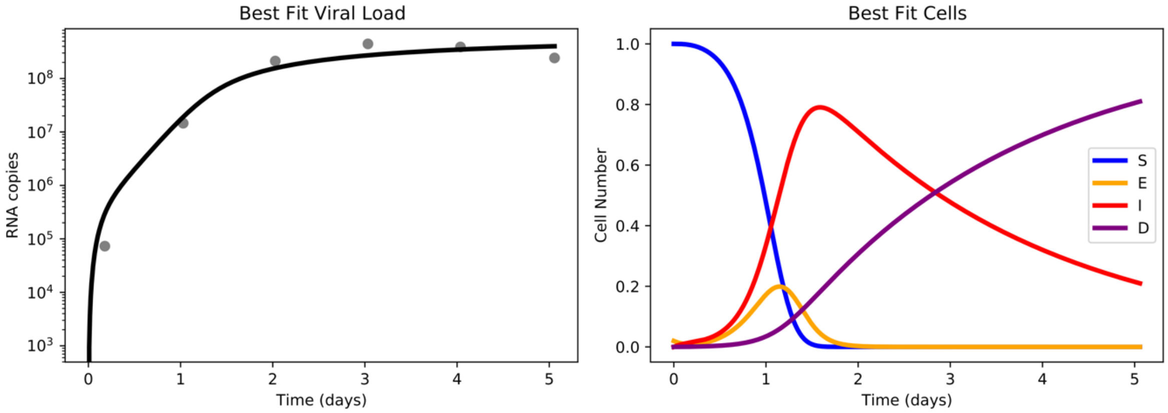

Figure 5.6. Best Fits RSV Viral Load Data. SVM model parameter were estimated by fitting the RSV single infection viral load data. Strategy 1 best fit is shown and resulting infected cell dynamics as predicted by the model.

We also fit SVM (Equations 1-5) to HMPV viral load data using fitting strategy 2 (Table 5.2). Parameter estimates are reported in Table 5.2. The fitted model recapitulates the experimental data (Figure 5), except the first data point which was left out of the parameter fit as described above. The viral load increases slowly at from 0 to 3 dpi from 10^5 to 10^6 viral RNA copies. Viral load peaks at 5 dpi at 10^8 dpi. Under the target cell limited assumption, the model suggests that all susceptible cells (S) become infected by 3 dpi. The number of latently infected cells I peaks at 3 dpi, and the number of virus-producing cells peaks (I) peaks at 5 dpi. The death rate was fixed to 0 based on cilia beating data which suggest HMPV was not cytopathogenic.

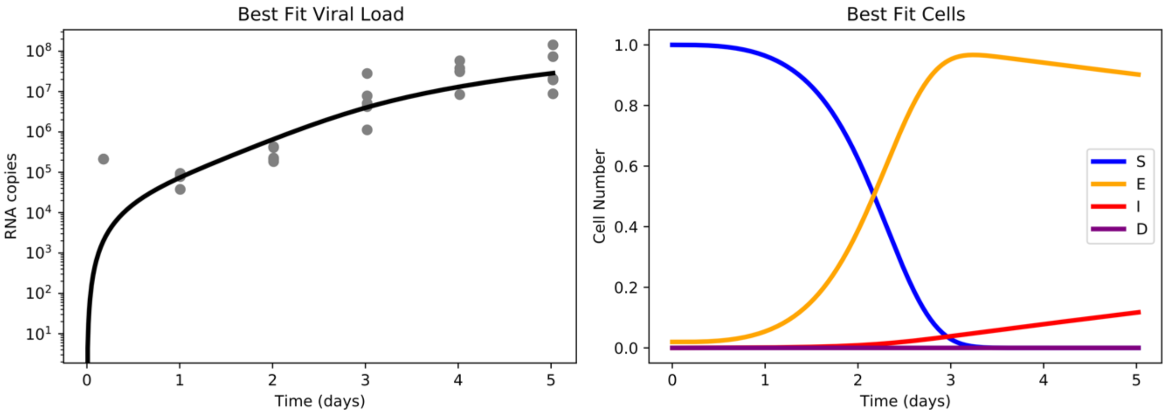

Figure 5.7. Best Fits HMPV Viral Load Data. SVM model parameter were estimated by fitting the HMPV to single infection viral load data. Strategy 1 best fit is shown and resulting infected cell dynamics as predicted by the model.

Parameter	RSV	HMPV
V0 (Fixed)	0.0	0.0
E0 (Fixed)	0.0196	0.0196
b	1.8772e-07	1.6028e-06
k	7.03285952	0.04166667
p	1.9827e+08	1.5549e+08
d (fixed)	0.4	0.0
C (fixed)	0.0	0.0

Table 5.2. Parameter Estimates Best Fits

Single Infection ABM Model Translation

After fitting the model to data and identifying the model parameters, we spatialized the ODE model following a previously developed method that translates ODEs to multicellular ABMs [157]. The spatialized model recapitulated the dynamics of the ODE model. Delays in the ODE model were associated with stochastic individual cell transitions and with the local diffusion of free virions in the extracellular environment. Note that, despite the delays, ABMs reach the same steady states as the ODE model. In the RSV spatial model, cell dynamics were delayed by about 1 d (Figure 5.8). All cells became infected within 2.5 d pi (~1.5 d pi in the ODE model), latently infected cells peaked at 2 d pi (~1 d pi in the ODE model), and virus-producing cells peak at 3 d pi (~2 d pi in the ODE model). The viral load increased slightly slower, from 10^5 to 10^7 viral RNA copies at 2 d pi and peaked at 10^8 viral RNA copies at 5 d pi. The spatial simulation was initiated at the same MOI as the ODE model and 1% of the cells were infected at the beginning of the simulation. When cells started to produce virus, cells in the vicinity of the originally infected cells became infected as well, creating small lesions called viral plaques. By 2 d pi, plaques started to fuse, and the rate of new infections began to decrease.

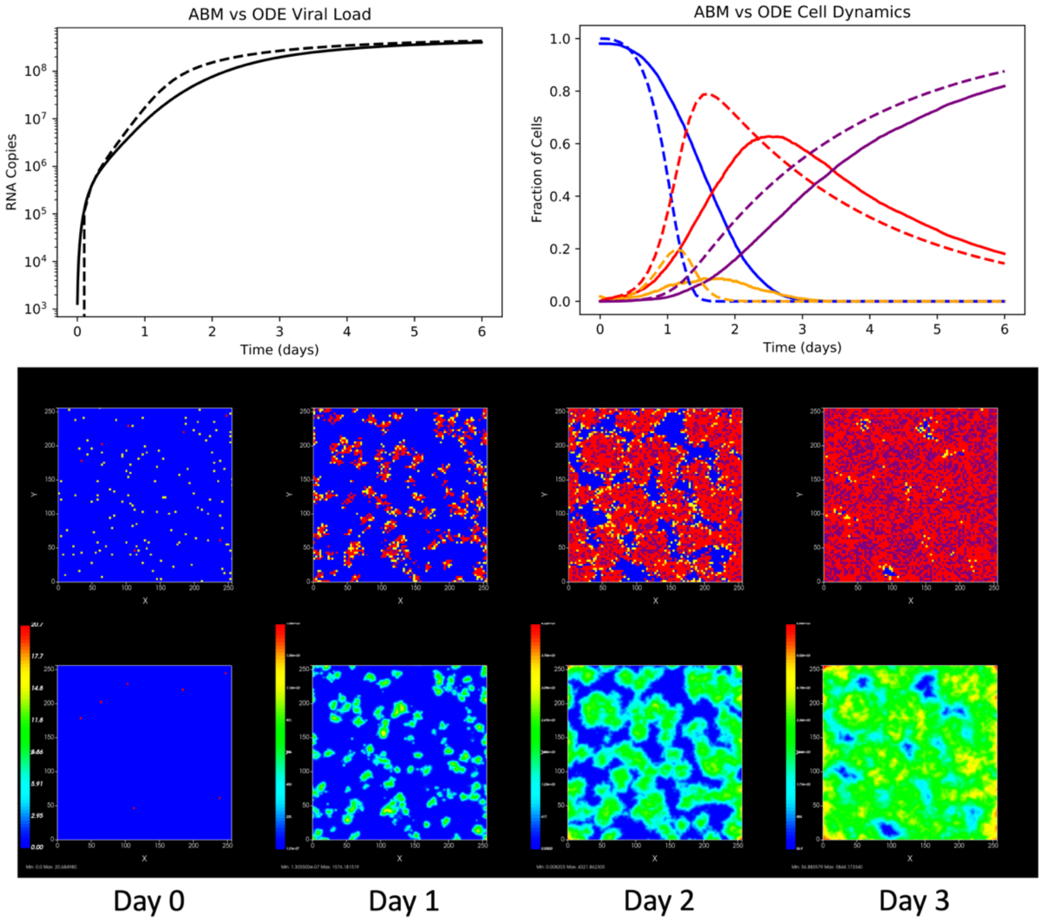

Figure 5.8. RSV single infection spatial ABM simulation. Comparison of RSV viral load and infected cells predicted dynamics in the ODE (dashed) and the ABM (solid). ABM dynamics are slightly delayed. Spatially resolved simulations show characteristic viral plaque formation.

In the HMPV spatial model, cell dynamics were significantly delayed by more than 3 d (Figure 5.8). Unlike in the ODE model where all cells are infected by 3 d pi, 40% of the cells remain uninfected by 6 d pi in the spatial model. Whereas in the ODE model latently infected cells peak at 3 d pi, cells were still entering the latently infected stage by 6 d pi in the spatial model, and the curve was increasing at the end of the simulation. In the ODE model, around 20% of the cells were in the virus-producing stage by the end of the simulation whereas less than 10% were virus-producing in the spatial model. The model suggested that viral load dynamics were also significantly delayed, an increase from 10^4 to 10^6 viral RNA copies over 5 days (3 days in the ODE model). The spatial model revealed small regions of viral plaques containing a small number of virus-producing cells at their center. Unlike in the RSV model, the model derived HMPV plaques did not fuse and remained isolated. The significant slowdown in the dynamics could be, in part, explained by the estimated long eclipse phase (around 60 hours).

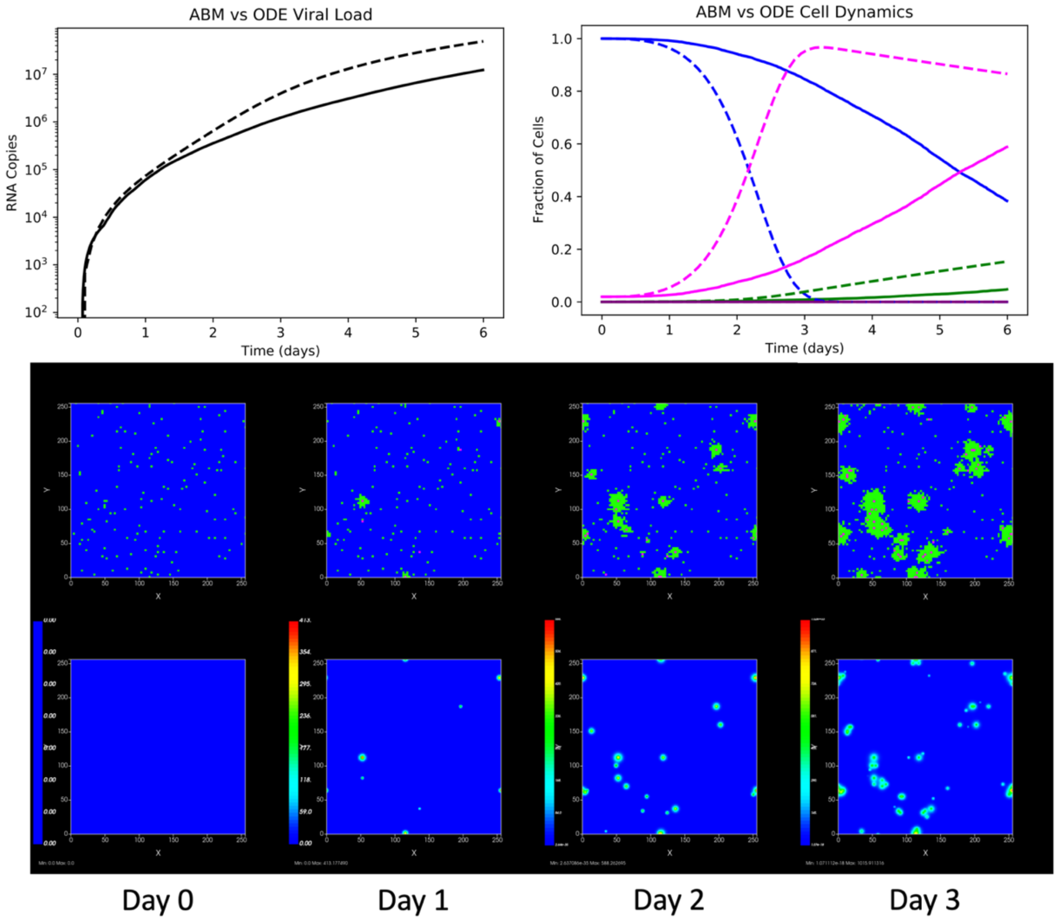

Figure 5.9. HMPV single infection spatial ABM simulation. Comparison of HMPV viral load and infected cells predicted dynamics in the ODE (dashed) and the ABM (solid). ABM dynamics are slightly delayed. Spatially resolved simulations show characteristic viral plaque formation.

Coinfection ABM Model

We combined the two single-infection spatial models to simulate co-infection of the same tissue by RSV and HMPV. We initialized the simulation with combined initial conditions from both ODE models: around 2% of the cells were infected at the beginning of the simulation (1% by HMPV and 1% by RSV). The rest of the parameters were adopted from the single infection model. Because the dynamics of RSV are faster than HMPV, RSV was able to outcompete HMPV. The dynamics of RSV remain unaffected by the presence of HMPV: latently infected cells peak at 2 dpi and virus-producing cells peak at 3 dpi. The dynamics of HMPV are significantly inhibited by the presence of RSV: latently infected cells peak at 3 dpi at around 10% compared to 20% of cells latently infected at that time in the single infection model and 60% latently infected at the end of the simulation. Viral load is also significantly decreased: from 10^8 viral RNA copies at 6 dpi to 10^6 in the dual infection. The spatial model shows how RSV viral plaques grow by day 1 and fuse by 2. HMPV viral plaques show at day 2 but are only able to infect the isolated areas of the simulation that have not been already infected by RSV. By the end of the simulation, the whole simulation domain is infected by either RSV or HMPV.

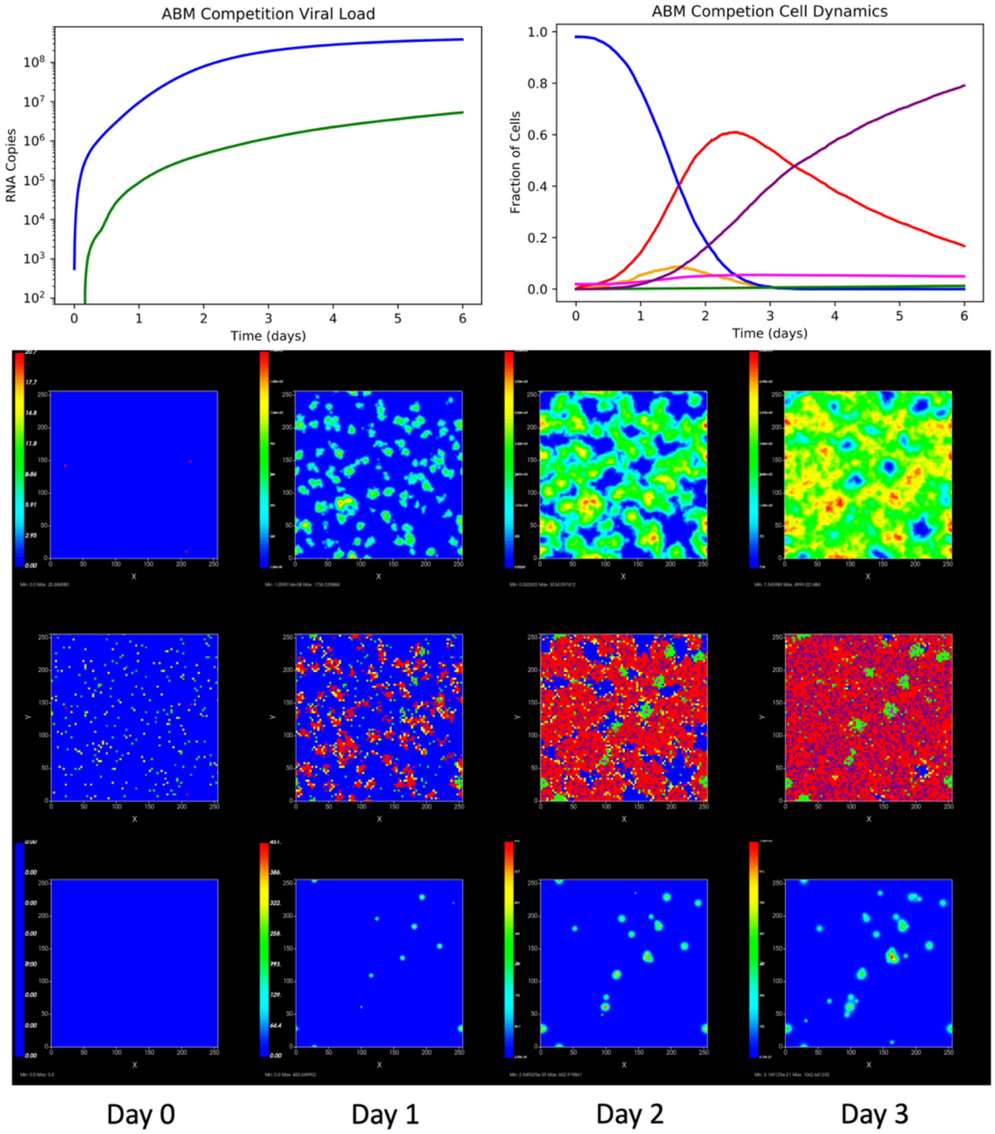

Figure 5.10. RSV-HMPV Dial Infection Spatial ABM Simulation. Coinfection was modeled and simulated by combining the two single infection ABM models. Spatial parameters (diffusion coefficient) were assumed to be the same for the two viruses. Other model parameters and initial conditions are adopted from the ODE estimated model parameters. ABM produces viral load, infected cell and spatial resolved coinfection dynamics that can be compared to further experimental data.

ABM Model Validation

By excluding the possibility of viruses infecting the same cell, competition for target cells was built into the model as the main mechanism of interaction between RSV and HMPV. To quantitatively validate this hypothesis, we compared simulation outcomes to additional data on the viral load fold change during co-infection. Viral loads were compared under different conditions: 1) when both viruses infected the tissue at the same time (RSV and HMPV), 2) when RSV infected the tissue 2 days after HMPV (HMPV then RSV) and 3) when HMPV infected the tissue 2 days after RSV (RSV then HMVP) (Figure 5.12). Co-infection viral loads were compared at 5 dpi with single infection viral loads. The experimental data shows that RSV viral load is unaffected by the presence of HMPV regardless of whether RSV infects at the same time or 2 dpi with HMPV (Figure 12A). The viral load of HMPV decreases 2 orders of magnitude when HMPV and RSV infect at the same time. Interestingly, the viral load decreases 1 order of magnitude when HMPV infects 2 dpi with RSV (Figure 12B).

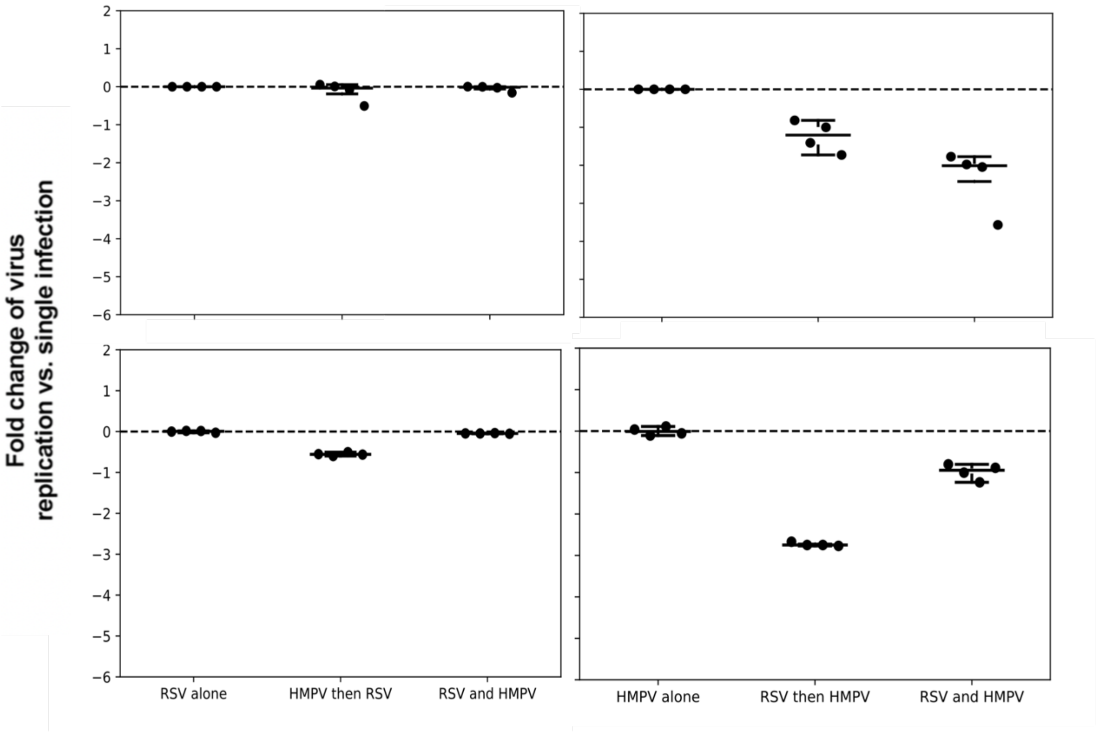

Figure 5.11. Coinfection ABM Model Validation. Viral load fold changes in single and coinfection experiments *ex vivo*. RSV is mostly unaffected by the presence of HMPV. HMPV is significantly inhibited by coinfection with RSV. The inhibition is stronger when both viruses coinfect tissue at the same time, than when HMPV infects the tissue two days after RSV. Adapted from [4].

We simulated all these different experimental conditions in the spatial model for 4 technical replicates (to match the number of replicates in the experimental data). In the case of RSV, the spatial model recapitulated the change in the viral load data (Figure 5.11). When RSV and HMPV infect the tissue at the same time, the viral load remains unchanged with respect to the single infection. When RSV infects 2 dpi with HMPV, the viral load changes decreased by about 1 order of magnitude, which is slightly higher than the observed experimental data. Variability between replicates is also smaller than the experimentally observed variability. This discrepancy suggests that HMPV is slightly more effective at infecting the tissue in the spatial model than in the experimental system or that a missing mechanism is involved in inhibiting HMPV in the presence of RSV.

In the case of HMPV, the model produced a slightly smaller fold change of HMPV when both viruses infect at the same time: 2 orders of magnitude in the experimental data versus 1 order of magnitude in the simulation. The variability is also smaller in the simulation than in the experimental data. Again, this discrepancy can be explained by two possibilities: either HMPV is slightly more infectious in the model than the experimental systems or a missing mechanism inhibits HMPV in the presence of RSV. The case where RSV infects 2 dpi with HMPV is the more interesting case because the fold change is smaller (1 order of magnitude) than when both viruses infect at the same time (2 orders of magnitude). The spatial model predicts an even bigger change in viral load (around 3 orders of magnitude) when HMPV infects the tissue 2 dpi with RSV. This discrepancy cannot be explained solely by a mismatch between the parameters of the model and the rates in the biological system.

Discussion

In this project, we implemented a proposed workflow to develop spatial agent-based models (ABMs) from the calibrated ODE model. We used the standard viral load model (SVM) to describe and quantify the viral load dynamics of RSV and HMPV single infections in an *ex vivo* model. We fixed some of the model parameters based on assumptions about the experimental design and the cytopathogenicity data (Table 5.1). We then estimated the remaining parameters for both viruses (Figure 5.6-5.7 and Table 5.2). We then translated the ODE models into spatial and multicellular ABMs. The translation was achieved by turning the rates in the ODE into transition probabilities for individual cells. The translation implies abandoning the "well-mixed" assumption built into the ODEs. Cell transitions become stochastic processes and exposure to free virions is dependent on local diffusion. The net effect of this translation was a slowdown in the dynamics of the ABM with respect to the ODEs. We showed that the dynamics of RSV were delayed by 1 day, whereas the dynamics of HMPV are delayed by about 3 days. The magnitude of the delay was dependent both on the size of the simulation domain (e.g., how many cells are being simulated) and the diffusion coefficient of the virus. A future direction for this project would be to quantify how the delay affects the overall simulation outcomes and the conclusion that can be drawn. The spatial simulations reproduced the observed patterns of viral plaques *in vitro*.

We combined the single infection ABM models to simulate RSV-HMPV coinfection in the same tissue. The coinfection model assumed that the only interaction between viruses was the competition of target cells. To quantify the magnitude of this inhibition, we compared simulation outputs to experimental fold change data during co-infection. We showed that the model was able to recapitulate RSV fold data and HMPV fold change data (when both viruses infect at the same time). Small discrepancies could be explained by a slightly higher infectivity of HMPV in the model or by a missing mechanism by which RSV inhibits HMPV. However, the model is currently unable to recapitulate experimental data when RSV infects earlier than HMPV. This discrepancy cannot be explained by inaccuracy in model parameters and, thus, suggests that the competition alone may be insufficient to explain the experimental data.

IFN mediated interaction is one type of viral-viral interaction where infection by one virus could inhibit the replication of a second virus by activating the interferon pathway. The experimental study that this project was based on showed that RSV elicited a stronger IFN response than HMPV and that HMPV was more sensitive to IFN than RSV. The antiviral response of IFN has been previously modeled by adding additional terms to the SVM [19]. For example, the model could be extended to include a state variable explicitly describing IFN titers. The state variable could have inhibitory effects on other variables of the model, typically the viral production rate (p) or the duration of the eclipse phase (1/k). This extension has not necessarily resulted in better fits of the SVM model to the data, mostly because viruses have ways of shutting down the IFN response or because the response can be implicitly correlated with the other parameters of the model [19].

In the context of co-infection, we could potentially explore interactions between viruses without the need of adding state variables to the SVM model. As a future direction of this project, we propose exploring the interaction between viruses by modeling direct inhibition of one virus

(virus 1) of any of the viral cycle steps of the second virus (virus 2) (Figure 5.12). For example, virus 1 could decrease the infectivity, extend the eclipse phase, or reduce the production of virus 2. The model structure and its functional form could suggest the types of interaction driving the dynamics of the biological system. Virtual experiments could be performed to suggest what experiments maximally differentiate between different interactions. Finally, such models could potentially clarify the clinical and epidemiological significance of viral co-infections.

A

$$\frac{dS}{dt} = \sum_{i=1}^{2} -f_i(V_{j\neq i})b_iV_iS$$

$$\frac{dE_i}{dt} = f_i(V_j)b_iV_iS - f_i(V_j)k_iE_i$$

$$\frac{dI_i}{dt} = f_i(V_j)k_iE_i - d_iI_i$$

$$\frac{dD_i}{dt} = d_iI_i$$

$$\frac{dV_i}{dt} = f_i(V_j)p_iI_i - c_iV_i$$

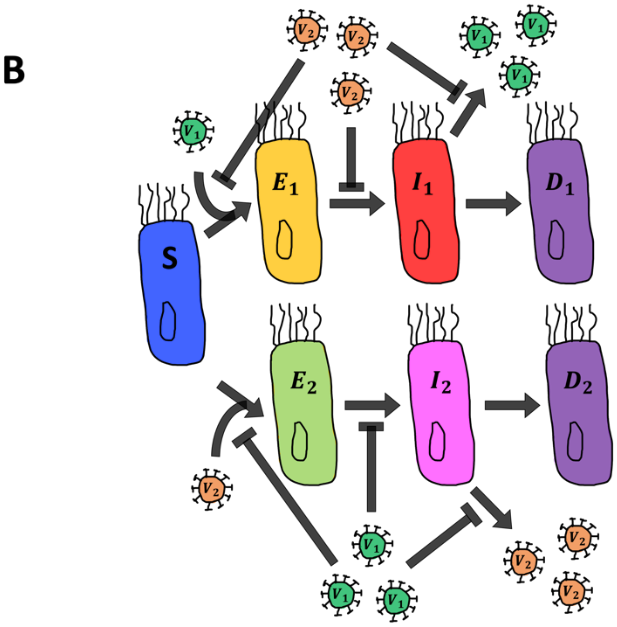

Figure 5.12 Mathematical Models of Possible Viral-Viral Interactions. Viral interactions can be modeled as each viruses modulating the parameters of the other virus. Mechanistic hypotheses about these interactions will determine which parameters are modulated and the functional form of the inhibition.

Appendix A

Modularity and Extensibility of Viral Infection Framework

Agent-based models are particularly well suited for modeling complex biological systems that span over multiple spatiotemporal scales. The architecture of ABMs can be organized in modules that resemble the functional units interacting in biological processes [7]. We have developed a modular framework to facilitate modeling of viral infection in epithelial tissue [159]. The framework supports independent development of functional modules to represent the different processes that determine viral infection dynamics. The original framework included epithelial cell modules, immune cell modules and molecular transport modules. The epithelial modules modeled processes such as viral internalization and replication, virally induced cell and cytokine production and release. Immune cell modules modeled activation, chemotaxis, and clearance of infected cells. Transport modules modeled diffusion of infectious virions and cytokines in the extracellular environment.

One of the key elements left out in the original publication was the Type I interferon response. Type I Interferon are a type of signaling molecules that virally infected cells produce to activate their internal response and to alert neighboring cells. The activation of the IFN pathway and the interferon stimulated genes lead to a persistent antiviral state in epithelial cells by blocking viral entry, downregulating viral replication, and blocking export of viral progeny [23]. By not incorporating explicitly the IFN response, we implicitly assumed that the IFN response is negligible or constant through the course of the infection [19]. The effect of interferon was implicitly represented in other parameters such as the length of the eclipse phase, the rate viral replication or the rate of viral export.

We have recently proposed a methodology to translate calibrated and validated cellular ODE systems into ABMs. The method translates the rates described by the ODEs into transition probabilities for individual cells. The method requires leaving behind the assumption built into ODEs that the biological compartments described by the equations are well-mixed and that dynamics can be averaged over the whole population [157]. Local diffusion of molecules and signals requires introducing additional transport parameters such as the diffusion coefficient and the decay rate of molecules. Other processes, such as rates of recruitment might require introducing additional models (such as seeding or queuing) and additional parameters [158].

Following this methodology, we translated an ODE model of IFN response to viral infection into ABM in CompuCell3D. The modeled had been previously calibrated in validated against data from Influenza infection [23]. The model described key intermediates of the IFN signaling pathway, intracellular recognition, paracrine signaling and regulation of viral replication by IFN. The multiscale and multicellular version of the model qualitatively replicated plaque growth patterns *in vitro*. Sensitivity analysis over the parameters of the model showed regimes that led to viral containment and uncontrolled growth. The model also suggests that the parameters of IFN signaling are identifiable in experimental conditions that lead to viral arrest.

In this project, we combined elements of the original viral infection model with the IFN model using the tools of the viral infection framework. The purpose was to add immune cell response to the IFN model and show how the modules published along the framework could be complemented by independently developed modules. First, we turned the components of the IFN model into modules of the framework. The modules are publicly available as add-on libraries that could be employed by users of the framework looking to explore the effects of IFN response with or without other components of the immune response (Figure A.1). Secondly, we added modules one at the time to construct a model of viral infection that included elements from both previously published models. Thirdly, we investigated how each of the parameters of each of the modules affected the overall dynamics of the systems by performing parameter sweeps and identifying qualitatively different simulation outcomes.

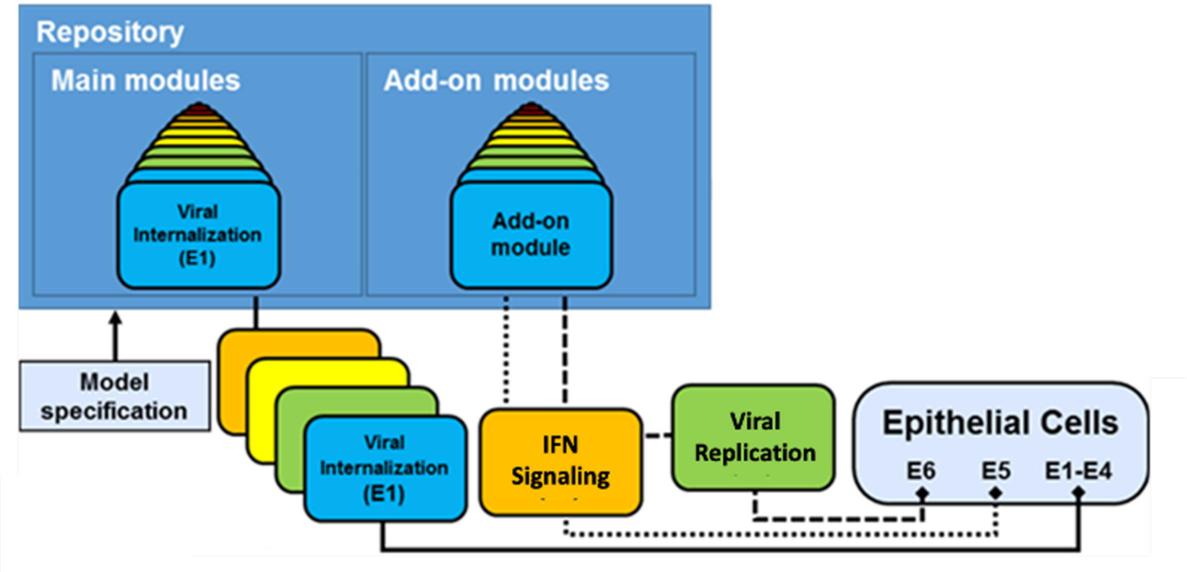
Repository
Main modules
Add-on modules
Viral Internalization (E1)
Add-on module
Model specification
Viral Internalization (E1)
IFN Signaling
Viral Replication
Epithelial Cells
E6
E5
E1-E4

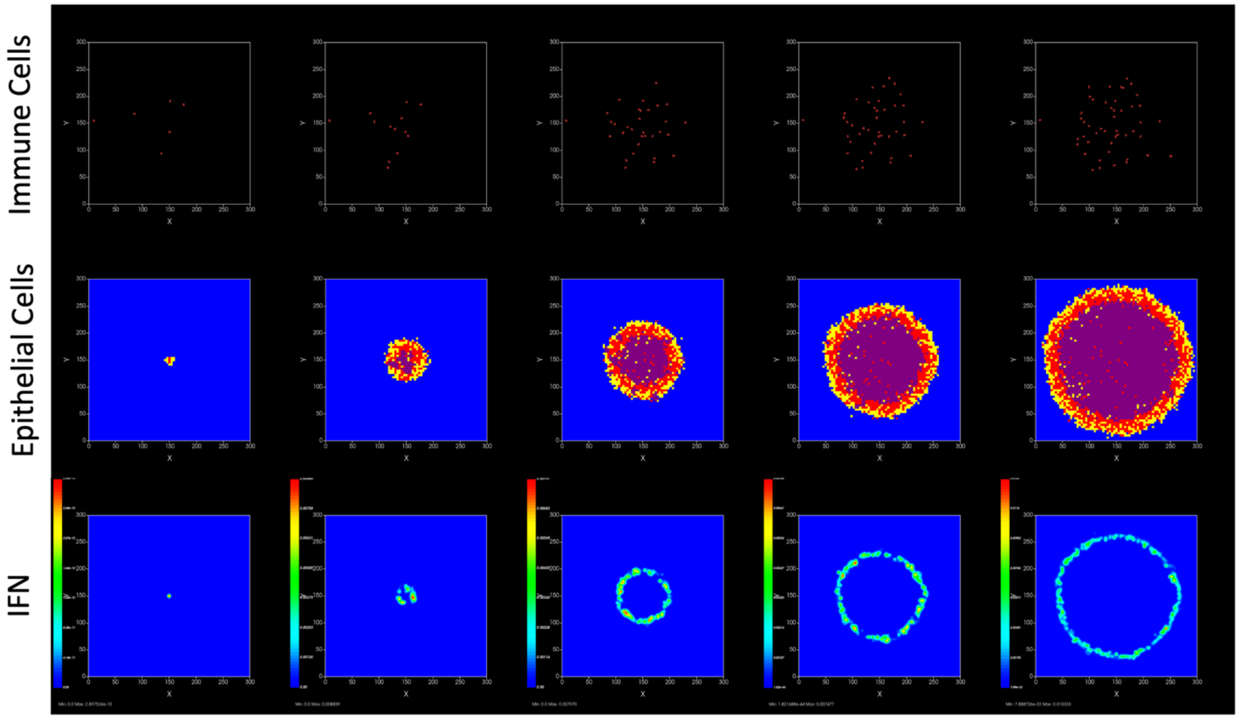

Figure A.1. **Combination of Libraries Used to Combine IFN model with Cellular Immune Response**. Adapted from [159].

Coupling IFN model with Lymph Node model and Immune Cell Recruitment

The first extension was to couple the IFN model with a model of immune cell recruitment (Figure A.2). The original framework includes a module that models the effect of inflammatory signals at the infection site have on nearby lymph nodes. In the original model, a generic cytokine served as a recruiting signal. An ODE described the state of the lymph node model. At a steady state, the immune recruitment model maintains a resident population of generic immune cells. In a pro-inflammatory state, the rate of change of the lymph node model is positive and immune cells are added to the simulation domain. In an anti-inflammatory state, the rate of change of the lymph node model is negative, and immune cells are removed from the simulation domain. From the original publication, we adopted the immune seeding model that seeded immune cells by sampling the simulation space and seeding immune cells in regions of higher concentration of recruiting signal.

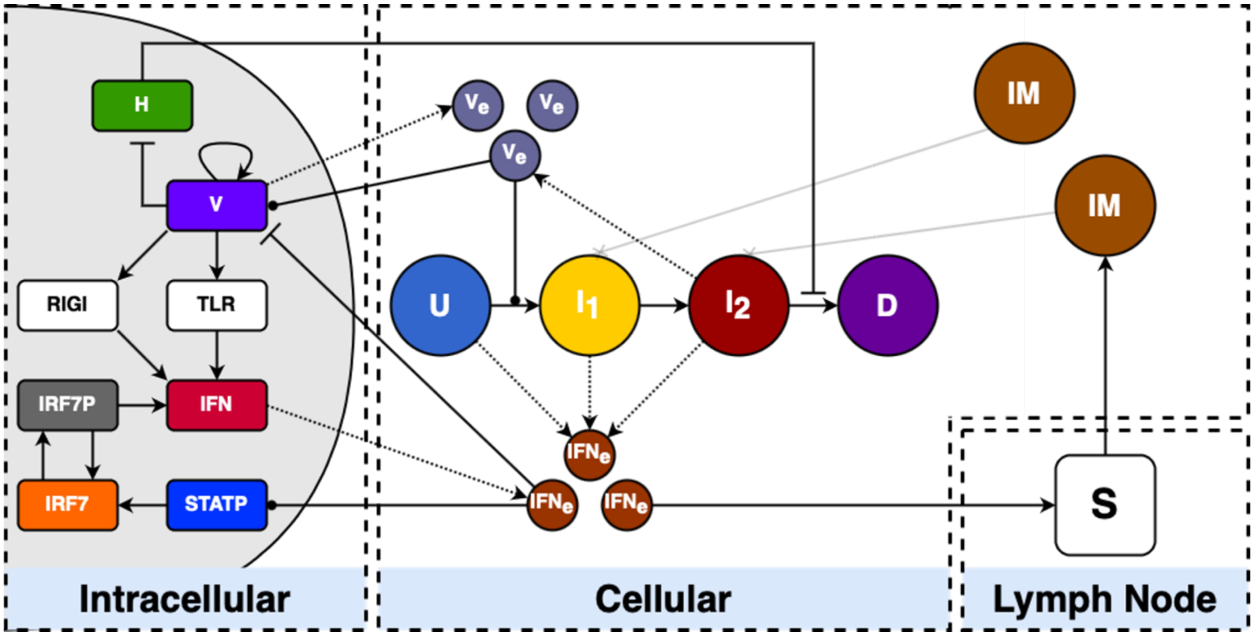

Figure A.2. Schematic Representation of Combination of IFN Model with Lymph Node and Immune Cell Recruitment Models.

We coupled both models by substituting the generic cytokine with extracellular IFN

$$\frac{dS}{dt} = \beta_{add} - \beta_{sub} N_{immune} + \frac{\alpha_{sig}}{\beta_{delay}} \boldsymbol{IFN_e} - \beta_{decay} S \quad \text{(A.1)}$$

Parameters β_{add} and β_{sub} determine the size of the resident immune cell population and were not altered in the coupling. Adjusting these parameters would correspond to modeling different types of tissues. The parameter α_{sig} is the transmission coefficient and determines how sensitive is the immune recruitment model to the IFN signal. Because the amplitude of IFN and the generic cytokine signals were not necessarily comparable, α_{sig} needed to be rescaled. The parameter β_{decay} describes the time scale of the anti-inflammatory response. This parameter described the persistence of the inflammatory signal. We performed single and two-dimensional parameter sweeps of α_{sig} and β_{decay} to explore how they affected the dynamics of the overall model.

$$\frac{dS}{dt} = \beta_{add} - \beta_{sub}N_{immune} + \frac{\alpha_{sig}}{\beta_{delay}} IFN_e - \beta_{decay}S$$

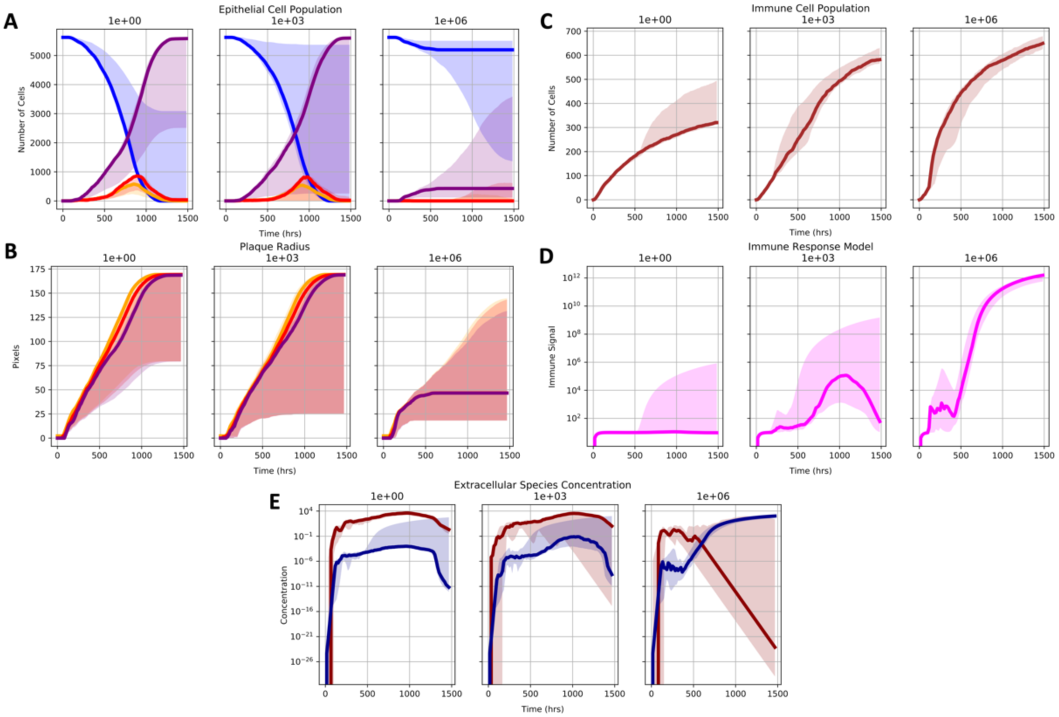

Figure A.3. Transmission Coefficient α_{sig} Parameter Sweep.

We first performed a logarithmic parameter sweep of the transmission coefficient α_{sig} with multipliers $10^0, 10^3$ and 10^6 of the baseline values in the original model. The parameter sweep shows that increasing α_{sig} moves the overall system from a regime where all cells get infected (Figure A.3A) and the plaque growth continuously (Figure A.3A) to regions where not all cells are infected at the end of the simulation and the plaque growth is arrested. The maximum number of immune cells recruited to the simulation domain increases as the value of the parameter increases, from 300 at the baseline value to 700 at 10^6 (Figure A.3C). The effect of the parameter variation on the state of the immune recruitment model is clear (Figure A.3D). At the baseline value, the immune recruitment signal is small and remains constant and through the course of the infection. At an intermediate multiplier, the immune recruitment model is more responsive to the IFN signal, as it increases when extracellular interferon starts to peak (Figure A.3E) but is insufficient to control the infection. When most cells have died, the immune model adopts an anti-inflammatory state, and the recruitment signal starts decreasing. When the multiplier is high, the immune recruitment model is highly sensitive to extracellular IFN and starts increasing early during the infection. Note that because extracellular IFNe persists high in cases of plaque containment, the immune recruitment signal continues to increase after the infection has already been contained.

$$\frac{dS}{dt} = \beta_{add} - \beta_{sub} N_{immune} + \frac{\alpha_{sig}}{\beta_{delay}} IFN_e - \beta_{decay} S$$

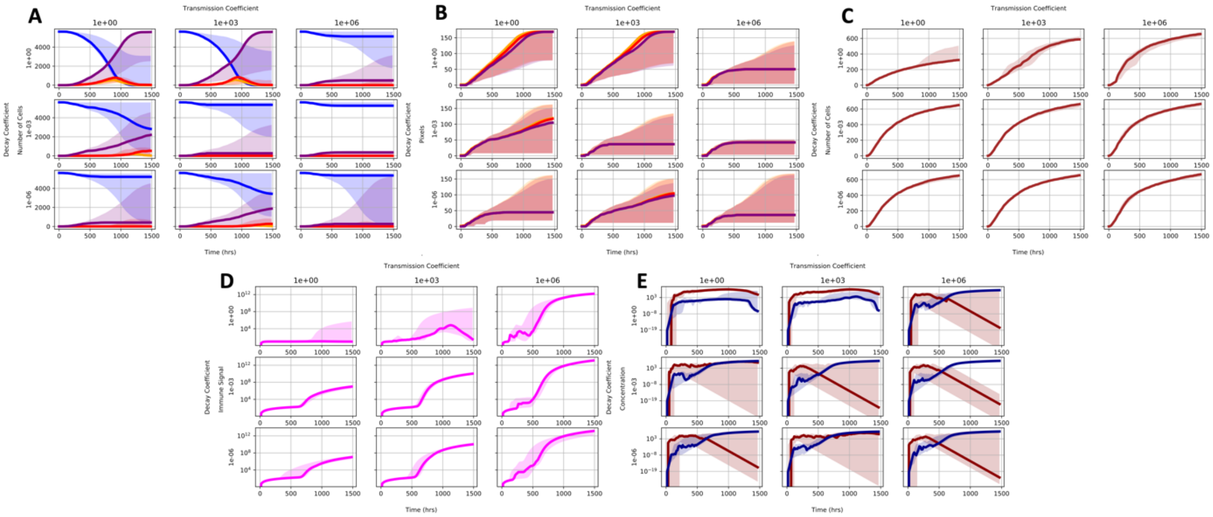

Figure A.4. Transmission coefficient α_{sig} and decay coefficient β_{decay} Parameter Sweep

Next, we performed a two-dimensional parameter sweep of the transmission coefficient α_{sig} and decay coefficient β_{decay}. As in the previous sweep, α_{sig} was varied over multipliers 10^0, 10^3 and 10^6 on the baseline value. β_{decay} was varied over multipliers 10^0, 10^{-3} and 10^{-6}. At the baseline values, the immune response is insufficient counter the progression of the infection and all cells get infected (Figure A.4A) and the plaque grows continuously (Figure A.4B). Decreasing the β_{decay} and increasing α_{sig} lead the systems from regions of uncontrolled viral growth to containment and to a doubling the number of recruited immune cells. Whereas increasing α_{sig} leads to higher peaks values of the immune recruitment model, decreasing β_{decay} leads to both more rapid activation and slower decline of the immune recruitment signal (Figure A.4D) even at similar levels of extracellular IFN (Figure A.4E). Combined α_{sig} and β_{decay} lead to earlier plaque containment, and bigger number of recruited of immune cells.

Coupling IFN model with Immune Cell Cytotoxicity

The second extension was adding cytotoxic immune cells activity module to the IFN model along with the immune cell recruitment model (Figure A.5). When immune cells were recruited to the simulation domain, they kill the immune cells they come into contact with. Because cells kill cells immediately upon contact, the effectiveness of immune cell killing is entirely dependent on their ability to sample the simulation space. Sego et al. already explored the effect of the parameters of the immune seeding model on the effectiveness of immune cell cytotoxicity [160]. An alternative approach is to test both the random movement and the chemotaxis of immune cells.

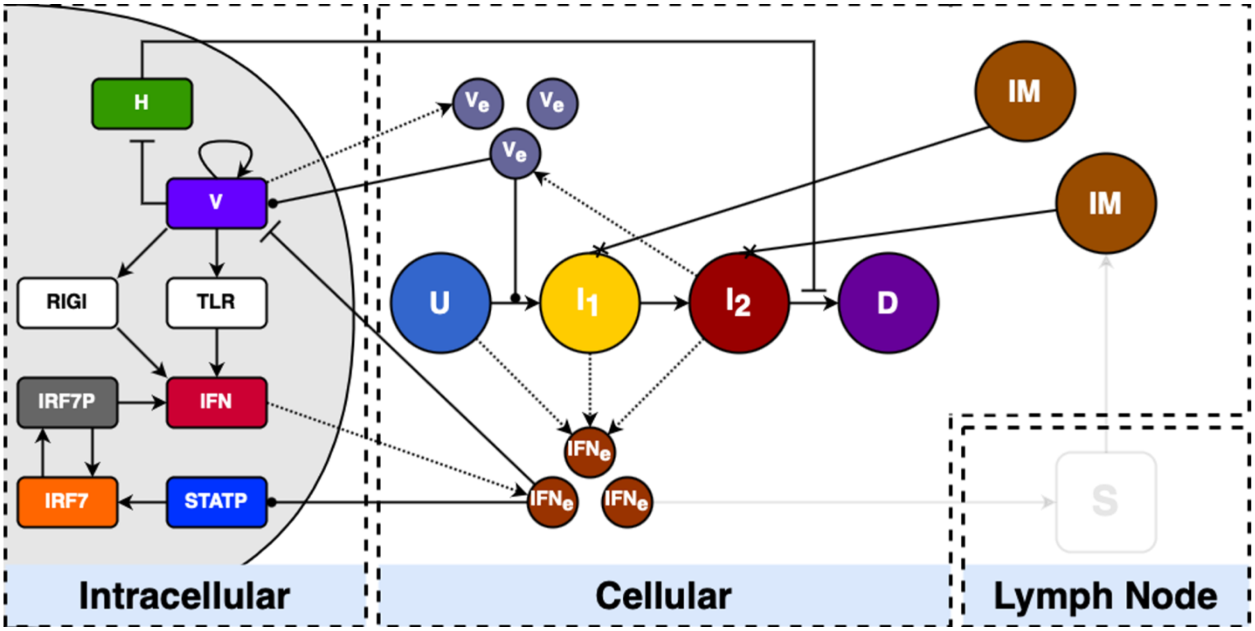

Figure A.5. Combining IFN Model with Immune Cell Cytotoxicity Model

Coupling the modules required instantiating a chemotaxis module that drives immune cell movement toward areas of the chemotaxis signal. As in the original mode, in the model extension extracellular virus served as the chemotaxis signal. The chemotaxis is modeled by adding an energy term to the Hamiltonian of the system.

$$\mathcal{H} = \lambda_{chemo}\left(\frac{\nabla C(x,t)}{C(x,t)+\epsilon}\right) \text{ (A.2)}$$

Because the levels of extracellular virus are not necessarily commensurable between the IFN and the original model, the chemotaxis parameter λ_{chemo} was modified such that immune cells were responsive to the extracellular virus but were not deformed by the strength of the chemotactic force. Varying the chemotaxis parameter was insufficient to produce significant changes in the dynamics of the system (data not shown). Thus, we extended the existing model to include a model of persistent random walk on top of the intrinsic cell motility and the chemotactic movement. Persistent random walk is implemented by introducing a slowly diffusing auxiliary chemical field that is consumed by motile cells. Cells will move in a quasi-random walk persisting in their movement before randomly changing direction. In this case, λ_{chemo} controls how much cell movement is due to intrinsic random motility versus persistent random walk.

$$\mathcal{H} = \lambda_{chemo}\left(\frac{\nabla C(x,t)}{C(x,t)+\epsilon}\right)$$

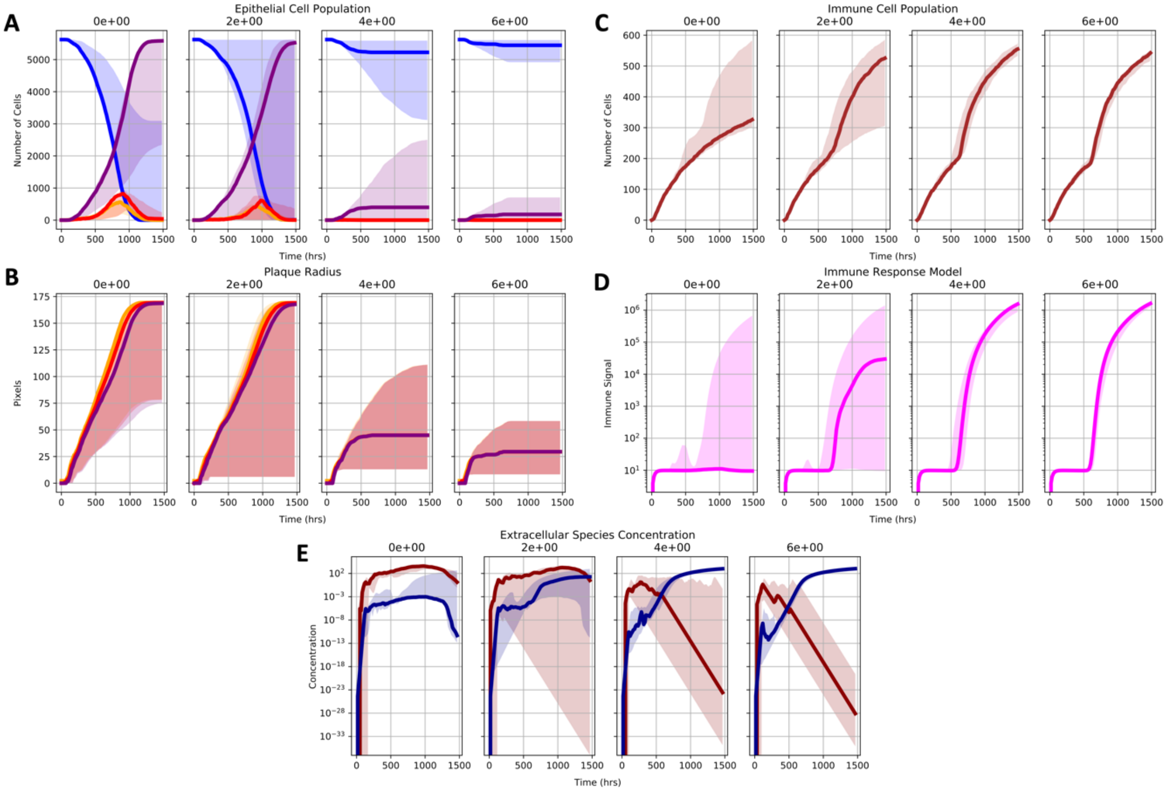

Figure A.6. Lambda Chemotaxis λ_{chemo} Parameter Sweep

We performed a parameter sweep of the lambda chemotaxis parameter controlling the persistent random walk over multipliers $0, 2, 4$ and 6. Increasing λ_{chemo} increases the ability of immune cells to sample the simulation domain and thus increases the effectiveness of cytotoxic killing, leading to higher viral containment (Figure A.6B) and to higher number of cells being uninfected at the end of the simulation (Figure A.6A). Interestingly, because of the feedback mechanism between the number of uninfected cells, the activation of the intracellular IFN pathway via paracrine signaling and the release of extracellular IFN (Figure A.6E), higher cytotoxic efficacy also leads to higher number of recruited immune cells (Figure A.6C) and higher peaks of the immune recruitment signal (Figure A.6D).

$$\frac{dS}{dt} = \beta_{add} - \beta_{sub}N_{immune} + \frac{\alpha_{sig}}{\beta_{delay}} IFN_e - \beta_{decay}S \qquad \mathcal{H} = \lambda_{chemo}\left(\frac{\nabla C(x,t)}{C(x,t)+\epsilon}\right)$$

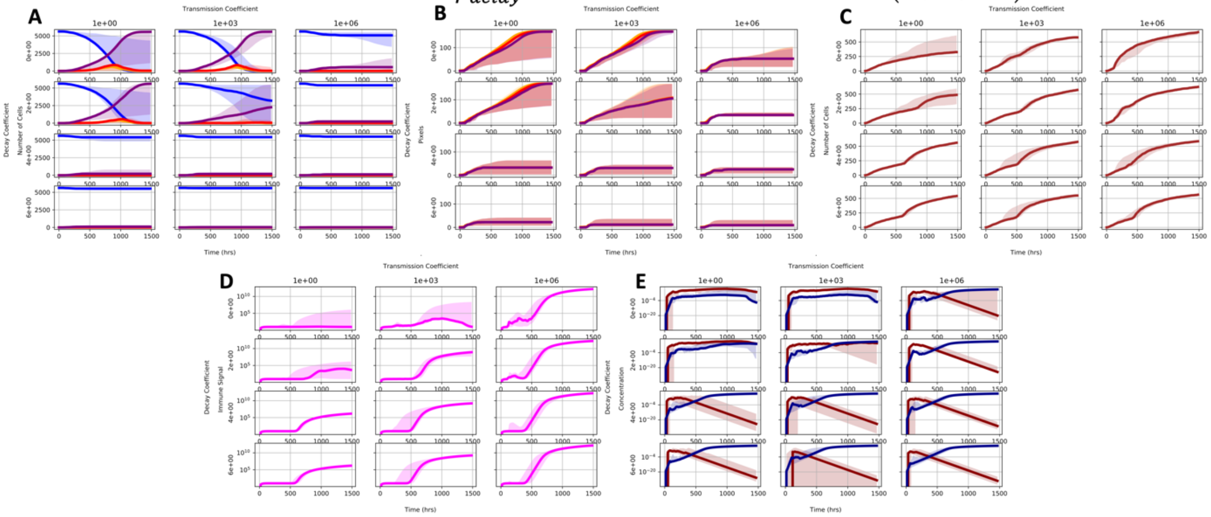

Figure A.&. Transmission coefficient α_{sig} and Lambda Chemotaxis λ_{chemo} Parameter Sweep

Lastly, we performed a two-dimensional parameter sweep of the lambda chemotaxis λ_{chemo} and the transmission coefficient α_{sig} parameters. As before, α_{sig} was varied over multipliers $10^0, 10^3$ and 10^6 on the baseline value and λ_{chemo} over multipliers $0, 2, 4$ and 6 on the baseline value. The combined effect of varying both parameters (increasing α_{sig} and λ_{chemo}) leads to strong containment of viral spread. For high values of either parameter, the infection fails to take over or only infects a small number of cells (Figure A.7A) and the plaque fails to growth beyond the first cycles of infection (Figure A.7B). At intermediate regions the plaque growth is slowed down by the immune response but is incapable of controlling the spread of the infection. Note that either strategy leads to containment even on the absence of the other. Slow number of highly motile cytotoxic immune cells are as effective as high number of less motile cells.

Interferon Pretreatment

After putting the new model together and identifying the effect of varying key model parameters, we performed a virtual experiment to quantify the effect of interferon pretreatment in the system. We had already performed a pre-treatment experiment in the original publication containing the IFN model. However, we did not test the effect of different pretreatment doses and didn't take into consideration cellular immune response. To model pretreatment, we added different levels of extracellular IFN at the beginning of the simulation. We tested pretreatment in a parameter region where the immune response was strong enough to slow down the spread of the infection but insufficient to contain plaque growth.

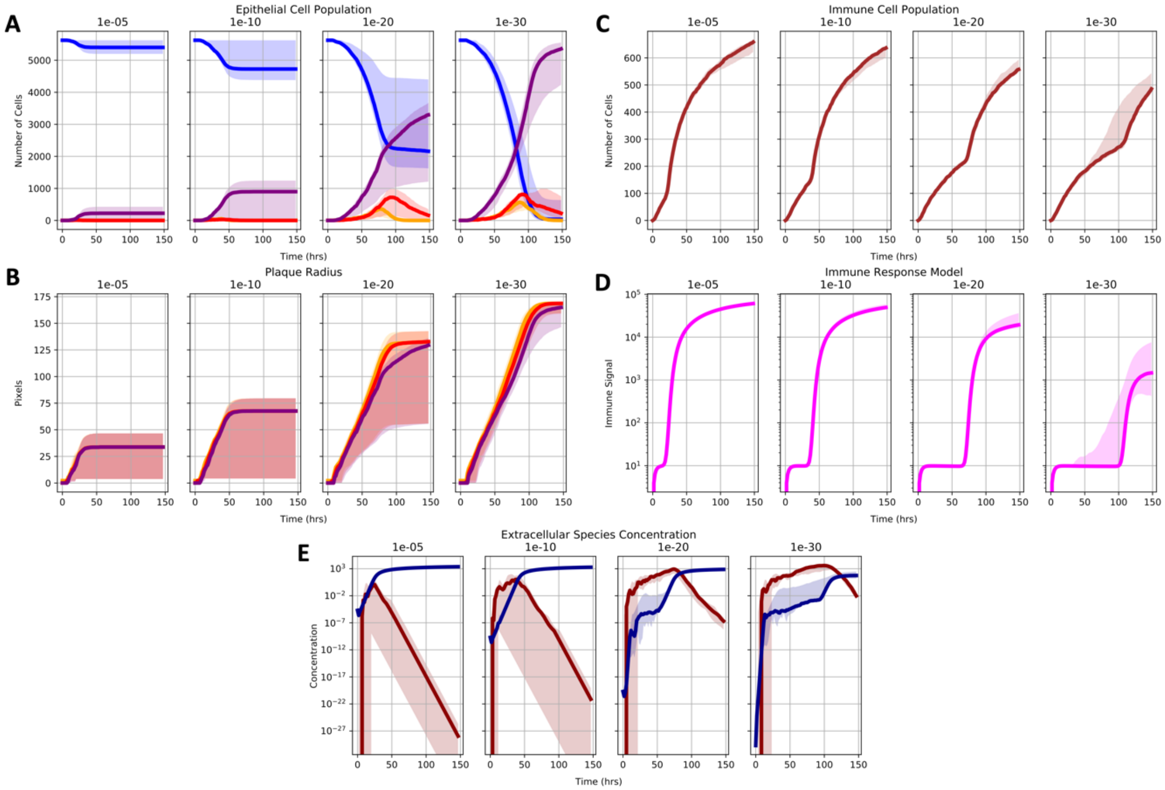

Figure A.8. Dose-Dependent Interferon Pretreatment

To determine starting doses, we took as a reference the concentration of extracellular IFN produced at the control parameters values. We then pre-stimulated the simulation domain with concentrations of $10^{-5}, 10^{-10}, 10^{-20}$ and $10^{-30}\ \mu M$. Higher concentrations of IFN pre-stimulation led to bigger number of uninfected cells at the end of the simulation (Figure A.8A) and smaller viral plaques (Figure A.8B). Higher concentrations also led to more recruited immune cell recruitment (Figure A.8C) and earlier activation of the immune recruitment signal (Figure A.8D). Note that regardless of the pre-stimulation concentration, extracellular IFN always reached the same steady state levels. If the IFN stimulation was too small, it had no significant effect on the dynamics of the system.

Discussion

Using the libraries available in our viral infection framework, we have integrated models of viral spread, interferon response, immune cell recruitment and cytotoxicity. Each of these processes have been incorporated into the framework as independent functional modules. Parameters corresponding to each module can be independently identified. In the case of the parameters of the IFN signaling pathway, these were previously identified using data from influenza infection. Combining parameters between calibrated and estimated parameters might help understand the biological significance of the parameters and what are reasonable ranges of their values.

We showed over what ranges parameters corresponding to the immune recruitment and immune cell cytotoxicity modules showed qualitatively distinct simulation outcomes: uncontained growth and plaque arrest. Both outcomes have been experimentally observed *in vitro*. The immune recruitment signal shows distinct outcomes when parameters such as the transmission coefficient and the decay constant are varied over 3 orders of magnitude. These results might suggest the spatiotemporal scales that characterize an effective immune response to viral infections. The immune cytotoxicity module shows uncontained growth when immune cells do not sample the simulation space effectively and containment when they are highly motile. We showed that there is a tradeoff between immune recruitment and increase motility, such that both low recruitment of highly motile and high recruitment of immotile cells lead to the same infection outcomes. These results suggests that additional data is required to distinguish the contribution of each mechanism to the course of infection. By performing a virtual experiment, we also showed how IFN prestimulation dose relates quantitatively to infection outcomes. Again, more data is necessary to identify the correspondence between biological and simulation ranges of the parameters.

References

[1] Villani AC, Sarkizova S, Hacohen N. Systems immunology: Learning the rules of the immune system. Annual review of immunology. 2018 Apr 26;36:813-42.

[2] Meier-Schellersheim M, Varma R, Angermann BR. Mechanistic models of cellular signaling, cytokine crosstalk, and cell-cell communication in immunology. Frontiers in immunology. 2019 Sep 25;10:2268.

[3] Pigozzo AB, Macedo GC, Dos Santos RW, Lobosco M. On the computational modeling of the innate immune system. InBMC bioinformatics 2013 Apr (Vol. 14, No. 6, pp. 1-20). BioMed Central.

[4] Bauer AL, Beauchemin CA, Perelson AS. Agent-based modeling of host–pathogen systems: The successes and challenges. Information sciences. 2009 Apr 29;179(10):1379-89.

[5] Mirsky HP, Miller MJ, Linderman JJ, Kirschner DE. Systems biology approaches for understanding cellular mechanisms of immunity in lymph nodes during infection. Journal of theoretical biology. 2011 Oct 21;287:160-70.

[6] Bonam SR, Partidos CD, Halmuthur SK, Muller S. An overview of novel adjuvants designed for improving vaccine efficacy. Trends in pharmacological sciences. 2017 Sep 1;38(9):771-93.

[7] An G. Concepts for developing a collaborative in silico model of the acute inflammatory response using agent-based modeling. Journal of critical care. 2006 Mar 1;21(1):105-10.

[8] Bartocci E, Lió P. Computational modeling, formal analysis, and tools for systems biology. PLoS computational biology. 2016 Jan 21;12(1):e1004591.

[9] Jarrett AM, Lima EA, Hormuth DA, McKenna MT, Feng X, Ekrut DA, Resende AC, Brock A, Yankeelov TE. Mathematical models of tumor cell proliferation: a review of the literature. Expert review of anticancer therapy. 2018 Dec 2;18(12):1271-86.

[10] Siettos CI, Russo L. Mathematical modeling of infectious disease dynamics. Virulence. 2013 May 15;4(4):295-306.

[11] Faeder, J.R., Blinov, M.L. and Hlavacek, W.S., 2009. Rule-based modeling of biochemical systems with BioNetGen. In Systems biology (pp. 113-167). Humana Press.

[12] Stoll G, Caron B, Viara E, Dugourd A, Zinovyev A, Naldi A, Kroemer G, Barillot E, Calzone L. MaBoSS 2.0: an environment for stochastic Boolean modeling. Bioinformatics. 2017 Jul 15;33(14):2226-8.

[13] Müssel C, Hopfensitz M, Kestler HA. BoolNet—an R package for generation, reconstruction and analysis of Boolean networks. Bioinformatics. 2010 May 15;26(10):1378-80.

[14] Metzcar J, Wang Y, Heiland R, Macklin P. A review of cell-based computational modeling in cancer biology. JCO clinical cancer informatics. 2019 Feb;2:1-3.

[15] Graudenzi A, Caravagna G, De Matteis G, Antoniotti M. Investigating the relation between stochastic differentiation, homeostasis and clonal expansion in intestinal crypts via multiscale modeling. PLoS One. 2014 May 28;9(5):e97272.

[16] Graw F, Perelson AS. Modeling viral spread. Annual review of virology. 2016 Sep 29;3:555-72.

[17] Yin J, Redovich J. Kinetic modeling of virus growth in cells. Microbiology and Molecular Biology Reviews. 2018 Jun 1;82(2):e00066-17.

[18] Kumberger P, Frey F, Schwarz US, Graw F. Multiscale modeling of virus replication and spread. FEBS letters. 2016 Jul;590(13):1972-86.

[19] Perelson AS, Ke R. Mechanistic Modeling of SARS-CoV-2 and Other Infectious Diseases and the Effects of Therapeutics. Clinical Pharmacology & Therapeutics. 2021 Apr;109(4):829-40.

[20] Beauchemin CA, Handel A. A review of mathematical models of influenza A infections within a host or cell culture: lessons learned and challenges ahead. BMC public health. 2011 Dec;11(1):1-5.

[21] Smith AM. Host-pathogen kinetics during influenza infection and coinfection: insights from predictive modeling. Immunological reviews. 2018 Sep;285(1):97-112.

[22] Altrock PM, Liu LL, Michor F. The mathematics of cancer: integrating quantitative models. Nature Reviews Cancer. 2015 Dec;15(12):730-45.

[23] Chamseddine IM, Rejniak KA. Hybrid modeling frameworks of tumor development and treatment. Wiley Interdisciplinary Reviews: Systems Biology and Medicine. 2020 Jan;12(1):e1461.

[24] Boedtkjer E, Pedersen SF. The acidic tumor microenvironment as a driver of cancer. Annual review of physiology. 2020 Feb 10;82:103-26.

[25] Shamsi M, Saghafian M, Dejam M, Sanati-Nezhad A. Mathematical modeling of the function of Warburg effect in tumor microenvironment. Scientific reports. 2018 Jun 11;8(1):1-3.

[26] Yuan Y. Spatial heterogeneity in the tumor microenvironment. Cold Spring Harbor perspectives in medicine. 2016 Aug 1;6(8):a026583.

[27] Norton KA, Gong C, Jamalian S, Popel AS. Multiscale agent-based and hybrid modeling of the tumor immune microenvironment. Processes. 2019 Jan;7(1):37.

[28] Serre R, Benzekry S, Padovani L, Meille C, André N, Ciccolini J, Barlesi F, Muracciole X, Barbolosi D. Mathematical modeling of cancer immunotherapy and its synergy with radiotherapy. Cancer research. 2016 Sep 1;76(17):4931-40.

[29] Rejniak KA, McCawley LJ. Current trends in mathematical modeling of tumor–microenvironment interactions: a survey of tools and applications. Experimental Biology and Medicine. 2010 Apr;235(4):411-23.

[30] Eftimie R, Bramson JL, Earn DJ. Interactions between the immune system and cancer: a brief review of non-spatial mathematical models. Bulletin of mathematical biology. 2011 Jan;73(1):2-32.

[31] Gatenby RA, Smallbone K, Maini PK, Rose F, Averill J, Nagle RB, Worrall L, Gillies RJ. Cellular adaptations to hypoxia and acidosis during somatic evolution of breast cancer. British journal of cancer. 2007 Aug;97(5):646-53.

[32] Anderson AR. A hybrid mathematical model of solid tumour invasion: the importance of cell adhesion. Mathematical medicine and biology: a journal of the IMA. 2005 Jun;22(2):163-86.

[33] Macklin P, Edgerton ME, Thompson AM, Cristini V. Patient-calibrated agent-based modelling of ductal carcinoma in situ (DCIS): from microscopic measurements to macroscopic predictions of clinical progression. Journal of theoretical biology. 2012 May 21;301:122-40.

[34] Swat MH, Thomas GL, Shirinifard A, Clendenon SG, Glazier JA. Emergent stratification in solid tumors selects for reduced cohesion of tumor cells: a multi-cell, virtual-tissue model of tumor evolution using compucell3d. PloS one. 2015 Jun 17;10(6):e0127972.

[35] Curtis LT, Rychahou P, Bae Y, Frieboes HB. A computational/experimental assessment of antitumor activity of polymer nanoassemblies for ph-controlled drug delivery to primary and metastatic tumors. Pharmaceutical research. 2016 Oct;33(10):2552-64.

[36] Pappalardo F, Forero IM, Pennisi M, Palazon A, Melero I, Motta S. SimB16: modeling induced immune system response against B16-melanoma. PloS one. 2011 Oct 19;6(10):e26523.

[37] Swat MH, Thomas GL, Belmonte JM, Shirinifard A, Hmeljak D, Glazier JA. Multi-scale modeling of tissues using CompuCell3D. Methods in cell biology. 2012 Jan 1;110:325-66.

[38] Eckhardt M, Hultquist JF, Kaake RM, Hüttenhain R, Krogan NJ. A systems approach to infectious disease. Nature Reviews Genetics. 2020;21: 339–354. doi:10.1038/s41576-020-0212-5

[39] Koelle K, Farrell AP, Brooke CB, Ke R. Within-host infectious disease models accommodating cellular coinfection, with an application to influenza†. Virus Evolution. 2019;5. doi:10.1093/ve/vez018

[40] Wang Y, Heiland R, Craig M, Davis C, Ford Versypt AN, Jenner A, et al. Rapid community-driven development of a SARS-CoV-2 tissue simulator. bioRxiv. 2020; 2020.04.02.019075. doi:10.1101/2020.04.02.019075

[41] Dee KU, Hammer DA, Shuler ML. A model of the binding, entry, uncoating, and RNA synthesis of Semliki Forest virus in baby hamster kidney (BHK-21) cells. Biotechnology and Bioengineering. 1995;46: 485–496. doi:10.1002/bit.260460513

[42] Boireau S, Maiuri P, Basyuk E, de la Mata M, Knezevich A, Pradet-Balade B, et al. The transcriptional cycle of HIV-1 in real-time and live cells. J Cell Biol. 2007;179: 291–304. doi:10.1083/jcb.200706018

[43] Yang Q, Catalano CE. A minimal kinetic model for a viral DNA packaging machine. Biochemistry. 2004;43: 289–299. doi:10.1021/bi035532h

[7] [44]Graw F, Perelson A. Spatial aspects of HIV infection. 2013. pp. 3–31. doi:10.1007/978-1-4614-4178-6_1

[45] Beauchemin C. Probing the effects of the well-mixed assumption on viral infection dynamics. J Theor Biol. 2006;242: 464–477. doi:10.1016/j.jtbi.2006.03.014

[46] Olafuyi O, Badhan RKS. Dose Optimization of Chloroquine by Pharmacokinetic Modeling During Pregnancy for the Treatment of Zika Virus Infection. JPharmSci. 2019;108: 661–673. doi:10.1016/j.xphs.2018.10.056

[47] Chua RL, Lukassen S, Trump S, Hennig BP, Wendisch D, Pott F, et al. COVID-19 severity correlates with airway epithelium–immune cell interactions identified by single-cell analysis. Nature Biotechnology. 2020;38: 970–979. doi:10.1038/s41587-020-0602-4

[48] Bocharov G, Meyerhans A, Bessonov N, Trofimchuk S, Volpert V. Spatiotemporal Dynamics of Virus Infection Spreading in Tissues. PLOS ONE. 2016;11: e0168576. doi:10.1371/journal.pone.0168576

[49] Strain MC, Richman DD, Wong JK, Levine H. Spatiotemporal Dynamics of HIV Propagation. Journal of Theoretical Biology. 2002;218: 85–96. doi:10.1006/jtbi.2002.3055

[50] Imle A, Kumberger P, Schnellbächer ND, Fehr J, Carrillo-Bustamante P, Ales J, et al. Experimental and computational analyses reveal that environmental restrictions shape HIV-1 spread in 3D cultures. Nat Commun. 2019;10: 2144. doi:10.1038/s41467-019-09879-3

[[51] Myers MA, Smith AP, Lane LC, Moquin DJ, Vogel P, Woolard S, et al. Dynamically linking influenza virus infection with lung injury to predict disease severity. bioRxiv. 2019; 555276. doi:10.1101/555276

[52] Akira S, Uematsu S, Takeuchi O. Pathogen Recognition and Innate Immunity. Cell. 2006;124: 783–801. doi:10.1016/j.cell.2006.02.015

[53] Ahlquist P, Noueiry AO, Lee W-M, Kushner DB, Dye BT. Host Factors in Positive-Strand RNA Virus Genome Replication. J Virol. 2003;77: 8181. doi:10.1128/JVI.77.15.8181-8186.2003

[54] Chou RC, Kim ND, Sadik CD, Seung E, Lan Y, Byrne MH, et al. Lipid-Cytokine-Chemokine Cascade Drives Neutrophil Recruitment in a Murine Model of Inflammatory Arthritis. Immunity. 2010;33: 266–278. doi:10.1016/j.immuni.2010.07.018

[55] Edelblum KL, Turner JR. Chapter 12 - Epithelial cells: structure, transport, and barrier function. In: Mestecky J, Strober W, Russell MW, Kelsall BL, Cheroutre H, Lambrecht BN, editors. Mucosal Immunology (Fourth Edition). Boston: Academic Press; 2015. pp. 187–210. doi:10.1016/B978-0-12-415847-4.00012-4

[56] Dusséaux M, Masse-Ranson G, Darche S, Ahodantin J, Li Y, Fiquet O, et al. Viral Load Affects the Immune Response to HBV in Mice With Humanized Immune System and Liver. Gastroenterology. 2017;153: 1647-1661.e9. doi:10.1053/j.gastro.2017.08.034

[57] Veiga-Parga T, Sehrawat S, Rouse BT. Role of Regulatory T Cells during Virus Infection. Immunol Rev. 2013;255: 182–196. doi:10.1111/imr.12085

[58] Le Page C, Génin P, Baines M, Hiscott J. Interferon activation and innate immunity. Rev Immunogenet. 2000;2: 374–386.

[59] Ploquin A, Zhou Y, Sullivan NJ. Ebola Immunity: Gaining a Winning Position in Lightning Chess. JI. 2018;201: 833–842. doi:10.4049/jimmunol.1700827

[60] Harcourt J, Tamin A, Lu X, Kamili S, Sakthivel SK, Murray J, et al. Severe Acute Respiratory Syndrome Coronavirus 2 from Patient with Coronavirus Disease, United States. Emerg Infect Dis. 2020;26: 1266–1273. doi:10.3201/eid2606.200516

[61] Cheng AH-D, Cheng DT. Heritage and early history of the boundary element method. Eng Anal Bound Elem. 2005;29: 268–302. doi:10.1016/j.enganabound.2004.12.001

[62] Zhao X, Wang W. Fisher waves in an epidemic model. Discrete Cont Dyn-B. 2004;4: 1117–1128. doi:10.3934/dcdsb.2004.4.1117

[63] Warren TK, Jordan R, Lo MK, Ray AS, Mackman RL, Soloveva V, et al. Therapeutic efficacy of the small molecule GS-5734 against Ebola virus in rhesus monkeys. Nature. 2016/03/02 ed. 2016;531: 381–385. doi:10.1038/nature17180

[64] Graner F, Glazier JA. Simulation of biological cell sorting using a two-dimensional extended Potts model. Phys Rev Lett. 1992;69: 2013–2016. doi:10.1103/PhysRevLett.69.2013

[65] Oyler-Yaniv A, Oyler-Yaniv J, Whitlock BM, Liu Z, Germain RN, Huse M, et al. A tunable diffusion-consumption mechanism of cytokine propagation enables plasticity in cell-to-cell communication in the immune system. Immunity. 2017;46: 609–620. doi:10.1016/j.immuni.2017.03.011

[66] Höfer T, Krichevsky O, Altan-Bonnet G. Competition for IL-2 between regulatory and effector T cells to chisel immune responses. Front Immunol. 2012;3: 268–268. doi:10.3389/fimmu.2012.00268

[67] Hugues S, Fetler L, Bonifaz L, Helft J, Amblard F, Amigorena S. Distinct T cell dynamics in lymph nodes during the induction of tolerance and immunity. Nature Immunology. 2004;5: 1235–1242. doi:10.1038/ni1134

[68] Walls AC, Park Y-J, Tortorici MA, Wall A, McGuire AT, Veesler D. Structure, Function, and Antigenicity of the SARS-CoV-2 Spike Glycoprotein. Cell. 2020;181: 281-292.e6. doi:10.1016/j.cell.2020.02.058

[69] Lai SK, Wang Y-Y, Wirtz D, Hanes J. Micro- and macrorheology of mucus. Adv Drug Deliv Rev. 2009;61: 86–100. doi:10.1016/j.addr.2008.09.012

[70] Stray SJ, Air GM. Apoptosis by influenza viruses correlates with efficiency of viral mRNA synthesis. Virus Res. 2001;77: 3–17. doi:10.1016/s0168-1702(01)00260-x

[71] World Health Organisation. Global Influenza Strategy Summary 2019-2030 Influenza. Glob Influ Strateg 2019-2030 Influ [Internet]. 2019 [cited 2020 Aug 5];1:1. Available from: https://apps.who.int/iris/handle/10665/311184

[72] THE GEOGRAPHY AND MORTALITY OF THE 1918 INFLUENZA PANDEMIC on JSTOR [Internet]. [cited 2020 Nov 30]. Available from: https://www.jstor.org/stable/44447656?seq=1#metadata_info_tab_contents

[73] Centro de Control y prevención de enfermedades. 1957-1958 Pandemic (H2N2 virus) | Pandemic Influenza (Flu) | CDC [Internet]. CDC-Centers for Disease Control and Prevention, National Center for Immunization and Respiratory Diseases (NCIRD). 2019 [cited 2021 May 18]. Available from: https://www.cdc.gov/flu/pandemic-resources/1957-1958-pandemic.html

[74] Centre for Disease Control and Prevention. 1968 Pandemic (H3N2 virus) | Pandemic Influenza (Flu) | CDC [Internet]. U.S. Department of Health & Human Services. 2019 [cited 2021 May 18]. Available from: https://www.cdc.gov/flu/pandemic-resources/1968-pandemic.html

[75] CDC. 2009 H1N1 Pandemic (H1N1pdm09 virus) | Pandemic Influenza (Flu) | CDC [Internet]. Centers for Disease Control and Prevention. 2009 [cited 2021 May 18]. Available from: https://www.cdc.gov/flu/pandemic-resources/2009-h1n1-pandemic.html

[76] Shibabaw T, Molla MD, Teferi B, Ayelign B. Role of ifn and complements system: Innate immunity in sars-cov-2 [Internet]. Vol. 13, Journal of Inflammation Research. Dove Medical Press Ltd; 2020 [cited 2021 Jun 18]. p. 507–18. Available from: http://doi.org/10.2147/JIR.S267280

[77] AbdelMassih AF, Ramzy D, Nathan L, Aziz S, Ashraf M, Youssef NH, et al. Possible molecular and paracrine involvement underlying the pathogenesis of COVID-19 cardiovascular complications. Cardiovasc Endocrinol Metab [Internet]. 2020 [cited 2020 May 11];Publish Ah:1–4. Available from: https://doi.org/10.1097/xce.0000000000000207

[78] Baskin CR, Bielefeldt-Ohmann H, Tumpey TM, Sabourin PJ, Long JP, García-Sastre A, et al. Early and sustained innate immune response defines pathology and death in nonhuman primates infected by highly pathogenic influenza virus. Proc Natl Acad Sci U S A [Internet]. 2009 Mar 3 [cited 2021 Jun 18];106(9):3455–60. Available from: https://www.pnas.org/content/106/9/3455

[79] Cilloniz C, Pantin-Jackwood MJ, Ni C, Goodman AG, Peng X, Proll SC, et al. Lethal Dissemination of H5N1 Influenza Virus Is Associated with Dysregulation of Inflammation and Lipoxin Signaling in a Mouse Model of Infection. J Virol [Internet]. 2010 Aug 1 [cited 2019 Sep 24];84(15):7613–24. Available from: http://www.ncbi.nlm.nih.gov/pubmed/20504916

[80] Shinya K, Okamura T, Sueta S, Kasai N, Tanaka M, Ginting TE, et al. Toll-like receptor pre-stimulation protects mice against lethal infection with highly pathogenic influenza viruses. Virol J [Internet]. 2011 [cited 2020 May 13];8:97. Available from: https://dx.doi.org/10.1186%2F1743-422X-8-97

[81] Lokugamage K, Hage A, de Vries M, Valero-Jimenez A, Schindewolf C, Dittmann M, et al. Type I interferon susceptibility distinguishes SARS-CoV-2 from SARS-CoV. J Virol [Internet]. 2020 [cited 2020 Aug 5];94(23). Available from: https://doi.org/10.1128/JVI.01410-20

[82] Qiao L, Phipps-Yonas H, Hartmann B, Moran TM, Sealfon SC, Hayot F. Immune response modeling of interferon beta-pretreated influenza virus-infected human dendritic cells. Biophys J [Internet]. 2010 Feb 17 [cited 2019 Sep 9];98(4):505–14. Available from: http://www.ncbi.nlm.nih.gov/pubmed/20159146

[83] Zhou Q, Chen V, Shannon CP, Wei X-S, Xiang X, Wang X, et al. Interferon-α2b Treatment for COVID-19. Front Immunol [Internet]. 2020 May 15 [cited 2020 Sep 18];11:1061. Available from: https://doi.org/10.3389/fimmu.2020.01061

[84] Gregg RW, Sarkar SN, Shoemaker JE. Mathematical modeling of the cGAS pathway reveals robustness of DNA sensing to TREX1 feedback. J Theor Biol [Internet]. 2019 Feb 7 [cited 2019 Jun 28];462:148–57. Available from: https://doi.org/10.1016/j.jtbi.2018.11.001

[85] Holder BP, Liao LE, Simon P, Boivin G, Beauchemin CAA. Design considerations in building in silico equivalents of common experimental influenza virus assays. Autoimmunity [Internet]. 2011 Jun 19 [cited 2020 Aug 5];44(4):282–93. Available from: https://doi.org/10.3109/08916934.2011.523267

[86] Saenz RA, Quinlivan M, Elton D, MacRae S, Blunden AS, Mumford JA, et al. Dynamics of Influenza Virus Infection and Pathology. J Virol [Internet]. 2010 Apr 15 [cited 2020 Dec 15];84(8):3974–83. Available from: https://dx.doi.org/10.1128%2FJVI.02078-09

[87] Roychoudhury P, Swan DA, Duke E, Corey L, Zhu J, Davé V, et al. Tissue-resident T cell-derived cytokines eliminate herpes simplex virus-2-infected cells. J Clin Invest [Internet]. 2020 Jun 1 [cited 2021 May 19];130(6):2903–19. Available from: https://doi.org/10.1172/JCI132583.

[88] Gregg RW, Shabnam F, Shoemaker JE. Agent-based modeling reveals benefits of heterogeneous and stochastic cell populations during cGAS-mediated IFNβ production. Bioinformatics [Internet]. 2021 Jun 16 [cited 2021 Jul 28];37(10):1428–34. Available from: https://doi.org/10.1093/bioinformatics/btaa969

[89] Davis JW, Hardy JL. In Vitro Studies with Modoc Virus in Vero Cells: Plaque Assay and Kinetics of Growth, Neutralization, and Thermal Inactivation. Appl Microbiol [Internet]. 1973 [cited 2020 Nov 30];26(3):344–8. Available from: https://doi.org/10.1128/am.26.3.344-348.1973

[90] Kropinski AM, Mazzocco A, Waddell TE, Lingohr E, Johnson RP. Enumeration of bacteriophages by double agar overlay plaque assay. Methods Mol Biol [Internet]. 2009 [cited 2020 Nov 30];501:69–76. Available from: https://dx.doi.org/10.1007/978-1-60327-164-6_7

[91] Hayden FG, Cote KM, Douglas RG. Plaque inhibition assay for drug susceptibility testing of influenza viruses. Antimicrob Agents Chemother [Internet]. 1980 May 1 [cited 2020 Nov 30];17(5):865–70. Available from: https://doi.org/10.1128/aac.17.5.865

[92] Weaver JJA, Shoemaker JE. Mathematical modeling of rna virus sensing pathways reveals paracrine signaling as the primary factor regulating excessive cytokine production. Processes

[Internet]. 2020 Jun 20 [cited 2020 Aug 5];8(6):1–16. Available from: https://doi.org/10.3390/pr8060719

[93] Smith AM, Perelson AS. Influenza A virus infection kinetics: Quantitative data and models [Internet]. Vol. 3, Wiley Interdisciplinary Reviews: Systems Biology and Medicine. NIH Public Access; 2011 [cited 2020 Aug 5]. p. 429–45. Available from: https://doi.org/10.1002/wsbm.129

[94] Sun L, Liu S, Chen ZJ. SnapShot: Pathways of Antiviral Innate Immunity. Cell [Internet]. 2010 Feb 5 [cited 2019 Sep 9];140(3):436-436.e2. Available from: https://doi.org/10.1016/j.cell.2010.01.041

[95] Dou D, Revol R, Östbye H, Wang H, Daniels R. Influenza A virus cell entry, replication, virion assembly and movement [Internet]. Vol. 9, Frontiers in Immunology. Frontiers Media SA; 2018 [cited 2019 Sep 9]. p. 1581. Available from: https://doi.org/10.3389/fimmu.2018.01581

[96] Baccam P, Beauchemin C, Macken CA, Hayden FG, Perelson AS. Kinetics of influenza A virus infection in humans. J Virol [Internet]. 2006 Aug 1 [cited 2019 Jul 2];80(15):7590–9. Available from: http://www.ncbi.nlm.nih.gov/pubmed/16840338

[97] Schneider WM, Chevillotte MD, Rice CM. Interferon-stimulated genes: A complex web of host defenses. Annu Rev Immunol [Internet]. 2014 [cited 2019 Sep 9];32:513–45. Available from: https://doi.org/10.1146/annurev-immunol-032713-120231

[98] Trinchieri G. Type I interferon: friend or foe? J Exp Med [Internet]. 2010 Sep 27 [cited 2019 Sep 23];207(10):2053–63. Available from: http://www.ncbi.nlm.nih.gov/pubmed/20837696

[99] Wu W, Zhang W, Duggan ES, Booth JL, Zou MH, Metcalf JP. RIG-I and TLR3 are both required for maximum interferon induction by influenza virus in human lung alveolar epithelial cells.

Virology [Internet]. 2015 Aug 1 [cited 2019 Dec 13];482:181–8. Available from: https://doi.org/10.1016/j.virol.2015.03.048

[100] Watanabe T, Kawakami E, Shoemaker JE, Lopes TJS, Matsuoka Y, Tomita Y, et al. Influenza virus-host interactome screen as a platform for antiviral drug development. Cell Host Microbe [Internet]. 2014 Dec 10 [cited 2021 Jul 28];16(6):795–805. Available from: https://doi.org/10.1016/j.chom.2014.11.002

[101] Shapira SD, Gat-Viks I, Shum BO V, Dricot A, de Grace MM, Wu L, et al. A physical and regulatory map of host-influenza interactions reveals pathways in H1N1 infection. Cell [Internet]. 2009 Dec 24 [cited 2019 Jun 26];139(7):1255–67. Available from: https://doi.org/10.1016/j.cell.2009.12.018

[102] Coppey M, Berezhkovskii AM, Sealfon SC, Shvartsman SY. Time and length scales of autocrine signals in three dimensions. Biophys J [Internet]. 2007 Sep 15 [cited 2020 Dec 7];93(6):1917–22. Available from: pmid:17720734

[103] Ding Y, Chen L, Wu W, Yang J, Yang Z, Liu S. Andrographolide inhibits influenza A virus-induced inflammation in a murine model through NF-κB and JAK-STAT signaling pathway. Microbes Infect [Internet]. 2017 Dec 1 [cited 2021 Jan 7];19(12):605–15. Available from: https://doi.org/10.1016/j.micinf.2017.08.009

[104] Yuan S, Peng L, Park JJ, Hu Y, Devarkar SC, Dong MB, et al. Nonstructural Protein 1 of SARS-CoV-2 Is a Potent Pathogenicity Factor Redirecting Host Protein Synthesis Machinery toward Viral RNA. Mol Cell [Internet]. 2020 Dec 17 [cited 2021 Jun 18];80(6):1055-1066.e6. Available from: https://doi.org/10.1016/j.molcel.2020.10.034

[105] Pichlmair A, Schulz O, Tan CP, Näslund TI, Liljeström P, Weber F, et al. RIG-I-mediated antiviral responses to single-stranded RNA bearing 5′-phosphates. Science (80-) [Internet]. 2006 Nov 10 [cited 2021 Jul 28];314(5801):997–1001. Available from: https://science.sciencemag.org/content/314/5801/997

[106] Stanley WM. The size of influenza virus. J Exp Med [Internet]. 1944 Mar 1 [cited 2021 Jul 12];79(3):267–83. Available from: http://rupress.org/jem/article-pdf/79/3/267/1182869/267.pdf

[107] Derynck R, Remaut E, Saman E, Stanssens P, Clercq E De, Content J, et al. Expression of human fibroblast interferon gene in escherichia coli. Nature [Internet]. 1980 [cited 2021 Jul 12];287(5779):193–7. Available from: https://www.nature.com/articles/287193a0

[108] Lee S, Hirohama M, Noguchi M, Nagata K, Kawaguchi A. Influenza A Virus Infection Triggers Pyroptosis and Apoptosis of Respiratory Epithelial Cells through the Type I Interferon Signaling Pathway in a Mutually Exclusive Manner. J Virol [Internet]

[109] Ashcraft KA, Peace RM, Betof AS, Dewhirst MW, Jones LW. (2016). Efficacy and mechanisms of aerobic exercise on cancer initiation, progression, and metastasis: A critical systematic review of in vivo preclinical data. Cancer research, 76(14), 4032–4050. https://doi.org/10.1158/0008-5472.CAN-16-0887

[110] Friedenreich CM (2011). Physical activity and breast cancer: review of the epidemiologic evidence and biologic mechanisms. Recent Results in Cancer Research 188: 125-39.

[111] Salem J et al (2018). Spectrum of cardiovascular toxicities of immune checkpoint inhibitors: A pharmacovigilance study. Lancet Oncol. 19(12): 1579–1589. https://doi:10.1016/S1470-2045(18)30608-9

[112] Pedersen L et al (2016). Voluntary running suppresses tumor growth through epinephrine- and IL-6-dependent NK cell mobilization and redistribution. Cell Metabolism 23, 1–9. http://dx.doi.org/10.1016/j.cmet.2016.01.011

[113] Ren L et al (2016). Hypoxia-induced CCL28 promotes recruitment of regulatory T cells and tumor growth in liver cancer. Oncotarget 7(46):75763-73.

[114] Hagar A et al (2018). Muscular endurance and progression rates of early-stage invasive ductal carcinoma: A pilot study. Breast J 24(5): 849-851

[115] Hagar A, Melo L, Hills G, Kenshur N, Dickinson S. (2020) A new aerobic fitness score based on lactate sensing during submaximal exercise. Appl Physiol Nutr Metab. 45(7):784-792. doi:10.1139/apnm-2019-0739

[116] Semenza GL (2016). The hypoxic tumor microenvironment: A driving force for breast cancer progression. Biochimica et Biophysica Acta 1863(3): 382-391. https://doi.org/10.1016/j.bbamcr.2015.05.036

[117] Hojman P, Gehl J, Christensen JF, Pedersen BK (2018) Molecular mechanisms linking exercise to cancer prevention and treatment. Cell Metabolism 27(1): 10-21. doi:10.1016/j.cmet.2017.09.015

[118] Shitara K and Nishikawa H. (2018), Regulatory T cells: a potential target in cancer immunotherapy. Ann NY Acad Sci. 1417: 104-115. doi:10.1111/nyas.13625A.

[119] Mendelsohn J et al (2015) The Molecular Basis of Cancer. Sounders, USA, pp. 274

[120] Kather JN et al (2018). Topography of cancer-associated immune cells in human solid tumors. eLife 7: e36967. https://doi.org/10.7554/eLife.36967

[121] Casciari JJ et al (1992). Variations in tumor cell growth rates and metabolism with oxygen concentration, glucose concentration, and extracellular pH. Journal of Cellular Physiology 151(2): 386-394

[122] Wagner BA, Venkataraman S, Buettner GR. The rate of oxygen utilization by cells. Free Radical Biology and Medicine. 2011 Aug 1;51(3):700-12.

[123] McMurtrey RJ (2016). Analytic models of oxygen and nutrient diffusion, metabolism dynamics, and architecture optimization in three-dimensional tissue constructs with applications and insights in cerebral organoids. Tissue Engineering Part C: Methods. 1;22(3):221-49.

[124] Petrova V, Annicchiarico-Petruzzelli M, Melino G, Amelio I (2018) The hypoxic tumour microenvironment. Oncogenesis 7(1):10. https://doi.org/10.1038/s41389-017-0011-9

[125] Bashkatov AN, Genina EA, Sinichkin YP, Kochubey, VI, Lakodina NA, & Tuchin VV. (2003). Glucose and mannitol diffusion in human dura mater. Biophysical journal, 85(5), 3310–3318. https://doi.org/10.1016/S0006-3495(03)74750-X

[126]. Serganova I, Rizwan A, Ni X, Thakur SB, Vider J, Russell J, Blasberg R, Koutcher JA (2011) Metabolic imaging: a link between lactate dehydrogenase A, lactate, and tumor phenotype. Clinical Cancer Research. 17(19):6250-61.

[127] Porterfield JS, Burke DC, Allison AC (1960). An estimate of the molecular weight of interferon as measured by its rate of diffusion through agar, Virology 12(2): 197-203. https://doi.org/10.1016/0042-6822(60)90194-X.

[128] McKeown SR (2014). Defining normoxia, physoxia and hypoxia in tumours—implications for treatment response. The British journal of radiology. 87(1035):20130676.

[129] Ligibel JA, Dillon D, Giobbie-Hurder A et al (2019). Impact of a pre-operative exercise intervention on breast cancer proliferation and gene expression: results from the pre-operative health and body (PreHAB) study. Clin Cancer Res. 25(17): 5398-5406.

[130] Li X, Gruosso T, Zuo D, Omeroglu A, Meterissian S, Guiot MC, Salazar A, Park M, Levine H (2019). Infiltration of CD8+ T cells into tumor cell clusters in triple-negative breast cancer. Proceedings of the National Academy of Sciences. 116(9):3678-87.

[131] Fischer DG, Hubbard WJ, Koren HS (1981). Tumor cell killing by freshly isolated peripheral blood monocytes. Cellular immunology. 58(2):426-35.

[132] Hagar A et al (2019). Endurance training slows breast tumor growth in mice by suppressing Treg cells recruitment to tumors. BMC cancer 19(1): 536. https://doi.org/10.1186/s12885-019-5745-7

[133] Marie LB et al (2020) Voluntary wheel running can lead to modulation of immune checkpoint molecule expression, Acta Oncologica, DOI: 10.1080/0284186X.2020.1817550

[134] Postow MA, Sidlow R, Hellmann MD. (2018). Immune-related adverse events associated with immune checkpoint blockade. NEJM 378(2): 158-168. https://doi:10.1056/NEJMra1703481

[135] Koelwyn GJ, Zhuang X, Tammela T et al (2020) Exercise and immunometabolic regulation in cancer. Nat Metab 2:849–857. https://doi.org/10.1038/s42255-020-00277-4

[136] Rose-John S (2012). IL-6 trans-signaling via the soluble IL-6 receptor: Importance for the pro-inflammatory activities of IL-6. Int. J. Biol. Sci. 8:1237-1247.

[137] Melo L, Hagar A (2019). How to train a mouse. Am J Cancer Res 9(6):1246-1253.

[138] Stöggl TL, Sperlich B (2015). The training intensity distribution among well-trained and elite endurance athletes. Frontiers in physiology, 6, 295 https://doi.org/10.3389/fphys.2015.00295

[139] Ben-Shoshan J et al (2008). Hypoxia controls CD4+CD25+ regulatory T-cell homeostasis via HIF1α. Eur. J. Immunol. 38: 2412-2418. https://doi:10.1002/eji.200838318

[140] Zhang X, Meng X, Chen Y, Leng SX, Zhang H. (2017) The Biology of aging and cancer: frailty, inflammation, and immunity. Cancer J. 23(4):201-205. doi:10.1097/PPO.0000000000000270

[141] Rothschilds AM, Wittrup KD (2019). What, why, where, and when: bringing timing to immuno-oncology. Trends in Immunology. 40(1): 12-21. https://doi.org/10.1016/j.it.2018.11.003

[142] Andersson P, Ostheimer C (2019). Editorial: Combinatorial approaches to enhance anti-tumor immunity: focus on immune checkpoint blockade therapy. Frontiers in Immunology. 10:2083. https://doi.org/10.3389/fimmu.2019.02083

[143] Feuillet F, Lina B, Rosa-Calatrava M, Boivin G. Ten years of human metapneumovirus research. Journal of Clinical Virology. 2012 Feb 1;53(2):97-105.

[144] Russell CJ, Penkert RR, Kim S, Hurwitz JL. Human metapneumovirus: a largely unrecognized threat to human health. Pathogens. 2020 Feb;9(2):109.

[145] Geiser J, Boivin G, Huang S, Constant S, Kaiser L, Tapparel C, Essaidi-Laziosi M. RSV and HMPV Infections in 3D Tissue Cultures: Mechanisms Involved in Virus-Host and Virus-Virus Interactions. Viruses. 2021 Jan;13(1):139.

[146] Moe N, Krokstad S, Stenseng IH, Christensen A, Skanke LH, Risnes KR, Nordbø SA, Døllner H. Comparing human metapneumovirus and respiratory syncytial virus: viral co-detections, genotypes and risk factors for severe disease. PLoS One. 2017 Jan 17;12(1):e0170200.

[147] Papenburg J, Hamelin MÈ, Ouhoummane N, Carbonneau J, Ouakki M, Raymond F, Robitaille L, Corbeil J, Caouette G, Frenette L, De Serres G. Comparison of risk factors for human

metapneumovirus and respiratory syncytial virus disease severity in young children. The Journal of infectious diseases. 2012 Jul 15;206(2):178-89.

[148] Louie JK, Schnurr DP, Pan CY, Kiang D, Carter C, Tougaw S, Ventura J, Norman A, Belmusto V, Rosenberg J, Trochet G. A summer outbreak of human metapneumovirus infection in a long-term-care facility. The Journal of infectious diseases. 2007 Sep 1;196(5):705-8.

[149] Semple MG, Cowell A, Dove W, Greensill J, McNamara PS, Halfhide C, Shears P, Smyth RL, Hart CA. Dual infection of infants by human metapneumovirus and human respiratory syncytial virus is strongly associated with severe bronchiolitis. The Journal of infectious diseases. 2005 Feb 1;191(3):382-6.

[150] Pinky L, Dobrovolny HM. Coinfections of the respiratory tract: viral competition for resources. PloS one. 2016 May 19;11(5):e0155589.

[151] The role of viral co-infections in the severity of acute respiratory infections among children infected with respiratory syncytial virus (RSV): A systematic review and meta-analysis. Journal of global health. 2020 Jun;10(1).

[152] Goto H, Ihira H, Morishita K, Tsuchiya M, Ohta K, Yumine N, Tsurudome M, Nishio M. Enhanced growth of influenza A virus by coinfection with human parainfluenza virus type 2. Medical microbiology and immunology. 2016 Jun;205(3):209-18.

[153] Chan KF, Carolan LA, Korenkov D, Druce J, McCaw J, Reading PC, Barr IG, Laurie KL. Investigating viral interference between influenza A virus and human respiratory syncytial virus in a ferret model of infection. The Journal of infectious diseases. 2018 Jul 2;218(3):406-17.

[154] McCullers JA, Rehg JE. Lethal synergism between influenza virus and Streptococcus pneumoniae: characterization of a mouse model and the role of platelet-activating factor receptor. The Journal of infectious diseases. 2002 Aug 1;186(3):341-50

[155] Smith AM, Adler FR, Ribeiro RM, Gutenkunst RN, McAuley JL, McCullers JA, Perelson AS. Kinetics of coinfection with influenza A virus and Streptococcus pneumoniae. PLoS pathogens. 2013 Mar 21;9(3):e1003238.

[156] DaPalma T, Doonan BP, Trager NM, Kasman LM. A systematic approach to virus–virus interactions. Virus research. 2010 Apr 1;149(1):1-9.

[157] Sego TJ, Aponte-Serrano JO, Gianlupi JF, Glazier JA. Generation of multicellular spatiotemporal models of population dynamics from ordinary differential equations, with applications in viral infection. BMC biology. 2021 Dec;19(1):1-24.

[158] Smith AP, Moquin DJ, Bernhauerova V, Smith AM. Influenza virus infection model with density dependence supports biphasic viral decay. Frontiers in microbiology. 2018 Jul 10;9:1554.

[159] Sego TJ, Aponte-Serrano JO, Ferrari Gianlupi J, Heaps SR, Breithaupt K, Brusch L, Crawshaw J, Osborne JM, Quardokus EM, Plemper RK, Glazier JA. A modular framework for multiscale, multicellular, spatiotemporal modeling of acute primary viral infection and immune response in epithelial tissues and its application to drug therapy timing and effectiveness. PLoS computational biology. 2020 Dec 21;16(12):e1008451.

[160] Sego TJ, Mochan ED, Ermentrout GB, Glazier JA. A multiscale multicellular spatiotemporal model of local influenza infection and immune response. Journal of Theoretical Biology. 2022 Jan 7;532:110918.

Curriculum Vitae
Josua Oscar Aponte-Serrano

EDUCATION

Indiana University, Bloomington, Indiana

- Ph.D. in Intelligent Systems Engineering — Aug 2017 – Dec 2021
  Concentration: Bioengineering
  Advisor: James Glazier
  Research Areas: Multiscale Modeling, Computational Bioengineering, Virtual Tissue
- M.S. in Intelligent Systems Engineering — Aug 2017 – Dec 2020
  Advisor: James Glazier
- M.A. in History and Philosophy of Science — Aug 2015 – May 2018
  Advisor: Amit Hagar

University of Puerto Rico, Rio Piedras, Puerto Rico

- M.A. in Philosophy — Aug 2011 – May 2015
  Advisor: Carlos Rojas-Osorio
  Thesis: Scientific Realism and the Structure of Explanatory Inferences

University of Puerto Rico, Mayaguez, Puerto Rico

- B.A. in Philosophy — Aug 2006 – May 2011
  Magna Cum Laude

RESEARCH EXPERIENCE

Intelligent Systems Engineering, Indiana University — Jan 2017 – Dec 2021

- Project**:** Network and Spatial Biological Modeling
  Supervisor: James Glazier

History and Philosophy of Science, Indiana University — Jan 2017 – Jan 2018

- Project: Cancer Metabolism and Immunoregulation
  Supervisor: Amit Hagar

TEACHING EXPERIENCE

Intelligent Systems Engineering, Indiana University — Aug 2017 – Dec 2021

- Courses: Computational Bioengineering, Network Dynamics

History and Philosophy of Science, Indiana University — Aug 2015 – Jan 2017

- Courses: Scientific Reasoning

Philosophy, University of Puerto Rico — Aug 2011 – May 2015

- Courses: Introduction to Philosophy

PUBLICATIONS

JOURNALS

J. Aponte-Serrano*, J.J.A Weaver*, T.J. Sego, J.A. Glazier, J.E. Shoemaker. "Multicellular spatial model of RNA virus replication and interferon responses reveals factors controlling plaque growth dynamics" *PLOS Computational Biology,* Sep 2021. doi:https://doi.org/10.1371/journal.pcbi.1008874

T.J. Sego, J. Aponte-Serrano, J.F. Ferrari-Gianlupi, J.A. Glazier "Generation of multicellular spatiotemporal models of population dynamics from ordinary differential equations, with applications in viral infection" *BMC biology*, Dec 2021.19(1):1-24.

J. Aponte-Serrano, A. Hagar, “Run for your life: an integrated virtual tissue platform for incorporating exercise oncology into immunotherapy” *Cancer Immunology, Immunotherapy*, Jan 2021. doi:10.1007/s00262-020-02790-7

T.J. Sego*, J Aponte-Serrano*, J. Ferrari-Gianlupi, SR. Heaps, K. Breithaupt K et al. “A modular framework for multiscale, multicellular, spatiotemporal modeling of acute primary viral infection and immune response in epithelial tissues and its application to drug therapy timing and effectiveness *PLOS Computational Biology*, Biology 16(12): e1008451. https://doi.org/10.1371/journal.pcbi.1008451

A. Hagar, Z. Wang, S. Koyama, J. Aponte-Serrano, L. Melo, S. Vargas, R. Carpenter, J. Foley, “Endurance training slows breast tumor growth in mice by suppressing Treg cells recruitment to tumors” *BMC Cancer*, vol. 19, no. 1, pp. 536, 2019.

COMPUTATIONAL TOOLS

Konstantinopoulos, J. Glazier, J. Aponte-Serrano (2021), ”A Vaccine Model for COVID-19,” https://nanohub.org/resources/covidvaccinemod. DOI: 10.21981/8274-M636.

J. Aponte-Serrano, J Glazier (2020), ”COVID-19 R0 Estimator,” https://nanohub.org/resources/r0estimator2. DOI: 10.21981/8Z8N-JD89.

J. Aponte-Serrano, T.J. Sego (2020), ”COVID 19 Virtual Tissue Model - Tissue Infection and Immune Response Dynamics,” https://nanohub.org/resources/cc3dcovid19. DOI: 10.21981/Q058-ZK57

CONFERENCES

J. Aponte Serrano Talk: “Integrating Validated Models of Viral Replication and Interferon Signaling into a Multi-Scale Spatial Framework to Identify Key Factors of Viral Infection Dynamics
Society of Mathematical Biology Annual Conference Jun 2021

J. Aponte Serrano, J. Glazier, Poster: “A Workflow for Replicating Computational Research in Biomechanics”, *at Southern California Systems Biology Conference*
Irvine, CA. Feb 2019

WORKSHOPS

Systems Modeling in the Pharmaceutical Industry - Problem Solving Workshop
Fields Institute, Toronto, ON Aug 2019

Hands-on Workshop on Computational Biophysics, National Center for Multiscale Modeling of Biological Systems
Pittsburgh, PA May 2019

Short Course in Systems Biology: Foundation for Interdisciplinary Careers, Center for Complex Biological Systems
University of California, Irvine, CA May 2018

CompuCell3D 12th User Training Workshop - Biocomplexity Institute
Bloomington, IN Aug 2017

AWARDS

Luddy Research Award, Luddy School of Informatics, Computing and Engineering

- In recognition of excellent performance in the domain of research in the school 2021

HSF Scholar, Hispanic Scholarship Fund
- For outstanding academic performance 2016

Honor Enrollment, University of Puerto Rico
- For attaining a GPA higher than 3.50 2007 – 2011

PROFESSIONAL AFFILIATIONS

Society for Industrial and Applied Mathematics
Society of Mathematical Biology
Philosophy of Science Association

CAMPUS ACTIVITIES

Academic Senate, University of Puerto Rico
- Student Senator Aug 2013 – May 2014

University Accessibility Center, University of Puerto Rico
- Academic Support Coordinator Aug 2009 – May 2011

LANGUAGES

Spanish: Native
English: Fluent

SKILLS

Python, Matlab, Mathematica, C++, LaTex, CompuCell, Tellurium, COPASI

INTERESTS

Bioengineering, Computational Biology, Modeling and Simulation, Scientific Computing, Martial Arts